INVESTIGATIONS ON ULTRAWIDEBAND FRACTAL MICROSTRIP PATCH ANTENNA ARRAYS FOR MIMO WIRELESS COMMUNICATION APPLICATIONS

A Thesis

Submitted in fulfilment of the requirement for the award of the degree

of

DOCTOR OF PHILOSOPHY

in

Electronics and Communication Engineering

Submitted By

ARASHPREET KAUR SOHI

Reg. No. 901806014

Under Supervision of

Dr. Amanpreet Kaur

(Associate Professor, ECED)

THAPAR INSTITUTE
OF ENGINEERING & TECHNOLOGY
(Deemed to be University)

DEPARTMENT OF ELECTRONICS AND COMMUNICATION ENGINEERING

THAPAR INSTITUTE OF ENGINEERING AND TECHNOLOGY, PATIALA, 147004

FEBRUARY, 2023

CERTIFICATE

I, **Arashpreet Kaur Sohi** hereby declare that the work contained in the thesis entitled **"INVESTIGATIONS ON ULTRAWIDEBAND FRACTAL MICROSTRIP PATCH ANTENNA ARRAYS FOR MIMO WIRELESS COMMUNICATION APPLICATIONS"** being submitted by me to **Department of Electronics and Communication Engineering, Thapar Institute of Engineering and Technology, Patiala** in fulfillment for the award of degree of "**Doctor of Philosophy**" is a record of authentic research world carried out by her under the supervision of **Dr. Amanpreet Kaur**. The matter presented in this thesis does not incorporate any material previously published or written by any other person except where due reference is made in the text. The results obtained in this thesis have not been submitted in part or full to any other institute or University for the award of degree or diploma.

Date: 6|9|2023

Arashpreet Kaur Sohi

Arashpreet Kaur Sohi

Reg. No. 901806014

This is to certify that the above statement made by the candidate is correct and true to the best of my knowledge and belief. She has worked under my supervision and fulfilled the requirements for the submission of this thesis which has reached the requisite standard.

Amanpreet Kaur

Dr. Amanpreet Kaur
Associate Professor
ECED
TIET, Patiala-147001, India

ACKNOWLEDGEMENT

I sincerely thank my creator, the almighty God, for the gift of life, knowledge, and strength to accomplish this work. This research work is by far the most significant accomplishment in my life, and it would be impossible without people who supported me and believed in me. I would like to extend my gratitude and sincere gratitude to my honorable, research advisor, **Dr. Amanpreet Kaur**, for her support and guidance during my study. She is a great professor with deep vision and, most importantly a kind person. She has always been willing to give me insights and pointers to tackle problems along the way, keeping a very keen interest in listening to my problems. She is always there when I needed to see her and attentive when I spoke with her. My respect for her grew and will always grow throughout my entire life. She always pointed me in the right direction when I lost the path and supported me when I was on the right path. I sincerely thank her for her exemplary guidance and encouragement. Her trust and support inspired me to make the right decisions in the most important moments, and I am glad to work with her. I would like to thank **Dr. Alpana Agarwal**, Head of the Electronics and Communication Engineering department, TIET, and all the doctoral committee members for sparing their valuable time for the progress monitoring of my research work and giving such insightful comments which helped me to improve my research from various perspectives. I would also like to thank the facilities provided by Thapar Institute of Engineering and Technology, Patiala, for the successful work. I gratefully acknowledge **Prof. Padmakumar Nair** (Director, TIET, Patiala) and **Dr. Rafat Siddique** (Dean, Research and Sponsored Projects, TIET, Patiala) for allowing me to work under their kind support. I would like to thank my friends for inspiring me and raising the bar.

This thesis is dedicated to my late grandfather, **S. Balbir Singh Sohi**, whose love for me knew no bounds and, who taught me the value of hard work. Next, I would like to thank my husband, who has been a constant source of encouragement and support during this process. A special feeling of gratitude to my loving parents, who have always loved me unconditionally and whose good examples have taught me to work hard for the things that I aspire to achieve. I also dedicate this thesis to my little daughter, **Niyamat,** who have made me stronger, better, and more fulfilled than I could have ever imagined.

TIET, Patiala (Punjab), India

ABSTRACT

Today, people around the globe are acknowledging the significance of wireless technology in their day-to-day activities such as entertainment, education, security and communication. With the tremendous development in the sector of mobile wireless technology (from the current 4G to the upcoming ultra-fast 5G standard), the demand for incorporating high speed, economical, wideband and low-powered ultra-wideband (UWB) antenna in modern wireless devices is increasing substantially. Moreover, the concept of multiple-input multiple-output (MIMO) antenna technology integrated in UWB systems helps to enhance signal-to-noise ratio (SNR) and data transmission speeds in a multipath propagation scenario.

The research presented in this thesis addresses the four major constraints namely miniaturization, large bandwidth, high inter-element isolation and band-notch characteristics while modeling portable UWB-MIMO antennas for the advanced integrated systems. For developing small-sized UWB-MIMO antennas, the application of iteratively generated fractal geometries with the notable attributes of self-similarity and space-filling are employed in the antenna designs. The designed compact fractal antenna arrays are incorporated with defected ground structure (DGS), offset feeding, stub loading and slot etching approaches to excite a large band of operation. The decoupling networks, inter-element spacing and DGS geometries play a vital role to overcome the coupling issue between the neighboring radiators in a compact MIMO configuration. At last, to filter out the unwanted interference caused by the existing licensed applications in the operational UWB range, various notch structures are integrated in the array design.

Objective 1 presents the modeling, simulation, and experimental analysis of six different dual-port MIMO antenna arrays incorporated with different fractals (Sierpinski Gasket, Pythagorean tree, Circular, Koch curve, Koch Snowflake, and Koch Anti-Snowflake) and DGS geometries for UWB characteristics. The first design demonstrates an aperture-coupled Sierpinski gasket fractal (2nd order) MPA array combined with archimedean spiral-shaped and X-shaped DGSs to cover a UWB spectrum of 4.3-11.6 GHz with an acceptable inter-element isolation ($S_{12}/S_{21} \leq -15.8$ dB) and maximal gain of 4.7dBi (at 9.2GHz). In the second design, an aperture coupled MPA array with a 2nd iterative circular fractal and rectangular spiral-shaped DGSs to excite an operational band of 4.6-16.8 GHz with a maximal gain of 4.57dBi (at 6.6GHz) and a high port-to-port isolation ($S_{12}/S_{21} \leq -19$ dB) between the array elements. The third design illustrates an offset-fed aperture coupled, modified Pythagorean tree fractal (2nd order) antenna array

integrated with hexagonal spiral-shaped DGS to cover a wide UWB range of 3.71-10.64GHz with a peak gain of 4.34dBi (at 9.4GHz) and a good degree of inter-port isolation ($S_{12}/S_{21} \leq$-16.1dB) characteristics. The fourth design presents a semi-circular MIMO antenna combined with 2nd iterative Koch-curve fractal and DGS approach to function in 4.395-10.184GHz (79.4% FBW) with a maximal gain of 3.84dBi (at 8.9GHz) and acceptable port-to-port isolation ($S_{12}/S_{21} \leq$-16.1dB) response. In the fifth design, a circular MIMO antenna integrated with a modified Koch-Snowflake fractal (4th iteration), offset-feeding, and DGS technique is designed to operate in a 3.3-18GHz spectrum with a considerable level of isolation ($S_{21}/S_{12} \leq$-16dB) and peak gain of 5.39dBi (at 13.5GHz). In the last design, a compact microstrip-fed Koch Anti-snowflake fractal MIMO antenna integrated with the DGS technique is designed to successfully cover a large frequency band from 2.48-15.42 GHz (144.6% FBW) with a peak gain of 5.16dBi (at 7.48 GHz) and significant degree of isolation ($S_{21}/S_{12} \leq$ -17dB) between the antenna ports. Therefore, the applicability of the above-mentioned antenna arrays to operate in portable UWB communication devices is supported by their compact dimensions, large operational band, high gain, good inter-element isolation, and excellent diversity performance characteristics.

In objective 2, the previously designed two-port Sierpinski gasket and Koch snowflake fractal MIMO antennas (in objective 1) are configured to four-port networks with some modifications in the ground geometry for improved operational bandwidth, port-to-port isolation, and diversity operation characteristics. The first design reports a quad-port, aperture-coupled Sierpinski gasket fractal (iterated to 2nd order) antenna, incorporated with spiral-shaped DGS and offset-feeding approach to effectively resonate in the 3.07-11GHz range. An optimum isolation response between the antenna ports is realized by carefully selecting the center-to-center spacing between the antenna elements and truncating an X-shaped slot from the center of the ground. In the second design, a microstrip-fed, quad-port Koch Snowflake fractal (4th iteration order) MIMO antenna is integrated with the DGSs and feedline modifications (tapering and offsetting) to convert the multi-resonant response generated by fractal geometry into the desired UWB spectrum (3.1-18GHz). A considerable isolation behavior is accomplished by carefully optimizing the separation distance between the array elements and incorporating the decoupling network (vertical ground stubs and semi-circular rings) in the common ground plane.

Objective 3 proposes band-notch functionality in the previously designed two dual-port and two quad-port fractal UWB-MIMO antennas in objective 1 and objective 2 respectively. In the

first design, the dual-port Pythagorean tree fractal (2nd iteration) UWB antenna successfully rejects the three interfering ranges (downlink C-band: 3.81-4.16GHz, WLAN: 5.22-5.84GHz, X-band: 7.84-8.44GHz) coherent in the functional UWB range by incorporating two L-shaped slits, a U-shaped slot, and an SRR pair respectively in each feedline of the proposed array. In the second design, a dual-port modified Koch anti-snowflake fractal (iterated up to 3rd order) UWB antenna is designed for filtering six interfering narrow bands (WiMAX (3.3-3.78 GHz), INSAT (reception: 4.52-4.9GHz), WLAN (5.16-5.84GHz), super-extended C-band (6.3-6.93GHz), ITU-8 (7.63-8.62GHz) and amateur radio (9.96-10.52GHz)) the excited operational band (2.48-15.42 GHz) by integrating a Z-shaped slit (patch), inverted L-shaped slit (patch), pair of L-shaped slits (reduced ground plane), two rectangular SRR pairs (feedline) and G-shaped slot (feedline) in the array design. In the third design, a quad-port aperture-coupled Sierpinski gasket fractal (iterated to 2nd order) antenna effectively eliminates the interference caused by C-band (at 4.01GHz), WLAN (at 5.56GHz), and radio-location (at 8.8GHz) band in the working UWB range by incorporating three distinct notch structures (circular SRRs, U-shaped slot, and rectangular SRRs) into each feedline of the array geometry. In the fourth design, a four-element Koch Snowflake fractal (4th iteration order) UWB array effectively suppresses the interfering C-band (downlink satellite: 4.01GHz), WLAN (at 5.56GHz), (uplink satellite: 6.882GHz), and ITU-8 (at 8.18GHz) from the functional UWB range by loading a modified Z-shaped slot (patch), rectangular SRR pair (reduced ground), rectangular SRR (patch) and U-shaped slot (feedline) in the array design. All the above-reported array designs exhibit admissible values of MIMO metrics like ECC, DG, MEG, CCL, and TARC that justify the application of the proposed arrays in UWB communication systems.

LIST OF PUBLICATIONS

P1 A.K. Sohi and A. Kaur, “A complementary Sierpinski gasket fractal antenna array integrated with a complementary Archimedean defected ground structure for portable 4G/5G UWB MIMO communication devices,” *Microwave and Optical Technology Lett*ers, vol. 62, pp. 2595-2605, 2020, doi: 10.1002/mop.32356. (IF: 1.311)

P2 A.K. Sohi and A. Kaur, “UWB aperture coupled circular fractal MIMO antenna with a complementary rectangular spiral defected ground structure (DGS) for 4G/WLAN/radar/satellite/international space station (ISS) communication systems,” *Journal of Electromagnetic Waves and Applications*, vol. 34, no. 17, pp. 2317-2338, 2020, doi: 10.1080/09205071.2020.1813638. (IF: 1.438)

P3 A.K. Sohi and A. Kaur, “A novel modified Koch-Snowflake fractal MIMO antenna for 4G/5G UWB communication gadgets,” *Microwave and Optical Technology Lett*ers, vol. 65, pp. 311-319, 2023, doi: 10.1002/mop.33479. (IF: 1.311)

P4 A.K. Sohi and A. Kaur, “Triple band-stop characteristics from an aperture coupled modified Pythagorean tree fractal-based UWB-MIMO antenna integrated with complementary hexagonal spiral defected ground structure,” *AEU - International Journal of Electronics and Communications*, vol. 137, 153805, 2021, doi: 10.1016/j.aeue.2021.153805. (IF: 3.169)

P5 A.K. Sohi and A. Kaur, “Sextuple band rejection functionality from a compact Koch anti-snowflake fractal UWB-MIMO antenna integrated with split-ring resonators and slots,” *AEU - International Journal of Electronics and Communications*, vol. 138, 153898, 2021, doi: 10.1016/j.aeue.2021.153898. (IF: 3.169)

P6 A.K. Sohi and A. Kaur, “Triple band-reject functionality from a four-element, offset-fed fractal UWB MIMO antenna incorporated with split ring resonators and U-shaped slot,” *Arabian Journal for Science and Engineering*, ACCEPTED. (IF: 2.807)

P7 A.K. Sohi and A. Kaur, “Slot and SRR-Loaded Quad-port, Hen-shaped Fractal UWB-MIMO Antenna with Quad Band-Reject Ability for Handheld 4G/5G Wireless Devices,” *Iranian Journal of Science and Technology, Transactions of Electrical Engineering*, ACCEPTED. (IF: 1.89)

OTHER PUBLICATIONS

1. A.K. Sohi and A. Kaur, “Hexa-band suppression characteristics from a fork-shaped UWB-MIMO antenna loaded with complementary split-ring resonator and slots,” *Journal of*

Electromagnetic Waves and Applications, vol. 34, no. 16, pp. 2194-2219, 2020, doi: 10.1080/09205071.2020.1809533. (IF: 1.438)

2. A.K. Sohi and A. Kaur, “Computational analysis of a dual-port semi-circular patch antenna combined with Koch curve fractals for ultra-wideband systems,” *Engineering Reports*, vol. 3, e12378, 2021, doi: 10.1002/eng2.12378.
3. A.K. Sohi and A. Kaur, "Compact-sized, Dual-element MIMO antenna together with Partial and Defected Ground Structure for 4G/5G UWB applications," *2022 3rd International Conference on Smart Electronics and Communication (ICOSEC)*, Trichy, India, 2022, pp. 583-589, doi: 10.1109/ICOSEC54921.2022.9951926.

LIST OF ABBREVIATIONS

1G	First Generation
4G	Fourth Generation
5G	Fifth Generation
IoT	Internet of Things
SNR	Signal-to-Noise Ratio
UWB	Ultrawideband
FCC	Federal Communications Commission
FBW	Fractional Bandwidth
MIMO	Multiple-Input Multiple-Output
MRC	Maximal-Ratio Combining
EGC	Equal-Gain Combining
SC	Selection Combining
SISO	Single-Input Single-Output
SIMO	Single-Input Multiple-Output
MISO	Multiple-Input Single-Output
ECC	Envelope Correlation Coefficient
DG	Diversity Gain
MEG	Mean Effective Gain
CCL	Channel Capacity Loss
TARC	Total Active Reflection Coefficient
2D	Two Dimensional
3D	Three Dimensional
MPA	Microstrip Patch Antenna
DGS	Defected Ground Structure
MTM	Metamaterial
SRR	Split Ring Resonator
CLL	Capacitively Loaded Loop
IFS	Iterated Function System
EMI	Electromagnetic Interference
WLAN	Wireless Local Area Network
WiMAX	Worldwide Interoperability for Microwave Access
GSM	Global System for Mobile Communication

ITU	International Telecommunication Union
INSAT	Indian National Satellite System
CSRR	Complementary Split Ring Resonator
IMT	International Mobile Telecommunication
RFID	Radio-Frequency Identification
Wi-Fi	Wireless Fidelity
LTE	Long Term Evolution
SAR	Specific Absorption Rate
UHF	Ultra-High Frequency
UMTS	Universal Mobile Telecommunication System
AMC	Artificial Magnetic Conductor
PCS	Personal Communication Services
MEMS	Microelectromechanical System
ISM	Industrial, Scientific, and Medical
ATC	Air Traffic Control
CPW	Coplanar Waveguide
VNA	Vector Network Analyzer
EM	Electromagnetic
CST MWS V’18	Computer Simulation Tool Microwave Studio Version 2018
VPM	Vastu Purusha Mandala
SMA	Sub Miniature Version A
FR	Flame Retardant

LIST OF SYMBOLS

Symbol	**Description**
ρ_e	Envelope Correlation Coefficient
Ω	Ohm
S_{ii}	Reflection Coefficient of the i^{th} and j^{th} port
S_{jj}	Isolation between the ‘i’ and ‘j’ ports
α^R	Correlation Matrix
ε_{eff}	Effective Dielectric Constant
ε_r	Relative Permittivity/Dielectric Constant
f_r	Resonant Frequency
$\tan \delta$	Loss Tangent
0th	Zeroth
1st	First
2nd	Second
3rd	Third
4th	Fourth
λ_g	Guided Wavelength
λ_o	Free-Space Wavelength

LIST OF FIGURES

LIST OF TABLES

TABLE OF CONTENTS

CHAPTER 1

INTRODUCTION

1.1 Overview

Wireless communication is one of the most dynamically growing technological sectors over the past few decades. The main aim of this sector is to achieve high-speed mobile communication with enhanced data rates and security [1]. This sector has experienced a remarkable upgrade from first-generation (1G) analog technology (introduced in the 1980s) to the present broadband fourth-generation (4G) wireless systems with the future development of ultra-fast fifth-generation (5G) cellular networks. This evolution towards the 5G technology is to design smart devices with super-fast internet speed, shorter delays, low battery consumption, high security, and reliable connectivity. The unlicensed sub-6GHz band of the emerging 5G technology plays a crucial role in the Internet of things (IoT) based industry applications like automated guided vehicles, surveillance cameras, industrial robotics, sensing systems, head-mounted displays for workers and control services like electricity grids, power plants, etc. [2]

To support more data handling capacity and a high signal-to-noise ratio (SNR), modern wireless devices deploying 4G/5G communication standards require large bandwidth. The ultrawideband (UWB) technology is an appropriate candidate for the present wireless communication scenario as it exhibits several inherent benefits such as high bandwidth communication over a wide range of radio spectrum, high data rates, and low power spectral density with highly secure communication. In February 2002, the Federal Communications Commission (FCC) in the United States officially permitted the utilization of an unlicensed radio band from 3.1 to 10.6 GHz with 109.5% fractional bandwidth (FBW) and an emission power restricted to -41.3 dBm/MHz for short-range UWB systems (as shown in Figure 1.1) [3]. The antenna transmission with the emitted signal bandwidth greater than 500MHz or 20% (FBW) of central frequency in this range is termed UWB technology.

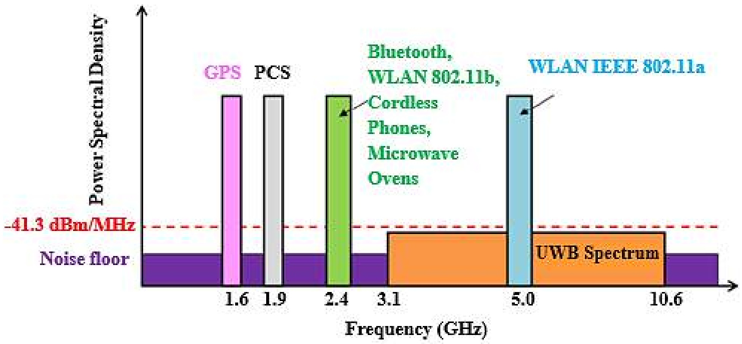

Figure 1.1 Spectrum allocation for UWB applications [3]

The underlying concept of the UWB radio system is to emit and receive ultra-short pulses (in the picosecond range) that comprises all the frequencies simultaneously, yielding a large instantaneous bandwidth in contrast to narrowband systems which send and receive sinusoidal waveforms covering a narrow frequency band. Figure 1.2 shows the frequency and time-domain comparison of the UWB and narrowband communications [4].

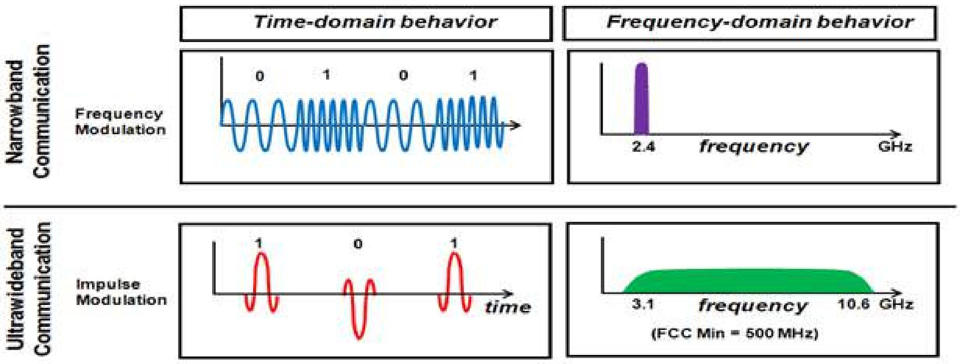

Figure 1.2 UWB versus Narrowband Communication [4]

Besides the commendable characteristics of the UWB technology, data transmissions between the two antennas in the UWB communication system are susceptible to signal reflections and diffraction which results in a multipath fading problem. To address this limitation, multiple-input multiple-output (MIMO) technology is adopted for UWB systems which is discussed in the following section.

1.2 Multiple Antenna Systems

For enhancing the spectral efficiency of the radio communication systems operating in a rich scattering environment, it is necessary to effectively utilize the available frequency bandwidth. Employing numerous antennas at transmission and reception terminals working at the same frequency band, together with the implementation of diversity combining schemes like maximal-ratio combining (MRC), equal-gain combining (EGC) and selection combining (SC) aids in improving the SNR and reliability of the communication system [5]. In the present section, different kinds of antenna technology based on one or more inputs/outputs are examined.

1.2.1 Single-Input Single-Output (SISO)

It is the simplest version of the radio communication link where a single antenna is utilized at the transmitter and receiver ends (as shown in Figure 1.3). In the SISO system, the radio wave traveling in a free space encounters the problem of the multipath fading effect which weakens the signal strength and degrades the overall system performance [6].

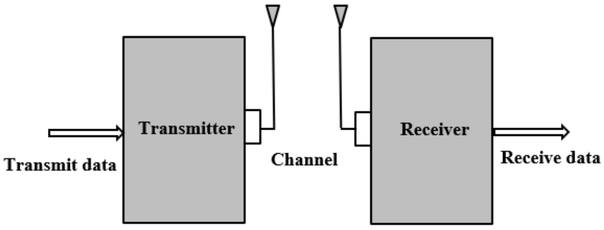

Figure 1.3 SISO System [6]

1.2.2 Single-Input Multiple-Output (SIMO)

In a SIMO system, a single antenna is used for transmission whereas multiple antennas are installed at the receiving end (as illustrated in Figure 1.4). It is also referred to as receive diversity system. The SIMO antenna technology is preferable for short-wave communication to overcome the ionospheric fading and interference effects. It can be easily implemented but requires additional processing at the receiver terminal [7].

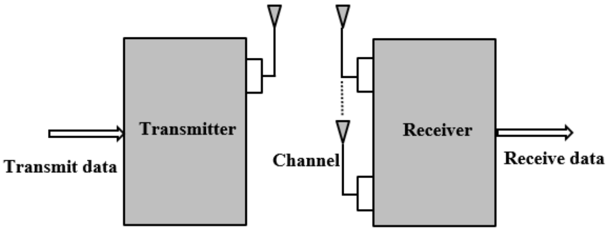

Figure 1.4 SIMO System [7]

1.2.3 Multiple-Input Single-Output (MISO)

In the MISO system, multiple antennas are employed at the transmitter terminal to broadcast multiple copies of the same information redundantly to a single receiving antenna as demonstrated in Figure 1.5. The receiver antenna receives an optimum signal which is then used to extract the original data. It is also referred to as transmit diversity. The MISO technology suffers less path loss and desires a reduced level of processing in comparison with SISO and SIMO methods [7].

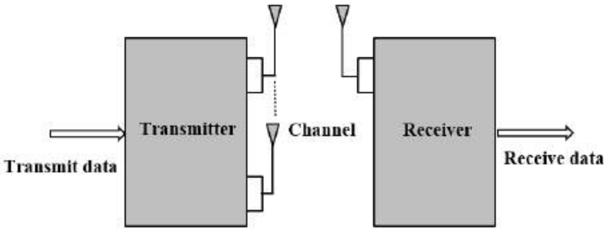

Figure 1.5 MISO System [7]

1.2.4 Multiple-Input Multiple-Output (MIMO)

In the MIMO system, multiple antennas are arranged at the transmission (source) and reception (destination) ends as depicted in Figure 1.6. The MIMO antenna technology takes the advantage of the different radio paths prevalent between the transmit and receive antennas and hence, the data is transferred over many radio paths at the same time. By creating several replicas of the same data, an optimum signal is achieved at the receiver end which enhances the SNR, channel capacity, data throughput capability, and radio link reliability in an environment that is rich in scattering [8].

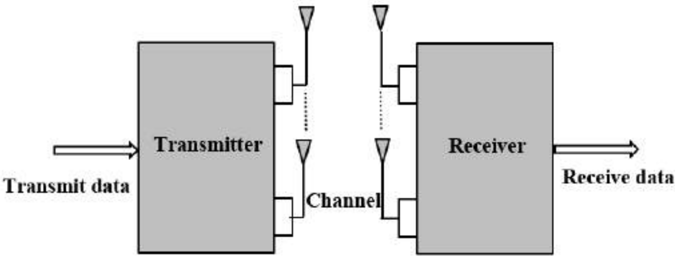

Figure 1.6 MIMO System [8]

1.3 Mathematical parameters governing the MIMO antenna performance

For operation in a rich multipath environment, some fundamental diversity metrics like envelope correlation coefficient (ECC), diversity gain (DG), mean effective gain (MEG), channel capacity loss (CCL), and total active reflection coefficient (TARC) that must be examined for governing the MIMO system performance and are detailed in this section.

1.3.1 Envelope Correlation Coefficient (ECC)

In a MIMO antenna configuration, the amount of mutual coupling between the different antenna radiators and the level of correlation between them in multipath propagation surroundings is assessed by the value of ECC (ρ_e). It is a crucial performance metric defined to evaluate the degree of correlation between the array elements functioning simultaneously in a MIMO configuration. For an uncorrelated diversity antenna system, ideally, the ECC value should be zero while practically ≤ 0.5 is desired for optimum diversity performance [6]. The far-field pattern (for greater accuracy) and scattering parameters (for a large frequency range) are two measures for computing the values of ECC at the antenna ports in any MIMO system [9]. As stated in [10], ECC evaluation using fields radiated by each port of the antenna array (as given in Equation 1), is increasingly complex and requires a longer time to process several data points against the S-parameter approach (assumes lossless array elements operating in the uniform domain) which provides a relatively simple expression and takes less computation time.

$$\rho_e = \frac{\left|\iint \overrightarrow{F_1}(\theta,\phi) * \overrightarrow{F_2}(\theta,\phi)\, d\Omega\right|^2}{\iint \left|\overrightarrow{F_1}(\theta,\phi)\right|^2 d\Omega \iint \left|\overrightarrow{F_2}(\theta,\phi)\right|^2 d\Omega} \tag{1}$$

where F_i (θ, ϕ) is the complex tri-dimensional (3D) field pattern of the antenna where the i^{th} element is energized and the symbols Ω, θ, and ϕ are solid, elevation, and azimuth angles respectively [10].

For a two-port MIMO antenna (N = 2), Equation 2 reports the ECC between port-i and port-j using the S-parameter technique [11].

$$\rho_e(i,j,2) = \frac{\left|S_{ii}^* S_{ij} + S_{ji}^* S_{jj}\right|^2}{(1-(|S_{ii}|^2+|S_{ji}|^2))(1-(|S_{jj}|^2+|S_{ij}|^2))} \tag{2}$$

where S_{ii} and S_{jj} represent the reflection coefficient of the i^{th} and j^{th} port respectively whereas S_{ij} depicts the isolation between the ‘i’ and ‘j’ ports.

1.3.2 Diversity Gain (DG)

In a MIMO communication system, DG is defined as the degree of effectiveness or increase in signal-to-interference ratio when a specific diversity combining scheme is being used. To realize an optimal quality and reliability of a wireless communication system, a high DG (nearly 10) is desired in the working frequency band. It is estimated from the ECC using Equation 3 [12].

$$DG = 10\sqrt{1-\rho_e} \tag{3}$$

1.3.3 Mean Effective Gain (MEG)

To characterize the impact of fading on the performance of any MIMO antenna system, MEG is a vital diversity parameter that can be investigated. MEG is a mathematical tool for estimating the average antenna gain in a real-life fading scenario [13]. By considering a uniform Rayleigh fading scenario with equivalent horizontal and vertical power densities, the MEG for a two-port MIMO antenna can be estimated by the S-parameter technique according to Equation (4, 5). For good channel characteristics, the MIMO antenna which meets the criterion of $|\mathrm{MEG}_i - \mathrm{MEG}_j| < 3$ dB is usually preferred [14].

$$\mathrm{MEG_i} = 0.5(1 - |\mathrm{S_{ii}}|^2 - \left|\mathrm{S_{ij}}\right|^2) \tag{4}$$

$$\mathrm{MEG_j} = 0.5(1 - \left|\mathrm{S_{ji}}\right|^2 - \left|\mathrm{S_{jj}}\right|^2) \tag{5}$$

For more accurate MEG analysis, it can be computed utilizing the far-field approach (Equation 6).

$$\mathrm{MEG} = \int_0^{2\pi}\int_0^{\pi}\left(\frac{\mathrm{XPR}}{1+\mathrm{XPR}}\mathrm{G}_\theta(\theta,\phi)\mathrm{P}_\theta(\theta,\phi) + \frac{1}{1+\mathrm{XPR}}\mathrm{G}_\phi(\theta,\phi)\mathrm{P}_\phi(\theta,\phi)\right)\sin\theta\, \mathrm{d}\theta\, \mathrm{d}\phi \tag{6}$$

where G_θ, G_ϕ represents power gain patterns, XPR is a cross-polarization ratio, and P_θ, P_ϕ are angular density functions of incident power in the respective θ and ϕ directions [15].

1.3.4 Channel Capacity Loss (CCL)

CCL is another important MIMO metric that indicates the highest threshold limit for continuous message transmission across the radio communication link with a loss value of not more than 0.4 bits/s/Hz for the complete working range of the MIMO antenna system [16]. For a two-port antenna, CCL is calculated from the correlation matrix (α^R) using Equations 7 [17].

$$\mathrm{CCL} = -\log_2 \det(\alpha^\mathrm{R}) = -\log_2 \det\left(\begin{bmatrix} 1-(|\mathrm{S_{11}}|^2 + |\mathrm{S_{12}}|^2) & -(\mathrm{S_{11}^*S_{12}} + \mathrm{S_{21}^*S_{12}}) \\ -(\mathrm{S_{22}^*S_{21}} + \mathrm{S_{12}^*S_{21}}) & 1-(|\mathrm{S_{22}}|^2 + |\mathrm{S_{21}}|^2) \end{bmatrix}\right) \tag{7}$$

1.3.5 Total Active Reflection Coefficient (TARC)

For a better representation of MIMO antenna performance in form of operational bandwidth and radiation characteristics, TARC is a crucial diversity metric defined as the square root of total reflected power divided by total incident power [17]. TARC is used to completely compress all the S-parameter details in a single curve for a multi-port antenna design. For good diversity performance, TARC lower than 0 dB is generally required. For the two-port antenna design, the TARC level can be estimated from Equation 8 [18].

$$\mathrm{TARC} = \sqrt{\frac{\left|\mathrm{S_{11}} + \mathrm{S_{12}}e^{j\theta}\right|^2 + \left|\mathrm{S_{21}} + \mathrm{S_{22}}e^{j\theta}\right|^2}{2}} \tag{8}$$

where ‘θ’ corresponds to the input feeding phase angle.

To comply with the demands of the advanced integrated systems, the key design challenges involved while engineering multi-port UWB antennas are a high degree of isolation, compactness, and suppression of the interfering frequency bands pre-existing in the UWB range. The following sections provide a detailed account of various inter-element isolation improvement schemes to reduce mutual coupling between the array elements, microstrip patch antenna (MPA) integrated with fractal geometries for antenna miniaturization and band-notch techniques for filtering the unwanted narrowband applications.

1.4 Isolation Enhancement Techniques for UWB-MIMO Antennas

In a multi-port antenna system, mutual coupling is described as the electromagnetic interactions between the closely-spaced array units. It arises due to the transmit power leakage from the activated antenna to the port of the non-triggered antenna in the array. Due to the space limitations of portable wireless devices, the MIMO configuration with closely arranged radiating elements will eventually give rise to severe mutual coupling between the array elements which severely degrades the array's performance due to the alteration of reflection coefficients, radiation patterns, and input impedance characteristics. The conventional approach of fixing the inter-element distance to λ/2 or greater for mitigating the effect of mutual coupling will result in large antenna dimensions which are not preferable for wireless portable gadgets [19]. Therefore, different approaches available in the literature for boosting the inter-element isolation response amongst the multi-port antenna system are listed in the further subsections of this chapter.

1.4.1 Defected Ground Structure (DGS) Technique

In this technique, the ground is made defected by truncating different kinds of slots (any shape or form) from its surface for realizing an optimum array performance. The defected ground geometry disrupts the shielded surface current distribution and does not involve any extra circuit for its implementation. This isolation technique helps in reducing the array size, improves array gain, provides a good front-to-back ratio, facilitates frequency shift (to cover a wide operational range), and mitigates high mutual coupling between the array elements [20]. In the published research, various DGS configurations such as dumbbell shape [21], Y-shaped [22], fork-shaped [23], H-shaped [24], T-shaped [25], etc., are available for achieving optimal ECC and inter-port isolation characteristics.

1.4.2 Neutralization Line Technique

By employing a metallic strip (with a smaller width) or lumped element, the neutralization line transfers the electromagnetic waves from one array element to the other in a MIMO antenna array system. Therefore, a reversed coupling is developed to reduce the existing electromagnetic coupling between the antenna elements [26]. This technique is simple to implement and aids in designing compact-sized MIMO antennas with a wider frequency bandwidth, enhanced inter-port isolation, and better radiation efficiency response. Adequate selection of path and location for the neutralization line is quite difficult but can be practiced with proper considerations [27].

1.4.3 Parasitic Element Technique

A parasitic element is described as an indirectly linked metallic structure that artificially generates an alternate coupling path between the antenna elements to alleviate the effect of strong mutual coupling between them [28] in a MIMO antenna array system. It is modeled between the array elements to introduce an inductive effect which helps in shifting the frequency range and boosting the isolation performance of the array. Apart from these advantages, the positioning of the parasitic element demands accurate attention and is quite complicated [29].

1.4.4 Decoupling Network Technique

The simplest and most widely used technique for improving the isolation response between the antenna elements is the decoupling network. By introducing negative decoupling, this technique decouples the input ports of neighbouring antenna units intending to mitigate the coupling existing between the neighbouring antennas in a MIMO system. Several types of decoupling networks such as T-shaped [30], F-shaped [31], inverted L-shaped shaped [32], etc., are proposed in the literature for improving the isolation characteristics between the antenna elements of the array. It also offers good far-field performance in terms of high antenna gain and efficiency [19].

1.4.5 Metamaterial (MTM) Technique

Metamaterials (MTM) are defined as materials with negative permittivity/permeability or both. MTMs can be utilized for boosting the isolation properties between the antenna elements of the array, this work owing to the presence of a band gap in the frequency response of the designed metamaterial. These band gaps operate as stop band filters and can mitigate the effect of mutual coupling prevalent between the adjacent antennas [33]. According to the reported literature, the most commonly employed MTM geometries for improving inter-element isolation properties are split ring resonators (SRR), complementary SRR, and capacitively loaded loops (CLL) [34].

Apart from a low mutual coupling between the elements of any array, another main requirement is a compact size for portable antenna gadgets and systems. Use of fractal antenna geometries is one way to achieve the requirement of small size and compact radiating structures.

1.5 Fractal Patch Antennas

The physical size constraints of portable and handheld gadgets pose a challenge to antenna designers to develop small-sized and low-profile MIMO antennas. To meet these specifications, the MPA is a suitable choice due to its innate benefits of low weight, simplicity to fabricate, mechanical robustness, and compact dimensions [35]. The use of fractal geometries in MPAs is one way to obtain the desired parameters of small size and robustness. The word fractal was originally proposed by B.B. Mandelbrot in the year 1997. It is borrowed from the Latin term ‘fractus’ which implies ‘broken’. In general, fractal engineering is a branch of mathematics that supports the law of nature to replicate itself and its statistical characteristics on different scales. The crystals, lightning thunder, snowflakes, tree branches, leaf veins, broccoli, etc. are some of the illustrations to represent the fractal geometries. Therefore, the application of iteratively generated fractal geometries with the notable attributes of self-similarity, self-affinity, and space-filling aids in configuring the compact and wideband UWB-MIMO antennas in a confined space. In contrast to a standard MPA, fractal geometries assist the antenna to resonate at lower frequencies with reduced dimensions. Further, for each increment in fractal iteration, the Q-factor reduces to a level that is not fulfilled by a conventional MPA [36]. The initiator (base stage) and iteration order (added or subtracted) indicate the size of the designed fractal. For any fractal structure, the self-similarity dimension is evaluated using the Hausdorff-Besicovitch dimensionality reported in Equation 9.

$$\mathrm{D} = \frac{\log(\mathrm{N})}{\log(1/S)} \tag{9}$$

here ‘N’ and ‘S’ are the number of scaled-down copies and scaling factor respectively [37].

The fractal geometry is constructed with the help of iterated function system (IFS) mathematical approach. This method works as per the set of affine transformations as given in Equation 2.

$$\mathrm{W}\begin{bmatrix} \mathrm{x} \\ \mathrm{y} \end{bmatrix} = \begin{bmatrix} \mathrm{a} & \mathrm{b} \\ \mathrm{c} & \mathrm{d} \end{bmatrix}\begin{bmatrix} \mathrm{x} \\ \mathrm{y} \end{bmatrix} + \begin{bmatrix} \mathrm{e} \\ \mathrm{f} \end{bmatrix} \tag{10}$$

where the variables ‘a’, ‘b’, ‘c’, and ‘d’ control rotation and scaling whereas the variables ‘e’ and ‘f’ controls the linear translation along the x-y axis [37].

For enhancing the frequency bandwidth of the fractal MPAs, a multi-layered arrangement or DGS technique can be incorporated into the antenna design [38]. The ground is made a DGS by truncating some compact shapes (single/periodic) from its surface which disturbs the shielded current flow and aids in accomplishing a controlled excitation and permits the transmission of the electromagnetic signals across the substrate. Furthermore, MPAs designed in combination with fractal structures provide a greater degree of flexibility to the antenna designers to realize the desired miniaturization and multiband/wideband characteristics from the compact MPAs.

In the published research, several innovative models of fractal geometries are developed to realize miniaturized antenna designs. Some standard fractal geometries reported in the literature are described in the next subsections of this chapter.

1.5.1 Sierpinski Gasket

The design process of the Sierpinski gasket fractal begins with an equilateral triangle (initiator). The 1st iteration of the Sierpinski gasket fractal is constructed by initially dividing the original triangle (0th iteration) into four equal triangles (with sides scaled down by 0.5) by connecting the midpoints of three sides of the initial triangle (0th iteration) and thereafter truncating the interior of the center triangle. Furthermore, the same structural approach is followed for the next iterations so that for each iteration the sides of the triangular slot are reduced by 0.5 as compared to the preceding iterations [37]. According to Figure 1.7, the red and white regions indicate the metal and truncated metal area respectively. The fundamental expression for estimating the resonance ($\mathrm{f}_{\mathrm{m,n}}$) excited by the initial equilateral triangle (0th iteration) is given in Equations (10-13).

$$\mathrm{f}_{\mathrm{m,n,l}} = \frac{2\mathrm{v}_{\mathrm{o}}}{3\mathrm{a}_{\mathrm{o}}\sqrt{\varepsilon_{\mathrm{r}}}}\sqrt{\mathrm{m}^2 + \mathrm{mn} + \mathrm{n}^2} \tag{10}$$

$$\mathrm{a} = \mathrm{a}_{\mathrm{o}} + \mathrm{h}_1(\varepsilon_{\mathrm{r}})^{-1/2} \tag{11}$$

$$\varepsilon_{\mathrm{eff}} = \frac{(\varepsilon_r+1)}{2} + \frac{(\varepsilon_r-1)}{4}\left(1 + \frac{12h_1}{a_o}\right)^{-1/2} \tag{12}$$

$$f_r = \frac{2v_o}{3a\sqrt{\varepsilon_{\mathrm{eff}}}}\sqrt{m^2 + mn + n^2} \tag{13}$$

where 'v_o', 'a_o', '$\varepsilon_{\mathrm{eff}}$', '$h_1$', and 'a' is the light speed, the side length of an equilateral triangle, the effective dielectric constant of the substrate, substrate thickness, and the effective side length of an equilateral triangle respectively, where 'm' and 'n' represent mode indices [39].

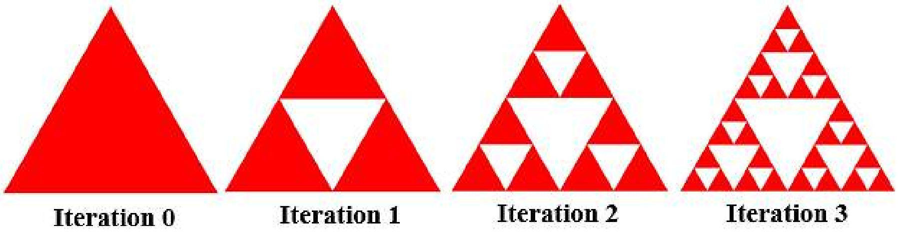

Figure 1.7 Different iteration stages for construction of Sierpinski Gasket fractal [37]

1.5.2 Sierpinski Carpet

The Sierpinski carpet fractal design initiates with a metal square (0th iteration). The 1st iteration of the Sierpinski carpet is generated by initially splitting the original square into nine identical squares (with sides scaled down by 0.333) and thereafter clipping off the interior of the middle square. Further, the 2nd iteration of the Sierpinski carpet fractal is constructed by partitioning each of the remaining eight metal squares into nine smaller squares and removing the middle square from each of the eight metal squares. The same strategy is adopted for the construction of the next iterations of the Sierpinski carpet fractal [40]. The side of the 0th iteration square (initiator) is evaluated using the basic transmission line equations [41]. As represented in Figure 1.8, the black/red region demonstrates the metallic part whereas the white region illustrates the trimmed area from the metal.

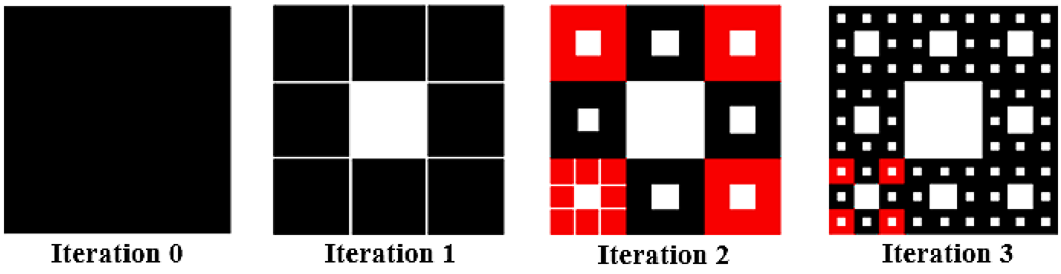

Figure 1.8 Different iteration stages for construction of Sierpinski Carpet fractal [40]

1.5.3 Pythagorean Tree

The construction of the Pythagorean tree fractal begins with the square (0th iteration). The 1st iteration of the Pythagorean tree fractal is developed by arranging two smaller squares (with a scaling factor of 0.707) on a large-sized base square (0th iteration) in such a manner that the three touching squares confine a right-angled isosceles triangle with a steep angle of 45° [42]. The same procedure is further repeated for the succeeding iterations. The resonance (f_r) excited by the Pythagorean tree fractal antenna is evaluated according to Equation 14.

$$f_r = \frac{0.24v_o}{h}\left(\frac{1}{s}\right) \qquad (14)$$

here ‘h’ and ‘s’ represent the height of the largest finger and the scaling factor of the Pythagorean tree fractal respectively [43]. As shown in Figure 1.9, the green colour illustrates the metallic region while the white region represents the dielectric substrate.

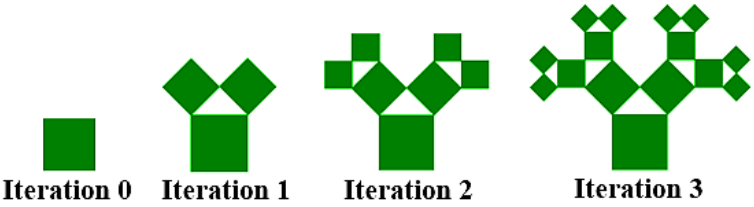

Figure 1.9 Various iteration stages for construction of Pythagorean Tree fractal geometry [43]

1.5.4 Koch Snowflake

The development of the Koch snowflake fractal starts with an equilateral triangle. The 1st iteration of the Koch snowflake fractal design is produced by dividing every side of the 0th-order equilateral triangle (ET) into three equivalent parts and placing a 0.333 scaled-down ET (facing outwards) in the central part of each side. Similarly, the next iteration stages by constructed by repeating this procedure. The expression for computing the resonant frequency ($f_{m,n}$) triggered by the initial equilateral triangle (0th iteration) is given in Equations (10-13) [44]. Figure 1.10 depicts the intermediate iterative stages in the design process of the Koch snowflake fractal where the black/red colour shows the metallic surface.

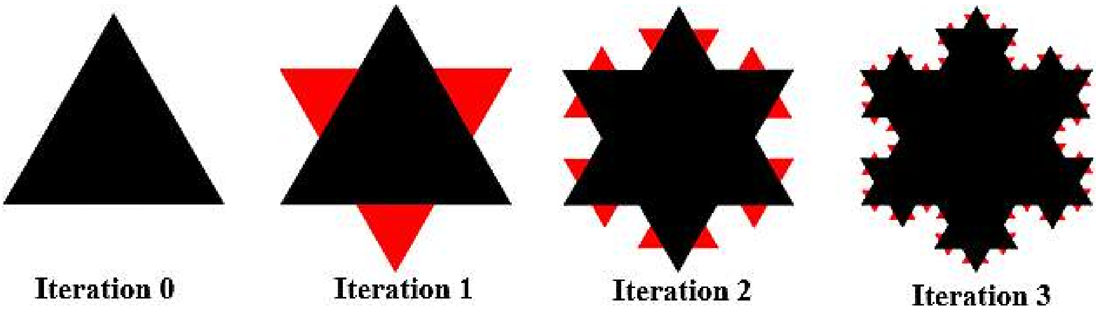

Figure 1.10 Different iteration stages for construction of Koch Snowflake fractal [44]

1.6 Feeding Techniques for Energizing the MPAs

The major techniques for energizing the MPA are categorized as contacting feeds (microstrip line and coaxial/probe feed) and non-contacting feeds (aperture coupled and proximity coupled). In microstrip line feed (as shown in Figure 1.11(a)), the edge of the radiating patch is joined to a conducting strip and has the disadvantage of narrow bandwidth and high surface wave radiations. In coaxial feed (as shown in Figure 1.11(b)), the inner conductor of the coaxial cable passes through the substrate layer and is joined to the patch whereas the outer conductor is connected to the ground. This feeding approach is difficult to implement and results in narrow bandwidth. In aperture-coupled feed, the radiating patch (top of the upper substrate) is triggered by the microstrip feedline (bottom of the lower substrate) through an aperture slot on the ground surface (top of the lower substrate) (as shown in Figure 1.11(c)). This approach provides a wide bandwidth but increases the overall antenna thickness. In proximity coupled feed (as shown in Figure 1.11(d)), the feedline is positioned between the two substrates, and the patch is configured on top of the upper substrate. This feed is hard to fabricate as it increases the overall antenna height [41]. Table 1.1 lists the comparison between the various feeding approaches for MPAs with their respective parameters.

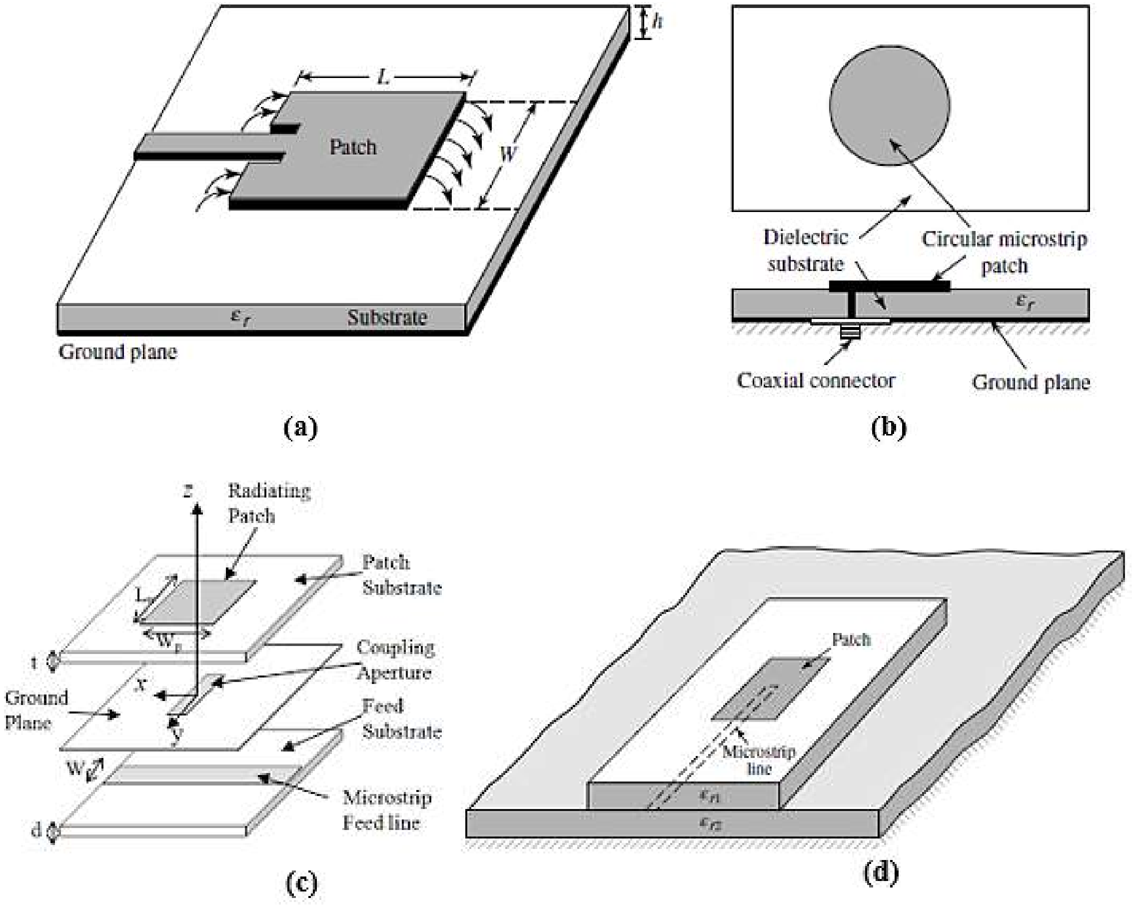

Figure 1.11 Feeding techniques (a) Microstrip Line Feed (b) Coaxial or Probe Feed (c) Aperture Coupled Feed (d) Proximity Coupled Feed [41]

Table 1.1 Comparison of various techniques for feeding MPA [41]

Properties/Feeds	Microstrip-line	Coaxial/Probe	Aperture Coupled	Proximity Coupled
Impedance Matching	Easy	Easy	Easy	Easy
Bandwidth	2-5%	2-5%	13%	21%
Spurious feed radiation	High	High	Low	High
Dependability	Very Good	Poor	Good	Good

Based on the observations from Table 1.1, aperture coupled and microstrip line feed techniques are considered optimum for activating UWB-MIMO antennas in the proposed doctoral research work. In aperture-coupled feed, a good degree of inter-port isolation can be realized as the power is transmitted to the radiating patch from the feed through the aperture ground. This scheme gives moderate spurious radiations with good impedance matching. In contrast to the proximity-coupled approach, the dual layer arrangement of an aperture-coupled MPA offers more options to the antenna designer to adjust a lot of parameters namely aperture length, width, shape, and stub dimensions to achieve the desired antenna performance. The proper selection of the aperture dimensions yields a 70% bandwidth improvement in comparison with other feeding approaches [45]. Another feeding technique; microstrip line feed is simplest to fabricate with low antenna thickness and its disadvantage of narrow bandwidth can be overcome by employing numerous bandwidth enhancement schemes like DGS [46], tuning stubs [47], parasitic structures [48], etc., reported in the literature.

The modeling of UWB fractal antenna arrays for MIMO systems requires a careful design process with a selection of optimized design parameters for a desired operational behavior. However, for some specific wireless communication applications, the MIMO antenna arrays are required to operate in specific bands with the least interference from the nearby bands. This involves the concept of band-notched antenna arrays which is explained in the next subsection of this chapter.

1.7 Concept of Band-Notch Filtering in UWB Antenna Arrays

To satisfy the requirements of modern and handheld electronic equipments, the third key challenge involved while engineering multi-port UWB antennas is the filtering of the electromagnetic interference (EMI) caused by the overlapping narrowband applications in the FCC's regulated 3.1-10.6 GHz range. The traditional approach of joining an antenna with an additional band-stop filter is not preferred for designing compact antennas as it increases the expenses as well as the complexity of the wireless system [49]. Recently in advanced communication systems, great attention is devoted to the designing of compact-sized antennas with multiband suppression ability without any need for extra band-stop filtering circuits. Researchers and antenna designers have reported single [50], dual [51], triple [52], quad [53], penta [54], and hexa [55] band-rejection antennas in literature for surmounting the interference problems in UWB communication systems. The prevalent filtering methods proposed in literature to avoid the negative influence of licensed disturbances in UWB systems includes inserting iron shaped and inverted U-shaped parasitic elements for rejecting 7.8-8.4 GHz for international telecommunication union (ITU) and 5-5.4 GHz for wireless local area network (WLAN) band respectively [56], rod-shaped parasitic structures for mitigating interference caused by WLAN (5.1-5.9 GHz) [57], a pair of rectangular parasitic strips for notching WLAN (5.15-5.9 GHz) [58], a pair of vertical parasitic strips for notching WLAN (5.15-5.85 GHz) [59], inverted T-shaped parasitic structure for WLAN (4.84-5.96 GHz) and worldwide interoperability for microwave access (WiMAX) (3.22-4.06 GHz) suppression [60] or etching two inverted L-shaped slits for notching WLAN (5.1-5.8 GHz) and Indian National Satellite System (INSAT) (6.7-7.1 GHz) bands [61], U-shaped slot for obstructing the interference caused by WLAN band at 5.5 GHz [62], unsymmetrical H-shaped and C-shaped slots for suppressing WLAN (4.8-5.9 GHz) and satellite communication in X-band (7.1-7.9 GHz) [63], C-shaped slot for notching 5.15-5.825 GHz (WLAN) [64], complementary split ring resonators (CSRR) to realize the notch functionality in range from 3.35-3.55 GHz (WiMAX) and 5.65-

5.95 GHz (WLAN) [51], etc. either from the radiating structure, feedline or ground plane have been used in the literature. The proposed doctoral research work also focuses on the design and development of band-notched MIMO antenna arrays for effective communication in the desired sub-bands of the unlicensed UWB (3.1-10.6GHz).

Based upon the literature review carried out in context to the design and development of fractal-based UWB MIMO antenna arrays and band-notched antenna arrays for MIMO communications, a few research gaps have been identified and mentioned in the next subsection of this chapter.

1.8 Research Gaps

A comprehensive literature survey is conducted in chapter 2 on the usage of fractal MIMO MPAs for high data-rate applications in UWB communication systems along with the narrowband interference rejection phenomenon. However, a few research gaps identified during the literature survey are presented below:

1. The formerly reported fractal MPA arrays in MIMO configuration had larger dimensions for their applicability in wireless portable devices except for laptops. The design and development of compact fractal MPA arrays for wireless handheld devices operating in 4G/5G and UWB range is an open area of research.

2. Mutual coupling between the adjacent elements of the MPA array in a MIMO configuration is a major issue of concern. The design of fractal MPA arrays with better isolation properties for UWB communication systems is also an open area of research.

3. The reported fractal geometries for MPA arrays in a MIMO configuration were mainly proposed for multiband/wideband operation since fractal geometries excite multiple resonances. The use of a defected ground geometry, which excites the same or nearby resonances to achieve an increased fractional bandwidth (> 100%) for a UWB of operation from multi-port MPAs is also an open area of research.

4. The literature survey in context to MPA arrays in a MIMO configuration shows that all the available work in this regard was carried out by designing MPAs with a simple microstrip feedline. Based upon the literature survey carried out in context to feeding techniques used with MPAs, it is concluded an electromagnetically coupled feeding mechanism, when used with fractal MIMO arrays offers a wider bandwidth, low cross-polarization levels, and more reliable antenna structures.

5. Unwanted interference caused by nearby narrow bands is also a major concerning factor in the UWB communication systems and needs to be avoided. Special notch structures can be integrated into the design of fractal MIMO MPA arrays to achieve the desired band rejection characteristics.

6. Some novel fractal geometries can be developed for realizing better operational and miniaturization characteristics from the MIMO MPAs.

1.9 Objectives of the Proposed Doctoral Research Work

Based on the research gaps outlined above, some objectives are proposed for the current doctoral research work as below:

1. To design, simulate, fabricate and test some compact fractal microstrip patch antenna arrays in MIMO configuration for portable 4G/5G UWB communication systems (with fractional bandwidth ≥ 100% and high isolation between the radiating elements).

2. To introduce band notch characteristics in the frequency response of the proposed UWB fractal antenna arrays (in MIMO configuration) to overcome the effects of interference between specific wireless communication bands (like WLAN and satellite communication bands).

3. To develop the proposed fractal UWB antenna arrays (2 × 2 MIMO configuration proposed in objective 1) to four-port networks in order to improve the diversity performance characteristics of the proposed arrays (like ECC, DG, CCL, MEG) for better operation in a receive diversity scheme.

1.10 Research Contribution

According to the above stated research objectives, the fundamental contribution of this thesis is to initially excite a multi-resonant response from the recursively generated fractal geometries and then utilize the concept of aperture-coupled feed, tapered and offset feeding, and DGS techniques resonant at the same bands to excite a UWB response from the designed array in a 2 × 2 and 4 × 4 configurations respectively. Chapter 3 and Chapter 4 present the design and development of 2 × 2 and 4 × 4 fractal arrays for UWB systems respectively. Secondly, to filter out the interfering narrow bands pre-existing in the UWB range for specific wireless communication applications, various notch elements are incorporated in the array design. Chapter 5 presents the design and development of band-notch fractal MIMO antenna arrays.

1.11 Thesis Organization

The major goal of this thesis work is to evidence the feasibility of some novel fractal MIMO antenna arrays for UWB communications. Since some specific applications require the least interference from the nearby bands, these are also designed with band-notch functionality for the application in 4G/5G portable UWB communication devices. The underlying information required for carrying out this research work is gained from the manuscripts published in several standard journals on UWB-MIMO communication systems and fractal engineering.

This thesis work is arranged into six chapters where each chapter initially provides a brief introduction about the work to be carried out and at the end concludes with the realized results.

Chapter 1: Introduction

This chapter provides a basic introduction to MIMO antennas integrated with fractal geometries for UWB applications. The chapter details some standard fractal geometries formerly published in the literature. To function in portable UWB devices, various techniques for accomplishing a high degree of inter-port isolation, compactness, and band-notch operation are also elaborated in this section. Research gaps based on published research, objectives and research contribution for the proposed doctoral research are also detailed in this chapter.

Chapter 2: Literature Survey

The formerly reported research carried in context to the multiband/wideband fractal MPA, UWB fractal MPA, band-notch UWB fractal MPA, fractal MIMO MPA for multiband/wideband, fractal MIMO MPA for UWB operation, and fractal UWB-MIMO MPA with band-notch capability are highlighted in this chapter. Lastly, the chapter conclusion stating the motivation to achieve the proposed objectives are also detailed in this chapter.

Chapter 3: Dual-Port Fractal MIMO Antennas for UWB Communication Systems

This chapter deals with the first objective of the proposed research work, mentioning the modeling, simulation, and experimental analysis of six different designs of two-port MIMO antenna incorporated with different fractals (Sierpinski Gasket, Pythagorean tree, Circular, Koch curve, Koch Snowflake, and Koch Anti-Snowflake) and DGS geometries, triggered by microstrip-feed and aperture coupled feeding approaches. The designed antenna arrays successfully realize the desired antenna performance in terms of compactness, UWB of operation, acceptable values of inter-element isolation, and diversity parameters (ECC, DG, MEG, CCL, and TARC). The fabricated arrays are tested for S-parameters and radiation characteristics using a vector network analyzer (VNA) and an anechoic chamber respectively. Simulated results present a good match with the measured ones which justifies their suitability for portable 4G/5G UWB communication systems.

Chapter 4: Four-port Fractal MIMO Antennas with Improved UWB and Isolation Characteristics

This chapter covers the third objective of the doctoral study, presenting the design and development of the proposed two-port Sierpinski gasket and Koch snowflake fractal MIMO antennas (in objective 1) to four-port networks with improved operational bandwidth, port-to-port isolation, and diversity characteristics by incorporating some modifications in the ground. The fabricated arrays are tested for S-parameters (VNA) and far-field (anechoic chamber) where a good match with simulated results verifies their potency for UWB-MIMO applications.

Chapter 5: Band-Notch Functionality from the Designed UWB Fractal MIMO Antennas

This chapter addresses the second objective of the research work. The two-port (Pythagorean Tree and Koch Anti-Snowflake) and four-port (Sierpinski Gasket and Koch Snowflake) fractal UWB-MIMO antennas designed in chapter 3 and chapter 4 respectively are integrated with various notch elements to combat the EMI caused by various narrowband applications (namely WiMAX, WLAN, and uplink/downlink satellite bands in C-band and X-band) pre-existing in the excited UWB spectrum. The experimental results (S-parameters, radiation, and diversity parameters) of the fabricated arrays are conducted for validating their real-world operability.

Chapter 6: Conclusion and Future Scope

At last, this chapter draws the conclusion of the research conducted in the proposed doctoral thesis as well as the possible scope of this doctoral study in the near future.

CHAPTER 2

LITERATURE SURVEY

This chapter presents a comprehensive analysis of the research work reported in the literature, in the field of design and usage of band-stop fractal MIMO MPA for UWB communication systems. The literature survey presented in this chapter begins with the investigation of fractal MPAs with multiband/wideband frequency response. As the MPAs integrated with fractal geometries aid in realizing a multi-resonant response, the next subsection of this chapter presents the literature survey in context to the study of fractal MPAs with UWB performance. Some selective frequency bands used for communication purposes suffer from interference from the adjacent bands, therefore band-notch properties are used in MPAs to overcome the interference from nearby frequency bands. The literature survey then emphasizes the research work available in the field of fractal UWB-MIMO MPAs with band rejection properties for specific narrowband applications.

2.1 Fractal MPAs with Multiband/Broadband Functionality

J.K. Park *et al.* (2008) [65] utilized the concept of recursive fractal structures and reduced ground for modeling the MPA for UWB systems. The antenna patch was constructed using the microstrip-fed 2nd iterative rectangular and trapezoidal fractal-based tree structures on a 30 × 20 mm^2 FR4 epoxy substrate with a partial ground surface to yield an FBW of 2.8-6.2 GHz (75.5%) and 2.7-6.4 GHz (81.3%) respectively. The dipole-like radiation characteristics and satisfactory gain (2-2.7 dBi) allow the successful operability of the designed antenna in UWB systems.

G. Srivatsun *et al.* (2011) [66] proposed a low-profile, fractal MPA for multiple wireless standards in communication systems. The antenna was excited using a coaxial-feeding scheme and modeled on an economically available 38.734 × 28.757 mm^2 FR4 substrate (ε_r = 4.4). The antenna design consisted of a rectangular patch that was made defected with 3rd iterative cantor-set fractal configuration to resonate at four frequencies of 1.9 GHz, 2.5 GHz, 2.65 GHz, and 2.66 GHz with maximal gain values of 5.82dBi, 5.04dBi, 4.78dBi and 5.4dBi respectively. The designed antenna proves to be a good candidate for portable devices functioning in wireless L-band.

B.S. Dhaliwal *et al.* (2013) [67] designed and developed a coaxial-fed, cross-stitch-shaped fractal MPA with multiband behavior. The antenna was developed on a 38.4 × 29.8 mm^2 FR4 epoxy substrate where the upper substrate consisted of a 2nd iterative plus-shaped carpet fractal radiator while a full metallic ground was photo-etched on the rear side of the substrate. The proposed antenna resonated at 2.299 GHz, 3.002 GHz, 3.689 GHz, 4.409 GHz, and 5.555 GHz with a maximal gain of 4.6dBi, thereby, making the antenna preferable for Bluetooth, WiMAX, international mobile telecommunications (IMT), C-band satellite and WLAN applications.

A. Reha *et al.* (2015) [68] modeled a CPW-fed tree fractal MPA for multiple wireless applications. The MPA was designed on a 40 × 40 mm^2 dielectric FR4 substrate of 1.6mm height. The antenna patch was composed of a 2nd iterative H-shaped tree fractal structure with a reduction factor of 2. It was noted that with the increasing iterations of the proposed tree fractal, the desired multi-band and broadband characteristics were realized. The designed MPA effectively radiates in the three frequency ranges of 3.86-3.94 GHz, 5.96-7.38 GHz, and 8.2-8.9 GHz with the gain deviating from the range of 0.1-2.8 dBi. Therefore, the proposed MPA is acceptable for wireless systems supporting WiMAX, C-band, WLAN, RFID, and UWB services.

B. Roy *et al.* (2016) [69] structured a microstrip-fed, wideband MPA integrated with a fractal-type DGS technique. The antenna patch exhibited a trigonal-shaped configuration and was photo-etched on a 33.5 × 28.5 mm^2 FR4 substrate with ε_r of 4.4. A rectangular slot combined with a 2nd iterative Koch curve fractal geometry (along its corners and edges) was truncated from the metallic ground surface which allows the antenna to cover the 2.5-6.6 GHz range with the gain values deviating between 2.5-5.8 GHz across the working band. Thus, the compact size, wideband performance, and acceptable gain verify the applicability of the designed antenna for supporting wireless services like WLAN and WiMAX.

J.S. Sivia *et al.* (2017) [70] discussed a microstrip-fed, circular MPA incorporated with fractal slots and a DGS approach suitable for multiband wireless communication systems. The antenna was arranged on a 55 × 46 × 1.57 mm^3 FR4 lossy substrate where the upper substrate surface comprised of a conventional circular radiator defected with cantor set fractals (with 1/3 scaling factor) up to the 3rd iteration order and its rear surface is composed of a reduced ground plane loaded with a semicircular slot. The designed antenna effectively resonates at 1.9 GHz, 3.7 GHz, 6 GHz, and 7.9 GHz frequencies, thereby, making it an adequate candidate for global system for mobile communication (GSM), WiMAX, C-band, and X-band satellite-based wireless applications.

N. Rao *et al.* (2017) [71] designed a novel hybrid fractal MPA with a full ground plane for C-band satellite communication systems. The proposed MPA was printed on a 1.5mm thick Rogers TMM4 substrate, occupying a total area of 66.63 × 66.63 mm^2. The top substrate surface consists of a microstrip-fed rectangular patch defected with 3rd iterative hybrid (Giuseppe Peano and Minkowski) fractal geometries. The antenna design resonated at 3.214 GHz frequency and provided a reduction of 37.25% patch area (with a fractal scaling factor of 0.5) in comparison to the conventional rectangular patch.

Y. Kumar *et al.* (2017) [72] designed a multiband, coaxially-fed, hybrid fractal MPA for operation in future communication networks. The antenna was configured on a 54 × 46 × 1.6 mm^3 FR4 substrate where its top layer consisted of a perturbed hybrid Sierpinski gasket and meander line fractal patch structure with the modified apex angle and a scaling factor of 50° and 1.2 respectively. The modified fractal geometry was developed according to the mathematical IFS technique. The bottom layer of the substrate incorporated an L-shaped metallic ground. The proposed antenna provided a hepta-band frequency response at 2.4 GHz, 4.437 GHz, 5.38 GHz, 7.01 GHz, 7.6 GHz, 8.4 GHz, and 9.09 GHz with the gain values varying in the 6-32 dBi range. The designed antenna is a useful candidate for multiple wireless applications like Bluetooth, WLAN, wireless fidelity (WiFi), ISM, 4G/5G, radio-frequency identification (RFID), and satellite-based applications.

G. Singh *et al.* (2018) [73] modeled a fractal MPA integrated with the DGS scheme for short-range public safety services. The antenna was configured on a 44 × 50 mm^2 dielectric FR4 substrate where the top surface comprised of a Fibonacci word fractal patch geometry iterated up to the 3rd order and the rear surface consisted of a ground plane loaded with two rectangular slots whose position was determined in accordance to the Whale Optimization Algorithm. The antenna design excited two resonant frequencies of 4.9 GHz (4.8-5.1 GHz) and 5.9 GHz (5.8-6.8 GHz) with a maximal gain of 2.3dBi and 4.7dBi in the respective frequency ranges, therefore validating its applicability in public safety wireless systems.

R. Mark *et al.* (2018) [74] proposed a ring fractal antenna integrated with a DGS approach for quad-band wireless applications. The antenna was printed on a 40 × 32 mm^2 FR4 substrate (ε_r = 4.4) where its upper surface comprised of a microstrip-fed 3rd iterative hexagonal nested ring fractal (with 0.734 scaling factor) radiator with a reduced ground slotted with dumbbell-type DGS on its rear surface. The proposed antenna functions in four frequency bands namely 1.69-1.88 GHz, 2.34-2.52 GHz, 3.07-3.59 GHz, and 4.17-6.26 GHz with the corresponding peak gains of 1.6 dBi, 2.15dBi, 2.75dBi, and 3.8dBi. Thus, the proposed antenna is an attractive candidate for wireless devices supporting GSM 1800, WLAN, and WiMAX standards.

S.S. Bhatia *et al.* (2018) [75] configured a novel fractal MPA incorporated with the DGS scheme for wideband operation. The antenna was modeled on a 45 × 44.92 × 1.6 mm^3 FR4 epoxy substrate where the upper substrate layer comprised of a hexagonal-shaped radiator combined with 3rd iterative meander type fractal (0.33 scaling factor) geometries (along its six edges) and seven 'plus' shaped slots (in the center and below the meander fractal elements in the patch configuration) to realize the enhanced the matching performance and realize the desired miniaturization. The lower substrate layer consisted of a partial metallic ground structure integrated with an inverted L-shaped stub on its right edge to excite the operational range of 3-5.48 GHz with a maximal gain of 5.1 dBi, thereby, making the antenna suitable for wireless communication standards namely WiMAX and WLAN.

I.S. Bangi *et al.* (2019) [76] designed a hybrid fractal MPA with the slotted ground for supporting multiple wireless standards. The proposed antenna covers a total area of 41.5 × 37 mm^2 and is photo-etched on a 1.6mm glass epoxy FR4 substrate. The antenna patch was constructed using 1st iteration order of three fractal geometries namely Koch, Minkowski, and Moore curves where the hybrid fractal (Koch and Minkowski) curve was overlayed along the segments of the Moore fractal curve. The back substrate layer consists of a metallic ground defected with a square slot. The antenna resonated at six frequencies (1.67GHz, 2.42GHz, 3.58GHz, 4.55GHz, 7.34GHz, 8.05GHz, and 9.52GHz) with a 20.1 dBi as the peak gain. Thus, the designed antenna is preferable for wireless handheld devices supporting multiple applications like Bluetooth, WiFi, WLAN, WiMAX, satellite, and some military applications.

N. Kaur *et al.* (2019) [77] developed an aperture-coupled fractal MPA with a DGS approach for C-band/X-band satellite/UWB applications. The antenna was developed on two 1.57mm thick FR4 substrates, each occupying an area of 27.5 × 42.5 mm^2, where the upper substrate incorporates the fractal patches and the bottom substrate was composed of a feed network. The top layer of upper FR4 comprised a 2nd iterative plus-shaped carpet fractal radiator with a scaling factor of 0.33. The top of the lower substrate consisted of a full metallic ground defected with an I-shaped slot whereas the microstrip line is printed on the rear side of the lower FR4. The designed antenna provides a quad-band operation in the frequency bands of 3.9-4.08 GHz, 4.8-5.06 GHz, 6.1-6.4 GHz, and 6.93-11.39 GHz with the corresponding bandwidths of 0.18 GHz, 0.26 GHz, 0.3 GHz and 4.46 GHz with a maximal gain value of 4dBi. Hence, the designed antenna is an appropriate candidate for integration in handheld communication systems supporting UWB, wireless sensor networks, and satellite-based and radio-navigation services.

D. Tiwari *et al.* (2020) [78] designed a compact-sized hexagonal fractal MPA with high gain for advanced communication systems. A 50 × 50 mm^2 FR4 substrate ($\varepsilon_r = 4.4$) was utilized for antenna modeling. The radiator geometry was formed using the 4th iterative hexagonal Sierpinski gasket fractal (with a scaling factor of 0.5) structure with a total of 240 fractal triangular slots that minimize the patch area by 68.4%. The antenna was excited using a coaxial feeding scheme and was resonant at six frequencies namely 3.46 GHz, 8.28 GHz, 12.26 GHz, 17.21 GHz, 23.4 GHz, and 26.01 GHz with the respective peak gains of 6dBi, 8.37dBi, 9.65dBi, 9dBi, 7.84dBi, and 9.34 dBi. The multi- frequency characteristics, miniaturized dimensions, and high gain values permit the proposed antenna's operation in wireless communication systems supporting 5G, internet of things (IoT) satellite, and radar services.

P. Iyampalam *et al.* (2020) [79] developed a compact, microstrip-fed fractal MPA with reduced ground for public safety applications. The antenna occupied a size of 35 × 35 mm^2 and was positioned on a 1.6 mm thick FR4 substrate. The square-shaped radiating patch was made defected with the 3rd iterative Sierpinski Knopp fractal with a scaling factor of 0.5. The antenna resonated at 4.97 GHz (4.9- 5.08 GHz) with a maximal gain of 1.6 dBi, therefore, making the antenna design preferable for public safety and emergency management applications.

S. Nallapaneni *et al.* (2021) [80] proposed a microstrip-fed, hexagonal-ring-shaped fractal MPA combined with parasitic structures and the DGS technique for the gain enhancement of multiple wireless applications. The antenna design was printed on a 37 × 28 × 1.6 mm^3 FR4 laminate where its top layer consisted of a 4th iterative nested hexagonal loop-shaped radiator while its rear side comprised of a Y-shaped structure joined orthogonally to the partial ground surface. Further, two semi-hexagonal ring-shaped parasitic elements were embedded in the patch design to improve the gain performance by 2dBi in each frequency range. The designed MPA operated in 1.96-2.22 GHz, 3.51-3.91 GHz, and 4.78-5.26 GHz spectrums with the corresponding gain of 2.07 dBi, 3.73 dBi, and 4.96 dBi, thereby, making the proposed MPA optimum for long term evolution (LTE), 5G, and WLAN applications.

H. Kaur *et al.* (2022) [81] developed a wearable fractal antenna integrated with the defected ground approach for wireless personal area networks. The antenna was configured on 80 × 80 mm^2 denim of thickness 0.56 mm. The top denim surface consisted of a tapered rectangular radiator defected with 2nd iterative hybrid fractal (Sierpinski and Minkowski) structures whereas the rear side comprised of a copper ground defected with a U-shaped slot. The designed antenna supported multiple wireless services like Bluetooth (2.41-2.49 GHz), WLAN (2.4-2.484 GHz, 5.725-5.85 GHz), WiMAX (2.5 GHz, 3.5 GHz, 4.5 GHz), and ISM (2.4-2.484 GHz, 5.15-5.825 GHz) band applications. Based on the specific absorption rate (SAR) investigations, the proposed array was found suitable for integration into future wearable smart watches and many other medical devices.

J.S. Sivia *et al.* (2022) [82] modeled a microstrip-fed, hybrid fractal-based MPA with the fractal-defected ground surface with operation in four wireless communication bands. The antenna was fabricated on an epoxy FR4 substrate with an overall volumetric dimension of 20 × 40 × 1.6 mm^3. The radiator geometry initially comprised two vertically superimposed hexagonal elements whose edges were later integrated with a hybrid fractal generator curve formed by combining the 2nd iterative Koch and Meander fractal curves with an indentation angle of 90° and 60° respectively. The reduced ground was also made defected with two similar hybrid fractal curves along its upper edge. The antenna effectively resonated at 1.6 GHz, 4.8 GHz, 6.9 GHz, 8.8 GHz frequencies with the respective frequency bandwidths of 2.09GHz, 1.36GHz, 0.86 GHz, and 1.51 GHz and offered a maximal gain of 6.85dBi. Hence, the designed antenna is suitable for GSM, 3G/4G, WiFi, Bluetooth, WiMAX, satellite, and radio navigation applications.

G. Bharti *et al.* (2022) [83] developed a compact, microstrip-fed fractal MPA with reduced ground defected with fractal slots for triggering a wide functional range. The antenna was printed on a 24 × 30 × 1.6mm^3 FR4 dielectric substrate where its upper surface was composed of a hexagonal-shaped radiator combined with 2nd iterative Minkowski fractal curves (along its edges) and the rear surface comprised of a reduced ground combined with inverted L-shaped stub and 2nd iterative Minkowski fractal curves (scaling factor of 0.33 and indentation angle of 90°) defected along its tapered corners. The designed antenna covered a large impedance bandwidth of 10.86 GHz (140.1%) and resonated at 4.4GHz, 7.1GHz, 10.8GHz, and 16.3GHz frequencies with a peak antenna gain of 4.54 dBi. Hence, the designed antenna is preferred for handheld wireless systems supporting applications like Bluetooth, WLAN, WiMAX, ISM, radio navigation, and satellite communications.

S. Palanisamy *et al.* (2022) [84] designed an aperture-coupled, novel fractal MPA for application in multiband wireless devices. The antenna was configured on two 50 × 50 mm^2 FR4 substrates with a relative permittivity of 4.4. The top layer of the upper substrate consisted of 2nd iterative three-leaf clove-shaped fractal radiator whereas the lower FR4 comprised of an aperture slot in the ground (top) and a feed combined with a stepped impedance resonator (bottom) for wide bandwidth of operation and minimized mismatch losses. The proposed MPA operated in four frequency ranges of 3.35-3.6 GHz, 5.156-5.825 GHz, 5.7-6.4 GHz, and 7.7-8.5 GHz with the respective peak gains of 7 dBi, 6.5 dBi, 6.2 dBi, and 5.8 dBi at the four bands, making the antenna design suitable for WiMAX, WLAN, intelligent transport systems and ITU-R services.

2.2 Fractal MPAs for UWB Applications

M. Naghshvarian-Jahromi (2008) [85] presented a hexagonal-shaped fractal MPA for wideband operation in three frequency ranges. The MPA was developed on a 70×60 mm^2 Rogers RO4003 substrate of 1.5mm thickness. The radiating element comprises a microstrip-fed, 3rd iterative Penta Gasket Koch configuration while a reduced ground structure was printed on the rear substrate layer. The proposed antenna operated in the 1.5-3 GHz, 6-12 GHz, and

13.5-20 GHz bands with FBW of 66.7%, 66.7%, and 38.8% respectively. The designed MPA exhibited a gain value greater than 4dBi for the three operational ranges which verifies its suitability for a wide range of wireless applications.

R. Kumar *et al.* (2010) [86] designed a CPW-fed square-shaped fractal antenna with reduced ground for UWB applications. The antenna was fabricated on a 71.8× 50 × 1.53 mm^3 FR4 substrate. The patch geometry initially comprised a square-shaped metallic structure, rotated by 45°. Later, a circular structure was trimmed out from the square patch, representing the first iteration level. This process was recursively repeated till the fourth iteration level to realize the needed miniaturization and wideband response. The CPW ground plane was also reduced and combined with two semi-circles of radius 6.4mm and 2.1 mm (each side of the feedline) along the upper edge of the ground. The proposed array works in a 2.235-15GHz (148.15% FBW) spectrum with a peak gain of 5 dBi, thus, validating its suitability for UWB communication systems.

J. Pourahmadazar *et al.* (2011) [43] designed a novel tree-shaped fractal MPA with a reduced ground for UWB applications. The antenna was printed on a 25 × 25 mm^2 FR4 substrate (with 1mm thickness). The patch design initially started with a T-shaped structure which was further combined with a modified 5th iterative Pythagorean tree-shaped fractal geometry (on its top) with a steep angle and scale factor of 10° and 1.24 respectively to generate a large operating range of 2.6-11.12 GHz with a 123.3% FBW. A semi-ellipse-shaped ground was etched on the rear surface of the FR4 to minimize the mismatch losses. It was noted that by increasing the iteration number, the desired matching and bandwidth of operation are realized which makes the proposed MPA suitable for UWB communication systems.

R. Kumar *et al.* (2011) [87] designed a CPW-fed, pentagonal fractal MPA with reduced ground for UWB applications. The antenna was modeled on a 58 × 52.45 × 1.53 mm^3 FR4 dielectric substrate where the radiating patch is formed using a circular monopole with 12 inscribed pentagonal fractal slots (arranged circularly) using the scale-down factor of 0.65. The fractal slots were iterated up to the 4th iteration order where the CPW ground was reduced and rounded at the corners to cover a wide bandwidth of operation from 2.5-15 GHz (142.8% FBW) with the maximal gain of 2.8 dBi across the working range. Thus, the antenna design was found to be appropriate for radar, microwave imaging, and UWB applications.

H. Oraizi *et al.* (2011) [88] developed a hybrid fractal MPA with the DGS approach for wireless communication devices. A square radiating patch was integrated with the 2nd iterative Giuseppe Peano (along the patch edges) and Sierpinski Carpet fractal (in the patch surface) and was developed on a 20 × 25 mm^2 FR4 substrate of 1.6 mm thickness. The proposed MPA was composed of a semi-elliptical ground and was excited using a tapered microstrip feed to cover a wide operating band of 1-15 GHz with good matching performance. An omnidirectional radiation pattern with adequate gain performance permitted the effective functioning of the proposed array in portable wireless gadgets.

R. Kumar *et al.* (2012) [89] modeled a CPW-fed, modified fractal MPA antenna for UWB applications. The antenna was fabricated on a 42 × 46 mm^2 dielectric FR4 substrate with ε_r and thickness of 4.3 and 1.53 mm respectively. In the beginning, the antenna patch comprised an apollonian gasket fractal structure defected with three equivalent circular geometries from its upper, left, and right edges. The fractal radiating unit was recursively iterated up to the 3rd order and rectangular CPW-based ground was integrated with two semicircles (different radii) on each side of the feed. The designed antenna functions in 3-18 GHz (FBW of 142.86%) with a peak gain of 7.9dBi. Therefore, the proposed antenna validated its usefulness in low-cost and portable wireless devices.

M. Susila *et al.* (2014) [90] developed a new circular fractal-based UWB antenna with the DGS technique for wireless communication gadgets. The antenna was designed on a readily available 32 × 34 × 1.6 mm^3 FR4 substrate with ε_r of 4.4. Initially, the upper FR4 layer was composed of a microstrip-fed circular radiator with a radius of 8.5 mm (0th iteration) which was further defected with two self-similar circular fractal (radius of 4 mm) geometry and an arc-shaped slot (just above the feedline) to form the 1st iterative smiley-shaped fractal structure. This iteration process was repeated till 2nd iteration for realizing the desired antenna miniaturization. The rear FR4 surface consisted of a reduced ground plane defected with a rectangular slot (just behind the feed) to excite a wide frequency response from 3.26-10.68 GHz with a 7.42 GHz frequency bandwidth. To minimize the mismatch losses, an N-shaped slit was truncated from the middle of the microstrip feedline. The antenna offered a peak gain and radiation efficiency of 4.83dB and 93.55% respectively. Hence, the designed antenna was found to be a suitable candidate for portable devices operating in wireless scenarios.

S. Singhal *et al.* (2015) [91] presented a CPW-fed, miniaturized, tree-shaped fractal MPA for UWB communication systems. The antenna was printed on a commercial dielectric FR4 substrate with a volumetric size of 18.5× 9.2 × 1.6 mm^3. The patch geometry consisted of 3rd iterative inner tapered Christmas tree-shaped fractal structure with a reduced CPW ground plane. The antenna functioned well in the 4.3-15.5 GHz range with the gain values deviating in the range of 1.39-4.51 dBi, thus, making the proposed antenna suitable for application in compact-sized wireless electronic gadgets.

S. Singhal *et al.* (2017) [92] proposed a miniaturized, asymmetrical-fed, ladder-shaped fractal MPA for UWB communication systems. The antenna was designed on a 16 × 12 × 1.6 mm^2 FR4 substrate where the radiating patch is constructed by combining the four iterations of an H-shaped metallic structure and the CPW-based ground was reduced and defected with two rectangular slots to enhance the bandwidth of operation and minimize mismatch losses. The proposed antenna covered a frequency bandwidth of 4.56-13.1 GHz with an average gain of 2.84dBi. Therefore, the proposed fractal antenna was found to be an appropriate candidate for UWB, ITU, radio navigation, radar, and satellite communication systems.

A.S. Brar *et al.* (2018) [93] modeled a microstrip-fed, modified fractal MPA with the full metallic ground for multiple wireless applications. The proposed antenna was arranged on 118 × 60 mm^2 FR4 substrates of 1.6 mm height. The top surface of the substrate was composed of a 1st iterative modified fractal patch formed by the combination of basic and inverted Minkowski curves. The designed antenna excited twenty-two resonances in the 0.1-8 GHz range with a peak gain of 20.5 dBi, thereby, validating its applicability for operation in ultra-high frequency (UHF), L, S, C, and X-band-based wireless applications.

S. Mohandoss *et al.* (2018) [94] developed a fractal-based patch antenna with the DGS technique for high-speed UWB communications. The antenna was configured on a commercial FR4 substrate with a total volumetric dimension of 32 × 32 × 1.6 mm^3. The upper substrate surface consisted of a microstrip-fed circular radiating element defected with inscribed pentagon-shaped fractal slots (iterated up to 3rd order with a scaling factor of 1.3) whereas the rear side of the substrate was composed of a partial ground structure with DGS. By truncating a U-shaped slot from the feed and tapering the ground corners, a large working range of 2.9-15 GHz (135% FBW) with a maximal gain of 5dBi was realized from the proposed antenna structure.

N. Kaur *et al.* (2020) [95] constructed a microstrip-fed, novel fractal patch antenna with the reduced ground for a wide operational range. The antenna was arranged on 37 × 62 mm^2 FR4 substrates of 1.6 mm thickness. The upper substrate layer was composed of a hexagonal ring-shaped patch embedded with 2nd iterative staircase-shaped fractal geometry whereas the lower substrate surface consisted of a reduced metallic ground. The proposed antenna operated in 1.86-9.6 GHz frequency bandwidth with gain values ranging from 2.9-6.99 dBi. The designed antenna was suitable for portable wireless systems supporting multiple wireless standards like universal mobile telecommunication system (UMTS), WiFi, Bluetooth, WLAN, WiMAX, ITU, and X-band satellite applications.

R. Kumar *et al.* (2020) [96] modeled a microstrip-fed, circular MPA with defected fractal geometry and reduced ground for UWB communication systems. The antenna was photo-etched on a 54 × 35 mm^2 FR4 substrate with 1.6 mm thickness. The circular radiating patch was made defected with hexagonal square (at an angle of 45°) fractal slots up to 3rd iteration order whereas the ground was reduced along the Y-axis to cover a wide functional band of 2.1-13.5 GHz (146% FBW) with a maximal and average gain of 7.2dBi and 3.9dBi respectively. The stable radiation characteristics, large impedance bandwidth, and gain make the proposed antenna acceptable for C-band, X-band, and Ku-band wireless communication applications.

S. Mohanty *et al.* (2021) [97] developed a wideband hybrid fractal antenna integrated with an artificial magnetic conductor (AMC) reflector for enhancing the antenna gain. The antenna was photo-etched on a 24 × 24 mm^2 sized FR4 substrate (ε_r = 4.3), where its top layer incorporated a microstrip-fed hybrid fractal structure formed by the combination of 1st iterative Sierpinski gasket and 2nd iterative Von Koch curve whereas the bottom layer comprised of a reduced and tapered ground with a rectangular slot (just behind the feed). The antenna effectively covered a 61.68% FBW in the spectrum of 3.7-7 GHz. By loading the antenna with Cesaro-shaped AMC, a high gain in a range of 8.7-13.8 dBi was realized which justified the suitability of the proposed antenna for futuristic multi-standard wireless devices.

N. Sharma *et al.* (2021) [98] developed a rhombus-type UWB fractal antenna combined with a stub-loaded and defected partial ground plane. A compact-sized 30 × 24 mm^2 FR4 substrate (ε_r = 4.3) sheet was employed for the antenna fabrication. Initially, the patch design was constructed by superimposing three concentric rings along each side of the microstrip-fed rhombus-shaped patch. Next, the 0th iterative patch design was scaled down by a factor of 0.8 to form the 1st iteration level of the rhombus-shaped element and the process was recursively repeated up till the 2nd iteration stage. To improve operational bandwidth response, the metallic ground was reduced and loaded with six concentric rings (along its upper edge) and an inverted L-shaped stub (along its left end). The antenna offers 167.19% FBW with a peak gain of 6.48dBi. Hence, the miniaturized size and wide frequency bandwidth allowed the successful operation of the proposed antenna in multi-standard portable wireless devices.

M.H. Reddy *et al.* (2022) [99] developed a UWB circular fractal MPA with a partially defected ground surface. The antenna was positioned on a commercially available 45 × 45 mm^2 FR4 substrate of 1.6 mm thickness. The microstrip-fed radiating patch consisted of a circular monopole defected with inscribed square circular fractal up to the 4th iteration order. The copper-based ground surface was reduced and made defected with a vertical slot (just behind the feed) to operate in the 2-10.8 GHz frequency range (137.5% FBW) with a maximum gain of 6.27 dBi. Hence, the designed MPA was preferable for commercial UWB and military applications.

2.3 Fractal UWB MPAs with the Band-Notch Capability

W.J. Lui *et al.* (2005) [100] developed a novel technique of notching an unwanted WLAN band by combining the UWB antenna with a fractal-shaped stub. The designed MPA was fabricated on a 48 ×41 mm^2 FR4 substrate with a height of 1mm. The upper FR4 layer comprised a microstrip-fed patch antenna with a combined square fractal stub on its top whereas the bottom FR4 layer was composed of a metallic ground defected with a rectangular slot. The designed MPA operated in the 2.66-10.76 GHz range with the suppression of the 4.95-5.85 GHz (WLAN) range. The antenna offered adequate radiation performance throughout the working range which verified its suitability for UWB communication systems.

W.J. Lui *et al.* (2006) [101] utilized the concept of fractal DGS to realize a stop-band ability from the compact fork-shaped MPA. The designed antenna was fabricated on a 1mm thick dielectric substrate with 28 × 24 mm^2 dimensions. The fork-shaped radiating patch was activated using a tapered microstrip feed to operate in the 2.85-12 GHz range with a good degree of matching performance. Further, a square-shaped slot with a 2nd iterative Koch fractal boundary was clipped from the metallic ground to notch 4.65-6.4 GHz frequency range. The stable radiation characteristics and an average gain of 2.5 dBi for the working range justify the antenna's operation in UWB devices.

D.O. Kim *et al.* (2011) [102] configured a CPW-fed, band-notched UWB MPA with fractal defects. The antenna was designed with a 0.812mm thick Roger's substrate ($\varepsilon_r = 3.38$) where the top substrate layer was composed of a staircase-shaped radiator defected with 3rd iterative Hilbert curve fractal (just above the feed) along with a partial ground with a rectangular slot (along its upper edge). The proposed MPA effectively resonated in a frequency bandwidth of 2.6-10.6 GHz with the filtration of unwanted WLAN in the range of 5.3-5.8 GHz. A peak gain of 4.5 dBi was realized from the proposed antenna with a sharp reduction in antenna gain (-0.5 dBi) for the WLAN band.

R. Ghatak *et al.* (2011) [103] arranged a CPW-fed, fractal UWB MPA with the WLAN rejection phenomenon. The antenna was designed on a low-cost, 40 × 38 mm^2 FR4 substrate with a 1.59mm height. To realize a wide bandwidth of operation (3-12 GHz), the circular radiating patch was made defected of a 2nd iterative circular Sierpinski carpet fractal configuration while two rectangular slots were clipped from the reduced ground surface. Further, a meandered-shaped slot was trimmed from the patch surface (just above the feed) to suppress the interfering 5.15-5.825 GHz (WLAN) range. The antenna gain showed a variation from 1.85-6 dBi in the working frequency band which justified its potency for UWB communication devices.

A. Karmakar *et al.* (2012) [104] modeled a compact CPW-fed UWB antenna with fractal slots for dual-band suppression characteristics. The antenna was printed on a 25 × 45.75 mm^2 Taconic substrate with 0.795 mm thickness. The antenna patch was then constructed using rectangular, semi-elliptical, and triangular geometries and functioned well in the 2.5-12 GHz range. To combat the interfering WLAN (5.15-5.85 GHz) application, a 2nd iterative Hilbert fractal slot was trimmed from the radiating element. Further, two symmetrical 2nd iterative Hilbert fractal slots were etched from the ground (around the feed) to suppress the unwanted satellite communications in X-band (7.9-8.4 GHz).

Y. Li *et al.* (2012) [105] proposed a compact CPW-fed fractal UWB MPA with band-reject capability. The antenna was fabricated on a 26 × 21 mm^2 FR4 substrate of 1.6 mm thickness. The radiating patch was developed by incorporating the 2nd iterative cantor set fractal in the rectangular patch to achieve the required miniaturization and wideband response. Further, to improve the matching characteristics, two symmetrical rectangular slots with tapered corners were made defected just behind the patch. To notch the interfering WLAN (5-6.3 GHz) application from the operating bandwidth of 2.8-11 GHz, an inverted T-shaped stub was embedded on the top of the rectangular slot. Thus, the designed antenna was suitable for the application in low-cost future wireless devices.

Y.K. Choukiker (2013) [106] designed a microstrip-fed, modified fractal antenna for UWB communication applications with the rejection capability of the WLAN band. The antenna structure was configured on a low-cost 1.6 mm thick FR4 substrate with 34 × 34 mm^2 as the total area. The upper FR4 surface was made up of the modified 3rd iterative Sierpinski square-shaped fractal patch geometry whereas a reduced ground with a vertical slot (just behind the feedline) was printed on the rear side of the FR4 substrate. The inverted U-shaped slot was introduced in the center of the feedline to notch the unwanted WLAN (5-6 GHz at 5.5 GHz) application in the working range of 3.1-10.6 GHz. The gain deviates in the range of 2-5 dBi which justifies the applicability of the designed UWB antenna in future handheld devices.

A. Karmakar *et al.* (2013) [107] developed a compact microstrip-fed UWB patch antenna integrated with fractal defects for triple band-suppression characteristics. The antenna was printed on a 1.6 mm high FR4 substrate, covering a total area of 30 × 35 mm^2. The top FR4 layer was composed of a stair-case-shaped square radiating element whereas a reduced copper ground was printed on its rear surface. The proposed antenna covered a large frequency bandwidth of 2.7-11 GHz (121% FBW) with gain values deviating in the range of 3-4dBi. Further, a 3rd iterative perturbed Hilbert curve fractal was etched from the radiator surface to eliminate the undesired 3.3-4.2 GHz and 5.15-5.825 GHz ranges corresponding to the WiMAX, satellite C-band (downlink) and WLAN applications.

M. Naser-Moghadasi *et al.* (2013) [108] designed a miniaturized CPW-fed fractal UWB MPA with a band-notch operation. The MPA was assembled on a 14 × 18 mm^2 FR4 substrate where its tree-shaped fractal radiating patch was combined with a folded T-type structure (in the middle) to reject the interference associated with WiMAX and C-band applications in 3.3-4.2 GHz. The antenna feed was tapered (on its top) while the ground plane was reduced and defected with the rectangular slots on its edges to operate in the 2.94-11.17 GHz range with 117% FBW. These characteristics of the proposed MPA make it suitable for portable UWB devices that demand low-profile antennas.

R. Ghatak *et al.* (2013) [109] modeled a CPW-fed circular fractal UWB MPA with the WLAN band-stop capability. The MPA was printed on a 58 × 44 mm^2 dielectric FR4 substrate where the circular radiating unit was slotted with 3rd iteration Apollonian fractal geometry based on Descartes's circle theorem. The reduced CPW ground with defected with two inverted L-shaped slits to introduce a notch for the WLAN band (5.125-5.825 GHz) in the functional range of 1-8-10.6 GHz (142% FBW). The omnidirectional far-field pattern and gain variations in the 2-6 dBi range validated the practicability of the proposed MPA for military, medical, and UWB applications.

F.B. Zarrabi *et al.* (2014) [110] proposed a UWB MPA with fractal defects for the suppression of two interfering bands. The antenna was printed on a 45 × 44 × 1.6 mm^3 FR4 dielectric substrate with ε_r of 4.4. The proposed antenna consisted of a microstrip-fed, tapered radiating element with the partial ground structure defected with a vertical slot (just behind the feed) to cover a large functional range of 2.2-12 GHz. Further, 1st iterative semi-Minkowski curve fractal slots were truncated from the patch surface to combat the EMI resulting from C-band (2.85-3.45 GHz at 3 GHz) and WLAN (4.85-5.5 GHz at 5 GHz) applications. The antenna gain fluctuated in the 2-6 dBi range which affirms the antenna’s operation in UWB communication gadgets.

K. Shambavi *et al.* (2014) [111] designed a compact, band-reject fractal MPA for UWB communication devices. The antenna was printed on a commercial FR4 substrate, covering a total area of 30 × 30 mm^2. The microstrip-fed, circular radiating patch was made defected with fractal slots to achieve the desired miniaturization (36%) and wideband frequency response. For the first iteration level, a diamond-shaped square was truncated from the circular patch and the recursive procedure was repeated for four iteration levels. The array ground was reduced and made defected with a square slot (just behind the feed) to cover a wide working band of 3.2-12.4 GHz with 5dBi as the average antenna gain. To suppress the undesired WLAN (5.09 to 5.97 GHz), mushroom-like EBG elements were embedded near the feed network. The compact size, large operational band, and sharp rejection behavior permitted the designed antenna’s integration into UWB devices.

V. Rajeshkumar *et al.* (2015) [112] presented a compact, microstrip-fed, U-shaped UWB fractal MPA for the suppression of unwanted WLAN frequency range. The antenna is printed on 20 × 20 × 1 mm^3 low-cost FR substrate where the upper substrate layer comprises a 3rd iterative U-shaped fractal radiating patch forming a tree-shaped geometry whereas the lower substrate surface incorporated a partial ground structure with a modified triangular CSRR (truncated just the feedline). The designed antenna works in the 2-13 GHz (149% FBW) with the rejection of the WLAN range from 5-6 GHz and gain values varying in the range of 1.25-3.5GHz. The compact dimensions, wider bandwidth, and rejection of interfering WLAN make the designed antenna preferable for future wireless communication systems.

A. Gorai *et al.* (2015) [113] designed a CPW-fed elliptical MPA with triple band rejection performance using fractal-shaped structures. The antenna was fabricated on a 0.8 mm thick Taconic TLY-5 substrate, occupying a total area of 41 × 45 mm^2. The elliptical radiating patch was made defected with a 3rd iterative Sierpinski curve fractal slot (scale down by 1/5) to improve the matching performance in a large frequency bandwidth of 2.8-12 GHz. Further, to notch the undesired WLAN narrow range, a 2nd iterative Kock fractal structure (scale down by 1/3) was etched from the patch surface just above the feedline. By positioning a 2nd iterative Sierpinski curve fractal-based ring resonator at the rear side of the substrate (just behind the feed), a notch at 6.8 GHz corresponding to the RFID range was realized. Further, two symmetrical 2nd iterative Minkowski fractal-shaped slots were etched from the ground to introduce a notch at 8.1 GHz. The designed antenna exhibited a peak gain of 4dBi and stable far-field patterns which affirmed the antenna's operability in wireless communication applications.

B. Biswas *et al.* (2015) [114] proposed a compact fractal UWB MPA with different fractal parasitic structures for WLAN notch operation. The antenna was fabricated on a 33.3 × 24.4 mm^2 FR4 dielectric substrate. The upper FR4 layer incorporated a microstrip-fed half-annular ring-shaped radiator combined with a horizontal C-shaped stub whereas its rear side incorporated a circular parasitic element and partial ground plane slotted with a rectangular defect to operate in a UWB spectrum from 3.1-10.6 GHz. Further, a 2nd iterative binary tree fractal geometry was embedded in the patch design to cover an additional Bluetooth range at 2.45 GHz. To yield a notch corresponding to WLAN (5.15-5.85 GHz) application, three different 3rd iterative fractal curves namely the Minkowski fractal, hybrid fractal (Hilbert and Minkowski), and Sierpinski arrowhead fractal were integrated individually in the antenna design along each side of the feed. The stable far-field patterns and acceptable gain performance in UWB (2.5-6 dBi) and Bluetooth (1-1.5 dBi) bands allow the application of the designed antenna in advanced wireless systems.

F.B. Zarrabi *et al.* (2016) [115] designed a circular UWB antenna defected with fractal slots for filtering three undesired wireless standards. The circular MPA activated with back feeding microstrip-line technique is printed on a 50 × 50 × 1.6 mm^3 glass epoxy FR4 dielectric substrate and covers a wide spectrum of 2-11 GHz. By embedding the combination of 1st iterative Koch fractal and T-shaped stub in the patch geometry, a triple band-stop performance is realized for personal communication services (PCS) at 2 GHz, WiMAX at 3.5 GHz, and WLAN at 5.8 GHz. The proposed antenna's gain deviates in the -3.5dBi to 6.5 dBi range which is suitable for modern UWB communication systems.

S. Tripathi (2016) [116] configured a compact UWB fractal MPA with triple band-reject functionality. The antenna occupied a compact area of 24.5 × 20 mm^2 on a commercial FR4 substrate. The radiator initially comprised of a microstrip fed octagonal shaped element whose edges were later combined with the 2nd iterative Sierpinski fractal geometry to realize the desired compactness and wideband characteristics. The rear FR4 side consisted of a partial ground structure with a vertical slot (just behind the feed) to energize a large frequency bandwidth of 3.1-10.6 GHz. To notch the wireless narrow bands namely WiMAX (3.2-4.1 GHz) and X-band (7.7-8.6 GHz), two C-shaped slots were truncated from the fractal radiating element respectively. Two C-shaped SRRs were etched from the reduced ground (around the feed) to eliminate the interfering WLAN band of 5.1-5.9 GHz. Hence, the proposed antenna serves to be an attractive candidate for handheld UWB systems.

Z. Hu *et al.* (2016) [117] designed a microstrip-fed, tree fractal UWB MPA with dual band-reject capability. The antenna design was assembled on a 30 × 23 mm^2 FR4 substrate with a height of 1mm. The upper FR4 layer consisted of a 3rd iterative rectangular-shaped tree fractal structure while a partial ground defected with rectangular (just behind the feed) and triangular (corners of the ground) slots were printed on the rear FR4 layer. The multi-resonance operation generated by the tree fractal was transformed into a UWB spectrum (2.62-11 GHz) by utilizing the concept of DGS. Further, the notch corresponding to WiMAX (3.3-4.08 GHz) and WLAN (5.04-6.03 GHz) was realized by truncating three U-shaped slots from the patch surface. An acceptable gain characteristic of the designed MPA verified its operation in UWB communication systems.

A. Gorai *et al.* (2017) [118] designed a compact quasi-self-complementary UWB fractal MPA with WLAN rejection ability. The proposed antenna was developed on a 1.59 mm thick FR4 substrate with dimensions of 18.5 × 39 mm^2. The half-hexagonal radiator, combined with 1st iterative Von Koch fractal geometry (along its edges), and a quasi-complementary ground defected with an arc-shaped slot were responsible for enhancing the matching characteristics throughout the functional band of 3.2-12 GHz. Further, to cover the Bluetooth band at 2.4 GHz, a meandered type stub was introduced in the defected ground surface. To suppress the interfering WLAN band, a 1st iterative quadratic fractal structure was truncated from the base of the radiating unit. Acceptable gain and time-domain operation of the MPA verified its applicability for wireless UWB systems.

R. Ghatak *et al.* (2018) [119] configured a miniaturized, CPW-fed, fractal UWB antenna with WLAN band-reject operation. The antenna patch was made up of a hexagonal-shaped radiating unit defected with the 2nd iterative hexagonal-shaped Sierpinski carpet fractal (scaled down by 1/3) geometry and Y-shaped band-notch element. The antenna was printed on an inexpensive 33 × 32 mm^2 FR4 substrate with a height of 1.59 mm. The designed MPA works in the 3-12 GHz spectrum along with the filtration of the 5.15-5.85 GHz (WLAN) range. A peak gain of 6dBi was accomplished from the antenna design which justified its diversified operation in wireless communication systems.

O.B. Safia *et al.* (2018) [120] assembled a CPW-fed, hexagonal UWB MPA defected with a fractal slot for band-stop functionality. The proposed MPA was printed on a 34 × 32.5 mm^2 FR4 substrate of 0.6 mm thickness. The designed hexagonal radiating patch was made slotted with the 5th iterative Gosper Island fractal (on its edges) with a $\sqrt{1/7}$ scaling factor whereas the reduced metallic ground was made defected with a triangular slot (from each corner) to function in the UWB spectrum from 3.1-10.6 GHz. Further, a Gosper Island fractal arm slot is truncated along the edges of the fractal patch to suppress the interfering 4-4.3 GHz band. The designed MPA offers a maximal gain of 6.9 dBi and good radiation characteristics which make it appropriate for futuristic handheld UWB devices.

N. Nemati *et al.* (2019) [121] designed a fractal UWB antenna integrated with the variable band-reject operation. The antenna was photo-etched on a 31.2 × 38.4 mm^2 FR4 substrate where its top surface comprised of an octagonal-shaped patch combined with the 1st iterative Koch curve fractal (along its edges) whereas its bottom layer consisted of a reduced curved ground with a rectangular slot. The antenna provided a UWB of operation in the 2.9-11 GHz range. To realize the band-notch function, two mirror-imaged C-slots are trimmed from the patch surface which is next combined with ten microelectromechanical systems (MEMS) switches to notch six different narrow bands at 5.4 GHz, 5.8 GHz, 6.1 GHz, 7 GHz, 7.9 GHz, and 8.4 GHz.

A.H. Nazeri *et al.* (2019) [122] developed a circular fractal UWB antenna with triple band-suppression ability. The antenna was modeled on a 21 × 25 mm^2 low-cost FR4 substrate of 1.6mm thickness and ε_r of 4.4. The fractal patch configuration was based on the binary tree fractal design where the line segments were replaced by circular units. The final CPW-fed patch design incorporated a 2nd iterative circular fractal geometry to minimize the patch area by 53% and operated in a wide frequency range of 3.1-10 GHz. To notch the interfering bands at 3.6 GHz (WiMAX) and 9 GHz (X-band), a U-shaped slot and C-shaped SRR were etched from the radiating unit. Also, two L-shaped slots (around the feed) are truncated from the reduced CPW-based ground to suppress the unwanted WLAN (at 5.6 GHz) applications. Therefore, the antenna design was supposed to be an appropriate candidate for modern wireless communication systems.

A.S.A. El-Hameed *et al.* (2019) [123] configured a quasi-self-complementary fractal UWB antenna with the elimination of three interfering narrow bands. The top patch layer was formed by the five iterations of the quasi-half of the Pythagorean tree fractal (scaling factor of 0.66) whereas the mirror-image counterpart of the quasi-half tree structure was trimmed from the ground surface. To enhance the matching characteristics, the ground was further loaded with two rectangular slots and a parasitic rectangular stub. The antenna was modeled on a 32 × 16 × 1.5 mm^3 commercial FR4 substrate with ε_r of 4.5. Two U-shaped slots (one in the ground and the other in the feedline) and two modified SRRs (around the feed) were inserted to filter the EMI caused by WiMAX (3.5 GHz), WLAN (5.5 GHz) and X-band satellite (7.8 GHz) bands respectively in the excited 2-11 GHz operational bandwidth. The proposed antenna offers the average gain and radiation efficiency of 2.2 dBi and 96% in the functional range, thereby, justifying the antenna operation for diverse wireless applications.

S.C. Puri *et al.* (2019) [124] modeled a compact, wing fractal MPA for UWB applications along with the elimination of three interfering narrow bands from its frequency range. The MPA was printed on a 36 × 36 × 1.6 mm^3 FR4 dielectric substrate. The microstrip-fed radiating patch was constructed using the 3rd iterative trapezoidal ring fractal geometries while the metallic ground surface was reduced and defected with two parasitic slots (around the feedline) and an arc-shaped slot (just behind the feed) to excite a large functional range of 2.2-10.8 GHz with the peak gain of 3.1 dBi. The notch characteristics corresponding to WiMAX (2.5-2.69 GHz) and C-band (3.3-4.2 GHz) applications were realized by incorporating the combination of third-fourth and second-third trapezoidal rings in antenna design respectively. The simple geometry and compact dimensions validate the usability of the proposed antenna for multiple C-band/UWB/X-band applications.

Q. Zou *et al.* (2021) [125] developed a compact-sized hexagonal fractal UWB antenna with band-notch characteristics. The antenna was photo-etched on a flexible 12.5 μm thick polyimide substrate of dimensions 20.5 × 13.9 mm^2. The fractal patch was constructed using four iterative hexagonal structures, defected with a circular slot using a scaling factor of 0.825 and 30° rotation angle for each new iteration. The CPW-based ground is reduced and made defected with two symmetrical CSRRs (one on each side of the feedline) to suppress the undesired X-band (uplink satellite) in the range of 7.9-8.41 GHz from the excited frequency bandwidth of 3.6-19.08 GHz with an average antenna gain of 3dBi. The proposed MPA was suitable for fusion in flexible and portable wireless electronic devices.

S. Kakkar *et al.* (2021) [126] proposed a CPW-fed, fractal UWB patch antenna with fractal-shaped DGS for the triple band-rejection phenomenon. The antenna was modeled on a 27 × 20 mm^2 FR4 substrate with 1.6mm height and ε_r of 4.4. The square radiating patch is modified to a 2nd iterative fork-shaped tree fractal geometry with the scaling factor of 1/5 whereas the metallic ground was made defected with a square slot (just behind the patch) to excite a 3.45-13.15 GHz frequency spectrum with the gain values greater than 2 dBi for the working range. To introduce a notch corresponding to the 4.42-4.66 GHz, 7.21-8.42 GHz, and 10.12-11.09 GHz narrow bands, 1st iterative meander curve fractals were truncated from the upper ground edge, lower ground edge, and middle of the CPW-feed respectively. Therefore, the meritorious operation of the proposed antenna allowed its effective implementation in emergency management applications.

C.M. Ramya *et al.* (2022) [127] developed a compact, CPW-fed UWB fractal antenna with WLAN rejection capability. The antenna was designed on a 1.6mm thick FR4 substrate with a total area of 28 × 27 mm^2. The initiator for the fractal patch was constructed by overlapping eight circular geometries and truncating the intersection region of the circular geometries. The circular triangular fractal patch geometry was iterated up to five levels with 0.7 as the scaling factor that provided multi-frequency characteristics and the required compactness. Further, by utilizing the concept of stepped feed and truncating two inverted L-shaped slots from the tapered ground surface, a large functional bandwidth range of 2.39-12.28 GHz was attained with the FBW and peak gain of 134.8% and 11.16 dBi respectively. To notch the interfering WLAN (5.45-6.27 GHz) band, a U-shaped slot was clipped off the feed. The compact dimensions, large working range, and EMI suppression functionality allowed for successful antenna implementation in portable 4G/5G UWB communication devices.

L. Zhang *et al.* (2022) [128] developed a CPW-fed, novel bionic-based fractal UWB MPA with the suppression of four unwanted narrow bands. The array was assembled on a 27 × 29 mm^2 FR4 substrate with 0.8 mm thickness. The circular radiating patch was combined with the 2nd iteration of bionic-shaped fractal elements (resulting in coronavirus geometry) whereas the partial ground structure defected with two circular slots to cover a wide functional range of 2.5-15 GHz. Further, to notch the undesired narrow bands namely 3.3-3.6 GHz (WiMAX), 5.1-5.8 GHz (WLAN), 7.1-7.8 GHz (X-band), and 8-9 GHz (ITU-8), four different notch elements like circular SRR (patch), L-shaped (ground), U-shaped (feed) and V-shaped (patch) respectively are embedded in the antenna design. Therefore, the compact size with suitable UWB operation allows the effective application of the antenna in UWB communication systems.

2.4 Fractal MIMO MPAs with Multiband/Broadband Characteristics

Y.K. Choukiker *et al.* (2014) [129] developed a two-port, coaxial-fed hybrid fractal-based MIMO antenna for supporting multiple wireless applications in portable electronic devices. The array was modeled on a 100 × 50 mm^2 FR4 (lossy) substrate where a hybrid fractal patch was printed on its upper surface whereas its lower surface incorporated a reduced ground with a decoupling structure. The conventional square-shaped patch geometry was made defected with a Koch curve (on its bottom) and Minkowski curve (on its top) fractals up to 2nd iteration order (each with 0.5 scaling factor) to support a dual-band operation in the range of 1.65-1.9 GHz (14% FBW) and 2.68-6.25GHz (80%). A T-stub stub along with a rectangular slot was loaded in the reduced ground surface to suppress a high level of mutual coupling ($S_{21}/S_{12} \leq -10$ dB, -15dB in the respective frequency bands) between the array ports.

A. Kaur *et al.* (2019) [39] designed and developed a two-port, microstrip-fed fractal antenna array for wireless MIMO communication systems particularly C-band and military services. The two-element array was modeled on a 136 × 136 mm^2 FR4 substrate where the upper surface comprises two complementary Sierpinski gasket fractal radiators (iterated up to 2nd order) whereas the metallic ground integrated with plus-shaped DGS was printed on its rear surface. The proposed array offered 8.2% FBW in the range of 4.74-5.15GHz with minimum isolation of 10dB in the working range. Acceptable values of diversity metrics like ECC (≤ 0.06) and DG (≥ 9.7) were realized from the proposed array.

A. Peristerianos *et al.* (2016) [130] developed a probe-fed, dual-element fractal MIMO antenna for operation in industrial, scientific, and medical (ISM) and WLAN bands. The array was positioned on a 0.812 thick Rogers RO3003 substrate (121.8 × 61.45 mm^2) where two Hilbert curve fractal radiators with curved corners (iterated up to 2nd order) are printed on the top layer while an L-shaped metallic ground was positioned on the back surface. The proposed array provided a dual-band operation in frequency ranges of 2.4-2.489 GHz and 5-6 GHz with a high degree of inter-port isolation ($S_{21}/S_{12} \leq -20$ dB) and acceptable ECC (≤ 0.1) performance.

J. Guterman *et al.* (2004) [131] designed a two-port fractal MPA array for functioning in multiple wireless applications like GSM 1800, universal mobile telecommunications system (UMTS), and high-performance radio LAN (HiperLAN2). The MIMO antenna was structured on a 100 × 45 mm^2 Duroid 5880 substrate. The upper substrate layer consisted of two probe-fed rectangular patches with Koch curve fractal edges (iterated up to 4th order) and a U-shaped slot to minimize the patch area by 23.8% whereas a finite ground layer is printed on the back of the substrate. The array provided a dual-band operation from 1.74-2 GHz and 5-5.4GHz with an adequate level of isolation between the array ports.

S. Rajkumar *et al.* (2017) [132] proposed a two-port Swastik-arm-shaped MIMO antenna for hepta-band wireless applications. The MIMO antenna was structured on a dielectric FR4 substrate with total dimensions of 82 × 40 × 0.8 mm^3 where the upper substrate consisted of two fractal patches with the full metallic ground on the back layer of the substrate. The Swastik-shaped radiators were combined with the first iteration of hybrid Quadric Koch Island fractal geometry and were excited using the coaxial-feeding technique. The proposed array excited seven frequency ranges of 0.95-1.02 GHz, 1.73-1.79GHz, 2.68-2.85 GHz, 3.66-3.7 GHz, 4.2-4.4 GHz, 5.5-5.65 GHz, and 5.93-6.13 GHz with adequate isolation ($S_{21}/S_{12} \leq$ -17dB) and ECC ($\leq$ 0.05) performance between the array ports, thereby, making it suitable for GSM900, GSM1800, LTE advanced, WLAN and UWB applications.

S. Rajkumar *et al.* (2017) [133] modeled a two-element, pentaband fractal MIMO antenna for ISM wireless services. The array is positioned on a dielectric 50 × 51 mm^2 FR4 substrate where the top layer comprises two coaxial-fed hybrid fractal patches, designed using the combination of modified Dragon curve (3rd iteration) and inverted Koch curve (1st iteration) fractals and the lower layer consisted of a full metallic ground plane. The proposed array excited five resonances at 433 MHz, 2.4 GHz, 3.9 GHz, 4.7 GHz, and 5.8 GHz with $S_{21}/S_{12} \leq$ -16dB across the operating frequency ranges. The array offered a good diversity performance in terms of ECC ($\leq$ 0.01), DG ($\geq$ 9.9), and CCL ($\leq$ 0.4 bits/s/Hz), making it a preferred choice for ISM, fixed satellite-based, and UWB applications.

S. Chouhan *et al.* (2019) [134] designed a two-port, fractal MIMO antenna with DGS for operation in portable electronic gadgets supporting multiple wireless services. The array was structured on a dielectric 37 × 56 × 1.6 mm^3 FR4 substrate where the top surface comprised two microstrip-fed spider-shaped fractal radiators (4th iteration) whereas the back surface consisted of a reduced ground with two Y-shaped stubs. The array effectively resonates in the four frequency ranges of 2.24-2.5 GHz, 3.6-3.99 GHz, 4.4-4.6 GHz, and 5.71-5.9 GHz while keeping the inter-element isolation level less than 10dB across the excited bands. A peak gain and ECC of 2dBi and 0.08 was achieved throughout the working bands, thereby, validating the potency of the proposed array for WLAN, WiMAX, WiFi, Bluetooth, and C-band communication systems.

N. Sharma *et al.* (2021) [135] modeled a two-element, hybrid fractal antenna array for portable electronic devices supporting numerous wireless services. The proposed array was coaxially fed with a full ground plane and was fabricated on a 1.47mm thick dielectric FR4 substrate. The upper substrate layer incorporated two rectangular-shaped radiators whose boundaries were made defected with 1st iterative Koch and Minkowski fractal structures. The proposed array functions in four frequency ranges namely 2.42-2.48 GHz, 3.64-3.72 GHz, 4.3-4.36 GHz, and 5.82-5.94 GHz while keeping a minimum isolation of 17dB between the array ports. A peak gain and minimum ECC value of 4.81dBi and 0.0002 was realized from the array, thereby, making it suitable for mobile devices supporting applications like Bluetooth, Wi-Fi, WiMAX, and HiperLAN.

P.B. Saha *et al.* (2020) [136] designed a four-element, microstrip-fed fractal MIMO antenna with disconnected reduced grounds for WiMAX and X-band satellite applications. The array was arranged on a 68.4 × 52 mm^2 FR4 substrate where its top surface comprised of four symmetric square-shaped patches defected with 3rd iterative Minkowski fractal loops while the partial metallic ground was printed on its rear side. The proposed MIMO antenna supports wireless applications like WiMAX (5.47-5.87 GHz) and X-band-based air traffic control

(ATC) radar systems (7.11-7.48 GHz, 9-9.56 GHz) and maintains a significant degree of isolation ($S_{21}/S_{12} \leq$ -26dB) and ECC ($\leq$ 0.07) between the array ports. A good similitude between the simulation and measurement results verifies the array's operation for next-generation communication gadgets.

M. Alibakhshikenari *et al.* (2019) [137] configured a fractal-based EBG isolator between the radiating elements for suppression of strong inter-port coupling effect. The array was arranged on a 70 × 37 mm^2 FR4 dielectric substrate where its top layer comprised of two closed-spaced microstrip-fed square radiators combined with an EBG based fractal isolator (interlinked Y-shaped structures with upturned T-shaped slot) in the middle and a reduced ground on its rear plane. The array operates in five frequency bands of 8.7-11.7 GHz, 11.9-14.6 GHz, 15.6-17.1 GHz, 22-26 GHz, and 29-34.2 GHz with minimum isolation of 20 dB between the array ports. The antenna gain fluctuates in the 4.7-9.15 dBi range which makes it adequate for X, Ku, K, and Ka-band of applications.

2.5 Fractal MIMO MPAs for UWB of Operation

K. Trivedi *et al.* (2017) [138] modeled a dual-port fractal dielectric resonator antenna array for a wideband operation desired for MIMO wireless applications. The array was designed on a 60 × 60 mm^2 Rogers TMMi substrate where the upper surface consisted of new tree-shaped fractal radiators (iterated up to 3rd order) with a conformal feeding approach where the lower layer comprised of a finite ground surface defected with C-shaped slots. The designed array functioned in the 3.95-10.4 GHz range with 89.9% FBW and an adequate level of isolation ($S_{21}/S_{12} \leq$ -15 dB) between the array elements. A favorable match between the simulated and measured responses validates the array's functionality for wireless MIMO applications.

R. Gurjar *et al.* (2018) [139] configured a dual-port, microstrip-fed, compact self-similar fractal MIMO antenna on a readily available FR4 substrate for UWB communication systems. The two modified Sierpinski carpet fractal (2nd iteration order with 1/3 scaling factor) radiating elements were responsible for realizing a large operational range from 3.1-12.5 GHz and this lowered the patch area by 29% as compared to a simple rectangular structure (0th iteration). A T-shaped stub combined with a vertical slot was integrated into the reduced ground structure to accomplish minimum isolation of 16 dB between the array elements. This array configuration offered a peak gain and ECC of 4dBi and 0.05 respectively.

A.T. Abed (2019) [140] discussed a dual-element fractal MIMO antenna for 3G/4G/WLAN/WiMAX/5G operation in portable communication gadgets. The proposed array was activated by the coplanar waveguide feeding (CPW) approach and printed on a 0.8mm thick FR4 substrate with a total area of 40 × 50 mm^2. The array was composed of two orthogonally-arranged sunflower-shaped fractal (3rd iteration order) radiating elements with a scaling factor of 0.5. It supported a dual-band of operation from 2-2.9 GHz and 5-10 GHz with FBW of 36.7% and 66.6% respectively. The isolation performance between the array ports was enhanced (20 dB) by joining a metallic strip to the outer boundaries of the reduced ground.

S. Singhal (2019) [141] modeled a four-element Christmas tree-shaped fractal antenna for UWB-MIMO applications. The array was arranged on a 1.6 mm thick FR4 epoxy substrate and was energized by the CPW feeding technique. The antenna structure consisted of four orthogonally positioned, microstrip-fed tree fractal (3rd order of iteration) radiators and a reduced ground that was made defected with rectangular slots to operate in a large frequency spectrum of 4.8-19.4 GHz with 120% FBW. A '+' shaped stub (rotated at an angle of 86°) to boost inter-port isolation (15 dB) and ECC (< 0.5) characteristics of the array.

R. Gurjar *et al.* (2019) [142] presented a two-element, microstrip-fed 8-shaped fractal-based MIMO antenna for portable UWB devices. The array was modeled on a 40 × 26 mm^2 Rogers substrate with a thickness of 0.8 mm. For constructing each 8-shaped radiator, the rectangular metallic patch was made defected with two Sierpinski carpet fractal geometries (each with the scaling factors of 1/5 and 1/3 in vertical and horizontal directions respectively) up to the 2nd iteration to lower the patch metallic area by 29.8% and excited a frequency bandwidth of 3-10.6 GHz. A T-shaped ground stub was extended vertically from the reduced ground and was further made defected with five vertical slots to improve the port-to-port isolation ($S_{21}/S_{12} \leq$ -19 dB) and diversity operation characteristics of the array.

S. Bukkawar *et al.* (2019) [143] configured a two-port, square-shaped MIMO antenna with a fractal-inspired decoupling structure for operation in the UWB domain. The array was designed on a 30 × 60 mm^2 Roger's substrate with a dielectric constant (ε_r) of 2.2. The upper substrate layer comprised two square-shaped radiating units loaded with stubs, slots, and SRR that were arranged orthogonally. The reduced ground planes were joined by a symmetrical Sierpinski gasket (iterated up to 2nd order) fractal-inspired isolating structure to suppress the mutual coupling between the array elements and deliver a significant diversity performance. The proposed array covered a wide operational range of 3.1-19GHz with minimum isolation and ECC values of 15 dB and 0.01 respectively. The simulation outcomes present a good similitude with the experimental data and validate its usability for future high data-rate wireless applications.

R. Gurjar *et al.* (2020) [40] designed a novel two-port fractal MIMO antenna for UWB applications. The proposed antenna was configured on a 1.57 mm thick FR4 dielectric substrate where the top layer comprised of two microstrip-fed modified Sierpinski carpet fractal (with the scaling factor of 1/3) radiators and the bottom layer (ground) was composed of a funnel-shaped decoupler with a vertical slot. This fractal geometry (iterated up to 2nd order) was developed according to IFS scheme and reduces the patch metallic area by 59% in contrast to the basic rectangular geometry (0th iteration). The proposed array configuration provided a good UWB operation in the range of 3-12.6 GHz with minimum isolation and maximum ECC of 16.3 dB and 0.05 respectively.

E. A. Andrade-González *et al.* (2021) [144] developed a four-port fractal MIMO antenna for UWB communication systems. The MIMO antenna was developed on an 85 × 85 × 1.27 mm^3 Duroid dielectric substrate. The top substrate layer consisted of four circular radiators defected with inscribed Fibonacci fractal circles to realize the desired miniaturization and wideband performance from the array whereas the lower layer incorporated the reduced ground with DGS configuration to excite an operational range of 3.6-13.8 GHz. The orthogonal arrangement of the radiating elements as well as a parasitic cross-shaped metallic strip (inserted in the middle of the upper substrate layer) are primarily responsible for accomplishing a good degree of inter-element isolation ($S_{21}/S_{12} \leq$ -15dB) response across the functional bandwidth.

A. Mohanty *et al.* (2021) [145] designed a two-port fractal MIMO antenna for application in multi-standard wireless UWB systems. The array was designed on a 1.6 mm thick dielectric FR4 substrate, occupying an overall area of 32 × 64 mm^2. The array consisted of two Koch Snowflake fractal (2nd iteration order) patches with contorted microstrip feeds (upper substrate layer) and a reduced ground with a slotted Π-shaped decoupler (lower substrate layer) to cover a large frequency bandwidth of 2.7-10.5 GHz (118.18% FBW) with a reduced level of coupling between the antenna elements. The array exhibited a significant ECC (≤ 0.17) and CCL (≤ 0.4 bits/s/Hz) performance, therefore, making it a preferred choice for multidisciplinary, portable MIMO communication systems.

A. Mohanty *et al.* (2021) [146] investigated a dual-element, fractal MIMO antenna for UWB applications. The MIMO antenna was modeled on a commercially available FR4 substrate (thickness = 1.6 mm) with a total dimension of 32 × 64 mm^2. The array comprised two orthogonally placed Koch Snowflake fractal (2nd iteration) radiators with contorted feeds and separate reduced ground planes. The proposed array covers a wide frequency bandwidth of 2.4-10.2 GHz (123.8% FBW) while maintaining a good port-to-port isolation ($S_{21}/S_{12} \leq$ -17dB) response without the need for any decoupling structure. A significant diversity performance in terms of low ECC (≤ 0.15), high DG (≥ 9.68), and low CCL (≤ 0.3 bits/s/Hz) was realized which governs the suitability of the designed array for portable UWB sensors and wearable gadgets.

R. Gurjar *et al.* (2021) [147] designed a miniaturized, dual-port U-shaped UWB array integrated with a novel fractal geometry in the reduced ground plane for enhancing the inter-port isolation response. The array was configured on a glass epoxy FR4 substrate (thickness of 0.8 mm) where the upper substrate layer incorporated two microstrip-fed U-shaped radiators whereas its rear surface comprised of a reduced ground with a vertical decoupler combined with a novel complementary 1st iterative Minkowski fractal geometry and a rectangular slot (at its bottom). The designed array operated in a 3.06-13.41 GHz spectrum with 125.68% FBW and provides a minimum port-to-port isolation of 17.4 dB across the working range. The array offered a high gain of 6 dBi at 13.5 GHz with a significant diversity performance operation. The simulated results exhibit a good resemblance with the experimental ones which validates the array's operation in the desired UWB communication system.

H.T. Sediq *et al.* (2022) [148] developed a novel fractal-based, two-port UWB MIMO antenna for operation in the S, C, X, Ku, and K bands of frequencies. The array was fabricated on a 26 × 36 mm^2 FR4 substrate where the upper surface of the substrate comprised of two symmetrically arranged, microstrip-fed, 2nd iterative semi-epsilon shaped fractal geometries whereas its rear surface was composed of a reduced defected ground combined with two mirror-imaged, inverted L-shaped stubs. The proposed array worked in a large bandwidth of 2.26-18.05 GHz with ECC, CCL, and peak gain of <0.004, < 0.3 bits/s/Hz, and 7.8 dBi respectively. The good radiation and diversity operation of the array suggested its successful utilization in 4G/5G UWB communication systems.

2.6 Fractal UWB-MIMO MPAs with Band-Notch Characteristic

J. Banerjee *et al.* (2017) [149] modeled a dual-element, band-reject hammer-shaped UWB array with a fractal slotted ground surface. The array was fabricated on a 26.75 × 41.5 mm^2 FR4 substrate of thickness and ε_r of 1.6 mm and 4.4 respectively. The array was composed of two identical CPW-fed hammer-shaped radiating units with a ground plane defected with the modified Minkowski fractal, iterated up to 3rd order with a scaling factor of 1/3, to excite a wide operational range of 3.1-11.5 GHz with an acceptable level of isolation between the array ports. A pair of rectangular parasitic strips were added on the rear side of the substrate to realize a minimum isolation of 19dB. To realize the band-notch performance corresponding to WLAN (5.15-5.85 GHz) standard, an inverted C-shaped slot was clipped off from the lower edge of each radiating element. Further, two vertical slots were etched from the ground surface to effectively suppress the EMI resulting from WiMAX (3.3-3.7 GHz) and downlink satellite communication in C-band (3.7-4.2 GHz). A maximal gain of 3.88 dBi and low ECC (0.0048) values were realized from the proposed antenna which verified its implementation in UWB MIMO communication systems.

P. Debnath *et al.* (2018) [150] configured a compact, dual-element, band-notched UWB array with a reduced ground incorporated with fractal-shaped units. The two orthogonal-positioned rectangular radiators combined with circular and square slots are printed on a commercial FR4 dielectric substrate with 46 × 46 × 0.8 mm^3 dimensions and were excited using CPW feeds. A parasitic 3rd iterative Minkowski fractal (scale down by 0.33) structure arranged in the middle of the ground along with a 3rd iterative Minkowski fractal ground stub (at an angle of 45°) placed on the top of rectangular decoupler were responsible for enhancing the inter-element isolation ($S_{21}/S_{12} \leq -17$dB) characteristics. To yield a notch at 5.5 GHz corresponding to the WLAN band in the working 3.1-12 GHz, a modified E-shaped element was truncated from the middle of each radiating unit. A low ECC (≤ 0.002) with 4dBi as the average gain was realized for the operational range from the proposed UWB array which justified its potency for UWB-MIMO communication gadgets.

A. Gorai *et al.* (2018) [151] developed a compact, microstrip-fed, two-port fractal MIMO antenna with dual-band elimination ability. The array was printed on a 30 × 41 × 1.59 mm^3 FR4 substrate where the upper surface was composed of two symmetrically positioned quasi-self-complementary circular radiators to cover a wide frequency bandwidth of 2.2-11 GHz with 133.3% FBW and a maximal gain of 4 dBi. To enhance the isolation characteristics, a Hilbert fractal slot (iterated up to 2nd order) was introduced in the reduced ground configuration. To suppress the interference resulting from WLAN (at 5.5 GHz) and X-band satellite communication (at 8.1 GHz), parasitic strips of Levy's fractal geometries are amalgamated near the feed structures.

G. Irene *et al.* (2018) [152] configured a compact, microstrip-fed, dual-port hexagonal-shaped fractal UWB antenna with the rejection of five interfering narrow bands. The MIMO antenna was arranged on a 1.6mm thick FR4 substrate where the top layer consisted of two microstrip-fed, hexagonal radiating patches whose boundaries were made defected with 2nd order Kock curve fractal geometries whereas the rear surface comprised of a metallic ground defected with a ring structure and two slots (just behind the feeds). The array resonated in the frequency range of 3.1-13.6 GHz with $S_{21}/S_{12} \leq$ -19 dB across the excited band. To eradicate the EMI associated with C-band and X-band satellite-based communication ranges (3.7-4 GHz, 5.75-6.05 GHz, 7.45-7.55 GHz, 7.75-7.9 GHz, and 8.025-8.4 GHz) prevalent in the operational UWB spectrum, a spiral-shaped slot is etched from each fractal radiating unit. The proposed array realized a high gain of 5dBi and a minimum ECC of 0.17 throughout the functional bandwidth.

S. Rajkumar *et al.* (2019) [153] developed a quad-element, fractal UWB MPA array with WLAN band-reject ability. The proposed quad-port array exhibited compact dimensions and was fabricated on a 40 × 40 × 1.6 mm^3 Rogers 5880 substrate. The upper substrate surface comprised four, orthogonally positioned, rectangular radiating units, each joined with 1st iteration of a hexagonal molecule fractal on its upper edge while the lower substrate surface incorporated a separate semi-circular metallic ground for each monopole. The proposed array excited a large operational band of 2.4-10.6 GHz with a high degree of inter-element isolation. To yield a notch at 5.4 GHz corresponding to the WLAN band, a C-shaped slot is truncated from each fractal radiator. The designed array exhibited ECC < 0.02 and CCL ≤ 0.2 bits/s/Hz (except for the notched range) which verified the potency of the proposed array for application in modern wireless devices.

A. Bhattacharya *et al.* (2019) [154] modeled a dual-port fractal UWB-MIMO antenna with dual-band rejection capability. The MIMO antenna was configured on a 1.5 mm thick Arlon AR 600 where its upper surface consists of two stepped rectangular radiators combined with 2nd order Koch curve fractal (on its top) and reduced ground with DGS printed in its upper surface. A T-shaped decoupler was erected vertically from the middle of the reduced ground to suppress the high degree of coupling prevalent between the array elements. The designed array effectively operated in the ultrawideband range of 8.6 GHz from 2-10.6 GHz. To combat the EMI caused by WiMAX (at 3.5 GHz) and WLAN (at 5.2 GHz) applications, a U-shaped slot (center of each fractal radiator) and two horizontal stubs (bottom of the T-shaped decoupler) were inserted in the array structure.

R. Sampath *et al.* (2019) [155] developed a dual-element, hybrid fractal MIMO antenna with DGS for portable UWB communication devices combined with the WLAN band-notch feature. The array was configured on a 40 × 20 mm^2 dielectric FR4 substrate (height = 1.6 mm). The upper substrate layer consisted of two microstrip-fed, hybrid fractal radiators, formed by the combination of Sierpinski and Koch curve fractals (iterated up to 1st order) which reduced the patch area by 33%. The proposed array operated in 2.5-11 GHz with gain values greater than 3dBi across the operating bandwidth. A reduced and stepped common ground plane combined with a vertical stub helped in minimizing the strong mutual coupling prevalent between the array ports. A U-shaped slot was truncated from the center of each radiating patch to introduce a notch corresponding to the WLAN band. The array offers significant MIMO performance in terms of ECC (≤ 0.1) and CCL (≤ 0.1 bits/s/Hz) which justifies its suitability for MIMO and higher-density packaging services.

A. Bhattacharya *et al.* (2019) [156] designed a two-port, microstrip-fed fractal UWB-MIMO antenna with WiMAX rejection capability. The MIMO structure was modeled on a 36 × 63 mm^2 Arlon AR600 substrate of height 1mm. The two stepped rectangular radiating elements combined with the 2nd iterative Koch curve fractals on its upper edge were printed on the top layer of the substrate whereas the partial ground plane with stepped slots was etched on the lower layer of the substrate. The designed array effectively excited a frequency range of 3-11.1 GHz with a peak gain of 3.1dBi and an ECC level lower than 0.1 across the working bandwidth. For filtering the unwanted WiMAX range (at 3.5GHz), a rectangular SRR was truncated from each radiating unit. A reasonable resemblance between the simulation and measurement results justifies the array's potency for the portable communication systems operating in the UWB domain.

A. Bhattacharjee *et al.* (2021) [157] developed a two-element, microstrip-fed, fractal UWB-MIMO antenna with dual-band suppression characteristics. The array was developed on Rogers R4350B (dielectric constant of 3.5mm) substrate. The upper substrate surface comprised two tapered-fed, quadrilateral radiating elements defected with 2nd order Koch curve fractals (on the upper edge of each patch geometry) whereas the lower surface incorporated a reduced ground configuration combined with a T-shaped decoupler and two Minkowski curve square-shaped fractal geometries combined on the top of the isolation structure. The designed array successfully functioned in 3.1-20GHz (with 146% FWB) with a good inter-port isolation ($S_{21}/S_{12} \leq$ -16dB) performance across the working range. Further, to eradicate the unwanted WLAN (5.09-5.8 GHz) application, two strips (inclined at 45°) were introduced in the T-shaped isolation element.

Y. Cai *et al.* (2021) [158] designed a highly isolated, orthogonal placed, dual-port fractal-based UWB-MIMO antenna array with triple-band suppression characteristics. The array was fabricated on a 1.6mm FR4 substrate, covering a total surface area of 50 × 30 mm^2. The upper layer of FR4 consisted of two microstrip-fed, rectangular radiating patches defected with slots and 2nd iterative Minkowski fractal structures whereas the rear surface consisted of two independent metallic ground planes with I-shaped stubs to excite the 2.2-10.8 GHz frequency range with ECC lower than 0.01 for the entire band of operation. To notch the undesired WiMAX (at 3.8 GHz), WLAN (at 5.6 GHz), and downlink X-band (at 7.5 GHz), two C-shaped slots and an SRR were etched from each patch configuration.

H. Sudarsan *et al.* (2021) [159] designed a compact, triple-band stop two-element fractal MIMO antenna array with a novel DGS approach for UWB applications. The antenna was printed on a 65 × 35 × 1.6 mm^3 FR4 substrate where its upper layer incorporated two microstrip-fed, 3rd iterative square fractal (0.33 scaling factor) radiating elements and reduced tapered ground loaded with DGS and SRRs. The proposed array operated in 2.35-9.04 GHz frequency bandwidth while maintaining $S_{21}/S_{12} \leq$ -15dB across the working range. The DGS approach and SRR (positioned in the center between two separate ground planes) filter the EMI caused by WiMAX, WLAN, and X-band in the range of 3.4-3.9 GHz and 4.95-6.6 GHz. The adequate diversity performance of the proposed array justified its functioning in wireless communication devices.

B. Punna *et al.* (2022) [160] developed a four-element UWB fractal-based MIMO antenna with dual-band suppression capability. The array covered a total area of 40 × 40 mm^2 and was printed on a readily available 1.6mm thick FR4 substrate. The top substrate surface was comprised of quad orthogonally positioned octagonal-shaped patch antennas incorporated with 2nd iterative Koch fractal configuration along the edges to realize the desired compact dimensions and wideband performance whereas the bottom substrate surface consisted of four separate and reduced ground planes, each made defected with T-shaped slot. The array operated in a large frequency bandwidth of 2.53-12.32 GHz with a high degree of isolation between the antenna elements. To eliminate the EMI resulting from WLAN (5.17-5.88 GHz) and X-band (8.08-9.71 GHz) satellite applications, C-shaped and U-shaped slots were trimmed from each fractal radiator. The array design exhibited considerable diversity characteristics in terms of ECC ≤ 0.0013 and TARC ≤ -2.97 dB which validates its operation in portable wireless systems.

A. Mohanty *et al.* (2022) [161] proposed a dual band-notched, microstrip-fed quad-port fractal antenna for UWB applications. The array was assembled on a 1.57 mm thick FR4 substrate with the overall dimensions of 64 × 64 mm^2. The upper substrate layer was composed of four orthogonally positioned 3^{rd} iterative Kock Snowflake fractal radiators with contorted feeds whereas the lower substrate layer was composed of common slotted ground without a decoupling structure. The array operated in 2.08-10.4GHz UWB range and provides a minimal inter-element isolation of 20dB across the operational band by incorporating a metallic conducting probe at the back of the ground structure. To reject the interreference introduced by Bluetooth WiMAX bands (2.27-3.62GHz), a π-shaped inverted L-shaped notch structure was truncated from the middle of each fractal radiator. The array offerd a peak gain of 9.5dBi with a sharp reduction of gain (-4dBi) at the notched band.

P.K. Keshari *et al.* (2022) [162] developed a quad-port, fractal UWB array with dual-band suppression functionality. The array was assembled on a 30 × 30 mm^2 FR4 substrate where the modified Minkowski fractal geometry and an upturned L-shaped stub incorporated in the reduced ground plane were responsible for realizing the desired miniaturization and high inter-port isolation characteristics. The proposed array operated in 3.1-12GHz range with a minimal isolation of 22dB between the array ports. To eliminate the EMI resulting from WLAN (5-5.9 GHz) and X-band (downlink satellite: 7.1-7.9 GHz) applications, a C-shaped and U-shaped slot were etched from the patch surface.

J. Banerjee *et al.* (2022) [163] modeled a dual-port, dual band-notched CPW fed MIMO with fractal-based neutralization line for portable UWB devices. The proposed array occupied a total area of 26.5 × 29.84 mm^2. The radiator geometry was combined with Koch curve fractal border and cross-connected C-type parasitic structures and reduced ground was combined DGSs to operates in 2.64-12GHz spectrum with dual band-notches at 3.3GHz and 4.5 GHz. To achieve a high degree of isolation, a Hilbert fractal-based neutralization line was integrated between the two antenna units. A good agreement was realized between the simulation and experimental results which validated the array’s operation in handheld UWB-MIMO systems.

2.7 Chapter Conclusion

In the comprehensive literature survey carried out in context to fractal MIMO arrays for 4G/5G communications, it is observed that the major design constraints while engineering antennas for modern 4G/5G communication gadgets lie in their miniaturization and high inter-element isolation characteristics. Due to the space limitations, the MIMO antenna system configured with closely-packed radiators leads to the problem of a strong mutual correlation between them, which deteriorates the isolation and capacity response of the antenna array. Therefore, the application of iteratively generated fractal geometries (with the notable attributes of self-similarity and space-filling) and various isolation enhancement approaches is an open area of research for developing small-sized, high-isolated UWB-MIMO antennas. Furthermore, UWB-MIMO antennas functioning in modern electronic equipment are prone to unwanted interferences caused by the existing licensed applications in the FCC’s regulated 3.1-10.6 GHz range. Therefore, to realize a UWB of operation with printed MIMO antenna arrays, to support higher data rates for future-generation communication systems, the proposed doctoral research work presents the design and development of fractal MIMO MPAs with certain decoupling networks /isolation methods and notch structures to realize the desired array’s diversity and band-notch characteristics for specific wireless communication bands.

CHAPTER 3

Dual-Port Fractal MIMO Antennas for UWB Communication Systems

This chapter presents the design and development of six different MPA arrays to achieve the first objective of the proposed doctoral research work. Due to the space constraints inside the portable electronic gadgets, the antenna designers are more focused to model compact-sized antenna structures with good antenna performance. Therefore, the recursively iterated fractal geometries with notable attributes of self-similarity, self-affinity, and space-filling are incorporated in the conventional MPA arrays to accomplish the desired miniaturization and multiband/wideband frequency response. In this chapter, six different models of fractal geometries namely complementary Sierpinski gasket, Circular, modified Pythagorean tree, modified Hen-shaped Koch Snowflake, Koch curve, and modified Koch Anti-Snowflake are employed in the two-port array configuration. For further enhancing the frequency bandwidth of the fractal antenna arrays, the aperture-coupled feeding mechanism, DGS, offset-feeding, stub-loading, and slot-etching techniques are also applied in the array design. Inter-element spacing and integration of various decoupling structures (in the ground configuration) play a vital role in realizing an optimum port-to-port isolation response. The designed two-port fractal UWB-MIMO antennas are fabricated and tested for S-parameters and radiation characteristics through the Keysight VNA (model no. E5063A) and anechoic chamber respectively.

The subsequent sections of this chapter illustrate the modeling, simulation, and experimental examination of various two-port fractal antenna arrays for 4G/5G UWB communication systems and are organized as follows: Section 3.1 presents an aperture-coupled Sierpinski gasket fractal UWB array combined with spiral-shaped DGS. Section 3.2 presents an aperture-coupled circular fractal UWB-MIMO antenna integrated with rectangular spiral DGS. Likewise, Section 3.3 demonstrates an aperture-coupled, modified Pythagorean tree fractal-based UWB-MIMO antenna integrated with complementary hexagonal spiral DGS. Section 3.4 illustrates microstrip-fed, semi-circular UWB-MIMO combined with Koch curve fractal and a reduced defected ground with a funnel-shaped decoupler. Section 3.5 demonstrate an offset-fed, hen-shaped Koch Snowflake fractal UWB-MIMO antenna with a partial ground surface which is further incorporated with an H-shaped decoupler and DGS technique. Lastly, Section 3.6 presents a microstrip-fed Koch Anti-Snowflake fractal UWB antenna with a reduced defected ground integrated with a square funnel-shaped decoupler and DGS approach.

3.1 Design and Development of Complementary Sierpinski Gasket Fractal MIMO Antenna

This section presents the modeling, simulation and measurement analysis of an aperture coupled Sierpinski gasket fractal MPA array for 4G/5G UWB devices. The proposed MPA array is configured on two FR4 substrates with dual Sierpinski gasket fractal (2nd order) radiators on the upper substrate and feed network on the rear FR4 substrate. Aperture-coupled technique excites the fractal elements, where the apertures etched in the ground are transformed to archimedean spiral-shaped DGS (inter-linked by X-shaped slot) to enhance the matching performance at the excited bands. The designed MPA array leads to metallic area miniaturization of 46% by employing the fractal concept and operates in the UWB range of

4.3-11.6 GHz with a maximal gain value of 4.7dBi and acceptable inter-port isolation ($S_{21}/S_{12} \leq 15.8$ dB) for the whole working band. Various diversity parameters (ECC, DG, MEG and CCL) are analyzed to justify the array's application in a diversity combining schemes to improve the overall SNR and support high data-rate desired for 4G/5G multimedia operations.

3.1.1 Array Configuration

The main aim of designing the proposed array is to get a multiband behavior from the complementary Sierpinski gasket fractal patch antenna array (optimized up to 2nd order of iteration) and then improve the bandwidth at each band using a DGS to obtain UWB operational characteristics. In order to achieve an optimum isolation between the two radiating antennas in the proposed array (for radiating uncorrelated signals), the spacing between the elements is the main governing factor. The design steps followed for the same are therefore explained as follows:

Figure 3.1(a) shows the top view of the designed fractal MPA array with two elements for MIMO applications. The proposed dual-layered (both layers of FR-4) array has two complementary Sierpinski gasket fractal equilateral triangular patches (optimized to 2nd iteration) printed on the upper layer of FR4 substrate having a relative permittivity (ε_r), loss tangent (tan δ) and thickness (h) of 4.4, 0.024 and 1.57mm respectively (with overall dimensions of 41×99.4 mm^2). The antenna design process starts with the 0th order of iteration of an equilateral triangle with side length 's' calculated for a resonant frequency of 6.8GHz using Equations (10-13) mentioned in chapter 1.

The proposed fractal array is an aperture coupled antenna array to achieve a broad impedance bandwidth. Therefore, the lower substrate layer of FR-4 has a slotted ground layer of copper on its top and two copper feedlines (for two fractal patches) at its bottom. Figure 3.1(b) shows the top view of the lower FR-4 substrate (also called feed substrate). The ground layer consists of two aperture slots (centered under the fractal patches) to facilitate the mechanism of microwave power transfer from the feedlines to the actively radiating patches. This is explained in detail in Section 3.1.2.2. These slots are then modified to two-arm complementary archimedean spirals where the outer filaments of each archimedean spiral are combined with the horizontal 'ɭ' shaped slot and interconnected with a modified 'X' shaped slot. The two archimedean spirals in the ground layer are mirror images of each other so that the proposed array elements transmit uncorrelated signals. The archimedean spiral for each Sierpinski gasket fractal is of complementary nature as the width of the arm slot 'g' (substrate region) is equivalent to the spacing 's_0' between the two adjacent arm slots (metal region). The initial driving frequency of the archimedean spiral that is chosen while designing is the lowest frequency at which the length of each spiral arm is equal to $\lambda_g/4$ (where λ_g is the guided wavelength) [164]. Each arm of the archimedean spiral covers 3 rounds with 12 filaments, where the length of the filaments is calculated using Equations (15, 16).

$$a_1 = a \text{ for } a = 24g \tag{15}$$

$$a_{2i} = a_{2i+1} = a - (4i - 2)\, g \text{ for different values of } i = 1,2,3,4,5 \text{ respectively} \tag{16}$$

Each of the optimized Sierpinski gasket fractal radiator is fed using a microstrip transmission line (50 Ω drive point impedance), with optimized dimensions of 24.5 × 3 × 0.035 mm^3 and is printed on the bottom layer of the feed substrate. In order to enhance port-to-port isolation, to radiate uncorrelated signals from the two antennas in the array; the separation distance between the centers of two fractal radiators is kept as 54.4 mm. Additionally, a vertical slot is clipped off from the bottom of each microstrip feed line to minimize impedance mismatch losses and extend the bandwidth of operation as shown in Figure 3.1(c). Table 3.1 shows the optimized geometrical dimensions of the proposed complementary fractal MPA array.

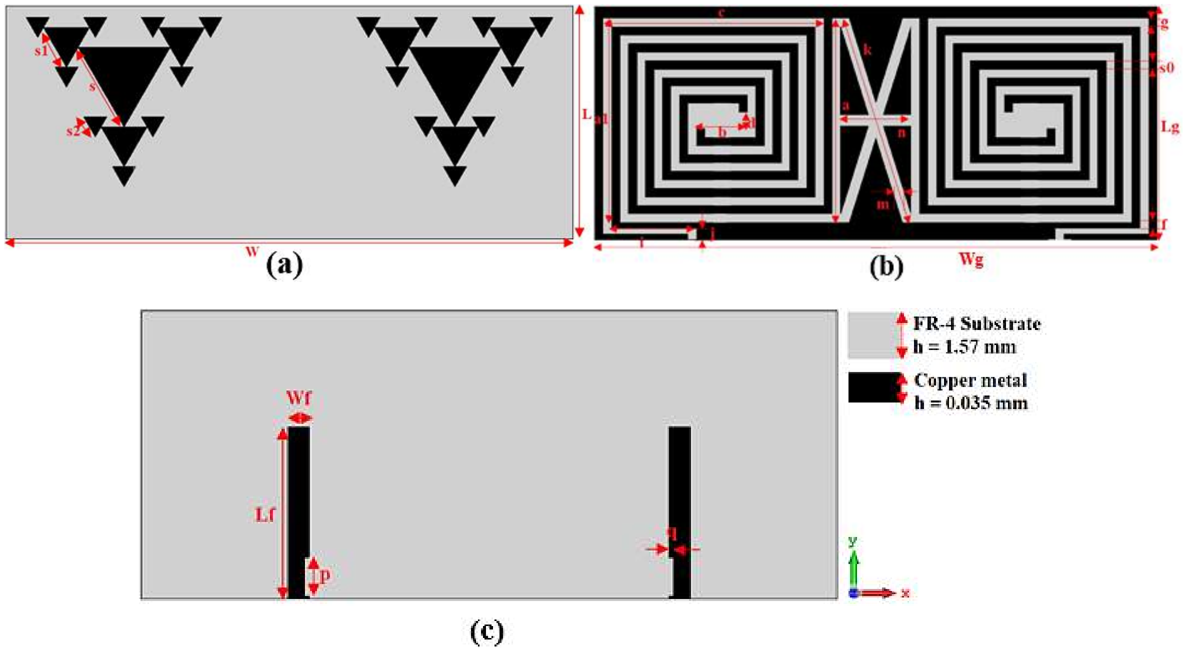

Figure 3.1 (a) Complementary Sierpinski gasket fractal radiators (top of upper FR4) (b) Ground with spiral-shaped DGS (top of lower FR4) (c) Two slotted microstrip feeds (back of lower FR4)

Table 3.1 Optimized geometrical dimensions of proposed fractal MPA array

Parameter	L	W	s	s1	s2	Lg	Wg	Lf	Wf	a	b	c
Value (mm)	41	99.4	16.16	8.08	4.04	41	99.4	24.5	3	36	9	39
Parameter	g	s0	i	j	k	m	n	p	q	a1	f	d
Value (mm)	1.5	1.5	15	2	38.08	1.5	12.4	5.5	0.65	36	1	3

3.1.2 Parametric Optimization of Proposed Antenna Array

3.1.2.1 Optimization of the Iteration Order for the Complementary Sierpinski Gasket Fractal

Figure 3.2(a) shows the intermediate design steps followed to reach the final designed Sierpinski gasket fractal up to the 2nd order of iteration. Figure 3.2(b) shows the S-parameter (S_{11}/ S_{22} (dB)) results of the proposed Sierpinski gasket fractal MPA array for three iteration levels (0 to 2) up to 2nd order. Since the main aim of this array design is to achieve the UWB of operation with an impedance matching criterion ($S_{11}/S_{22} \leq -15$ dB), the S_{11} and S_{22} results obtained for 2nd order of iteration shown by the red and pink curve respectively in Figure 3.2(b) (with 91.8% FBW) are selected for the proposed design. Figure 3.2(c) shows the transmission parameter (S_{12}/S_{21}(dB)) for all the three levels of iterations versus frequency. Since the third level (2nd order) of iteration for the proposed Sierpinski gasket fractal gives good port-to-port isolation ($S_{21}/S_{12} \geq -15.8$ dB), it is the selected geometry for UWB-MIMO applications.

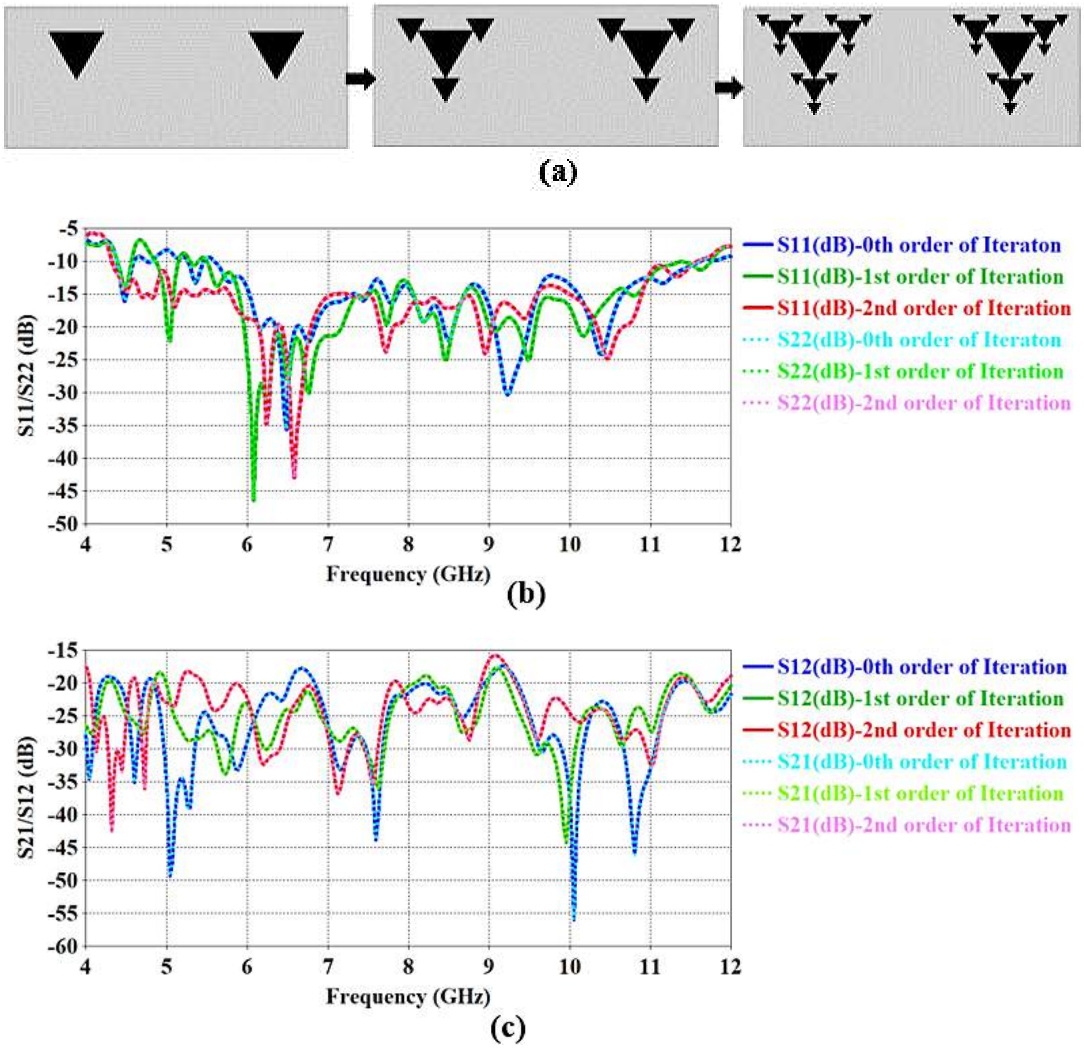

Figure 3.2 (a) Steps followed for obtaining 2nd iterative complementary Sierpinski gasket fractal radiators (b) S_{11}/S_{22} (dB) (c) S_{21}/S_{12} (dB) variations versus frequency

3.1.2.2 Optimization of Aperture Slots in the Ground

The proposed Sierpinski gasket fractal MPA array is fed using an aperture coupled feeding mechanism as it leads to better coupling of electromagnetic (EM) waves to the patch and provides a better impedance bandwidth. Therefore, the two aperture slots in the ground layer for the two-element array are modified to two complementary archimedean spirals that are mirror images of each other. Figure 3.3(b) shows the S-parameter results obtained while optimizing the aperture slots (three DGS geometries shown in Figure 3.3(a)) in the ground to the final interconnected complementary archimedean spiral DGS, to excite the required UWB of operation.

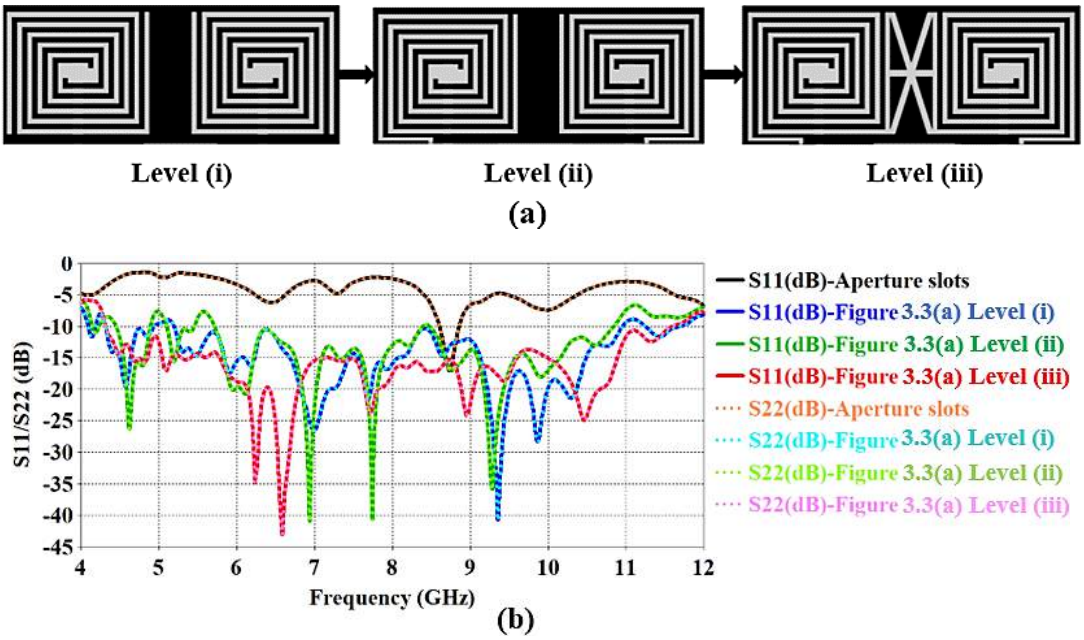

Figure 3.3 (a) Steps for obtaining the final optimized ground plane geometry (Level (iii)) of the proposed MPA array (b) S_{11}/S_{22} (dB) variations versus frequency

3.1.2.3 Effect of Etching Slot in the Feedline

To enhance the impedance matching at UWB excited by the proposed array, a vertical slot is etched from the bottom of each feed line. Figure 3.4 shows the comparative graphs of the two feedline configurations; with and without a slot in the feedline. Since the red-coloured curve shows improved peak return losses of -23.9dB, -24.2dB and -24.9dB at 7.7 GHz, 8.9 GHz and 10.5 GHz respectively, it is the selected feedline geometry for the proposed antenna elements in the array.

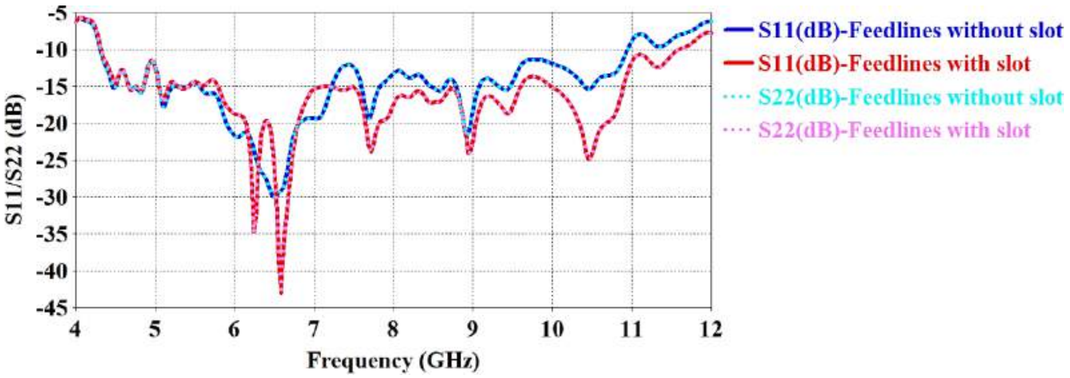

Figure 3.4 Effect of etching a slot from feedlines on return loss (S_{11}/S_{22}) characteristics

3.1.3 Simulation and Measurement Results

The validation of the proposed array's simulated results for MIMO applications is done by fabricating it on two low-cost commercially available FR4 epoxy substrate layers (ε_r of 4.4 and thickness of 1.57 mm) using photolithography process. On the upper layer, two complementary Sierpinski gasket fractals are printed and the lower layer consists of a ground with DGS on its top and feedlines at its bottom. To energize the fractal patches, two 50 Ω sub miniature version

A (SMA) connectors are soldered at the feed points of the fabricated prototype of the proposed MPA array. Figure 3.5 shows the snapshot of the fabricated prototype of the proposed fractal array which was tested for S-parameters (frequency range 100KHz-18 GHz) and gain using the Agilent's E5063A VNA and an anechoic chamber (frequency range of 20 KHz-20 GHz) with a calibrated horn antenna as the transmitter.

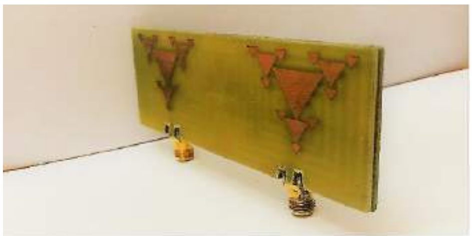

Figure 3.5 Snapshot of the fabricated two-element complementary fractal MPA array

3.1.1 Return loss (S_{11}/S_{22}) and Isolation (S_{21}/S_{21}) Performance

A comparative plot between simulated and measured S_{11}/S_{22} (dB) response with respect to frequency is shown in Figure 3.6(a). It shows the simulated operational bandwidth of 7.3 GHz (for both the ports) from 4.3-11.6GHz with a peak S_{11}/S_{22}(dB) of -45.1dB at a frequency of 6.6GHz. For port-1, the measured S_{11}(dB) response shows a wideband frequency response in the range of 5.7-12GHz. Additionally, the proposed prototype excites two frequency ranges of 4.1-4.25GHz and 4.7-5.3 GHz with impedance bandwidths of 0.15 GHz and 0.6 GHz respectively. For port-2, the measured S_{22} (dB) response shows a dual-band operation from 5.2-5.38GHz and 5.65-12GHz with impedance bandwidths of 0.18GHz and 6.35GHz respectively. A reasonable agreement is achieved between the simulated and measured S_{11}/S_{22} (dB) results. A slight shift in measured impedance bandwidth and resonances is observed. The main reason for this variation could be due to impedance mismatches as the proposed array is tested in an open-air environment. Secondly, the misalignment of the two layers of antenna while assembling and some fabrication errors also introduce some impedance mismatch and cause a slight shift in the measured impedance bandwidth results. Figure 3.6(b) shows a comparative plot of the simulation and tested transmission coefficients (S_{21}/S_{12}) of the designed MPA array against frequency. A considerable port-to-port isolation (simulated S_{21}/S_{12} $\leq$ -15.8 dB, measured S_{21}/S_{12} $\leq$ -17.9 dB) is achieved for the entire operational band of the array which ensures a reduced effect of mutual coupling between the array elements.

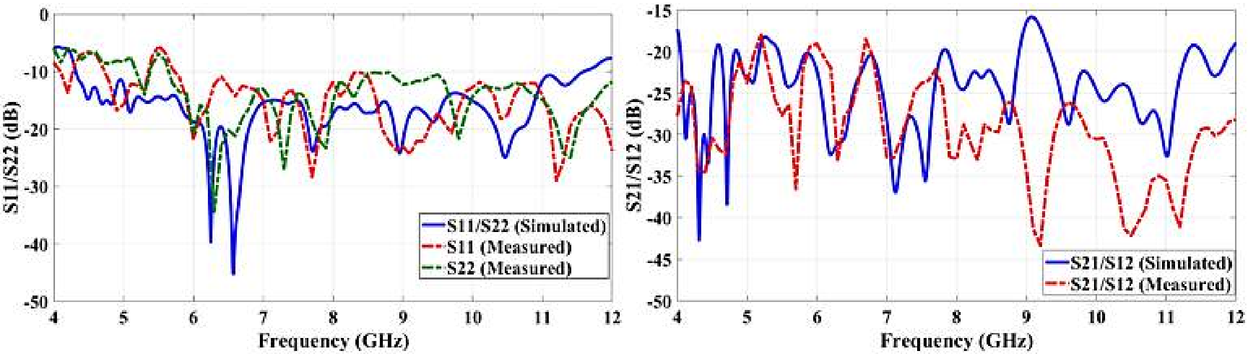

(a) (b)

Figure 3.6 Simulated and measured (a) S_{11}/S_{22}(dB) (b) S_{21}/S_{21}(dB) plot versus frequency plot

3.1.2 Radiation Characteristics

The simulated three-dimensional (3D) radiation pattern of the proposed fractal MPA array with one port energized (with 1W excitation power) and the other port terminated with a 50 Ω matched load at the frequency of 9.2GHz is shown in Figure 3.7(a, b). For port-1 excited and port-2 terminated with a matched load, a maximal gain of 4.7dBi (at 9.2 GHz) is achieved. A similar process for port 2 leads to achievement of same results in terms of gain for the second antenna also. Since the two fractal patches, their DGS and feedlines are mirror images of each other, to radiate uncorrelated signals, their far-field gain patterns also show a complementary behaviour to support this uncorrelation amongst the signals transmitted/received by the two antennas in an array. Figure 3.8 shows the comparative plot of simulated and measured broadband gain (dBi) as the function of frequency for the proposed MPA array. The measured results show the maximum gain of 4.32 dBi at 9GHz frequency which is close to the peak simulated gain. To examine the radiation characteristics of the proposed array, the normalized simulated and measured co and cross-polarization far-field patterns in E-plane and H-plane (excited port-1, terminated port-2) are shown in Figure 3.9 at resonant frequencies of 6.6GHz and 10.5GHz respectively. A considerable similitude is observed between the simulated and measured radiation patterns. It is observed that the proposed MPA array maintains almost an omnidirectional pattern and can be successfully proposed for short-range UWB applications to support multimedia-rich wireless services.

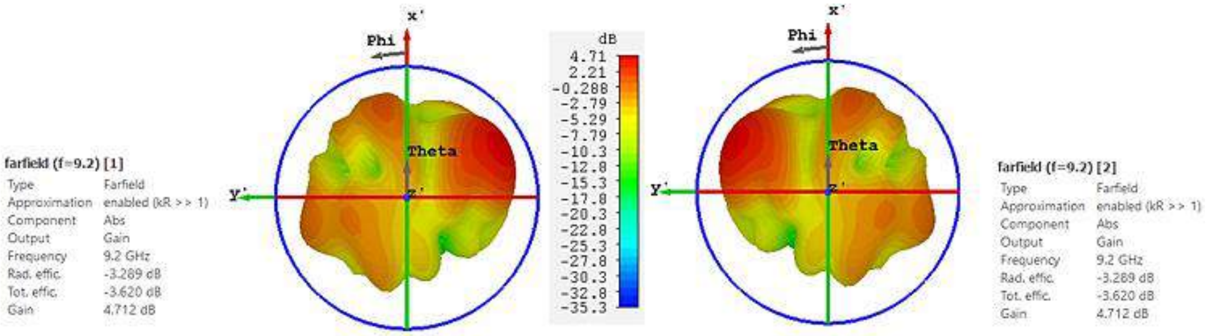

(a) (b)

Figure 3.7 Peak gain (3D view) at the 9.2 GHz frequency due to (a) port-1 (b) port-2 excitations

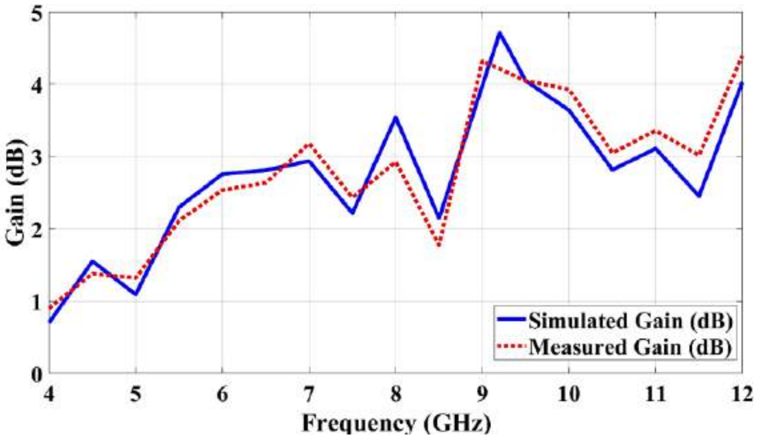

Figure 3.8 Broadband gain (dBi) versus frequency of the proposed fractal array

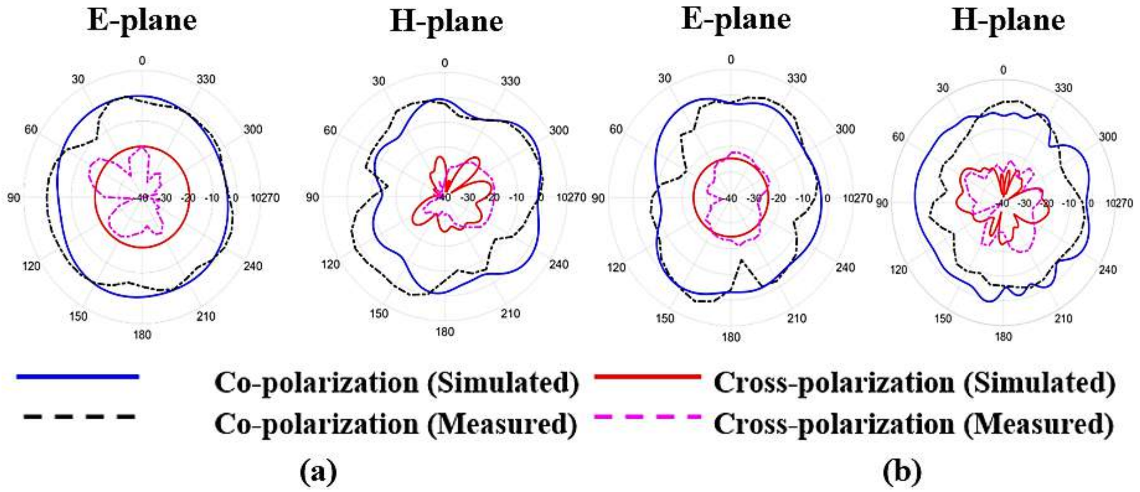

Figure 3.9 Simulated and measured 2D far-field patterns for port-1 excitation in E-plane and H-plane at (a) 6.6GHz (b) 10.5GHz

3.1.4 Diversity Performance Metrics

The proposed MPA array can be used to implement diversity schemes at the receiver terminal for enhancing the SNR in order to support high data rates. Therefore, in this section, some important diversity parameters like ECC, DG, MEG and CCL are analyzed for the proposed array to determine its performance in a rich scattering environment.

3.1.4.1 Envelope Correlation Coefficient

For a two-port network, ECC measures the amount of correlation between the signals transmitted/received by the two active antenna elements in an array. Assuming a uniform multipath environment with no antenna losses, the value of ECC can be calculated from S-parameters using Equation 2 given in chapter 1. Figure 3.10(a) shows the comparison plot of simulated and measured ECC values for the entire operational band from 4.3-11.6GHz. The simulated ECC (≤0.002) values are found in close agreement with measured ECC (≤0.0057) values which allows the proposed array to be successfully implemented for UWB-MIMO applications.

3.1.4.2 Diversity Gain

In a MIMO communication system, DG is defined as the degree of effectiveness or increase in SNR when a diversity combining scheme is being used. It can be calculated from ECC using Equation 3 in chapter 1. Figure 3.10(b) shows the simulated and measured DG variation with respect to the frequency in the operational range from 4.3-11.6GHz. The DG values ≥ 9.99 (simulated) and ≥9.971 (measured) in 4.3-11.6GHz range confirms a good diversity performance of the proposed array, thereby making it suitable for proposed UWB-MIMO applications.

3.1.4.3 Mean Effective Gain

MEG is the statistical measure of the average antenna gain in a fading environment and determines the effect of fading on the communication link quality. For a two-port network, MEG for port-1 and port-2 is calculated by using Equations (4,5) in chapter 1. Figure 3.10(c) shows the variation of MEG (for port-1 and port-2) and their difference with respect to frequency for the proposed MPA array. The peak simulated MEG of -3.57 dB (at 4.9GHz) is obtained for both the ports of the array with overall MEG $\geq$ -3.9 dB and $|MEG_1-MEG_2| = 0$ dB. A maximum measured MEG value of -3.01 dB at 7.1 GHz (port-1) and -3.011 dB at 5.6 GHz (port-2) with overall MEG $\geq$ -5.1dB and -1.38 dB $< |MEG_1-MEG_2| < 1.17$ dB is achieved. This makes the proposed fractal array suitable for implementation in the real communication environments which are subjected to signal fading.

3.1.4.4 Channel Capacity Loss

CCL measures the effect of cross-coupling between the received signals on channel capacity and is calculated using Equation 7 given in chapter 1. For applicability in a practical communication scenario, the maximum attainable limit of CCL should be 0.4 bits/s/Hz. Figure 3.10(d) shows the comparative plot of simulated and measured CCL with respect to the frequency. The simulated CCL is $\leq$ 0.37 bits/s/Hz for the operational band from 4.3-11.6GHz. The measured CCL is $\leq$ 0.4 bits/s/Hz for the whole application band except in 4.3-4.55 GHz, 5-5.18 GHz and 5.4-5.62 GHz bands which makes the proposed array a suitable choice for practical wireless communication systems implementing the MIMO technology.

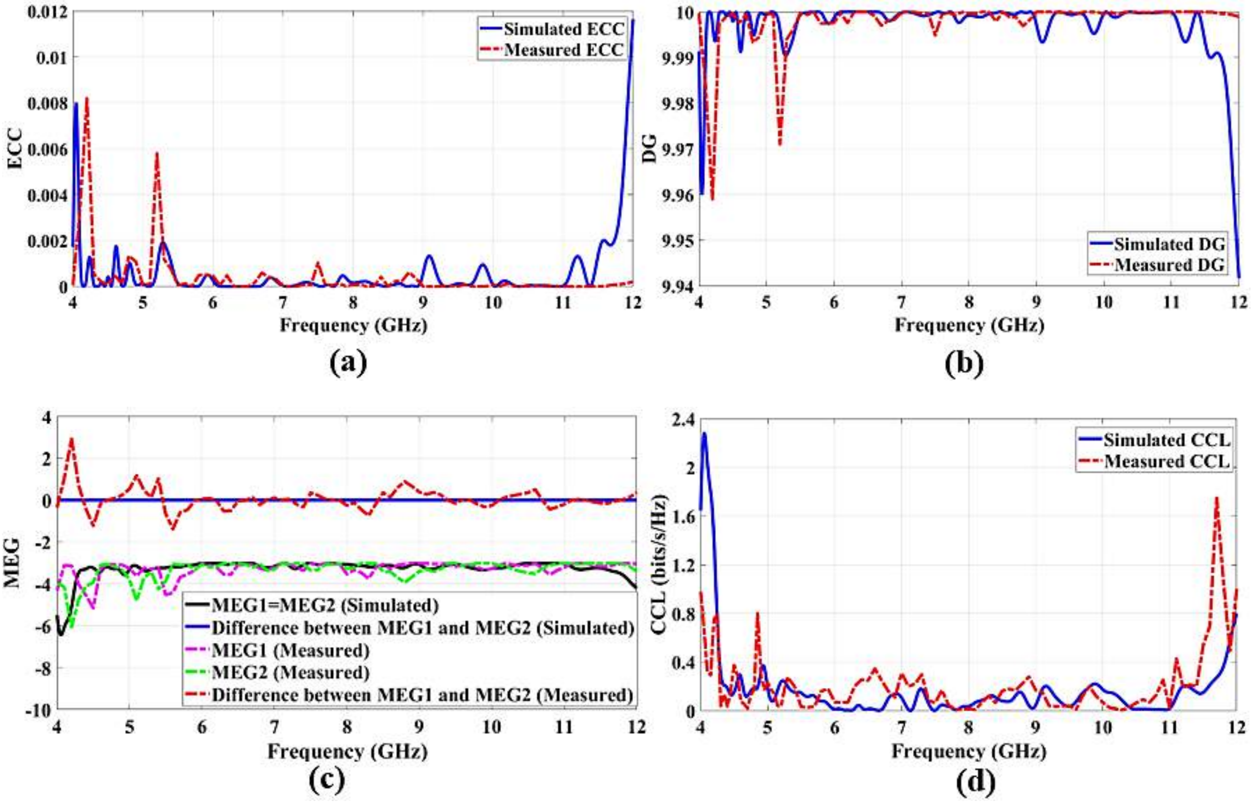

Figure 3.10 Simulated and measured (a) ECC (b) DG (c) MEG (d) CCL (bits/s/Hz) characteristics versus frequency plots

The following section of this chapter demonstrates the next proposed MIMO fractal geometry with two circular fractal radiators and ground defected with spiral-shaped slots for UWB applications.

3.2 Design and Development of Circular Fractal UWB-MIMO Antenna

In this section, a dual-port aperture coupled circular fractal MPA array is designed, developed, and experimentally tested for its usage in 4G, 5G, radar, satellite, and international space station (ISS) communication systems, covering C-band, X-band, and Ku-band of frequencies. The proposed MPA array is assembled on dual FR4 substrates where the upper substrate consists of two circular fractal radiators (iterated up to 2nd order) and the lower FR4 substrate layer consists of a feed network. The fractal patches are energized with aperture-coupled feed technique where the apertures truncated from the ground are transformed into the spiral-shaped DGS, to achieve the desired operational band (4.6-16.8GHz) with an improved impedance matching and high isolation ($S_{21} \leq$ -19dB) between the array elements. For implementation in MIMO systems, the diversity performance of the proposed array is analyzed in terms of ECC, DG, MEG, CCL and TARC. To validate the simulated results, the proposed prototype is tested for S-parameters and radiation characteristics.

3.2.1 Array Configuration

The main goal of the proposed MPA array is to achieve a multi-frequency response from the circular fractal geometry (up to 2nd order of iteration) and then realize the UWB behavior using DGS and aperture coupled feeding mechanism. The inter-element spacing is kept as an odd multiple of λ/2 to achieve optimum port-to-port isolation between the array elements.

As shown in Figure 3.11(a-d), the proposed fractal MPA array is designed on two FR4 substrate layers, each with ε_r, height (h1) and tan δ of 4.4, 1.57 mm, 0.02 respectively. It is modeled and simulated using a 3D electromagnetic simulation tool (CST MWS V'18). The proposed array is positioned in the x-y plane (z-axis as the normal direction) with the overall volumetric dimensions of $34 \times 68.7 \times 3.245$ mm^3. Figure 3.10(a) shows the top view of the upper FR4 layer which consists of two self-similar circular fractals (up to 2nd order of iteration) radiators with separation distance kept as 41.78 mm (from their centers). This circular fractal geometry is inspired by the concept of Vastu Purusha Mandala (VPM) fractal geometry which is broadly used in the architecture of ancient Indian temples. The radius 'r1'of the circular patches (0th order of iteration) is computed for a resonant frequency of 11.1GHz using Equation 17 [165].

$$\mathrm{r1} = \frac{87.94}{\mathrm{f_r}\sqrt{\varepsilon_r}} \tag{17}$$

where r1, f_r and ε_r is the radius of the circular patch (in mm), resonating frequency (in GHz) and relative permittivity of the FR4 substrate. Figure 3.11(b) shows the expanded view with the dimensional details of the proposed circular fractal geometry where 'r1', 'r2' and 'r3' represent the radius of 0th, 1st and 2nd order of iteration.

The lower FR4 substrate (feed substrate) consists of a metallic ground with DGS (on its top) and two metallic microstrip feeds (at its bottom). Figure 3.11(c) shows the top view of the lower substrate which consists of two aperture slots (centered under the radiating patches), to support the process of coupling of power from feedlines to the fractal radiators. These aperture slots are converted to complementary rectangular spirals slots (mirror images of each other) with a tree-shaped DGS (etched from the center of the lower substrate) to achieve UWB characteristics from the proposed array. Each rectangular spiral (with 8 number turns) is further modified with a rectangular slot (placed transverse to the aperture slot), a spiral slot (attached at the bottom of the rectangular spiral), and a horizontal ‘˥’ shaped slot (attached to the upper edge of the rectangular spiral) to fulfill the required criterion of high impedance matching ($S_{11}/S_{22} \leq$ -15dB) for the proposed array to operate in a practical scenario. The rectangular spirals exhibit complementary configuration as the width ‘g1’ of each slot arm is equal to the gap ‘g’ between the two adjoining slot arms. The rectangular spiral geometry is chosen due to its easy implementation in the array design, where the optimized length and width of the outermost (a × b) and innermost (u × v) loops (calculated using Equations (18-21)) of the spiral are responsible for exciting both lower and higher-order resonances respectively.

$$a \approx \frac{c}{2f_{min}\sqrt{\varepsilon_{eff}}} \tag{18}$$

$$b \approx \frac{c}{2f_{min}\sqrt{\varepsilon_{eff}}} \tag{19}$$

$$u \approx \frac{c}{2f_{max}\sqrt{\varepsilon_{eff}}} \tag{20}$$

$$v \approx \frac{c}{2f_{max}\sqrt{\varepsilon_{eff}}} \tag{21}$$

where c is the speed of light, ε_{eff} is the effective dielectric constant of FR4 substrate ($\approx (\varepsilon_r+1)/2$), f_{min} and f_{max} is the lower and higher-order resonance respectively [166]. As shown in Figure 3.11(d), two 50 Ω microstrip feed lines (bottom of the lower substrate) are used to energize the circular fractal radiators where the optimized dimensions for each feedline are 21 × 4 × 0.035 mm^3. Table 3.2 gives the optimized geometric values of the proposed fractal array.

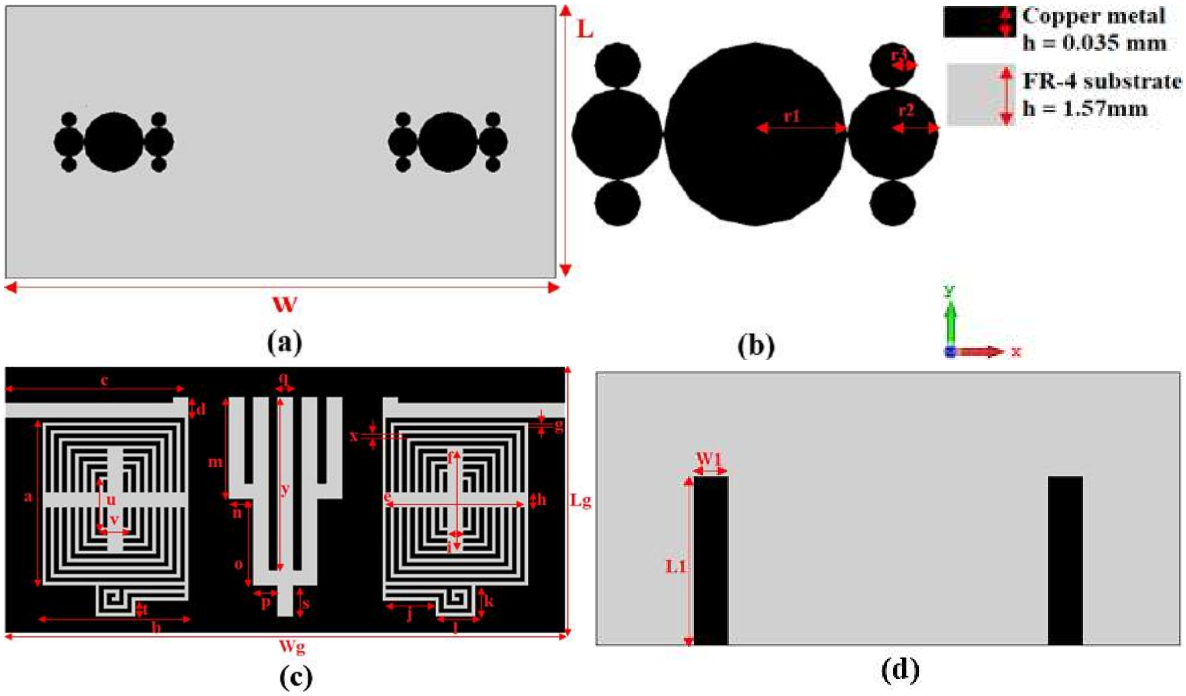

Figure 3.11 Top view (upper substrate) showing two circular fractal patches (b) Expanded view of the circular fractal geometry (c) Top view (lower substrate) of a ground plane defected with rectangular spirals and a tree-shaped slots (d) Back view (lower substrate) with two feedlines

Table 3.2 Optimized dimensions (mm) of the proposed fractal MPA array

Parameter	L	W	a	b	c	d	e	f	g	h	r2	r3
Value (mm)	34	68.7	21	18	22.5	2.75	17	13	0.5	2	1.875	0.9375
Parameter	i	j	k	l	m	n	o	p	q	r1	s	t
Value (mm)	2	6.5	4	5	13.125	3	11.125	3	2	3.75	4	2
Parameter	Lg	Wg	L1	W1	u	v	x	y				
Value (mm)	34	68.7	21	4	7	4	0.5	22.25				

3.2.2 Parametric Analysis of the Proposed Fractal MPA Array

In this subsection, the effect of geometrical variations of various antenna design parameters such as iteration order of circular fractal, defects in the ground plane, and width of feedline are analyzed and optimized in terms of simulated S-parameter results to achieve an optimum array performance suitable for 4G/5G, radar, satellite and ISS communication systems. The parametric study and optimization are carried out in CST MWS V’18 with hexahedral mesh settings of 15 cells/λ.

3.2.2.1 Effect of Iteration Stages of Circular Fractal Geometry

Figure 3.12(a-c) shows the step-by-step generation process followed to design a final optimized iteration model of circular fractal geometry (up to 2nd order of iteration) while keeping the other design parameters constant. The corresponding S_{11}/S_{22} (dB) and S_{21}/S_{12} (dB) characteristics for the three levels of iteration of the proposed circular fractal configuration are shown in Figure 3.13(a, b) respectively. As the main objective of the proposed array is to achieve UWB range with minimum mismatch losses ($S_{11}/S_{22} \leq -15$dB), the circular fractal geometry iterated up to 2nd order (Figure 3.12(c)) provides the best S_{11}/S_{22}(dB) results (shown by red and pink curves in Figure 3.12(a)) with high FBW (114%) and a better impedance matching over the entire operational band (4.6-16.8GHz) as compared to the 0th and 1st iteration order (Figure 3.12(a, b) respectively).

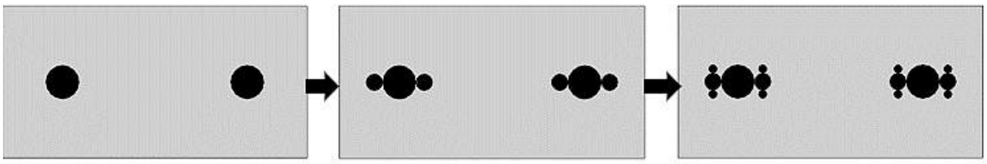
(a) (b) (c)

Figure 3.12 Steps followed to design the final circular fractal geometry (2nd order of iteration)

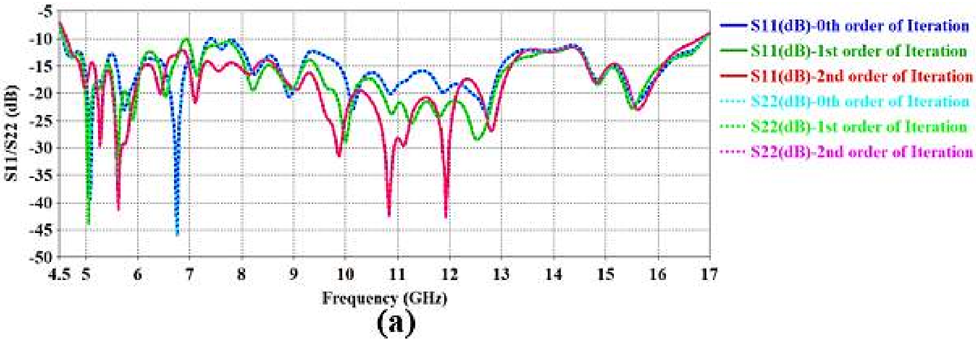

(a)

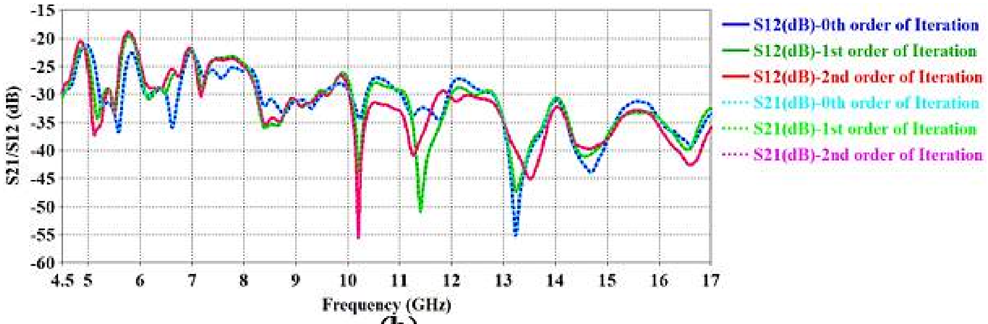

(b)

Figure 3.13 (a) S_{11}/S_{22} (dB) (b) S_{21}/S_{12} (dB) versus frequency for different iterations of circular fractal geometry

3.2.2.2 Effect of Geometrical Variations of the Ground Plane Configuration

The stepwise structural variation in the ground plane of the proposed fractal array is demonstrated in Figure 3.14 and the corresponding return loss characteristics for the various development stages are shown in Figure 3.15(a, b). The proposed array is energized using an aperture-coupled feeding technique for maximum power transfer between the fractal radiators and 50 Ω microstrip feedlines. This coupling mechanism provides a wider impedance bandwidth with a good reflection coefficient [45]. So, the aperture slots (initially etched from the ground plane) are converted to modified complementary rectangular spirals (mirror images of each other) as shown in Figure 3.14(c), to achieve a wide frequency band from 6.8-16.9 GHz (85% FBW) with an additional wireless local area network (WLAN) band from 5.2-6 GHz (black and grey curves in Figure 3.15(a)). To shift the frequency band towards left and improve the impedance matching of the excited operational band, a three-branched tree-shaped DGS is etched from the center of the upper layer of the lower FR4 substrate (Figure 3.14(f)). The introduction of this tree-shaped DGS results in larger current loops which provide a continuous frequency band from 4.6-16.8 GHz (FBW of 114%) with a peak return loss of -42.3 dB (at 10.8 GHz frequency) and a good impedance matching performance (red and pink curves in Figure 3.15(b)).

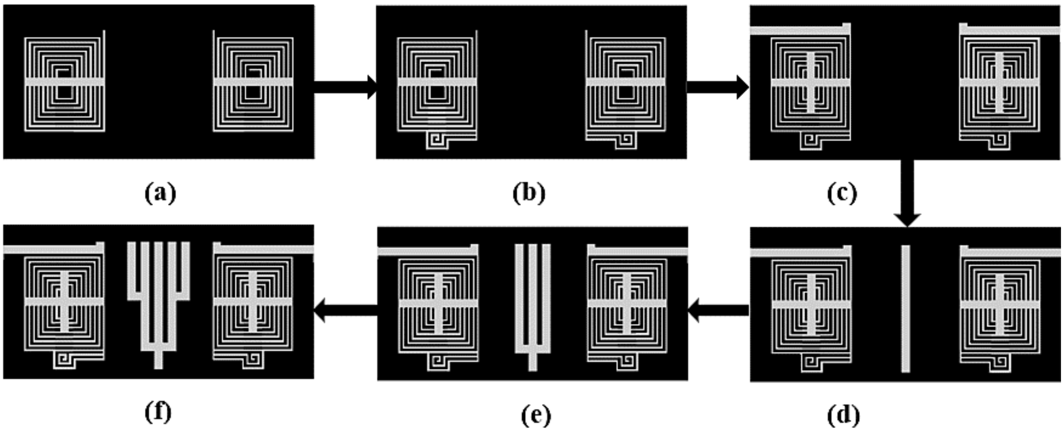
(a) (b) (c)

(f) (e) (d)

Figure 3.14 Geometrical variations in the ground plane of the proposed fractal array

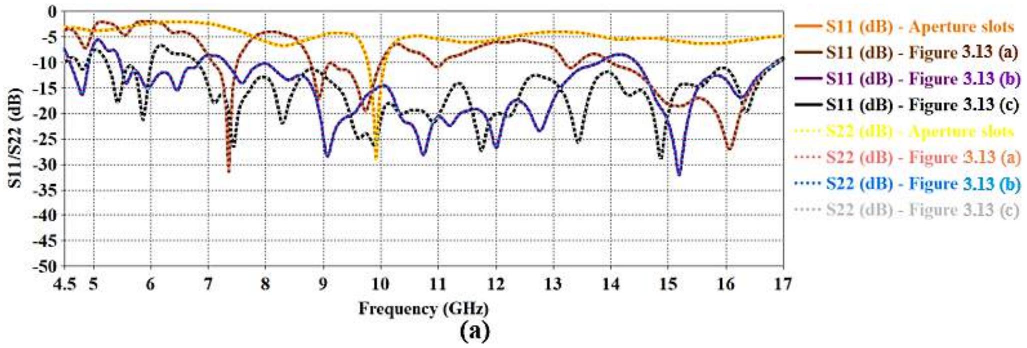

Figure 3.15 (a) Variation of S_{11}/S_{22} (dB) versus the frequency corresponding to the ground plane geometry shown in Figure 3.14(a-b)

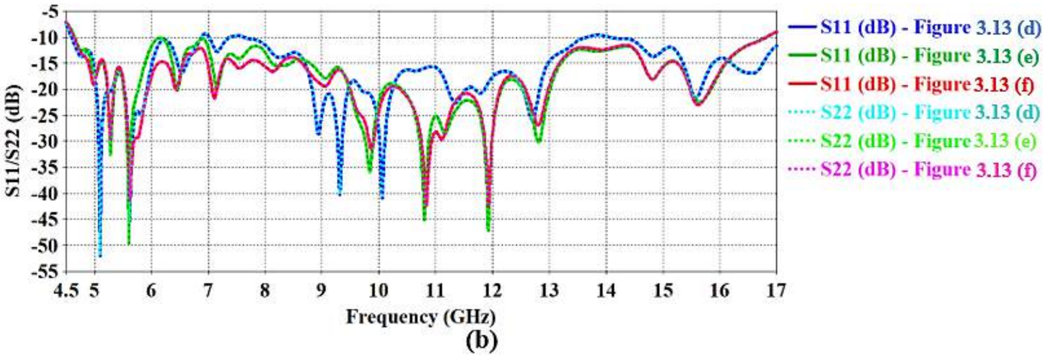

Figure 3.15 (b) Variation of S_{11}/S_{22} (dB) versus the frequency corresponding to the ground plane geometry shown in Figure 3.13(d-f)

3.2.3 Simulated and Measured Analysis

To authenticate the simulated performance of the proposed fractal array in the free space scenario, the proposed array is fabricated on two commercially available FR4 substrates (ε_r of 4.4 and height of 1.57 mm) using the photolithography process. Figure 3.16(a-d) shows snapshots of the circular fractal patches (top view of the upper substrate), ground plane configuration with DGS (top view of the lower substrate), feedlines (back view of the lower substrate), and the assembled view of the fabricated prototype. To energize the fractal radiating patches, the proposed array is soldered with two SMA (50 Ω) connectors. The fabricated prototype is tested using a Keysight E5063A VNA (100 KHz-18 GHz) and anechoic chamber for measuring the S-parameter and radiation pattern values.

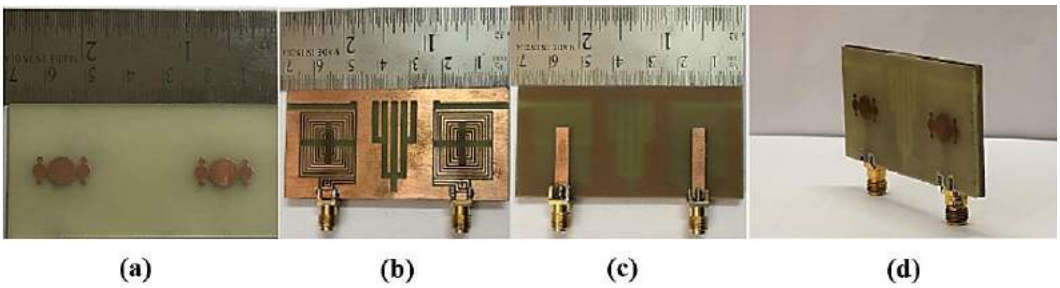

Figure 3.16 Snapshots of the fabricated fractal array showing (a) Front view (upper substrate) with circular fractal patches (b) Front view (lower substrate) with the ground plane (c) Back view (lower substrate) with two feedlines (d) Assembled geometry

3.2.3.1 Reflection and Transmission Coefficients

A comparison plot of simulated and measured S_{11}/S_{22} and S_{21}/S_{12} response (in dB on the Y-axis) versus frequency (in GHz on the X-axis) is shown in Figure 3.16(a, b) respectively. It covers the simulated frequency band from 4.6-16.8 GHz (S_{11} / $S_{22} \leq$ -10dB) with 114% FBW (for both ports) and shows a peak return loss of -43.2 dB at 10.8 GHz frequency. For port-1, the measured S_{11} (dB) response shows a wide frequency band from 8-17 GHz (with an impedance bandwidth of 9 GHz) for X-band and Ku-band applications, along with two additional bands from 5.52-5.68 GHz (impedance bandwidth of 0.16 GHz) and 6.72-7.28 GHz (impedance bandwidth of 0.56 GHz) for C-band communication systems. For port-2, the measured S_{22} (dB) curve shows the wideband characteristics from 8.48-17 GHz (66.9 % FBW), along with two C-band frequencies from 4.7-5.3 GHz and 7.44-7.92 GHz with an impedance bandwidth of 0.6 GHz and 0.48 GHz respectively. Hence, the simulated S-parameter results (for both the ports) show a reasonable matching with the fabricated ones with a slight variation in the measured impedance bandwidth and resonant frequencies as compared to the simulated ones. These variations are due to the fabrication errors (during the photolithography process) or the environmental effects (reflections from the surrounding objects) introduced while testing of the proposed array in an open space. Also, in the aperture-coupled arrangement, the two antenna layers of the fabricated prototype are joined using an adhesive glue which may vary the effective dielectric constant of the substrate and cause a shift in resonances. As shown in Figure 3.17(b), a close agreement is achieved between the simulated S_{21} ($\leq$-19dB) and measured S_{21} ($\leq$ -23.24dB) results which ensures a high degree of isolation between the fractal radiators and fulfills the criteria essential for MIMO implementation in 4G/5G, satellite, radar, and ISS communication systems.

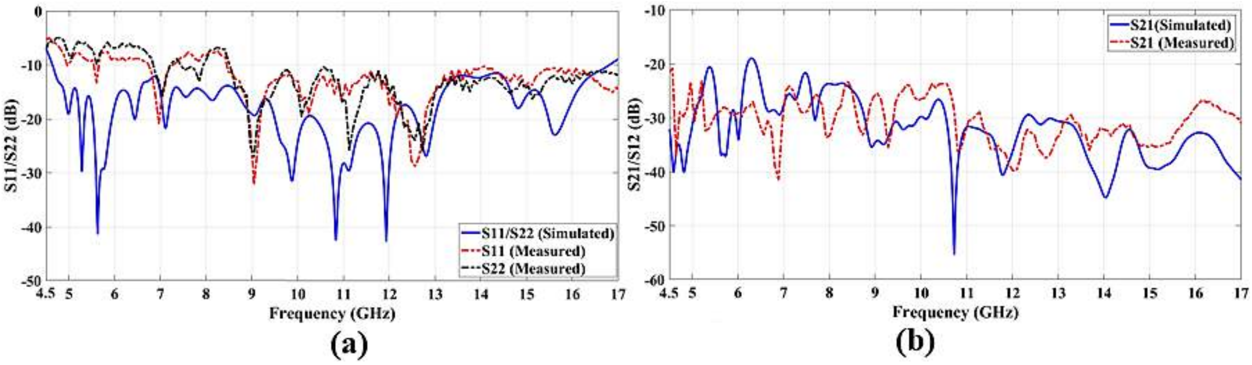

(a) (b)

Figure 3.17 Simulated and measured (a) S_{11}/S_{22} (dB) (b) S_{21}/S_{12} (dB) performance versus frequency

3.2.3.2 Far-field Characteristics

Figure 3.18(a-d) shows the normalized simulated and measured 2D far-field patterns (co and cross-polarization) in both E-plane (y-z plane) and H-plane (x-z plane) for the proposed array (with port-1 energized) at the four resonant frequencies of 5.61 GHz, 7.1 GHz, 10.8 GHz, and 15.6 GHz respectively. A close resemblance is achieved between simulated and measured 2D radiation characteristics (in both E and H planes). The proposed fractal array shows a nearly good omnidirectional radiation pattern at both lower and higher-order resonances with the main lobe magnitude of co-polarization fields much higher than that of cross-polarized fields (in both E and H planes). Such radiation performance of the proposed array makes it a good perspective for high data rate 4G/5G, satellite, radar, and ISS systems.

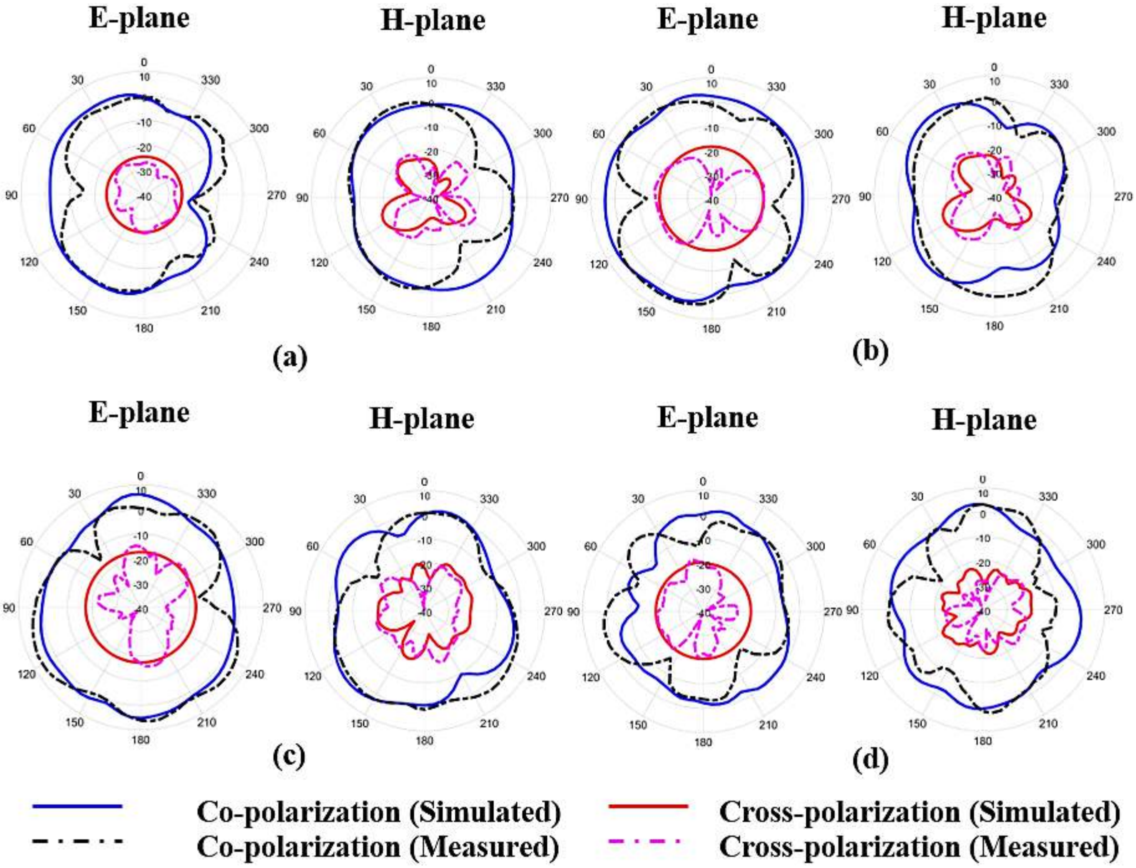

Figure 3.18 Simulated and measured 2D far-field patterns in the E-plane and H-plane of the proposed array (for Port-1) at (a) 5.61 GHz (b) 7.1 GHz (c) 10.8 GHz (d) 15.6 GHz

Figure 3.19 shows the comparative plot of the simulated and measured gain (dB) for the proposed array in the operational range from 4.6-16.8GHz. A maximal gain (simulated) of 4.57dBi at 6.6GHz frequency with an overall average gain of 2.4 dB is achieved. The measured gain varies from 0.95 dBi to 4.12 dBi which is close to the simulated gain values.

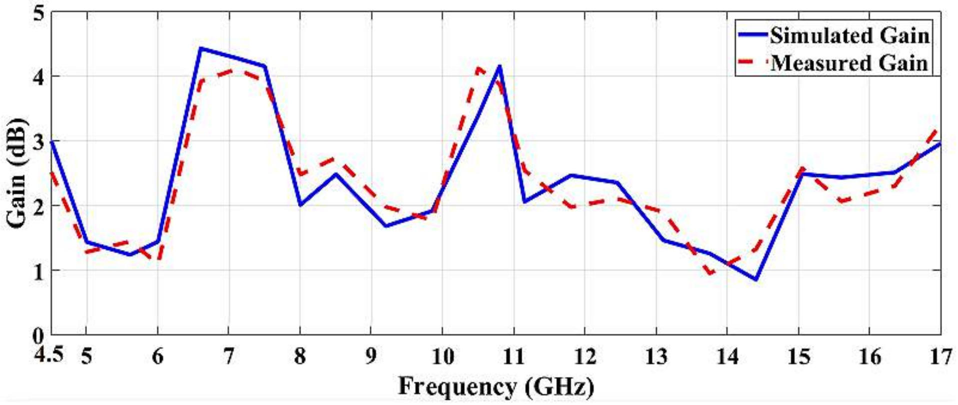

Figure 3.19 Simulated and measured broadband gain (dBi) characteristics of the proposed array

3.2.3.3 Surface Current Distribution

Port-1 of the proposed fractal array is activated with 1W of input power (in CST MWS V’18) to see the distribution of the simulated current on the radiating patch, ground plane, and feedline at four resonances of 5.61 GHz, 7.1 GHz, 10.8 GHz, and 15.6 GHz. At 5.6 GHz frequency, Figure 3.20(a) shows that the current is uniformly distributed over the entire patch, ground, and feedline but the highest current of 210 A/m is present along the width of the seventh loop of the rectangular spiral slot. Figure 3.20(b) shows a maximum current of 111.7 A/m (at 7.1 GHz) concentrated along the width of the outermost loop of the rectangular spiral slot. At 10.8 GHz frequency, Figure 3.20(c) shows a maximum current of 138.5 A/m distributed along the width of the second loop of the rectangular spiral slot. Figure 3.20(d) shows that more magnitude of current (100.7 A/m) is present along the width of the spiral geometry that was etched from the bottom of the rectangular spiral. Hence, the incorporation of rectangular spiral geometry in the ground plane of the proposed array is responsible for exciting both lower and higher-order resonances (also justified by Equations (19-21)). Also, for excited port-1, a very less magnitude of the current is coupled to the non-excited fractal radiator (Port-2) at all four resonances. Hence, the effect of mutual coupling is minimum and maximum energy is radiated by the fractal radiator connected with port-1.

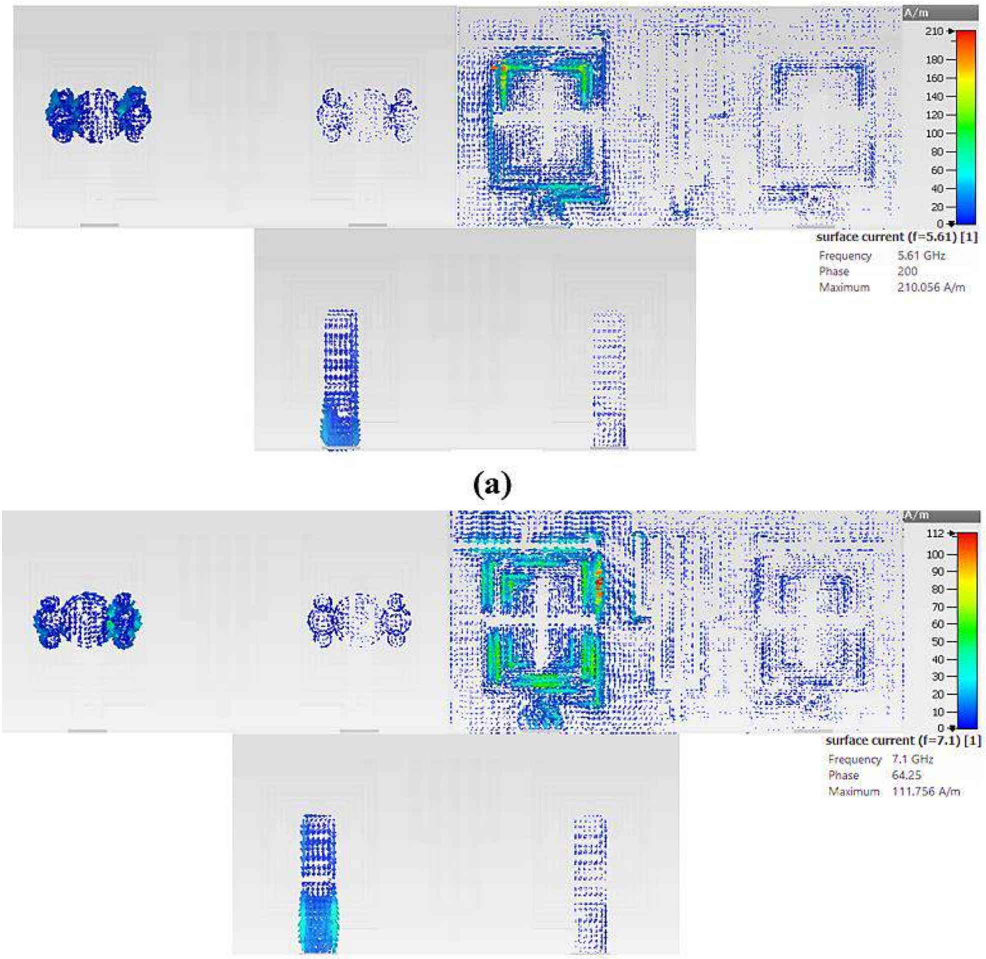

(a)

(b)

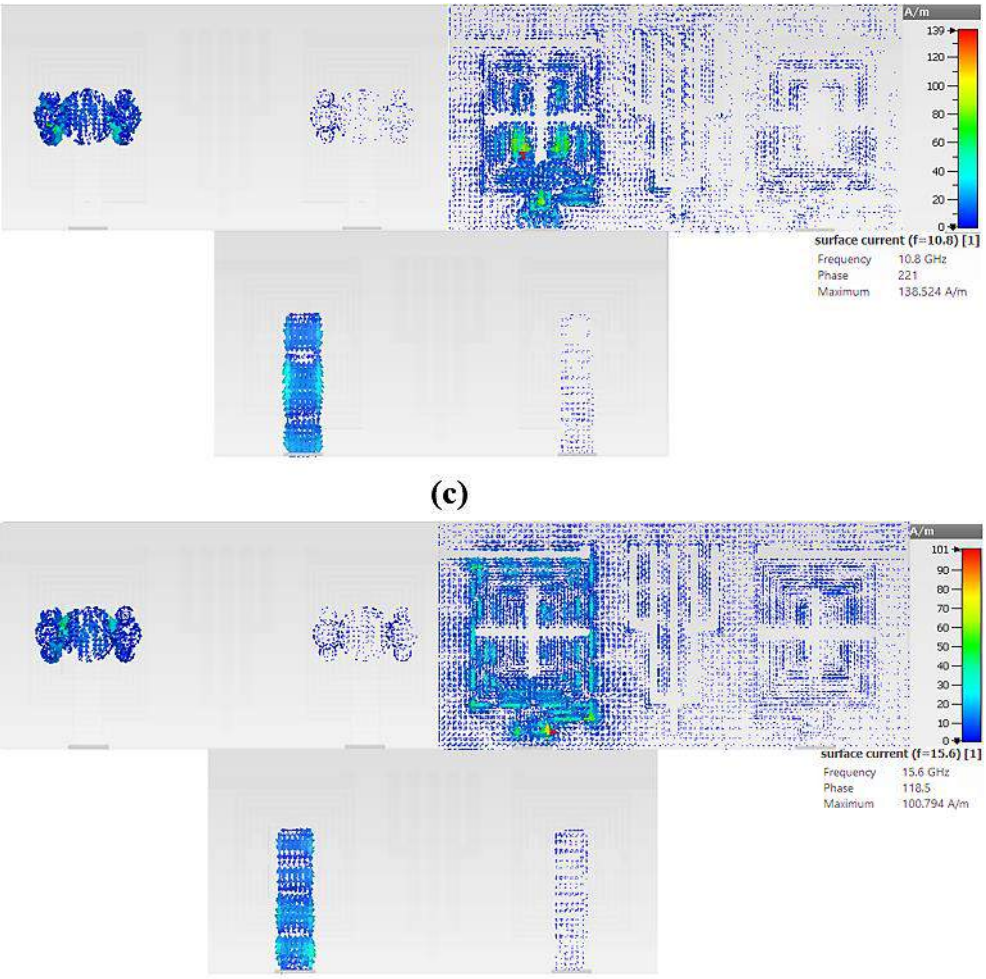

(c)

(d)

Figure 3.20 Surface current distribution (for port-1) on the fractal patch, ground plane, and feedline at the resonant frequencies of (a) 5.61 GHz (b) 7.1 GHz (c) 10.8 GHz (d) 15.6 GHz

3.2.4 Diversity Performance Metrics

3.2.4.1 Envelope Correlation Coefficient

A threshold ECC value of less than 0.5 is acceptable to receive an uncorrelated signal at the two ports. Assuming a uniform multipath environment, ECC can be computed from S-parameters (using Equations (2) given in chapter 1) and plotted in Figure 3.21(a) for the operational band from 4.6-16.8GHz. Low values of ECC (≤ 0.0009 (simulated), ≤ 0.00727 (measured)) allow the successful implementation of the proposed array in high data rate and reliable UWB-MIMO communication systems.

3.2.4.2 Diversity Gain

In a MIMO system, DG is computed with the help of ECC values as represented by Equation 3 in chapter 1. Figure 3.21(b) shows the comparative plot of simulated and measured DG versus the frequency. Optimum values of DG (≥ 9.996 (simulated), ≥ 9.963 (measured)) for the frequency band from 4.6-16.8 GHz ensures a good diversity performance of the proposed array.

3.2.4.3 Mean Effective Gain

Using the simulated and measured S-parameter values, MEG for port-1 and port-2 is computed using Equations (4, 5) given in chapter 1. As shown in Figure 3.21(c), the proposed array provides a good diversity performance with a maximum simulated MEG of -3.01dB at 5GHz frequency (for both ports) with the $|MEG_1 - MEG_2| = 0$ dB and a peak measured MEG of -3.01dB at 12.8GHz (port-1) and -3.011dB at 14.7GHz (port-2) with $-1.3\text{dB} < |MEG_1 - MEG_2| < 2.7\text{dB}$.

3.2.4.4 Channel Capacity Loss

For the proposed dual-port antenna, CCL (bits/s/Hz) is calculated using Equation (7) given in chapter 1. As shown in Figure 3.21(d), the simulated CCL≤0.36 bits/s/Hz and measured CCL≤0.4 bits/s/Hz (except in the frequency bands from 4.6-5.24 GHz, 5.68-5.82 GHz, 6-6.78 GHz, and 7.9-8.56 GHz) is achieved for the operational band from 4.6-16.8GHz which indicates an acceptable antenna performance for achieving a reliable transmission rate in a rich scattering environment.

3.2.4.5 Total Active Reflection Coefficient

For the proposed dual-port antenna array, TARC can be mathematically computed by using Equation (8) given in chapter 1. Figure 3.21(e, f) shows the simulated and measured TARC (dB) curves of the proposed array where ‘θ’ is varied from 0˚ to 180˚ with a step size of 30˚. When compared with Figure 3.17(a), a good agreement is achieved between the TARC and simple reflection coefficient (S_{11}) curves (both simulated and measured). It is observed that the impedance bandwidth and resonant peaks of the proposed array are nominally affected by the entire set of feeding phase angle variations.

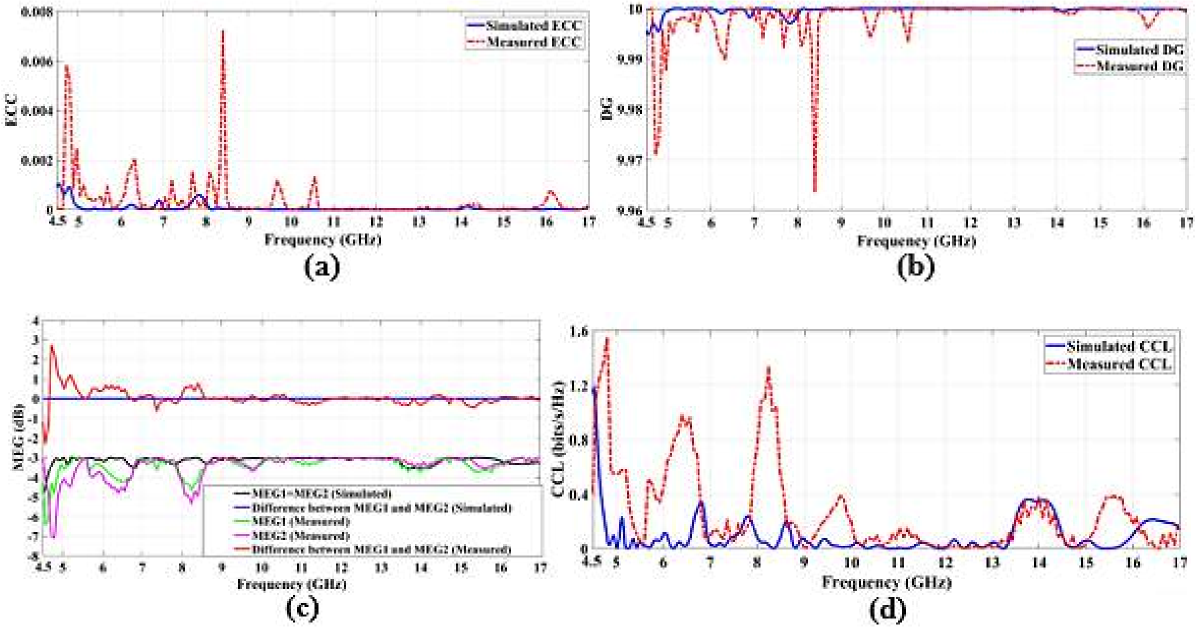

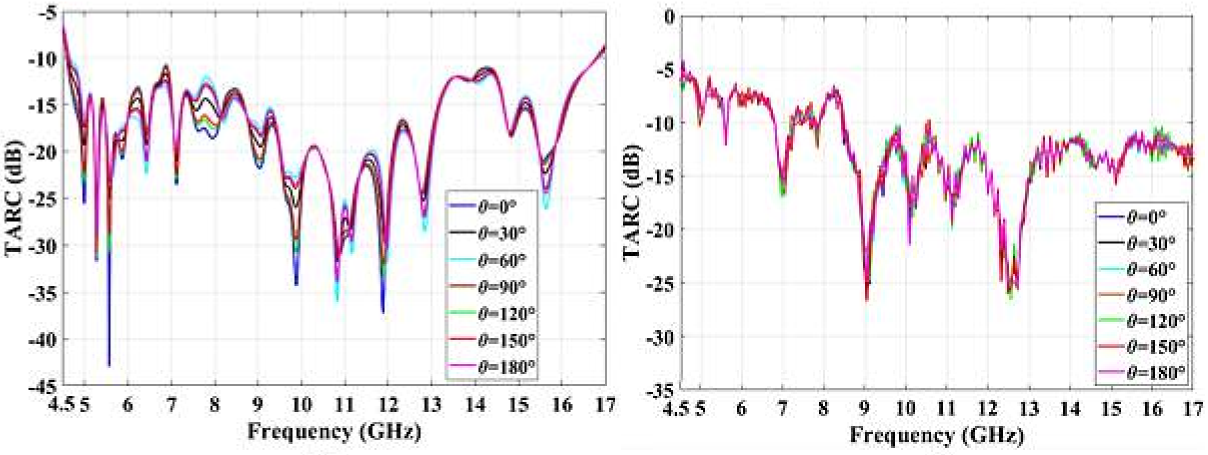

(e) (f)

Figure 3.21 Simulated and measured (a) ECC (b) DG (c) MEG (d) CCL (bits/s/Hz) (e) TARC (simulated) (f) TARC (measured) characteristics versus frequency plots

The subsequent section of this chapter presents a new design on fractal MIMO antenna with two modified Pythagorean tree fractal radiators and ground defected with spiral-shaped slots for realizing UWB characteristics.

3.3 Design and Development of Modified Pythagorean Tree Fractal UWB-MIMO Antenna

In this section, an aperture-coupled two-port modified Pythagorean tree fractal antenna is modeled and experimentally examined for ultra-wideband applications. The designed array is configured on dual FR4 substrates where the upper substrate incorporates two modified Pythagorean tree fractal radiators and the lower substrate consists of a feed network. The notable feature of the proposed tree fractal is the elimination of the base square (0th iteration level) which lowers the total fractal height by 12.11mm. The multiband response generated by the fractal geometry is extended to a wide operational band by converting the apertures etched from the ground into the hexagonal spiral geometry. The proposed array offers 96.8% FBW (3.7-10.64GHz) with optimum port-to-port isolation ($S_{21} \leq -16.1$dB) characteristics. A detailed investigation of various diversity performance metrics and parametric optimization is conducted. The fabricated prototype is tested and compared with simulated results to verify the array's operation in a real-world scenario.

3.3.1 Array Configuration

The primary purpose of developing the proposed fractal array is to initially generate multiple resonances through the modified Pythagorean tree fractal MIMO antenna and then realize the desired UWB response by incorporating the spiral-shaped DGS in the common ground plane. Taking compactness and low correlation into account, the spacing between the two fractal elements is optimized to 41.5mm. The steps followed for designing this geometry are therefore detailed as follows:

The layout and geometrical parameters of the proposed fractal array are presented in Figure 3.22. The array elements are arranged on two 37.5×81.5 mm^2 FR4 (lossy) substrates, each with

ε_r of 4.4, height ($h_{FR\text{-}4}$) of 1.57 mm, and tan δ of 0.024 respectively. The proposed fractal array is modeled and simulated in the CST MWS v'18 software.

As depicted in Figure 3.22(a), the upper surface of the top substrate (also named as antenna substrate) is composed of two modified Pythagorean tree fractal patches, each with a steep angle 'p' of 10°. Each Pythagorean tree fractal geometry is configured along two equal arms of a right-angled isosceles triangle which is further amalgamated with a semi-circular ring at its base. The iteration level 'N', during the construction of modified Pythagorean tree fractal geometry, inserts 2^N squares on each equal side of the right-angle isosceles triangles with the reduction factor of 0.5077. The base square (0^{th} iteration level) of the standard Pythagorean tree fractal geometry is eradicated and initially, the main right-angled isosceles triangle radiator generates the desired resonance before the introduction of modified Pythagorean tree fractal geometry.

Aperture-coupled excitation technique is employed in the proposed fractal array to obtain a relatively wide impedance bandwidth. For this purpose, the lower substrate (also named as feed substrate) incorporates a copper-clad ground defected with two hexagonal spirals (on its upper surface) and a pair of 3mm ('f2') wide copper feedlines printed at its back. As shown in Figure 3.22(b), two aperture slots (positioned centrally under the radiators) are truncated from the common ground surface to aid the efficient coupling of EM energy from the transmission lines to the radiating patches. Each aperture slot is further integrated with a complementary hexagonal spiral (each with 6 windings) where the outermost segments of each spiral are joined via a 'X' shaped slot. The two hexagonal spiral slots etched from the common ground plane are mirror images to one another such that the proposed fractal array can broadcast potentially independent signals into the free space environment. The hexagonal spiral slot for each modified Pythagorean tree fractal shows a complementary behavior, which implies that the width 'w1' of each slot arm (a portion of FR-4 substrate) is the same as the spacing 'g1' between the two neighboring slot arms (a portion of copper). The inner 'r3' and outer 'r4' radius of the hexagonal spiral geometry governs the upper and lower order resonances, respectively, for supporting UWB communication systems. The ground is further defected with two rectangular slots (at the left and right corners) and a staircase-shaped slot (at the center) to realize 50 Ω characteristic impedance.

As depicted in Figure 3.22(c), the rear surface of the feed substrate is composed of two microstrip feedlines (each with 50 Ω input impedance), used to drive the modified Pythagorean tree fractal radiating patches. The two transmission lines are positioned at the left offset by 'd1' (from the center feed position) to shift the frequency range towards the lower side. Additionally, each feedline is integrated with a horizontal stub (at the upper edge) and a vertical slot (at the lower edge) to realize an acceptable impedance match across the entire operational band. Figure 3.22(d) shows the 3D layout of the proposed array, configured in the x-y plane with its thickness along the orthogonal z-axis. The optimized parametric values of the proposed array are listed in Table 3.3.

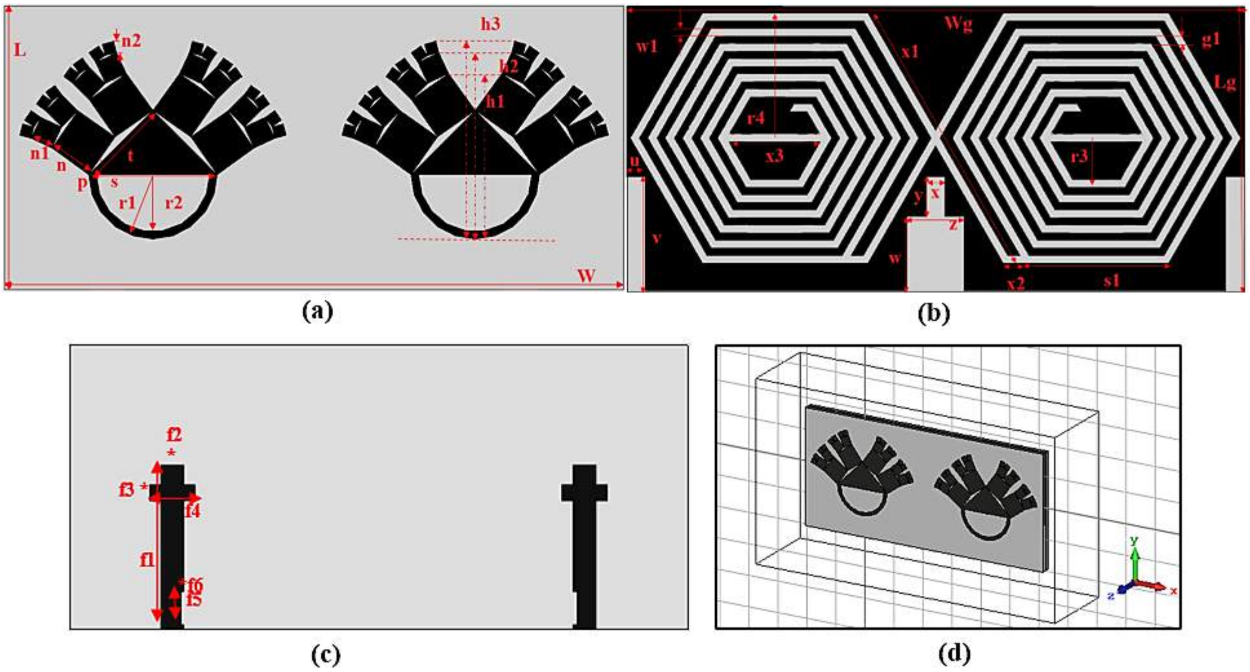

Figure 3.22 (a) Modified Pythagorean tree fractal patches (upper FR4 surface) (b) Ground defected with spiral DGS (top view of lower FR4) (c) Rear view of feed substrate (d) 3D view

Table 3.3 Design parameters with optimized values for the proposed two-port fractal antenna

Parameter	L	W	s	t	r1	r2	n	n1	n2	x	y	z
Unit (mm)	37.5	81.5	16.97	12	8.485	7.485	6.0924	3.0931	1.5704	2.5	5.25	7.5
Parameter	v	w	h1	h2	h3	Lg	Wg	w1	r3	r4	g1	x1
Unit (mm)	15	9.75	21.833	24.594	26.088	37.5	81.5	1	6.5	16.5	1	36.95
Parameter	x3	s1	f1	f2	f3	f4	f5	f6				
Unit (mm)	12.12	19.05	21.75	3	3	6	4.5	0.5				

3.3.2 Design Analysis of Proposed Fractal MIMO Antenna for UWB Applications

This section presents a detailed explanation of the structural variations in the patch, ground, and feedline configurations to realize the desired UWB behavior by employing the parametric sweep tool available in the time domain solver of CST version ’18 software.

3.3.2.1 Iterative Process for Modified Pythagorean Tree Fractal Configuration

The step-by-step design approach followed to realize the final optimized Pythagorean tree fractal patch geometry (up to three iteration levels) while keeping the ground and feedline configuration constant is demonstrated in Figure 3.23(a). The corresponding S_{11}/S_{22} (dB) and S_{21}/S_{12} (dB) simulated responses for different patch geometries are presented in Figure 3.23(b) and Figure 3.23(c) respectively. The patch design begins with a right-angled isosceles triangle of side length ‘t’ (Antenna I), calculated for generating a resonance at 7.1 GHz using Equations (22-25) [167].

$$f_{m,n} = \frac{c_0\sqrt{m^2+n^2}}{2t\sqrt{\varepsilon_{eff}}} \tag{22}$$

$$\varepsilon_{\mathrm{eff}} = \frac{(\varepsilon_r+1)}{2} + \frac{(\varepsilon_r-1)}{4}\left(1 + 12\frac{h_{\mathrm{FR-4}}}{t_0}\right)^{-1/2} \tag{23}$$

$$t = t_0(1 + q) \tag{24}$$

$$q = \left[\frac{h_{\mathrm{FR-4}}}{t_0}\left\{0.25\frac{t_0}{h_{\mathrm{FR-4}}} + 0.441 + 0.082\left(\frac{\varepsilon_{\mathrm{eff}} - 1}{\varepsilon_{\mathrm{eff}}^2}\right) + \right\} - \left(\frac{\varepsilon_{\mathrm{eff}} + 1}{2\pi\varepsilon_{\mathrm{eff}}}\right)\left(1.451 + \ln\left(0.25\frac{t_0}{h_{\mathrm{FR-4}}} + 0.94\right)\right)0.25\right]\left(\frac{\varepsilon_{\mathrm{eff}} + 0.3}{\varepsilon_{\mathrm{eff}} - 0.258}\right) \tag{25}$$

where ‘t’ is the effective side length of a right-angled isosceles triangle which is determined by utilizing the light speed ($c_0 = 3\times10^8$ m/s), the effective dielectric constant of FR4 substrate ($\varepsilon_{eff} = 3.2$), and the side length of a right-angled isosceles triangle ($t_0 = 10.23$ mm) for the dominant TM_{10} mode (where m and n are mode indices). Antenna II is constructed by introducing a semi-circular ring (with inner ‘r1’ and outer ‘r2’ radius) at the base of each right-angled isosceles triangle to enhance the matching performance, especially in the lower frequency region. Antenna III represents the first iteration of the modified Pythagorean tree fractal array where two squares (of side 6.0924 mm) are inserted on each equal arm of the right-angled isosceles triangles (with 8 squares in total). It is found that Antenna III operates in five frequency bands (green curve in Figure 3.23(b)) with FBWs of 9% (3.71-4.06 GHz), 21.94% (4.22-5.26 GHz), 37.1% (5.4-7.86 GHz), 23% (7.97-10.043 GHz) and 5.1% (10.073 -10.63 GHz) and exhibits poor isolation ($S_{21}/S_{12} \leq$ -11.5 dB) performance (green curve in Figure 3.23(c)). Next, Antenna IV illustrates the second iteration of the modified Pythagorean tree fractal array which inserts 16 squares (2 squares on each square of the first iteration) of side 3.0931mm in the array. The simulated results indicate that Antenna IV provides a triple-band operation (blue curve in Figure 3.23(b)) with FBWs of 75.24% (3.73-8.95 GHz), 7.54% (9.06-9.77 GHz) and 4.7% (10.12-10.61 GHz) and realize minimum isolation of 13.7 dB (blue curve in Figure 3.23(c)). As the primary focus of the proposed array is to realize an optimum impedance matching performance resulting in UWB and good inter-port isolation response, the 3rd iteration of the modified Pythagorean tree fractal array (Antenna V) is developed recursively (by adding 32 squares of side 1.5704 mm) to excite the UWB spectrum from 3.7-10.64GHz (96.8% FBW) with an improved level of isolation ($S_{12}/S_{21} \leq$-16.1dB) as shown by red curves in Figure 3.23(b) and Figure 3.23(c) respectively.

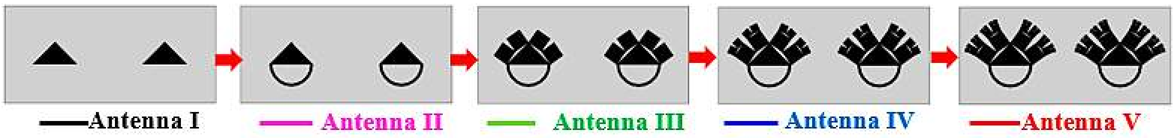

(a)

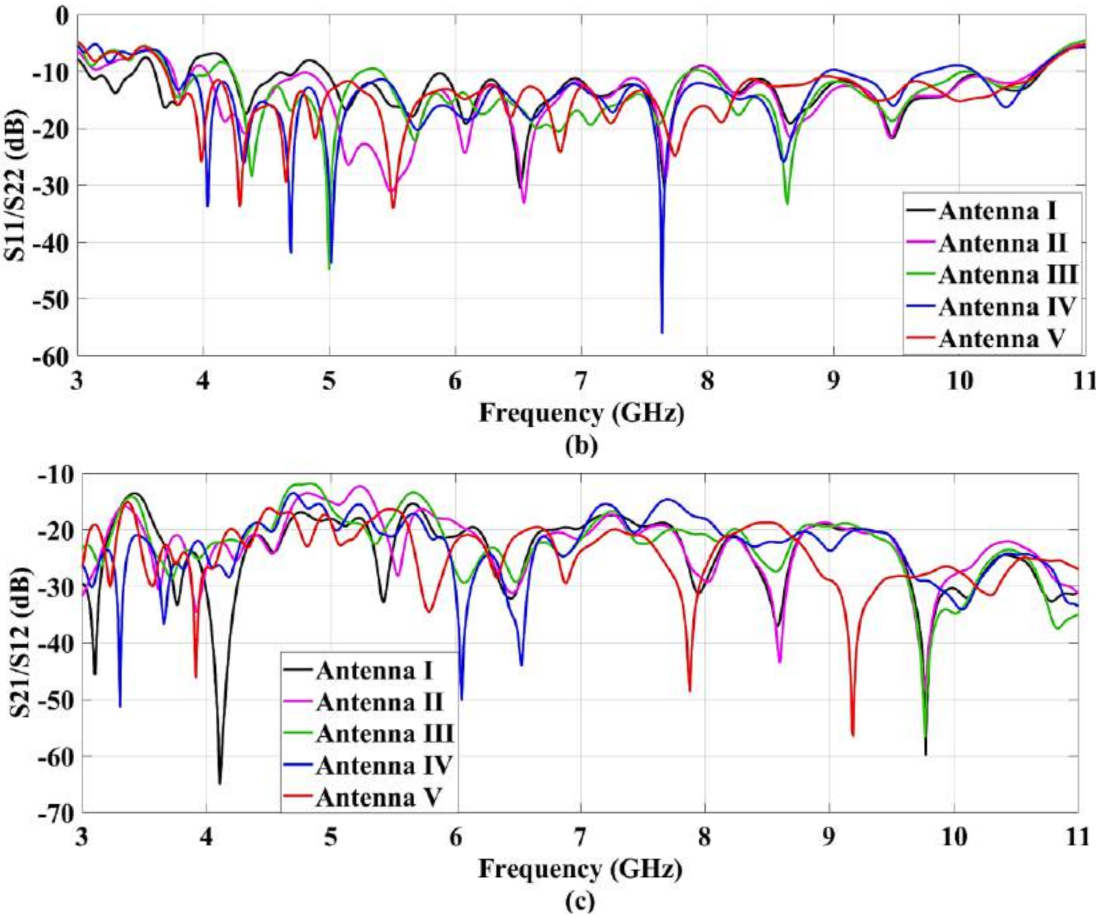

Figure 3.23 (a) Stepwise design approach for modified Pythagorean tree fractal radiators (b) Return loss (S_{11}/S_{22}) (c) Inter-port isolation (S_{21}/S_{12}) results versus frequency

3.3.2.2 Optimizing Inter-element Spacing and Effect of Modifying Apertures Etched in Ground Plane

The proposed array is driven by an aperture-coupled excitation scheme as it facilitates the maximal power transmission from the feedlines to the fractal antenna elements and offers a reasonably high bandwidth of operation [45]. Stages 1-3 in Figure 3.24(a) demonstrate the evolution steps for optimizing the inter-element spacing between the antenna elements using the parametric sweep tool available in CST version' 18 software. The corresponding S-parameter (S_{11}/S_{22}, S_{21}/S_{12}) performances as a function of frequency are depicted in Figure 3.24(b, c) respectively. Initially, the coupling apertures are etched from the ground plane beneath the fractal radiators (Stage 1) where the center-to-center distance between radiating elements is kept equal to $0.8\lambda_o$ while the patch and feedline geometries are kept fixed. For achieving a wide frequency response with an optimum isolation level, each coupling aperture (Stage 1) is transformed into complementary hexagonal spiral-shaped DGS with 6 windings (Stage 2) while keeping patch and feedline configuration constant. To extend the operational bandwidth and improve the isolation performance, the separation distance between the antenna elements is increased to $0.9\lambda_o$ (Stage 3). After optimizing the inter-element spacing of the proposed array design, for the next stages, the structural variations are incorporated in the ground plane of the proposed array while the patch and feedline configuration is kept fixed. The corresponding S_{11}/S_{22} and S_{21}/S_{12} results versus frequency for Stages 4-6 are shown in

Figure 3.24(d, e). As demonstrated by Stage 4 in Figure 3.24(a), the outermost segments of each hexagonal spiral are linked by an ‘X’ shape slot to cover the lower UWB region (green curve in Figure 3.24(d)). Further, the left and right corners of the ground are defected with two rectangular slots (Stage 5) to extend the operational range from 3.7-10.3 GHz (94.2%) but result in poor impedance matching (blue curve in Figure 3.24(d)) and a low degree of isolation (blue curve in Figure 3.24(e)). Finally, a staircase-like slot is etched from the middle of the ground geometry (Stage 5) to cover an upper UWB spectrum, resulting in an enhanced FBW (3.7-10.64 GHz, 96.8%) with optimum impedance match (red curve in Figure 3.24(d)) and an improved isolation performance between the antenna elements (red curve in Figure 3.24(e)).

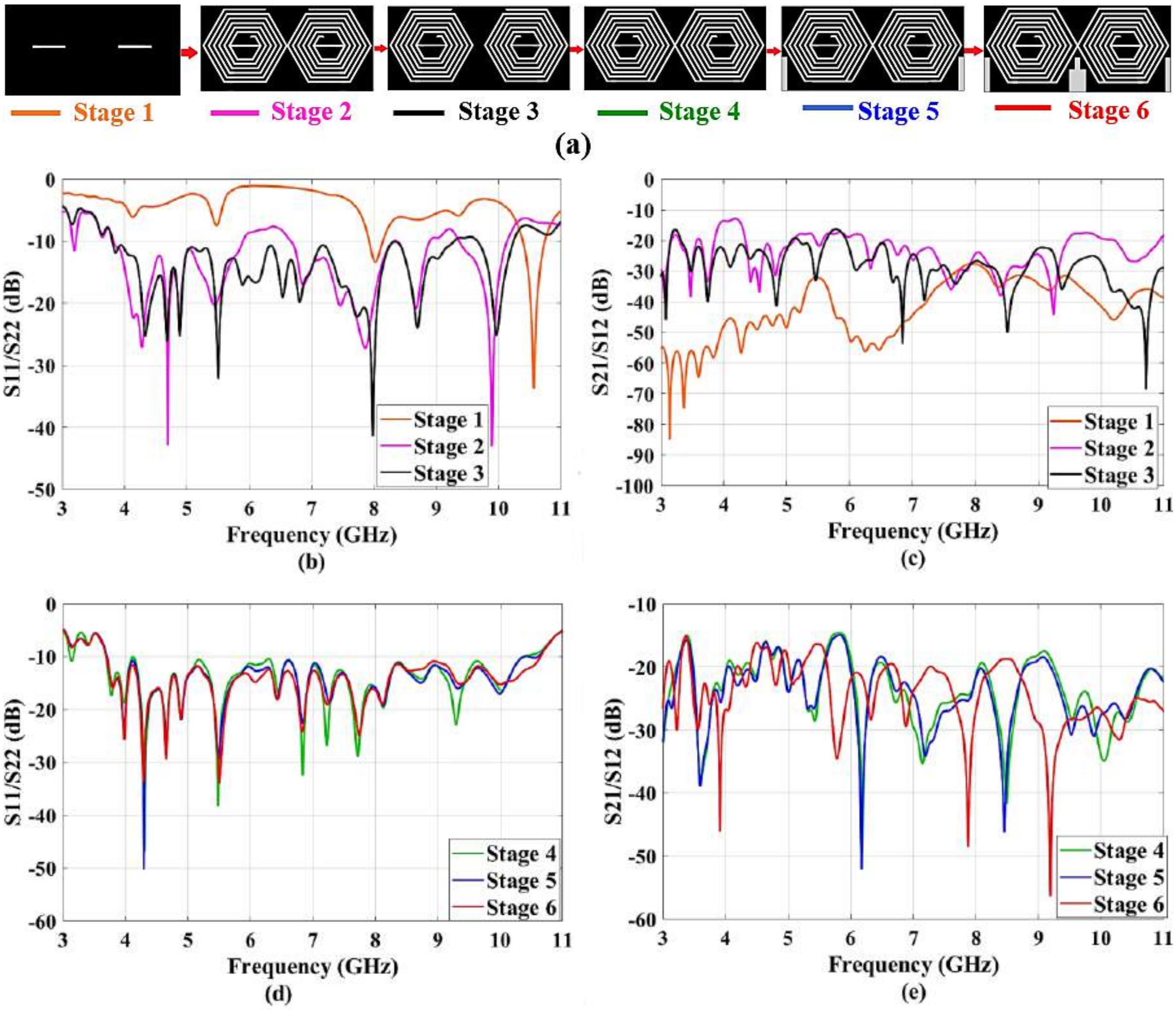

Figure 3.24 (a) Intermediate geometrical variations to obtain a final optimized ground plane configuration (b, c) simulated S_{11}/S_{22} (dB) and S_{21}/S_{12} (dB) for variation in inter-element spacing between the antenna elements (d, e) simulated S_{11}/S_{22} (dB) and S_{21}/S_{12} (dB) for the different stages of the ground plane by keeping patch and feedline design constant

3.3.2.3 Effect of Modifying Microstrip Feedlines

Figure 3.25(a) shows the intermediary steps for designing optimized feedlines while keeping patch and ground geometries constant. The simulated S_{11}/S_{22} (dB) results for different configurations of feedlines are shown in Figure 3.25(b). With the main purpose of minimizing signal reflections due to impedance mismatches, the two feedlines (left offset by 6 mm from the middle) are modified by a horizontal stub (at the top) and a vertical slot (at the bottom). As the red-colored curve in Figure 3.25(b) shows an acceptable impedance match across the entire functional range (3.7-10.64 GHz), so the 'Level IV' feed configuration is the preferred choice for the proposed fractal array.

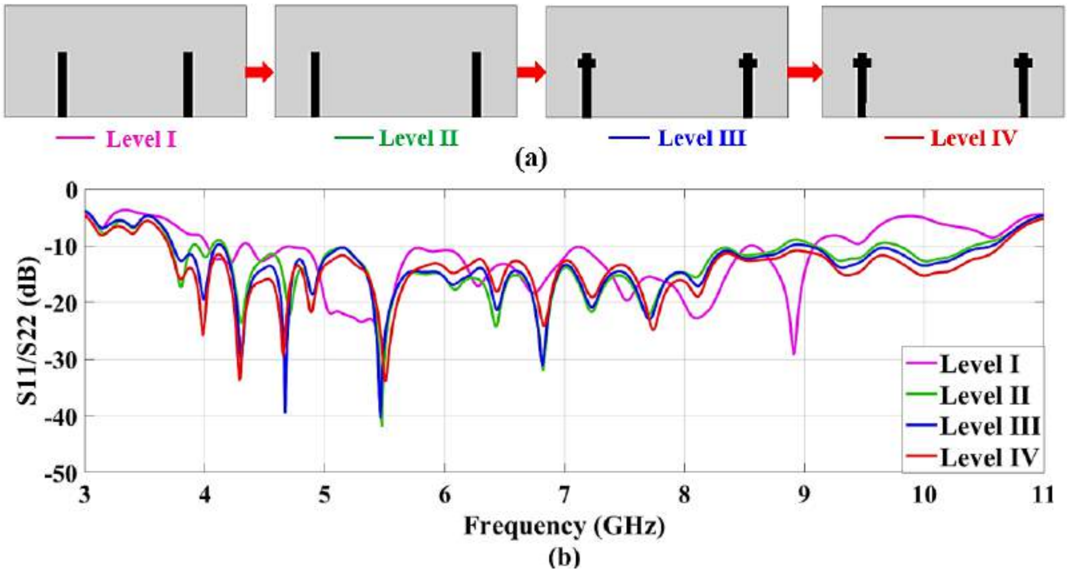

Figure 3.25 (a) Intermediate levels to obtain a final optimized microstrip feed line (b) Simulated return loss (S_{11}/S_{22} (dB)) versus frequency results for the different levels of feedlines

3.3.3 Simulation and Measurement Results

To practically validate the simulated results of the designed array, it is fabricated (using the photolithography technique) on a pair of 1.57mm FR4 substrates ($\varepsilon_r = 4.4$, tan $\delta = 0.024$). For supporting the UWB performance, Figure 3.26(a-c) displays the fabricated snapshots of the proposed modified Pythagorean tree fractal UWB-MIMO antenna. The proposed fractal array is fused with two 50 Ω SMA connectors at the feed points for energizing the fractal patches.

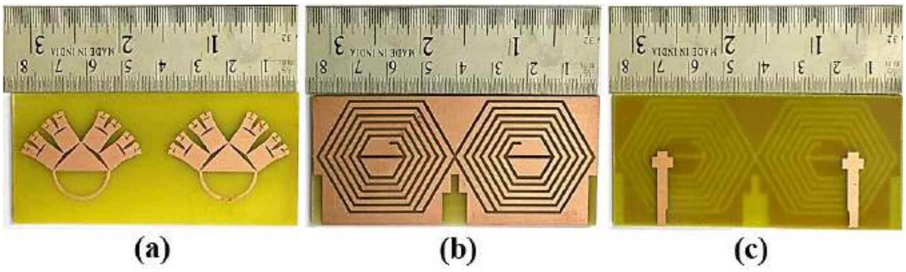

Figure 3.26 (a-c) Fabricated photographs of designed UWB Pythagorean tree fractal array

3.3.3.1 Scattering Parameters and Gain Performance

A comparison plot between the simulation and experimental S-parameter (dB) results against the frequency (GHz) for the designed UWB fractal array is shown in Figure 3.27(a, b). It offers a simulated impedance bandwidth of 6.94GHz from 3.7-10.64GHz (96.8%) with mutual coupling lower than -16.1dB over the complete band of operation. The measured S-parameter results illustrate that the fabricated UWB array can function in the 3.495-11.73GHz range (108.1%) and exhibit a low degree of mutual coupling ($S_{21} \leq$ -15.4dB) between the radiating antenna elements.

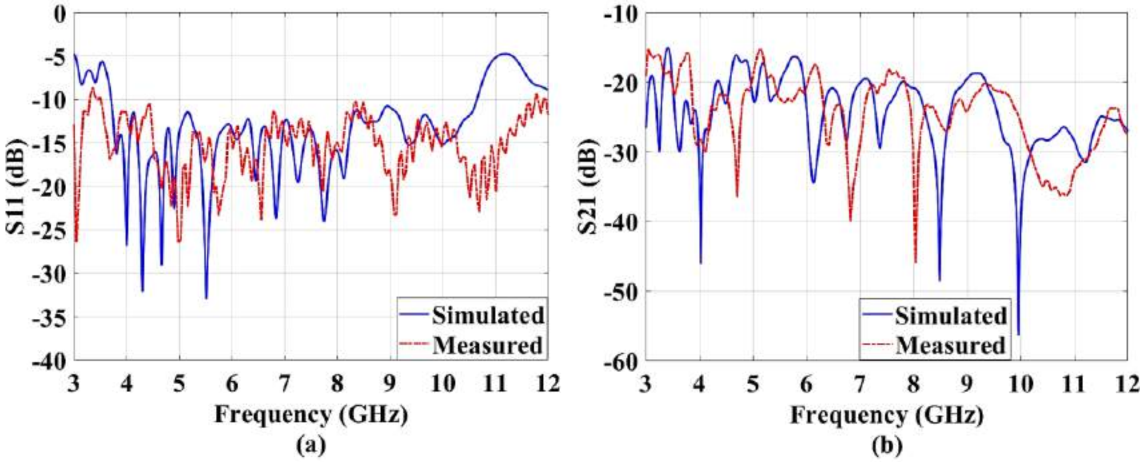

Figure 3.27 Variation of simulation and experimental (a) S_{11} (b) S_{21} against frequency for the designed UWB fractal MIMO antenna

For the energized port-1, the gain variations across the operational band for the proposed UWB fractal array are plotted in Figure 3.28. The proposed UWB array offers a maximal simulated gain of 4.34dBi (at 9.4 GHz) with an average gain of 2.11dBi across the entire operational range.

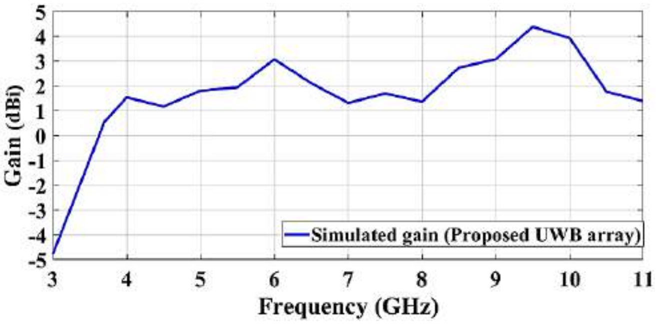

Figure 3.28 Broadband gain versus frequency for the proposed UWB fractal array

3.3.4 Diversity Performance Parameters

In this subsection, certain important diversity metrics namely ECC, DG, MEG, CCL, and TARC are estimated and studied to examine the behavior of the designed UWB-MIMO antenna in the multipath fading surroundings. For computing these diversity metrics, the MATLAB code is generated and also validated with the experimental values.

3.3.4.1 Envelope Correlation Coefficient

ECC is a crucial performance metric defined to evaluate the degree of correlation between the array elements functioning simultaneously in a MIMO configuration. For the proposed UWB array, as demonstrated in Figure 3.29(a), the ECC ≤ 0.006 (simulated) and ≤ 0.003 (measured) is realized across the UWB functional range from 3.7-10.64 GHz using the S-parameter method (Equation 1 in chapter 1).

3.3.4.2 Diversity Gain

To realize an optimal quality and reliability of a wireless communication system, a high DG (nearly 10) is desired in the working frequency band. It is estimated from the ECC using Equation 3 (given in chapter 1). According to Figure 3.29(b), the DG $\geq$ 9.968 (simulation) and $\geq$ 9.983 (experimental) achieved in the 3.7-10.64 GHz range affirms a meritorious diversity performance of the designed UWB array. High values of DG symbolize the accomplishment of a significant diversity operation from the designed fractal array imperative for UWB-MIMO applications.

3.3.4.3 Mean Effective Gain

As plotted in Figure 3.29(c), the MEG values (both simulated and experimental) for the proposed UWB array vary in the range of -3dB to -4dB for the whole working band with $|MEG_1-MEG_2|$ = 0dB (simulated) and -0.73dB < $|MEG_1-MEG_2|$ < 0.58dB (measured).

3.3.4.4 Channel Capacity Loss

According to Figure 3.29(d), CCL levels for the proposed UWB array are beneath 0.4 bits/s/Hz (both simulated and experimental) for the complete working range, which signifies that the proposed array exhibits a significant channel capacity across the operational band.

3.3.4.5 Total Active Reflection Coefficient

The TARC value of < -10dB (both simulated and measured) is observed over the complete band of operation for the proposed UWB array as illustrated in Figure 3.29(e), which is desirable for efficient MIMO antenna performance.

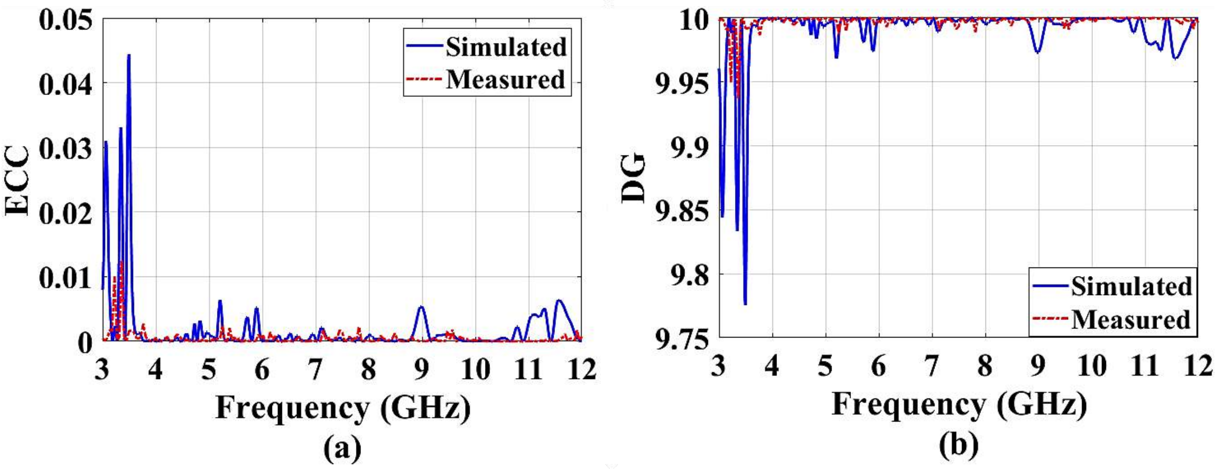

(a)

(b)

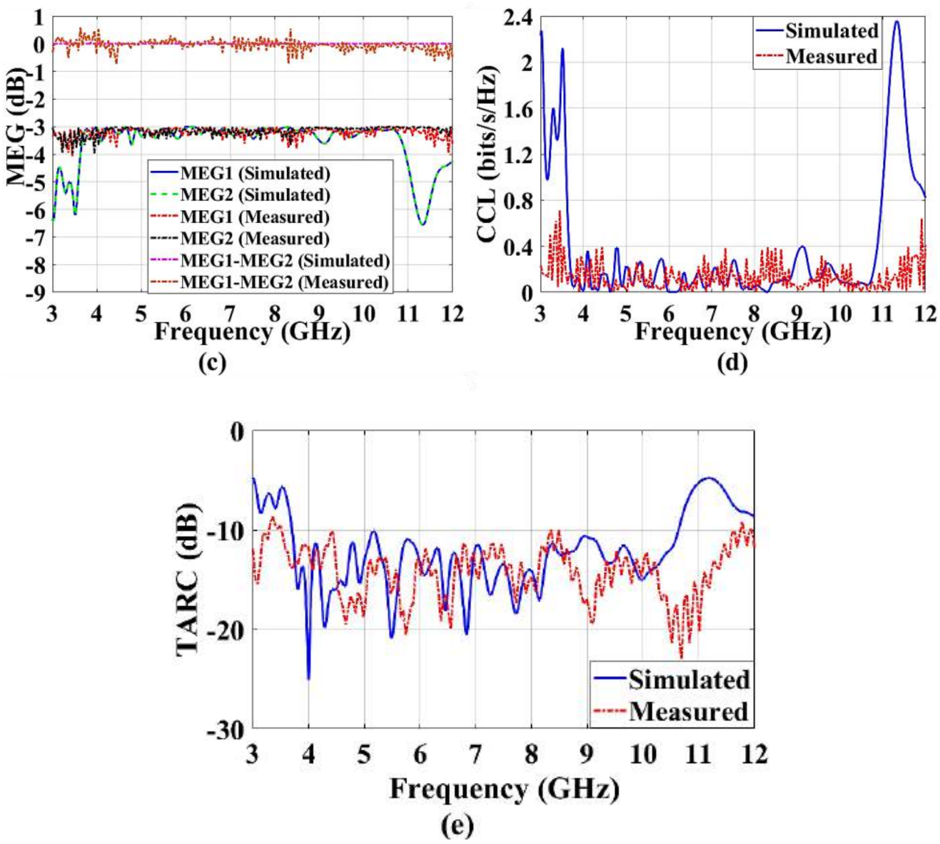

Figure 3.29 Simulated and measured (a) ECC (b) DG (c) MEG (d) CCL (e) TARC performances versus frequency for the proposed UWB fractal array

The succeeding section of this chapter presents the next proposed design on fractal MIMO antenna with two microstrip-fed semi-circular radiators combined with Koch curve fractal and a reduced defected ground for accomplishing the desired UWB of operation.

3.4 Design and Development of Semi-circular Koch curve fractal UWB-MIMO antenna

This section presents a two-port, microstrip-fed, semi-circular patch antenna integrated with Koch curve fractals for effective implementation in handheld ultra-wideband (UWB) systems. The proposed array is engraved on a 1.57 mm thick FR4 substrate where the upper substrate layer incorporates two optimized Koch curve fractal (2^{nd} iteration order) radiators whereas the lower substrate layer comprises a reduced defected ground combined with a funnel shaped decoupler. The proposed array provides optimum matching performance in a wide operational band (4.395-10.184 GHz) with good port-to-port isolation ($S_{21}/S_{12} \leq -16.8$ dB) and minimizes the patch area by 41.2% as compared to the conventional circular patch. The designed array's prototype is fabricated and experimented to justify the simulated S-parameter results.

3.4.1 Proposed Fractal Array Design

Figure 3.30(a, b) shows the geometry of the proposed 2 × 2 semi-circular MPA array with Koch curve fractals and a minimized ground with DGS for MIMO implementation in UWB radio systems. The proposed fractal array is modeled on an economical FR4 lossy substrate ($\varepsilon_r = 4.4$, $\tan \delta = 0.024$, and $h_t = 1.57$ mm) with a total volumetric size of 30.5 × 47 × 1.64 mm^3. As illustrated in Figure 3.30(a), the top substrate surface is composed of two semi-circular radiating patches where the upper edge of each radiator is combined with a Koch curve fractal (iterated up to 2nd order) geometry. The proposed fractal array is fed using two microstrip transmission lines, each with a characteristic impedance of 50Ω. A horizontal stub is loaded at the lower portion of each feedline to realize an enhanced matching performance in the excited operational band. Taking array compactness and good inter-port isolation into consideration, the separation distance between the fractal patches is fixed at 21.2 mm.

Figure 3.30(b) presents the ground configuration of the proposed fractal array integrated with a DGS technique (rear view of FR4 substrate). To realize a wideband operation from the proposed array, the length of the common ground plane is reduced to 12.5 mm ('Wg'). A funnel-shaped decoupling structure extends vertically (at an angle of 90°) from the reduced ground plane to obstruct the steady flow of current between the two fractal patches and hence minimize the effect of cross-coupling. To match the 50 Ω characteristic impedance from the proposed array, the upper edge of the reduced ground is defected with two mirror-imaged rectangular slots (situated behind the feedline). The base of each rectangular slot is further combined with a horizontal L-shaped slot to realize a high degree of isolation between the two ports of the proposed array. The parametric values of the optimized fractal array are mentioned in Table 3.4.

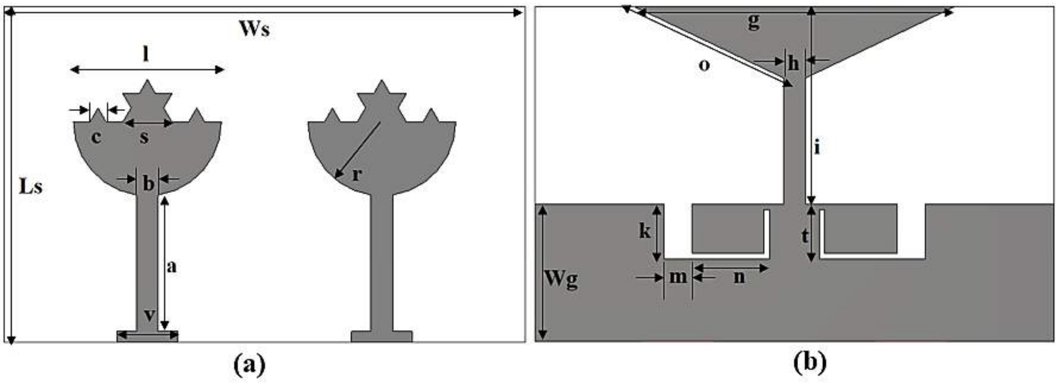

Figure 3.30 (a) Microstrip line fed Koch curve fractal radiators (b) Reduced ground with DGS

Table 3.4 Parametric values (mm) of the proposed fractal array

Parameter	Ls	Ws	a	b	c	v	s	l	r
Unit (mm)	30.5	47	12.3	2.4	1.489	5.5	4.466	13.4	6.7
Parameter	Wg	m	n	o	g	h	i	k	t
Unit (mm)	12.5	2.5	7.11	15	29.22	2	18	5	4.5

3.4.2 Study on Geometrical Variations of Proposed Fractal Array

3.4.1 Optimization of Koch Curve Fractal Radiators

Figure 3.31 demonstrates the stepwise approach followed to realize the final 2nd iterative Koch curve fractal patch geometry and the corresponding impedance bandwidth (S_{11}/S_{22}) characteristics of the proposed fractal array are presented in Figure 3.33. The recursive procedure followed to reach the 2nd order of iteration of the Koch curve fractal is shown in Figure 3.32. Initially, the array design starts with the circular radiating patches (Level I), each with optimized radius ‘r’, computed for a higher order of resonance ‘f_r’ (black curve in Figure 3.33) using Equation 17.

Level II is constructed by cutting off the upper half of circular patches resulting in semi-circular patch geometry, designed to excite lower as well as a higher order of resonances at 5.4 GHz and 9.2 GHz respectively (orange curve in Figure 3.33). Further, a horizontal stub is inserted at the lower end of each feedline (Level III) to provide a dual-band operation from 4.7-6.1 GHz and 7.35-10.2 GHz (blue curve in Figure 3.33). Level IV and Level V represent the proposed array structures after the application of the 1st and 2nd order iteration of the Koch curve fractal at the upper edge of semi-circular radiators (Level III). As illustrated in Figure 3.32, to construct the Koch curve fractal, initially, a straight line of length ‘l’ is considered (0th order of iteration). The length ‘l’ is further cut into three equal segments (each of length ‘l/3’) where the central segment is replaced by the two other segments of an equilateral triangle (each with length ‘l/3’) resulting in the 1st order of iteration. This process is iterated recursively to form the higher order of iterations. The self-similar repetitions of the proposed Koch curve fractal can be generated by the IFS approach, defined by the generalized matrix Equation (10) given in chapter 1.

Using a=cos θ/s, b = -sin θ/s, c = sin θ/s, and d = cos θ/s where s = 1/3 and θ = 60° for two segments of an equilateral triangle (one in clockwise, other in anticlockwise direction), the required IFS transformation for Koch curve fractal is calculated by Equations (26-29).

$$W_1\begin{bmatrix}x\\y\end{bmatrix}=\begin{bmatrix}1/3 & 0\\0 & 1/3\end{bmatrix}\begin{bmatrix}x\\y\end{bmatrix}+\begin{bmatrix}0\\0\end{bmatrix}\text{for }\theta = 0^\circ \tag{26}$$

$$W_2\begin{bmatrix}x\\y\end{bmatrix}=\begin{bmatrix}1/6 & -\sqrt{3}/6\\\sqrt{3}/6 & 1/6\end{bmatrix}\begin{bmatrix}x\\y\end{bmatrix}+\begin{bmatrix}1/3\\0\end{bmatrix}\text{for }\theta = 60^\circ \tag{27}$$

$$W_3\begin{bmatrix}x\\y\end{bmatrix}=\begin{bmatrix}1/6 & \sqrt{3}/6\\-\sqrt{3}/6 & 1/6\end{bmatrix}\begin{bmatrix}x\\y\end{bmatrix}+\begin{bmatrix}1/2\\\sqrt{3}/6\end{bmatrix}\text{for }\theta = -60^\circ \tag{28}$$

$$W_4\begin{bmatrix}x\\y\end{bmatrix}=\begin{bmatrix}1/3 & 0\\0 & 1/3\end{bmatrix}\begin{bmatrix}x\\y\end{bmatrix}+\begin{bmatrix}2/3\\0\end{bmatrix}\text{for }\theta = 0^\circ \tag{29}$$

The red-colored curve in Figure 3.33 (for Level IV) covers a wide functional band from 4.57-10.13 GHz (75.6% FBW) but exhibits a poor impedance matching performance. To minimize the mismatch losses in the excited frequency range, the Koch curve fractal is iterated up to the 2nd order. The final Koch curve fractal array (Level V) operates in the frequency band from 4.395-10.184 GHz (79.4% FBW) with an optimum matching characteristic (green-colored curve in Figure 3.33). Therefore, it can be concluded that the array geometry proposed in Level V helps in size miniaturization as it reduces the circular patch area by 41.2% (Level 1) and provides better matching characteristics across the entire range of operation due to the increment in the effective length of the surface current path by the introduction of fractal geometry.

Figure 3.31 Intermediate design steps for the construction of final optimized fractal radiators

Figure 3.32 Design procedure for construction of the Koch curve fractal up to 2nd iteration

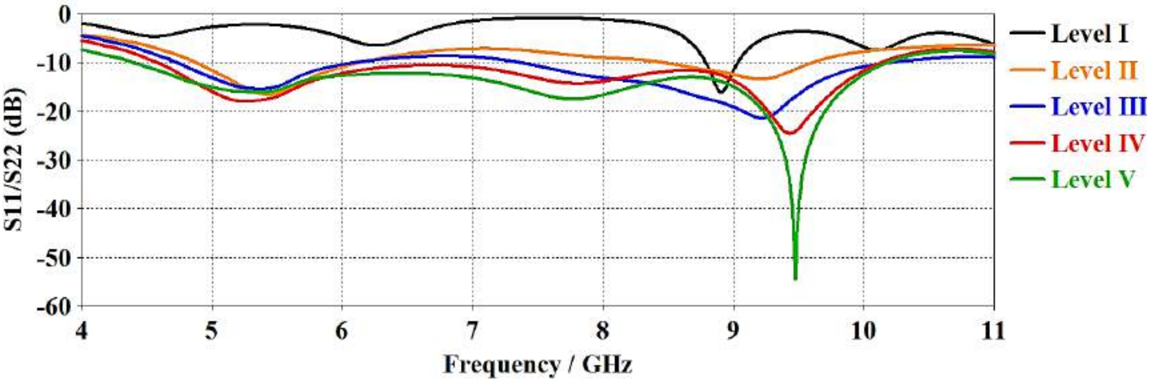

Figure 3.33 Comparison of S_{11}/S_{22} (dB) characteristics for geometrical variations in the patch

3.4.2 Optimization of Common Ground with DGS

Figure 3.34 demonstrates the evolutionary stages of the common ground plane with DGS to realize a wide functional band with a low degree of mutual coupling for a fixed Koch curve patch geometry (2nd iteration). Their corresponding S_{11}/S_{22} (dB) and S_{21}/S_{12} (dB) performances (relative to the frequency) are depicted in Figure 3.35 and Figure 3.36 respectively. Stage I demonstrates a full ground plane configuration of the proposed fractal array, responsible for exciting the resonances at 7.8 GHz and 9.6 GHz respectively (black curve in Figure 3.35) with a high degree of port-port isolation (black curve in Figure 3.36). Generally, reducing the ground along the Y-direction results in more fringing and therefore improves the bandwidth of operation. So, the ground is reduced to an optimized length of 12.5 mm (Stage II) to cover the frequency range from 4.58-9.33GHz (orange curve in Figure 3.35) with $S_{21}/S_{12} \leq -9.5$dB (orange curve in Figure 3.36). Further, to enhance the isolation and matching performance of the proposed array (blue curve in Figure 3.35 and Figure 3.36), a vertical stub is elongated (at an angle of 90˚) from the middle of the reduced ground plane (Stage III). Stage IV is constructed by embedding an upturned isosceles triangle at the upper end of the vertical stub. This funnel-shaped decoupling structure provides a dual-band operation from 4.44-5.97GHz and 6.79-9.9GHz (red curve in Figure 3.35) with a low degree of isolation ($S_{21}/S_{12} \leq -14$ dB) between the two ports (red curve in Figure 3.36). To minimize the effect of mismatch losses and mutual coupling in the working frequency band, the upper edges of the reduced ground are defected with two mirror-imaged rectangular slots (behind the feedlines), each combined with a horizontal L-shaped slot (Stage V). This ground plane configuration provides the best-optimized results with the widest impedance bandwidth of 5.789 GHz and S_{21}/S_{12} (dB) ≤ 16.8 dB (green curve in Figure 3.35 and Figure 3.36 respectively).

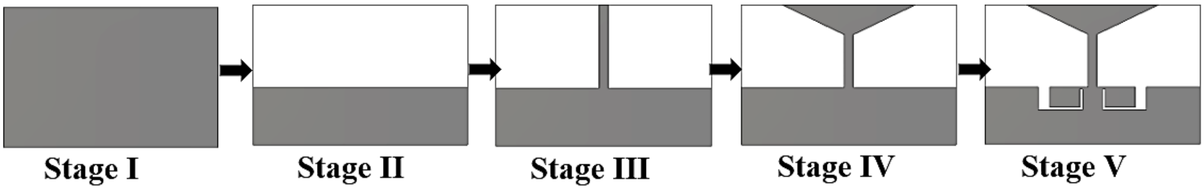

Figure 3.34 Geometrical variations in the ground plane geometry of the proposed fractal array

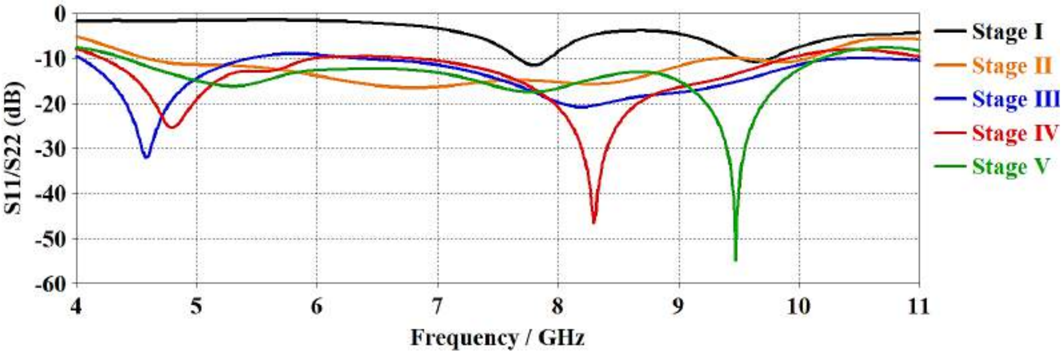

Figure 3.35 Comparison of S_{11}/S_{22} (dB) performance for variations in ground plane geometry

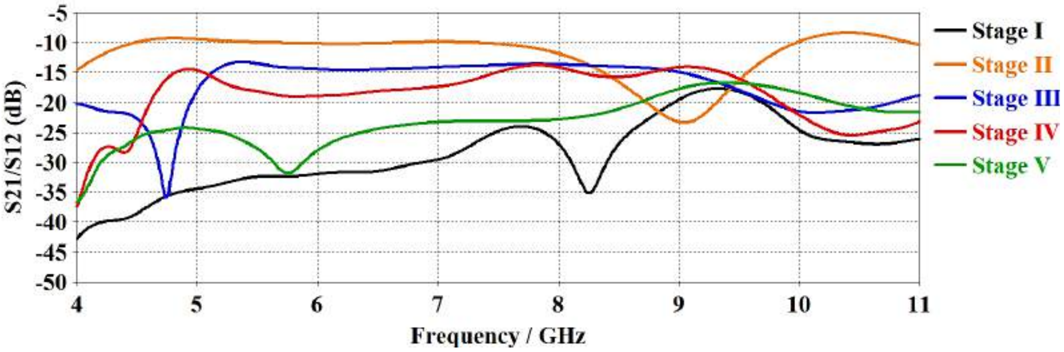

Figure 3.36 Comparison of S_{21}/S_{12} (dB) performance for variations in ground plane geometry

3.4.3 Simulated and Measured Responses

3.4.3.1 Return loss (S_{11}/S_{22} (dB)) and Isolation (S_{21}/S_{12} (dB)) Characteristics

To validate the array's performance in a real practical scenario, the proposed fractal array is fabricated using a photolithography process and is tested for S-parameters (S_{11}, S_{22}, S_{21}, S_{12}) values using VNA E5063A (100KHz-18GHz) under normal laboratory conditions. To energize the fractal patches, a 50Ω female SMA connector is soldered at the termination of each feedline as shown in Figure 3.37. Figure 3.38 shows the variation of the simulated and measured S_{11}/S_{22} (dB) and S_{21}/S_{12} (dB) as the function of frequency. The proposed fractal array covers a simulated operational band from 4.395-10.184GHz (79.4% FBW) and a peak S_{11}/S_{22}(dB) of -54.5dB at 9.4GHz frequency. The measured results on a VNA show a frequency band of 4.6-10.45GHz (S_{11}) and 4.55-10.32GHz (S_{22}) with the FBW of 77.7% GHz and 77.6% respectively. The simulated and measured S_{11}/S_{22} (dB) responses show an acceptable similitude of 95% and 97% match at the lower and frequency band respectively. A good port-to-port isolation

($S_{21}/S_{12} \leq$-16.8dB (simulated) and $S_{21}/S_{12} \leq$-19.3dB (measured)) is achieved for the entire operational band.

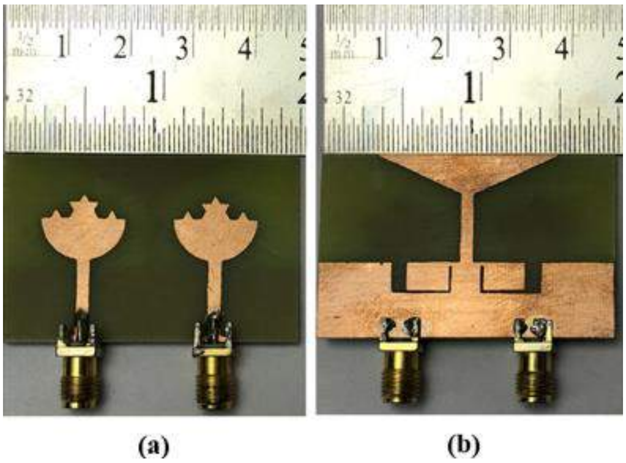

(a) (b)

Figure 3.37 Snapshots of the fabricated fractal array (a) Fractal radiators (b) Ground view

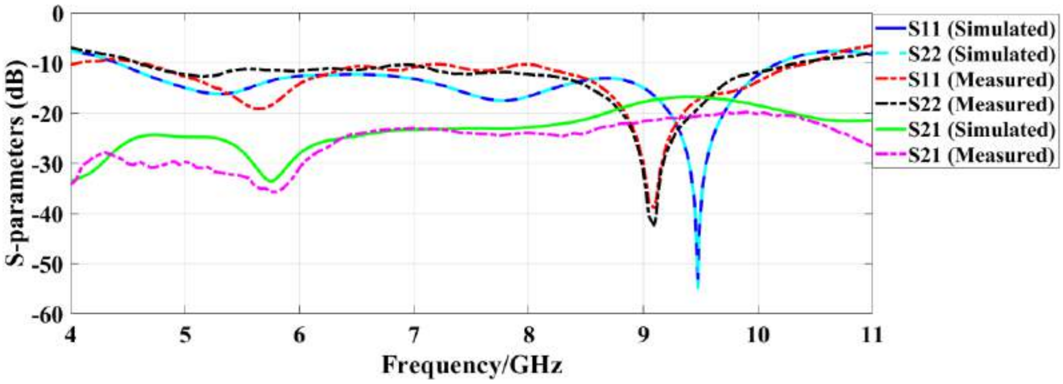

Figure 3.38 Simulated and measured (a) S_{11}/S_{22} (dB) (b) S_{21}/S_{12} (dB) results versus frequency

3.4.3.2 Radiation Analysis

Antenna gain quantifies the maximum distance that can be covered by the EM wave. Figure 3.39 shows the variation of antenna gain (in the broadside direction) for the activated port-1 in the functional range from 4.395-10.184GHz. Owing to the symmetrical arrangement of the antenna elements in the proposed array, gain values remain unchanged for the activated port-2 (with port-1 ceased by a 50 Ω load). Therefore, for the energized port-1, the proposed fractal array shows a maximum gain of 3.84 dBi at 8.9GHz frequency (simulated) and 3.81 dBi at 9.25GHz frequency (measured) with an average simulated gain of ≥ 1.2 dB.

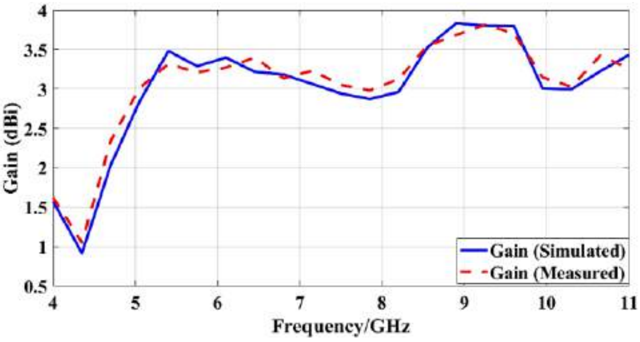

Figure 3.39 Variation of simulated and measured gain versus frequency for the excited port-1

Figure 3.40 (a-c) shows the simulated and experimental 2D far-field radiation patterns (co- and cross-polarization) for the proposed fractal array in the two reference planes, E-plane (y-z) and H-plane (x-z) at the three resonances of 5.4GHz, 7.78GHz and 9.47GHz for excited port-1. For activated port-1 and port-2 terminated, it is observed that the proposed fractal array exhibits a directional and an almost omnidirectional far-field pattern in the y-z and x-z plane respectively. The measured far-field patterns show a reasonable resemblance with the simulated ones making the proposed array suitable for a variety of wireless applications supported by the UWB spectrum.

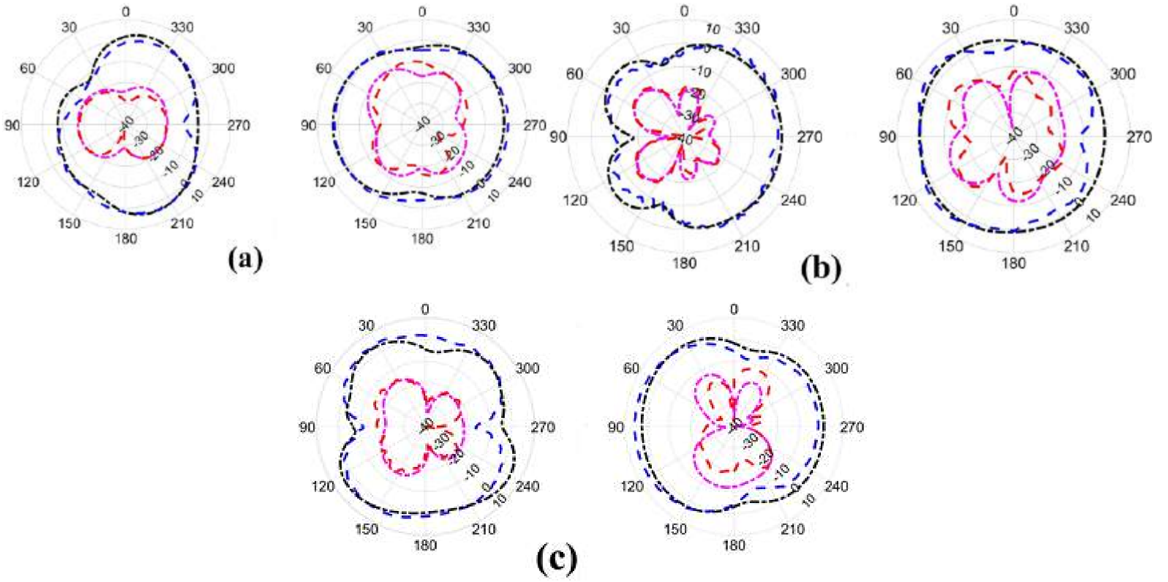

— · —	**Co-polarization (Simulated)**	— — —	**Co-polarization (Measured)**
— · —	**Cross-polarization (Simulated)**	— — —	**Cross-polarization (Measured)**

Figure 3.40 2D radiation pattern of the proposed MPA array in the y-z plane and x-z plane for the activated port-1 at (a) 5.4 GHz (b) 7.78 GHz (c) 9.47 GHz

3.4.3.3 Surface Current Distribution

To determine the influence of mutual coupling between the two array elements, Figure 3.41(a-d) shows the current distribution at 5.4GHz and 9.47GHz resonances for the activated port-1 and port-2 respectively. It is observed that the funnel-shaped stub and slotted ground plane decouple the energy from the fractal radiators and are mainly responsible for improving the isolation level between the two ports. This is also validated by the parametric analysis of the ground plane presented in Section 3.4.2. For port-1 excited by simulated 1W of power at the feed point (port-2 deactivated), the decoupling structure (inserted in the ground plane) allows a very small amount of current to flow through the non-activated antenna element (port-2) for the two resonances. For activated port-2 and port-1 terminated, a similar reduction of coupling current is observed. Hence, the proposed fractal array exhibits good isolation performance throughout the UWB of operation.

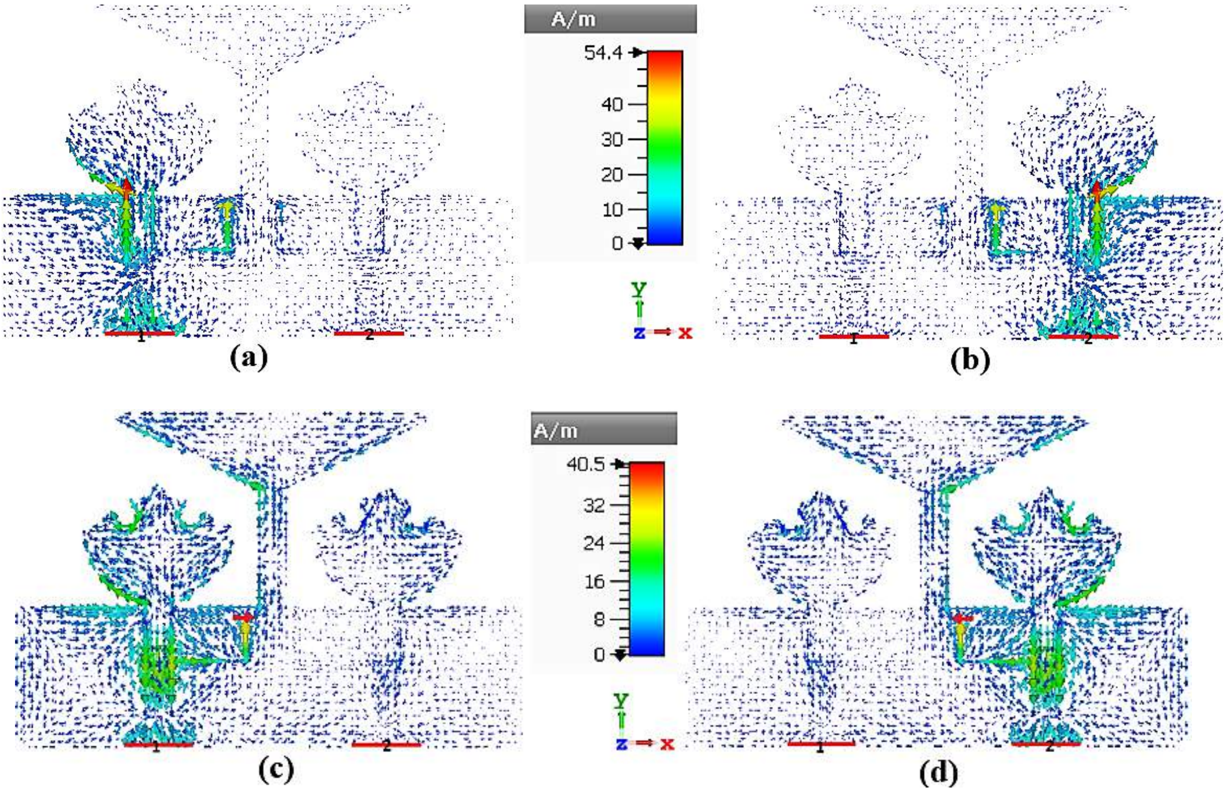

Figure 3.41 Surface current distributions for the proposed fractal array at (a) 5.4 GHz (Port-1) (b) 5.4 GHz (Port-2) (c) 9.47 GHz (Port-1) (d) 9.47 GHz (Port-2)

3.4.4 Diversity Performance Metrics

To characterize the feasibility of the proposed array for UWB systems, various diversity performance metrics such as ECC, DG, MEG, CCL, and TARC are analyzed in this subsection.

3.4.4.1 Envelope Correlation Coefficient and Diversity Gain

For a two-element MPA array, ECC and DG can be computed from S-parameters using Equations (2, 3) given in chapter 1. Figure 3.42(a, b) shows the variation of ECC and DG against the frequency. It illustrates a low level of ECC (≤ 0.0021 (simulated), ≤ 0.0023 (measured)) and a high degree of DG (≥ 9.989 (simulated), ≥ 9.988 (measured)) for a complete operational range which affirms a good diversity performance of the proposed array.

3.4.4.2 Channel Capacity Loss

CCL is the third significant diversity parameter that determines the degree of deterioration of array performance as a result of the correlation in the MIMO channel and is estimated using Equation 7 of chapter 1. Figure 3.42(c) shows a CCL level ≤ 0.4 bits/s/Hz (simulated and measured) for the entire operational range which indicates high port-to-port isolation between the array elements.

3.4.4.3 Mean Effective Gain

MEG is another important diversity metric as it determines the antenna gain performance by taking into account the real fading scenario. Assuming a uniform Rayleigh environment with identical vertical and horizontal polarization densities, MEG is equal to half of the radiation efficiency and is computed using Equation (4, 5) given in chapter 1. For good diversity performance, the difference in the magnitudes of MEG for two ports less than 3 dB is desired. As shown in Figure 3.42(d), a maximum MEG of -3.018dB (simulated) at 5.88 GHz frequency and -3.011dB (measured) at 6.2 GHz frequency is observed with an overall MEG ≥ -3.7 dB (simulated) and ≥ -3.85 dB (measured). The difference between the MEG for two ports is 0dB (simulated) and 0.69dB (tested) which makes the proposed array feasible for MIMO employment in UWB radio systems.

3.4.4.4 Total Active Reflection Coefficient

TARC is considered as the apparent return loss of the whole MIMO antenna system and for a two-port lossless MIMO antenna, TARC is mathematically computed from S-parameters using Equation 8 stated in chapter 1. As shown in Figure 3.42(e, f), TARC (dB) curves are plotted for variation in ‘θ’ (0˚, 30˚, 60˚, 90˚, 120˚, 150˚,180˚) against the frequency. The simulated and measured TARC values < -10 dB and < -8.9 dB respectively are observed for all variations of ‘θ’. The simulated and measured TARC resonance curves (at ‘θ’ = 30˚) show a good resemblance with the simulated and measured S_{11}/S_{22} (dB) curves respectively.

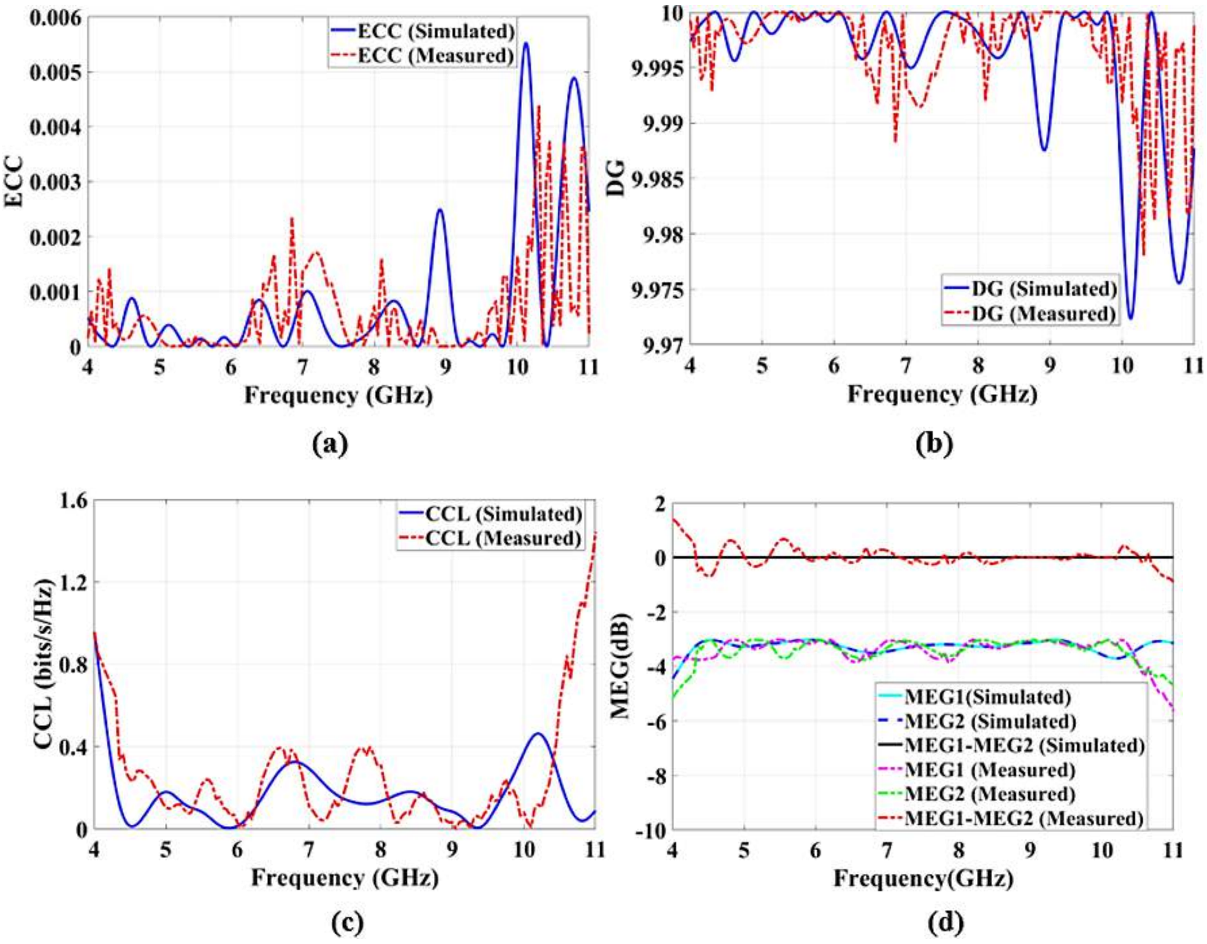

(a) (b)

(c) (d)

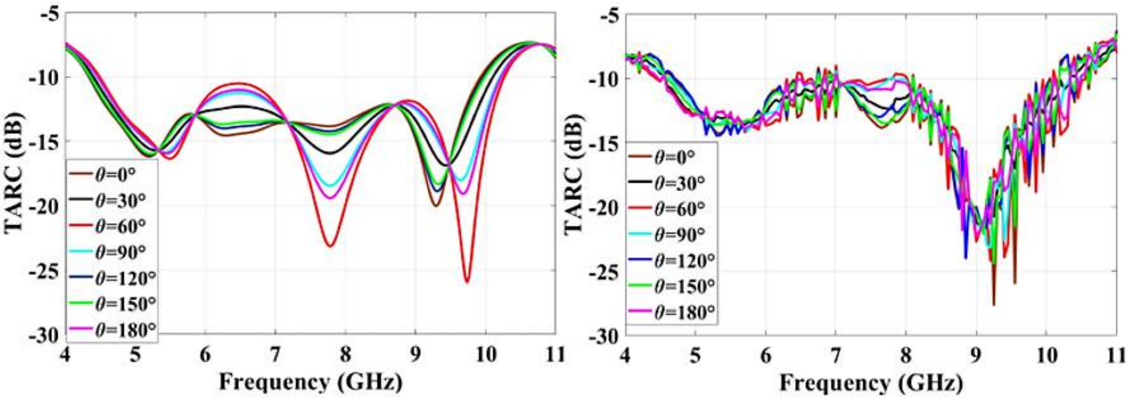

(e) (f)

Figure 3.42 Variation of (a) ECC (b) DG (c) CCL (d) MEG (e) TARC (simulated) (f) TARC (dB) (measured) versus frequency

The following section of this chapter introduces the next proposed design on fractal MIMO antenna with two microstrip-fed, Koch Snowflake fractal UWB array with a partial ground surface combined with an H-shaped decoupler and DGS method for realizing the desired UWB behavior.

3.5 Design and Development of modified Koch Snowflake Fractal UWB Array

This section introduces a dual-port, tapered-fed fractal antenna with a partial ground for effective implementation in portable UWB-MIMO devices. The array is modeled on a 1.57mm thick dielectric FR4 substrate where each circular radiator is defected with a modified 4th iterative Koch-Snowflake fractal that leads to 52.6% miniaturization of the patch area. The array yields 14.7GHz bandwidth by defecting the partial ground and offsetting the tapered feedlines. By embedding a decoupling network and DGS in the ground, significant isolation ($S_{21}/S_{12} \leq -16$dB) is accomplished. To justify the simulated results, the fabricated array is tested for S-parameters, radiation characteristics, and diversity metrics.

3.5.1 Array Geometry

The proposed array is arranged on a $41 \times 71 \times 1.57\text{mm}^3$ FR4 substrate with $\tan\delta$ of 0.024, and ε_r of 4.4. The top FR4 surface (Figure 3.43(a)) constitutes two microstrip-fed circular radiators, each defected with modified 4th order Koch-Snowflake fractal. The feedlines, with a 29.2mm center-to-center distance, are tapered and right-offset to realize a 50Ω matching and left-shift the spectrum to accomplish the lower UWB. Figure 3.43(b) presents the detailed iteration stages of the modified Koch-Snowflake fractal. Conventionally, the Koch-Snowflake fractal is constructed by partitioning each line of the equilateral triangle into three equal regions and adding a newly iterated triangular copy (scaled-down by 0.333) in the middle of each line of the previous iteration. The proposed novel fractal is recursively developed by splitting each line of the 0th order equilateral triangle into two equal parts and placing a newly iterated copy (0.5 scaling factor) on the first half of the line. The process is repeated for every iteration and ‘s0’, ‘s1’, ‘s2’, ‘s3’, and ‘s4’ are the respective sides for 0th, 1st, 2nd, 3rd, and 4th fractal iterations.

The rear FR4 surface (Figure 3.43(c)) presents a partial defected ground. To limit coupling between radiating antennas, an H-shaped decoupler is projected perpendicular to ground.

Further, two rectangular (behind feedlines) and plus-shaped (around H-shaped decoupler) slots are etched from the ground to realize a significant bandwidth and port isolation improvement. Also, a rectangular stub is inserted on the upper ground edge to attain a sufficient impedance match across the working band. Table 3.5 lists the array's parametric dimensions.

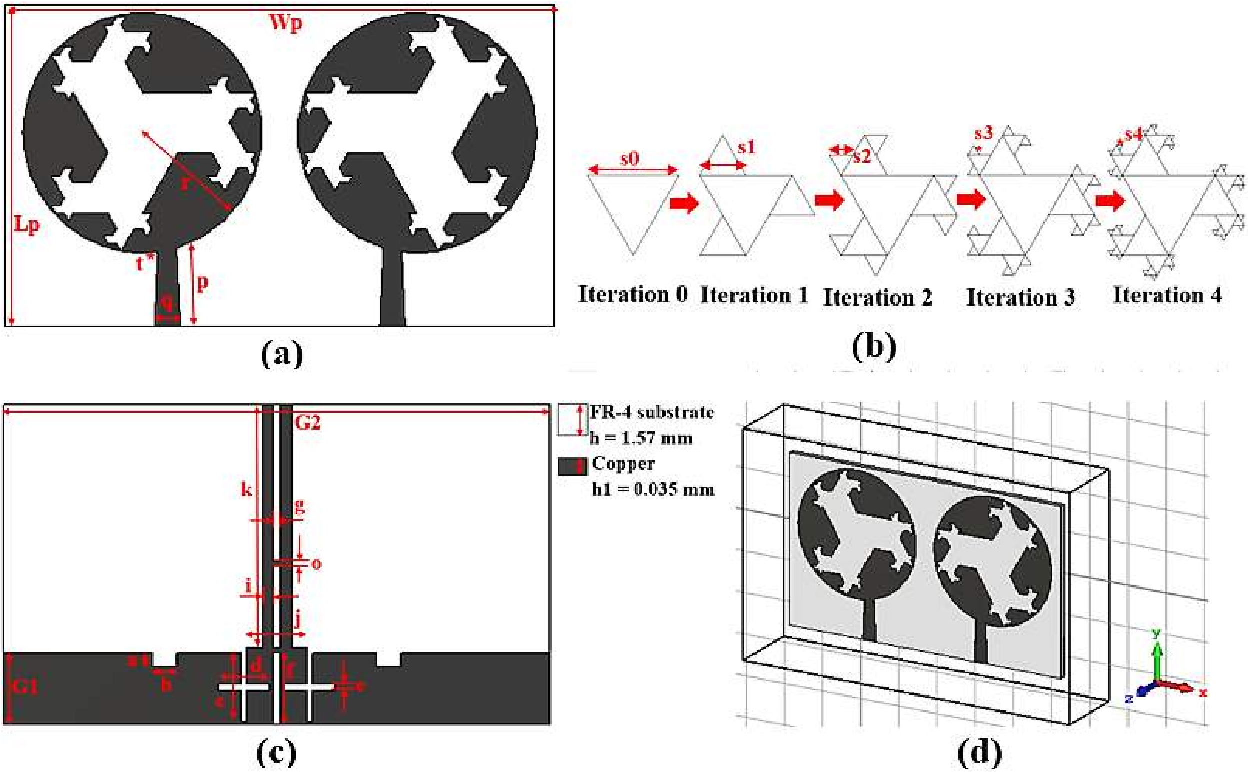

Figure 3.43 (a)Fractal radiators (top FR4 layer) (b) Iterations of modified Koch-Snowflake fractal (c)Partial defected ground (rear FR4 view)

Table 3.5 Designed array's optimized geometrical values (mm)

Parameter	Lp	Wp	t	q	p	r	s0	o	b	c	f	k
Unit (mm)	41	71	0.5	3.4	10.5	13.3	18	0.7	3.2	8.8	9.3	31.45
Parameter	s1	s2	s3	s4	G1	G2	a	i	d	e	g	j
Unit (mm)	9	4.5	2.25	1.125	9.3	71	1.63	1.45	6.65	0.75	0.9	7.8

3.5.2 Parametric Analysis

3.5.2.1 Fractal patch iterative process

Figure 3.44(a) displays the step-by-step optimization of the modified fractal radiators (fixing ground and feedlines constant) and their respective S_{11}/S_{21}(dB) are illustrated in Figure 3.44(b, c). Initially, the array constitutes two circular patches (Antenna I), each with an optimized radius 'r', estimated using Equation 17 for generating a resonance at 3.4GHz (black curve in Figure 3.44(b)).

Next, Antenna II is constructed by truncating an equilateral triangle (0th iteration) from the middle of each patch to minimize the metallic area and offer a better impedance match, especially in the lower spectrum (brown curve in Figure 3.44(b)). The side 's0' for 0th order triangle is evaluated using expressions (10-13) (given in chapter 1) for 5.88GHz. Taking compactness, wide bandwidth, and low mutual coupling into account, the modified Koch-Snowflake fractal recursively iterated till 4th order (Antenna VI) is preferred patch design as it yields a 46.7% patch miniaturization (compared to Antenna I), operates in 3.3-18GHz with good matching (red curve in Figure 3.44 (c)), and admissible inter-port isolation ($S_{21}/S_{12} \leq$-16dB) (blue curve in Figure 3.44(c)) response.

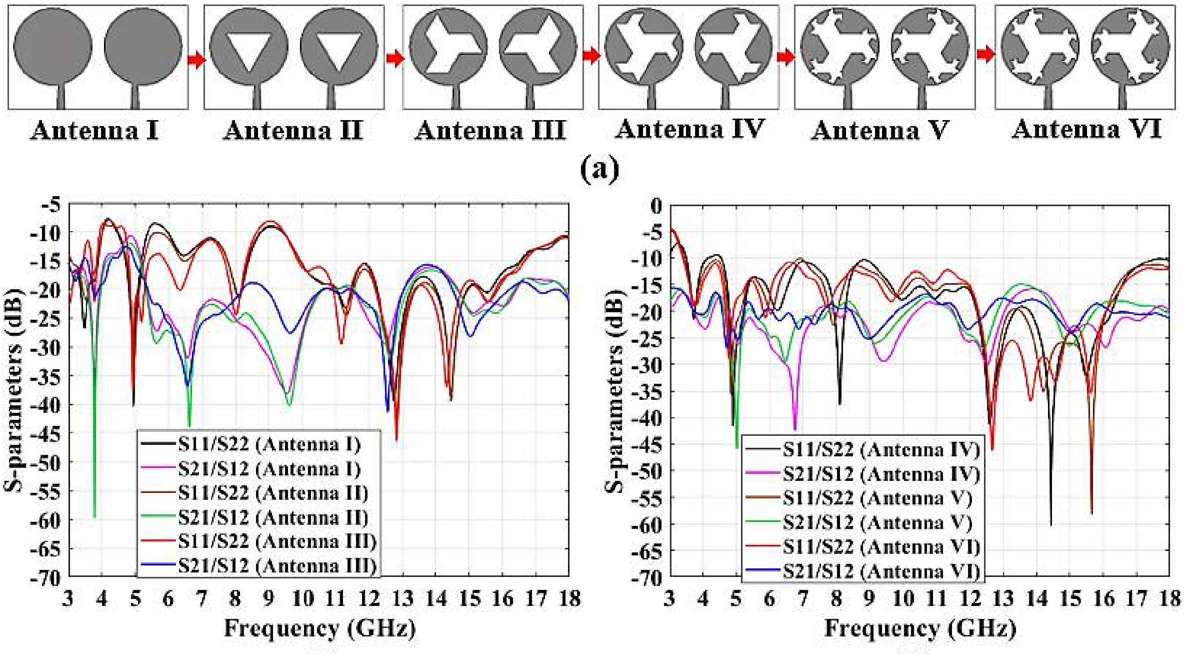

(a)

(b)

(c)

Figure 3.44 (a) Patch optimization (b, c) S_{11}/S_{21} (dB) for different patch configurations

3.5.2.2 Role of DGS

The ground optimization procedure (Stage I-V) while keeping the top FR4 layer fixed is illustrated in Figure 3.45(a) and their corresponding S_{11}/S_{21}(dB) is given in Figure 3.45(b, c). Usually, fringing fields are responsible for the antenna power radiation which can be escalated by reducing the ground's Y-dimension. So, Stage I depicts the partial ground with optimized 'G1' to realize pentaband functionality (black curve in Figure 3.45(b)). To limit the mismatch losses, ground is made DGS by cutting two rectangular slots (Stage II) to achieve a triple-band operation (brown curve in Figure 3.45(a)). Stage I-II is prone to high mutual coupling between the antenna ports. Therefore, to cover a wide spectrum with permissible inter-port isolation, the ground is integrated with H-shaped decoupler (Stage III) and plus-shaped slots (Stage IV). Lastly, to meet the matching criteria, a rectangular stub is fused at the junction of H-shaped decoupler and upper ground edge (Stage V). Therefore, Stage V is selected as it realizes the desired UWB performance.

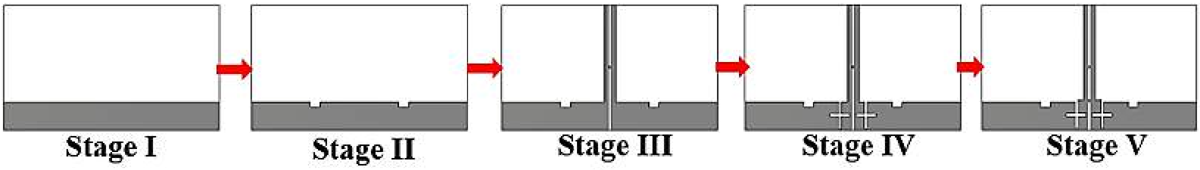

(a)

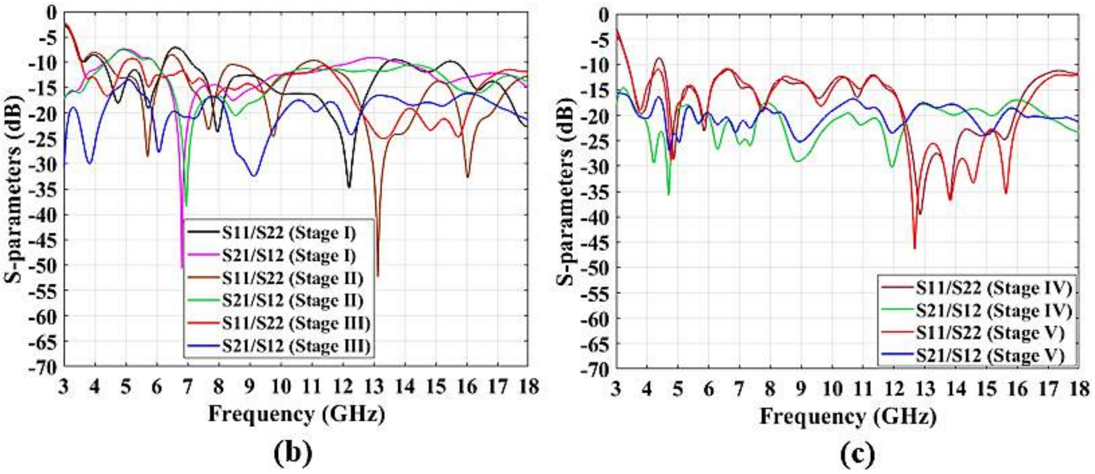

Figure 3.45 (a) Evolution of final ground (b, c) S_{11}/S_{21}(dB) for various ground structures

3.5.2.3 Feedline Optimization

To realize a 50Ω match and acceptable isolation across the UWB, the array's feedlines are right offset by 3.2mm (Level II) and tapered (Level III) as demonstrated in Figure 3.46(a) (keeping patch and ground plane configuration constant). The red curves in Figures 3.46(b, c) (Level III) indicate a large 3.3-18GHz range with a minimal 16dB isolation respectively.

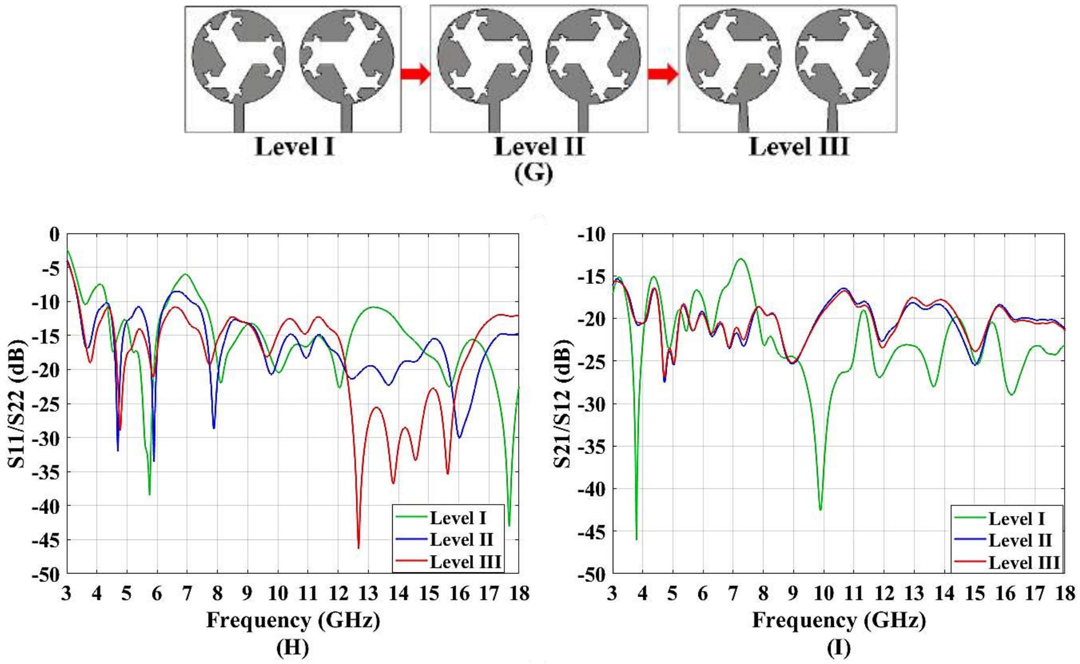

Figure 3.46 (a) Feedline optimization (b, c) S_{11}/S_{21}(dB) for feedline geometries

3.5.3 Simulated and Measured Results

To justify the array's realistic operability, it is fabricated (Figure 3.47(a)) and tested for S-parameters and radiation properties on a VNA and anechoic chamber respectively.

The deviation between simulated and experimental S_{11}/S_{22} and S_{21}/S_{12} coefficients of the designed array is depicted in Figure 3.47(b, c) respectively. It yields a simulated 138% FBW (3.3-18GHz) with favorable matching and inter-port isolation ($S_{21}/S_{12} \leq -16$dB) across the operating band. The simulation results indicate an agreeable similitude with the experimented ones as the fabricated array functions in the 3.28-18GHz (138.35% FBW) while accomplishing acceptable isolation ($S_{21}/S_{12} \leq -17.4$dB) performance. For the activated port-1/terminated port-2, Figure 3.47(d) depicts array's maximal gain of 5.39dBi (simulated) at 13.5GHz. A similar gain is realized by energizing port-2/terminating port-1. Due to the mirror-image layout, the tri-dimensional radiation patterns also assert a complementary behavior to validate the uncorrelated signal radiations by antenna elements. Figure 3.47(e) depicts the peak measured gain of 5.19dBi (13.4GHz) with 3.8dBi average gain throughout the operational bandwidth which closely resembles the simulated results. Figure 3.47(f, g) displays a normalized bi-dimensional far-field pattern (simulated/measured) along YZ-plane (E-plane) and XZ-plane (H-plane) at 4.77GHz and 7.735GHz respectively, on triggering port-1 and fusing port-2 with a matched load. Observations reveal a directional and quasi-omnidirectional pattern in YZ-plane and XZ-plane respectively. A little discrepancy between measured/simulated results occurs due to the incorrect connector soldering, inevitable fabrication errors, feed-cable impediments, and potential reflections from the inactive port.

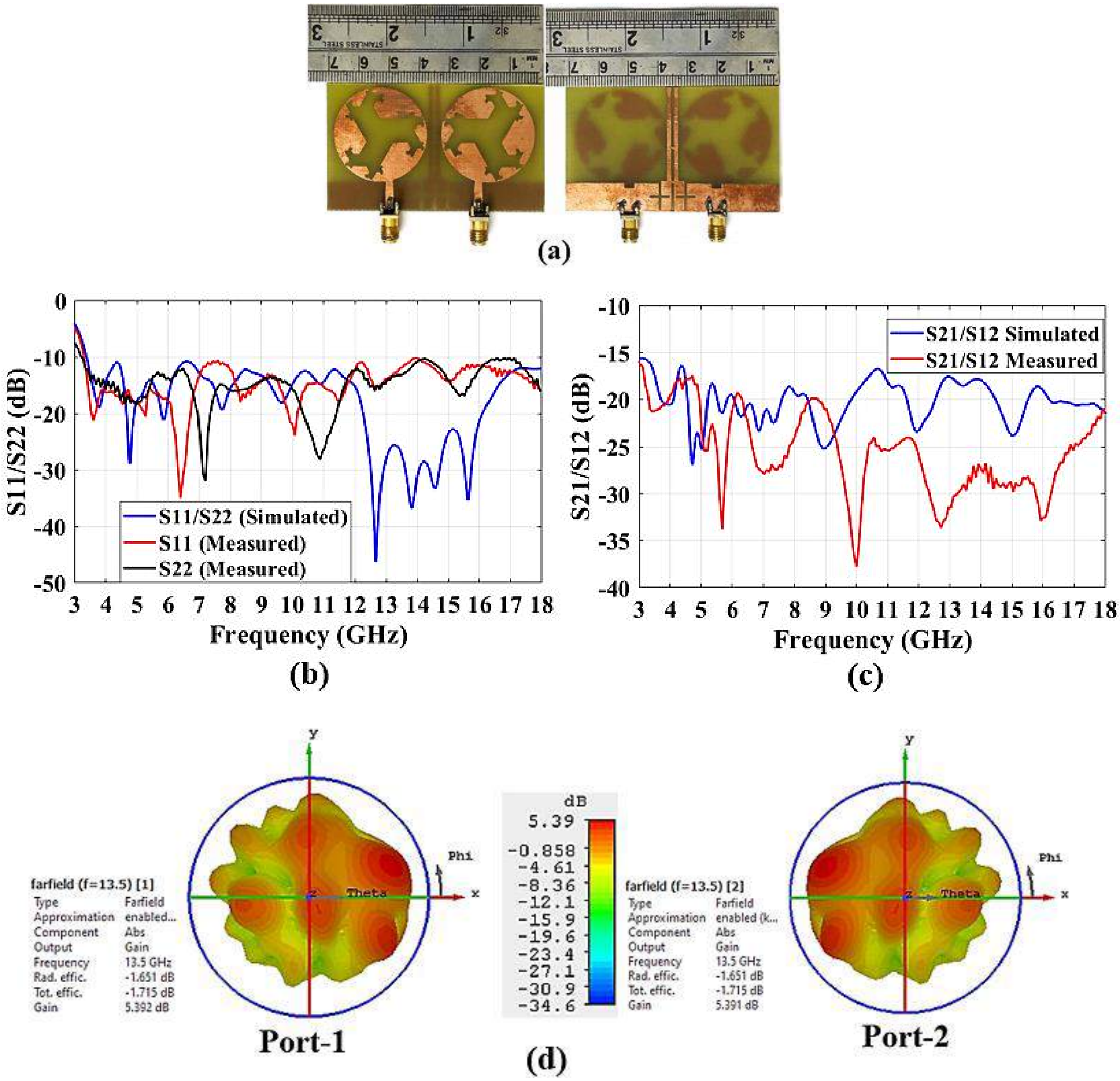

(a)

(b)

(c)

(d)

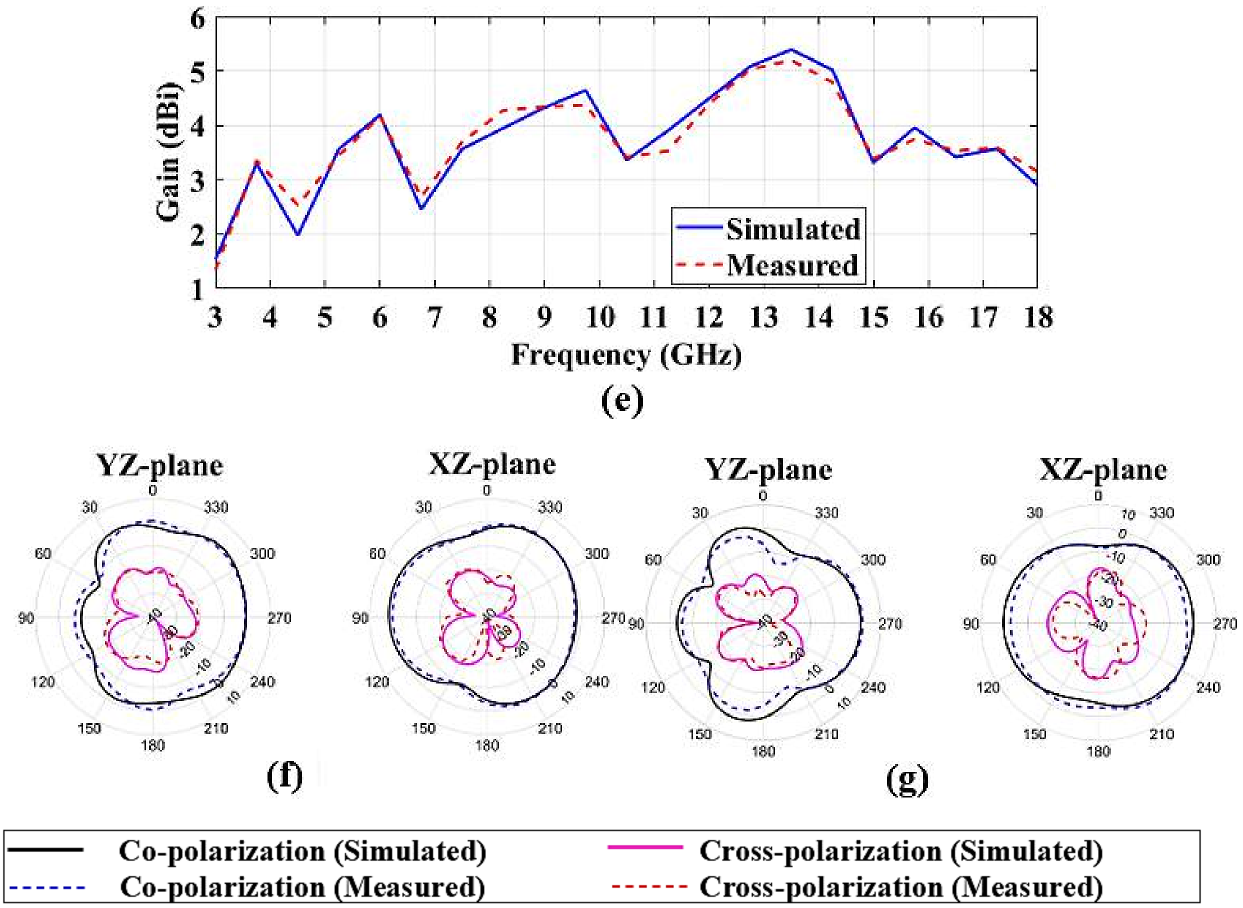

(e)

(f)

(g)

Figure 3.47 (a)Fabricated array (b) S_{11}(dB) (c)S_{21}(dB) results (d) 3D far-field pattern at 13.5GHz (e) Broadband gain(dBi) (f, g) 2D far-field pattern at 4.77GHz and 7.735GHz

3.5.4 Diversity Performance Metrics

To assess the array's real-world operation, ECC characterizes the field correlation between the two array ports and is determined from S-parameters (by assuming a uniform multipath environment with no antenna losses) and far-field patterns using Equations (1, 2) given in chapter 1 respectively. DG identifies signal-to-ratio ratio enhancement of the mixed-signal (at receiver) by utilizing some diversity scheme and computed through Equation 3 (given in chapter 1). In fading environment, MEG estimates average antenna gain and is evaluated through Equation (4, 5). For two-port antenna, $|MEG_i\text{-}MEG_j|<3dB$ is desired. CCL assigns the upper bound on information rate which is broadcasted consistently through the communication link and is correlation matrix (α^R) calculates it using Equation 7 (given in chapter 1).

Figure 3.48(a-d) report ECC≤0.02 (simulated/tested S-parameter), simulated ECC≤0.04 (far-field), DG≥9.899 (simulated/tested S-parameter), simulated DG≤9.798 (far-field), $|MEG_1\text{-}MEG_2|=0dB$(simulated), $-0.724dB<|MEG_1\text{-}MEG_2|<0.5379dB$ (measured) and CCL≤0.4bits/s/Hz (simulated/tested) varying in their admissible levels across the operating band, therefore, indicate array's significant diversity performance.

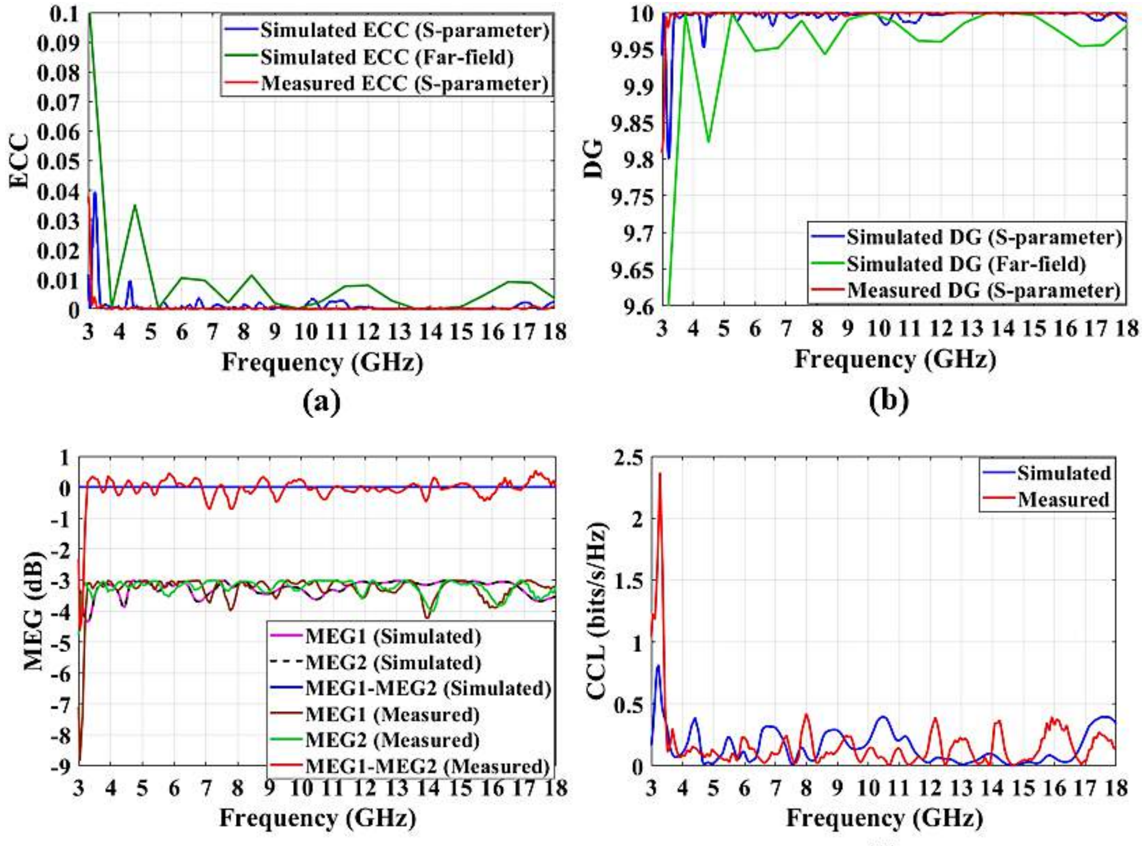

(a) (b) (c) (d)

Figure 3.48 Simulated and tested (a) ECC (b) DG (c) MEG (d) CCL versus frequency

The next section of this chapter investigates a new fractal MIMO with two microstrip-fed Koch Anti-Snowflake fractal UWB antenna with a partial ground surface combined with funnel-shaped decoupler and DGS method for realizing the desired UWB of operation.

3.6 Design and Development of Koch Anti-Snowflake Fractal MIMO Antenna

In this section, a dual-port modified Koch Anti-snowflake fractal antenna is designed, simulated and experimentally verified for ultra-wideband performance. The designed array is modeled on a 1.57 mm high FR4 substrate. It is composed of two microstrip-fed modified Koch Anti-snowflake fractal (iterated up to 3rd order) patches and a defected ground plane, aimed to achieve 144.6% FBW (2.48-15.42GHz) with optimum isolation characteristics and minimizes the patch area by 42.4% as compared to the circular configuration. For verifying the simulated results, the array prototype is tested for UWB performance.

3.6.1 Array Configuration

The geometric configuration of the proposed sextuple band-reject UWB array with a modified Koch Anti-Snowflake fractal radiators and reduced ground with DGS is illustrated in Figure 3.49. The proposed array of dimensions 29.5×43.5mm^2 is realized on an economical FR4 lossy substrate with a ε_r, tan δ, and height of 4.4, 0.02 and 1.57 mm respectively. As depicted in Figure 3.49(a), the top substrate layer is composed of two identical semi-circular radiators, each combined with a modified Koch Anti-snowflake fractal (iterated up to 3rd order) geometry with a scaling factor of 0.33. Two 2.6mm wide microstrip transmission lines (with center-to-center spacing of 24.17mm) are used to energize the fractal radiating elements. To reduce the mismatch losses across the excited operational band, a horizontal stub is inserted at the lower portion of each feedline.

Figure 3.49(b) presents an expanded view of intermediary iteration stages of Koch Anti-snowflake fractal, iterated up to 3rdorder. The proposed Koch Anti-snowflake fractal design is modified by dividing the initial equilateral triangle from the center into two equal parts in such a way that the metallic upper part is joined on the top and the lower part is etched from the center of each semi-circular radiator. The proposed Koch Anti-snowflake fractal is recursively constructed using Koch curve fractal where the three outer segments of an initial equilateral triangle (Iteration 0) are replaced by three copies of Koch curves (with the scaling factor of 0.33) such that the middle segment of each Koch curve bends inwards (at an angle of 60°) for every iteration [76]. The parameters ‘n’, ‘n1’, ‘n2’ and ‘n3’ represent the sides for the 0th, 1st, 2nd and 3rd order of iteration of Koch Anti-snowflake fractal design respectively. The designed Koch Anti-snowflake fractal is constructed with the help of IFS approach using Equation 10 given in chapter 1. The W_1 to W_{12} set presents the transformations of the proposed fractal geometry for the first iteration.

$$W_1 = \begin{bmatrix} \frac{1}{6} & -\frac{\sqrt{3}}{6} \\ \frac{\sqrt{3}}{6} & \frac{1}{6} \end{bmatrix} \begin{bmatrix} x \\ y \end{bmatrix} + \begin{bmatrix} \frac{1}{2} \\ 0 \end{bmatrix}, W_2 = \begin{bmatrix} -\frac{1}{6} & -\frac{\sqrt{3}}{6} \\ \frac{\sqrt{3}}{6} & -\frac{1}{6} \end{bmatrix} \begin{bmatrix} x \\ y \end{bmatrix} + \begin{bmatrix} \frac{2}{3} \\ \frac{\sqrt{3}}{6} \end{bmatrix}, W_3 = \begin{bmatrix} \frac{1}{3} & 0 \\ 0 & \frac{1}{3} \end{bmatrix} \begin{bmatrix} x \\ y \end{bmatrix} + \begin{bmatrix} \frac{1}{2} \\ \frac{\sqrt{3}}{3} \end{bmatrix},$$

$$W_4 = \begin{bmatrix} \frac{1}{6} & -\frac{\sqrt{3}}{6} \\ \frac{\sqrt{3}}{6} & \frac{1}{6} \end{bmatrix} \begin{bmatrix} x \\ y \end{bmatrix} + \begin{bmatrix} \frac{5}{6} \\ \frac{\sqrt{3}}{3} \end{bmatrix}, W_5 = \begin{bmatrix} -\frac{1}{3} & 0 \\ 0 & -\frac{1}{3} \end{bmatrix} \begin{bmatrix} x \\ y \end{bmatrix} + \begin{bmatrix} 1 \\ \frac{\sqrt{3}}{2} \end{bmatrix}, W_6 = \begin{bmatrix} -\frac{1}{6} & \frac{\sqrt{3}}{6} \\ -\frac{\sqrt{3}}{6} & -\frac{1}{6} \end{bmatrix} \begin{bmatrix} x \\ y \end{bmatrix} + \begin{bmatrix} \frac{2}{3} \\ \frac{\sqrt{3}}{2} \end{bmatrix},$$

$$W_7 = \begin{bmatrix} -\frac{1}{6} & -\frac{\sqrt{3}}{6} \\ \frac{\sqrt{3}}{6} & -\frac{1}{6} \end{bmatrix} \begin{bmatrix} x \\ y \end{bmatrix} + \begin{bmatrix} \frac{1}{2} \\ \frac{\sqrt{3}}{3} \end{bmatrix}, W_8 = \begin{bmatrix} -\frac{1}{3} & 0 \\ 0 & -\frac{1}{3} \end{bmatrix} \begin{bmatrix} x \\ y \end{bmatrix} + \begin{bmatrix} \frac{1}{3} \\ \frac{\sqrt{3}}{2} \end{bmatrix}, W_9 = \begin{bmatrix} \frac{1}{6} & \frac{\sqrt{3}}{6} \\ -\frac{\sqrt{3}}{6} & \frac{1}{6} \end{bmatrix} \begin{bmatrix} x \\ y \end{bmatrix} + \begin{bmatrix} 0 \\ \frac{\sqrt{3}}{2} \end{bmatrix},$$

$$W_{10} = \begin{bmatrix} \frac{1}{3} & 0 \\ 0 & \frac{1}{3} \end{bmatrix} \begin{bmatrix} x \\ y \end{bmatrix} + \begin{bmatrix} \frac{1}{6} \\ \frac{\sqrt{3}}{3} \end{bmatrix}, W_{11} = \begin{bmatrix} -\frac{1}{6} & \frac{\sqrt{3}}{6} \\ -\frac{\sqrt{3}}{6} & -\frac{1}{6} \end{bmatrix} \begin{bmatrix} x \\ y \end{bmatrix} + \begin{bmatrix} \frac{1}{2} \\ \frac{\sqrt{3}}{3} \end{bmatrix}, W_{12} = \begin{bmatrix} \frac{1}{6} & \frac{\sqrt{3}}{6} \\ -\frac{\sqrt{3}}{6} & \frac{1}{6} \end{bmatrix} \begin{bmatrix} x \\ y \end{bmatrix} + \begin{bmatrix} \frac{1}{3} \\ \frac{\sqrt{3}}{6} \end{bmatrix}$$

For the first iteration of the designed fractal, the generator curve is formed as per Equation 30.

$$W = W_1 \cup W_2 \cup W_3 \cup W_4 \cup W_5 \cup W_6 \cup W_7 \cup W_8 \cup W_9 \cup W_{10} \cup W_{11} \cup W_{12} \qquad (30)$$

As illustrated in Figure 3.49(c), the back layer of the FR-4 substrate is composed of a reduced, defective ground plane. Decreasing the ground length along y-dimension (‘Lg’ = 10.3mm) provides an improved bandwidth of operation. A square funnel-shaped decoupling structure is extended vertically from the center of the reduced ground to realize an optimum isolation level between the two antenna ports. Table 3.6 lists the optimized parametric values (mm) for the proposed MIMO antenna.

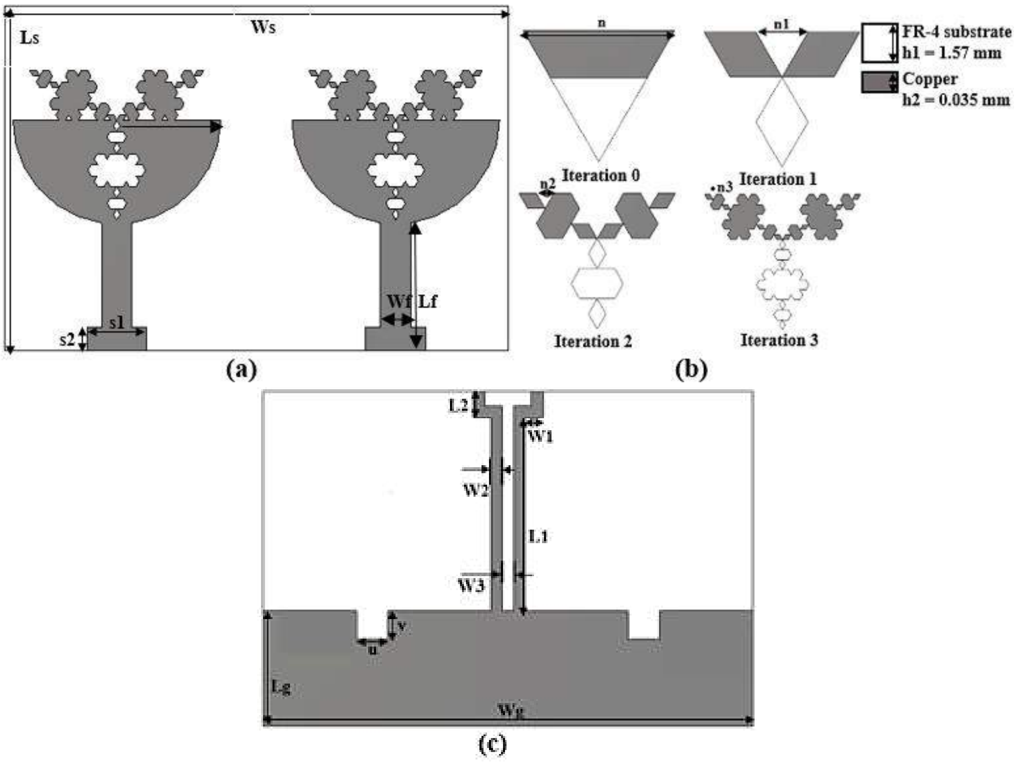

Figure 3.49 Proposed array geometry (a) Koch Anti-snowflake fractal radiators (b) expanded fractal configuration (c) reduced ground with DGS

Table 3.6 Optimized values (mm) of the geometrical parameters

Parameters	Ls	Ws	r	Lf	Wf	s1	s2	n	n1	n2
Values (mm)	29.5	43.5	9	11	2.6	5.2	2	15	5	1.667
Parameters	n3	Lg	Wg	u	v	L1	L2	W1	W2	W3
Values (mm)	0.556	10.3	43.5	2.8	2.5	17.26	2.34	1.59	1	1

3.6.2 Parametric Analysis

3.6.2.1 Optimization of Koch Anti-Snowflake fractal patch

Figure 3.50 demonstrates the stepwise geometrical process followed to design the optimized microstrip-fed Koch Anti-snowflake fractal radiators (up to 3rd order of iteration) while the ground configuration is kept fixed. The simulated S-parameter (S_{11}/S_{22}, S_{21}/S_{12}) response for Stage I and Stage II against frequency are presented in Figure 3.51 whereas the simulated $S_{11}/S_{22}$and S_{21}/S_{12} results for Stage III-VII are presented in Figure 3.52(a, b) respectively. The array design initially begins with two circular radiators of optimized radius ‘r’ (Stage I), evaluated for exciting a resonance ‘f_r’ at 6.6 GHz (shown by the pink curve in Figure 3.51) using Equation 17.

Stage II is constructed by clipping off the upper half of the circular radiating elements to reduce the metallic area and shifts the resonant frequencies towards the lower frequency end (purple curve in Figure 3.51). Stage III represents the 0th iteration order of Koch Anti-snowflake fractal where an equilateral triangle of side ‘n’ is inserted at the center of each semi-circular radiator in such a way that the upper half of the triangle is joined at the top and the lower half of the triangle is etched from the middle of each semi-circular radiator. This patch geometry operates in five frequency regions (green curve in Figure 3.52(a)) with a percentage FBW of 22.95% (2.43-3.06GHz), 48.18% (3.12-5.1GHz), 23.4% (5.62-7.11GHz), 22.35% (7.67-9.6GHz) and 45.9% (10.03-16GHz) with an optimum isolation ($S_{21}/S_{12} \leq$ -15dB) level (green curve in Figure 3.52(b)). Stage IV displays the 1st iteration order of Koch Anti-snowflake fractal which is designed by substituting all three segments of an equilateral triangle by three Koch curves (facing inwards). According to the blue curve in Figure 3.52(a), Stage III functions in three frequency bands with FBW of 20.4% (2.42-2.97GHz), 96.75% (3.26-9.37 GHz), and 47.1% (9.9-16GHz). The Koch Anti-snowflake fractal patch geometry is further iterated up to 2nd order (Stage V) to cover a wide operational range from 3.29-16 GHz (131.78% FBW) along with a low-frequency band from 2.4-2.96GHz (20.9% FBW) as shown by the orange curve in Figure 3.52(a). It is found that patch geometry represented by Stage V provides poor matching performance, especially at 9.52GHz frequency. To reduce mismatch losses, Stage VI represents the Koch Anti-snowflake fractal patch iterated up to 3rd order. This patch structure yields a better matching performance and operates in a large frequency range from 3.24-16GHz along with a low-frequency band from 2.38-2.93GHz (20.7% FBW). The patch geometry represented in Stage VI minimizes the patch area by 42.4% in comparison to the circular configuration (displayed in Stage I). As the primary aim of the proposed array is to realize a large functional bandwidth with optimal matching and isolation performance, a horizontal stub is loaded at the lower end of each feedline (Stage VII). This final optimized patch yields 144.6% FBW (2.48-15.42GHz) with enhanced impedance matching and inter-port isolation ($S_{21}/S_{12} \leq$ -16.8dB) results.

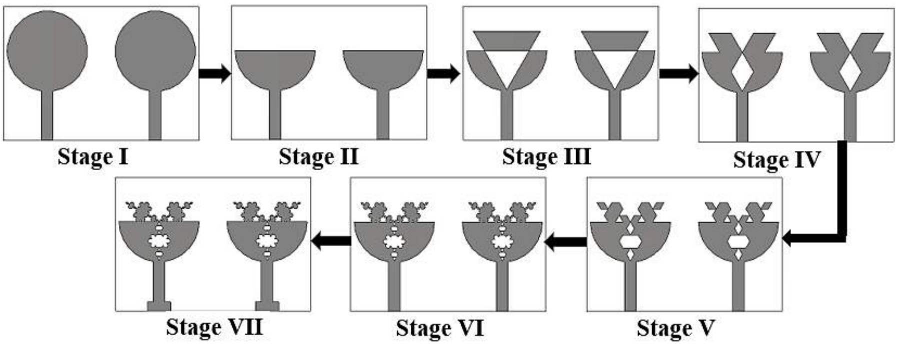

Figure 3.50 Optimization of the Koch Anti-snowflake patch array for realizing UWB performance

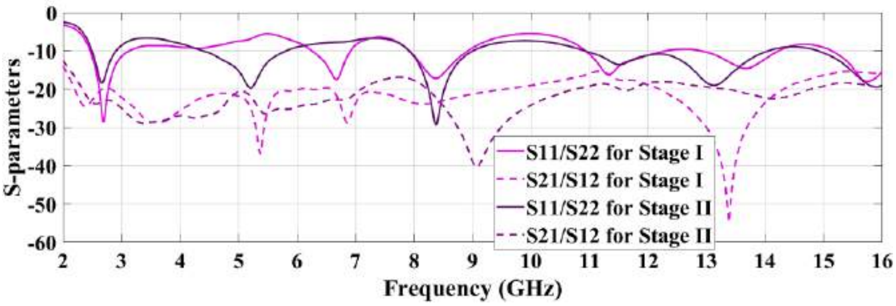

Figure 3.51 Variation of S-parameters against frequency for the patch designs represented by Stage I-II

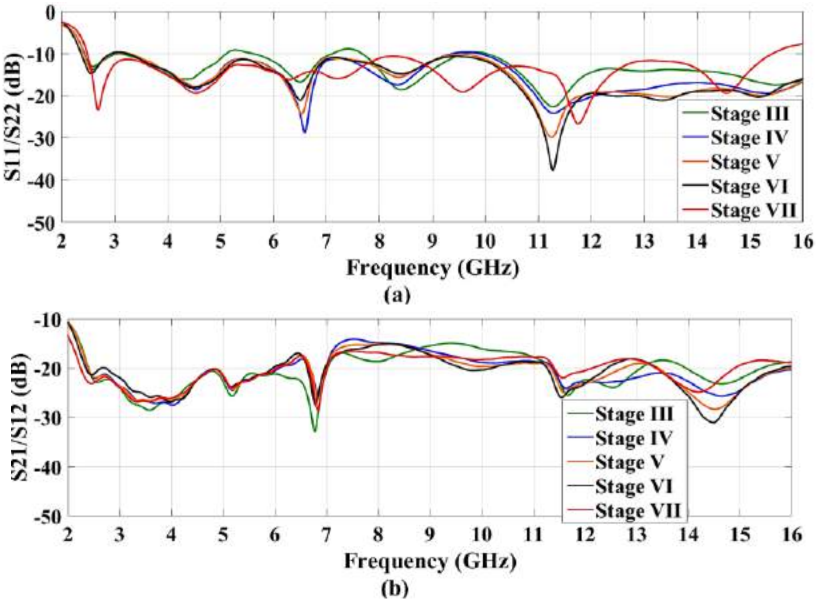

Figure 3.52 Simulated (a) S_{11}/S_{22}(b) S_{21}/S_{12}performance for patch designs shown in Stage III-VII

3.6.2.2 Optimization of the Ground Geometry

Figure 3.53 illustrates the evolutionary approach adopted for optimizing the common ground structure of the proposed array to accomplish a large bandwidth of operation with high inter-element isolation for a fixed configuration of fractal patches. The respective S_{11}/S_{22} (dB) and S_{21}/S_{12} (dB) responses (versus frequency) for the different levels of ground geometry are presented in Figure 3.54(a, b) respectively. In general, the power radiated by the antenna is determined by the fringing fields which can be increased by decreasing the length of the ground structure along the Y-axis. Therefore, Level I display the reduced ground plane (with an optimized 'Lg' = 10.3mm) of the proposed array which functions in triple-frequency bands from 3.81-9.22GHz (83.04% FBW), 9.52-10.32GHz (8.06% FBW), and 11.58-15.53GHz (29.14% FBW) respectively (green curve in Figure 3.54(a)). Furthermore, two symmetrical square-shaped defects (just behind the feedlines) are introduced in the reduced ground plane (Level II) to realize a dual-band operation from 3.76-9.9GHz (89.9% FBW) and 10.8-15.9GHz (38.2% FBW) respectively (blue curve in Figure 3.54(a)). But the ground configurations reported in Level I and Level II exhibits poor inter-element isolation characteristics (green and blue curve in Figure 3.54(b) respectively). So, a funnel-shaped decoupling structure is elongated from the center of the reduced ground (Level III) for covering a large FBW of 144.6% (2.48-15.42GHz) (red curve in Figure 3.54(a)) with an optimal isolation ($S_{21}/S_{12} \leq -16.8$dB) (red curve in Figure 3.54(b)).

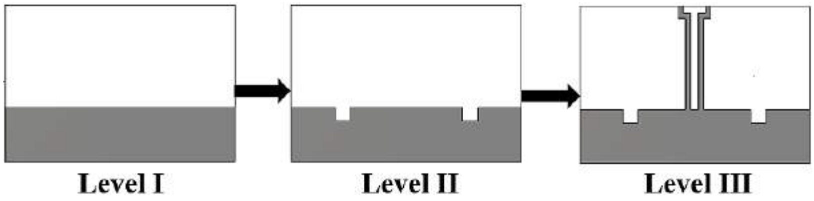

Figure 3.53 Structural variations in the common ground plane for obtaining UWB performance

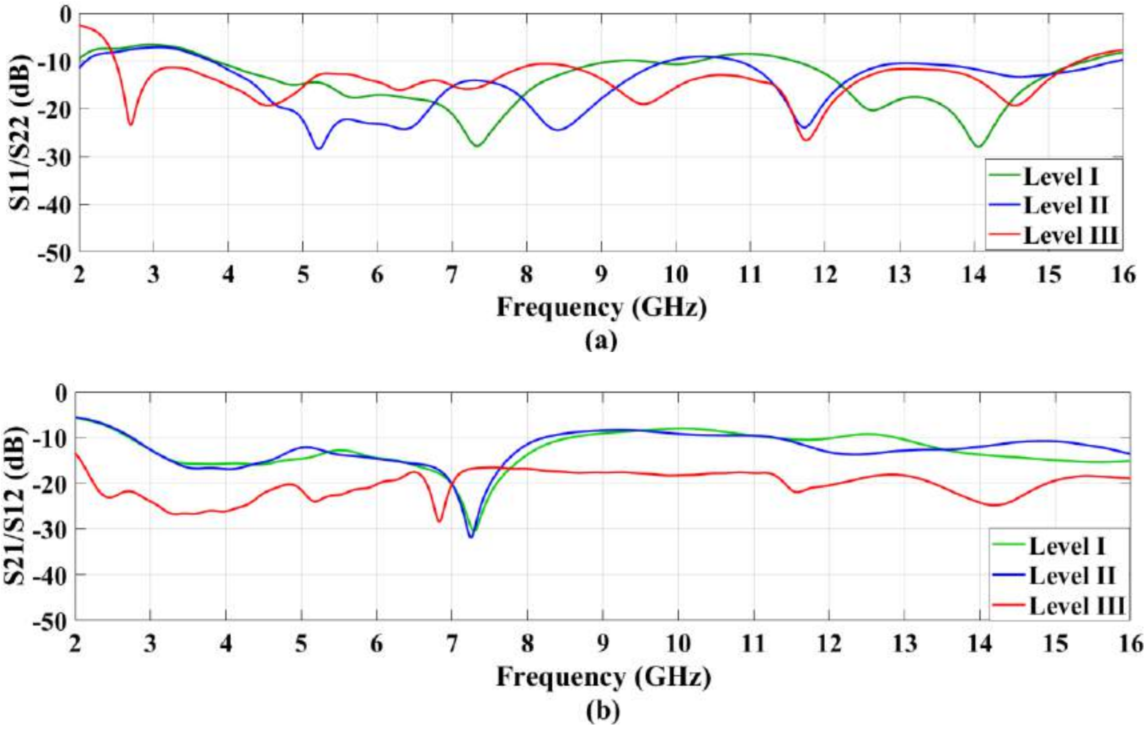

Figure 3.54 Simulated (a) S_{11}/S_{22} (dB) (b) S_{21}/S_{12} (dB)response for different ground geometries

3.6.3 Simulation and Experimental Analysis

The authentication of the simulation results of the proposed fractal array for realistic UWB-MIMO applications is carried out by fabricating it on a 1.57mm thick FR4 substrate ($\varepsilon_r = 4.4$) according to the photolithography process. For affirming the UWB operation, Figure 3.55(a, b) presents the fabricated images of the Koch Anti-snowflake fractal patches joined to two microstrip lines (top substrate layer) and reduced defected ground (bottom substrate layer) respectively. Each feed point of the designed array is soldered with a 50Ω SMA connector for activating the fractal patches.

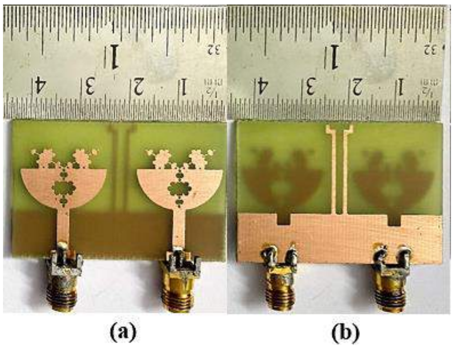

Figure 3.55 Fabricated images of the designed array (a) Fractal patches (b) Ground configuration

The present section reports the experimental analysis of the fabricated array for S-parameters and far-field characteristics utilizing a Keysight (model E5063A) VNA (working in 100 KHz-18 GHz band) and an anechoic chamber (functioning in 20 KHz-20 GHz band) respectively.

3.6.3.1 Scattering Parameters and Broadband Gain

The simulation and fabricated S-parameter (S_{11}/S_{21}) performance versus frequency for the designed UWB array is depicted in Figure 3.56(a, b). It functions in the simulated frequency range of 2.48-15.42 GHz (with 144.6% FBW) with the minimum inter-port isolation of 17 dB across the entire functional range. The experimental S-parameter performance reveals that the fabricated UWB array offers an FBW of 147.6% in the range from 2.34-15.52 GHz and ensures a high level of isolation ($S_{21} \leq -18.1$ dB) between the two antenna ports.

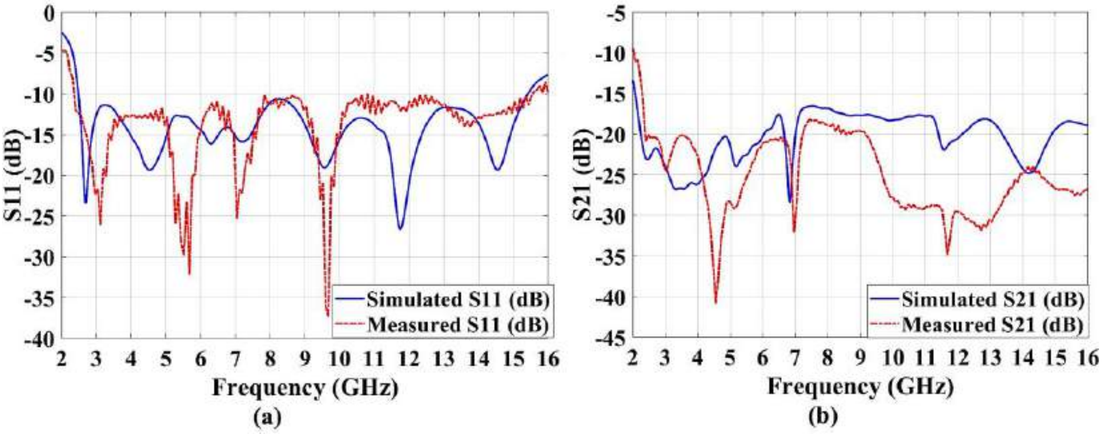

Figure 3.56 Variation of simulated and tested (a) S_{11} (dB) (b) S_{21} (dB) response against frequency

Figure 3.57 demonstrates the variations of the gain curves for the designed UWB fractal array for the activated port-1. For the proposed UWB fractal array, an average simulated gain of 3.58 dBi is observed across the complete working range with a peak gain of 5.16 dBi at 7.48 GHz.

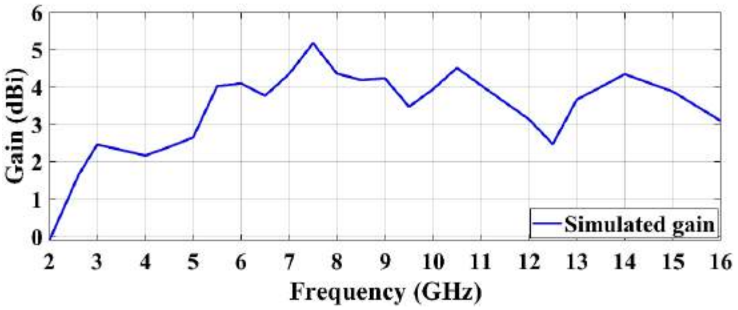

Figure 3.57 Simulated gain against frequency plot for the excited port-1

3.6.4 Diversity Analysis

For operation in a rich multipath environment, some key diversity metrics like ECC, DG, MEG, CCL, and TARC that must be studied for designing MIMO antenna are given in this subsection.

3.6.4.1 Envelope Correlation Coefficient and Diversity Gain

ECC is defined as the square of the correlation coefficient and is used for estimating the degree of field correlation between the radiating patches operating within a MIMO antenna system. Assuming the antenna operation in uniform propagation surroundings, Equation 2 (stated in chapter 1) provides a generalized expression for assessing ECC between the input ports of the antenna array. DG specifies the enhancement in signal quality and reliability of the MIMO antenna system by utilizing some diversity combining approach at the receiver end. It is evaluated from the ECC values as given in Equation 3 (chapter 1). Figure 3.58(a) reveals ECC <0.009 (simulation) and <0.0089 (tested) across the working range of 2.48-15.42 GHz for the designed UWB-MIMO antenna. Figure 3.58(b) depicts the lower limit of DG is 9.956 (simulation as well as measurement) in the desired functional band for the designed UWB-MIMO antenna (without notches). Therefore, low ECC and high DG values of the designed array signifies a reliable diversity operation, essential for UWB-MIMO communication systems.

3.6.4.2 Mean Effective Gain

To characterize the impact of fading on the communication performance of the designed MIMO antenna, MEG is a vital diversity parameter to be investigated. For a dual-port MIMO antenna, MEG values are evaluated from its S-parameters (simulated and experimental) according to Equation (4, 5) as explained in chapter 1. For an effective MIMO antenna operation, the variation between the MEG for two antenna ports must be lower than 3 dB. Figure 3.58(c) plots the variation of MEG curves (both tested and simulated) against frequency for the designed UWB MIMO antenna. A high MEG (about -3dB) is observed over the complete simulated and experimental frequency range where the simulated $|MEG_1 - MEG_2|$ = 0 dB and experimental $|MEG_1 - MEG_2|$ varies from -0.63dB to 0.37dB which indicates that the designed UWB array exhibits an optimum gain performance across the operational range.

3.6.4.3 Channel Capacity Loss

The degraded operational performance of the MIMO system is estimated in terms of CCL, which is calculated from its correlation matrix using Equation 7 (given in chapter 1). The highest permissible level of CCL is 0.4 bits/s/Hz. For the designed UWB-MIMO antenna, Figure 3.58(d) show CCL (< 0.4 bits/s/Hz) for the simulation as well as measurement results.

3.6.4.4 Total Active Reflection Coefficient

TARC is used to completely compress all the S-parameter details in a single curve for a multi-port antenna array and can be estimated from Equation 8 (given in chapter 1). Generally, the TARC<0 dB is acceptable for a significant diversity operation of the MIMO antenna. According to Figure 3.58(e, f), the designed UWB fractal array exhibits a TARC<-8.8 dB (simulation) and < -6.9dB (measured) respectively, for the excited UWB domain.

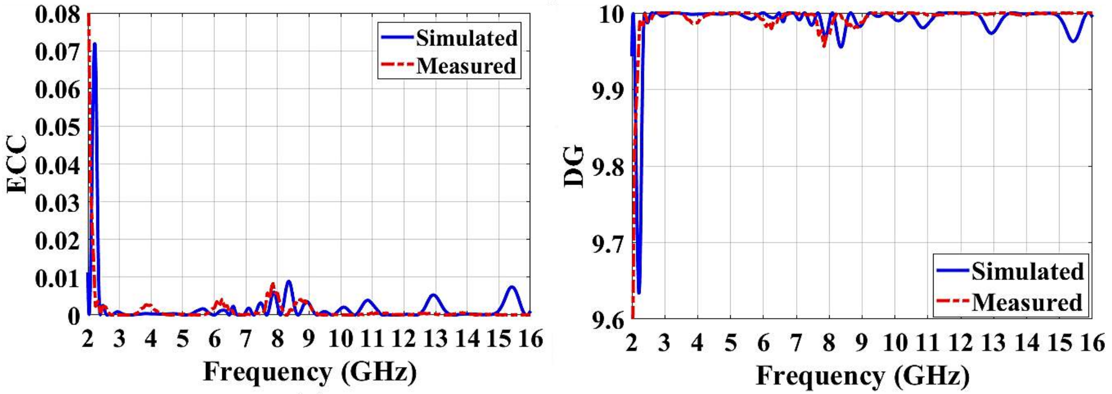

(a) (b)

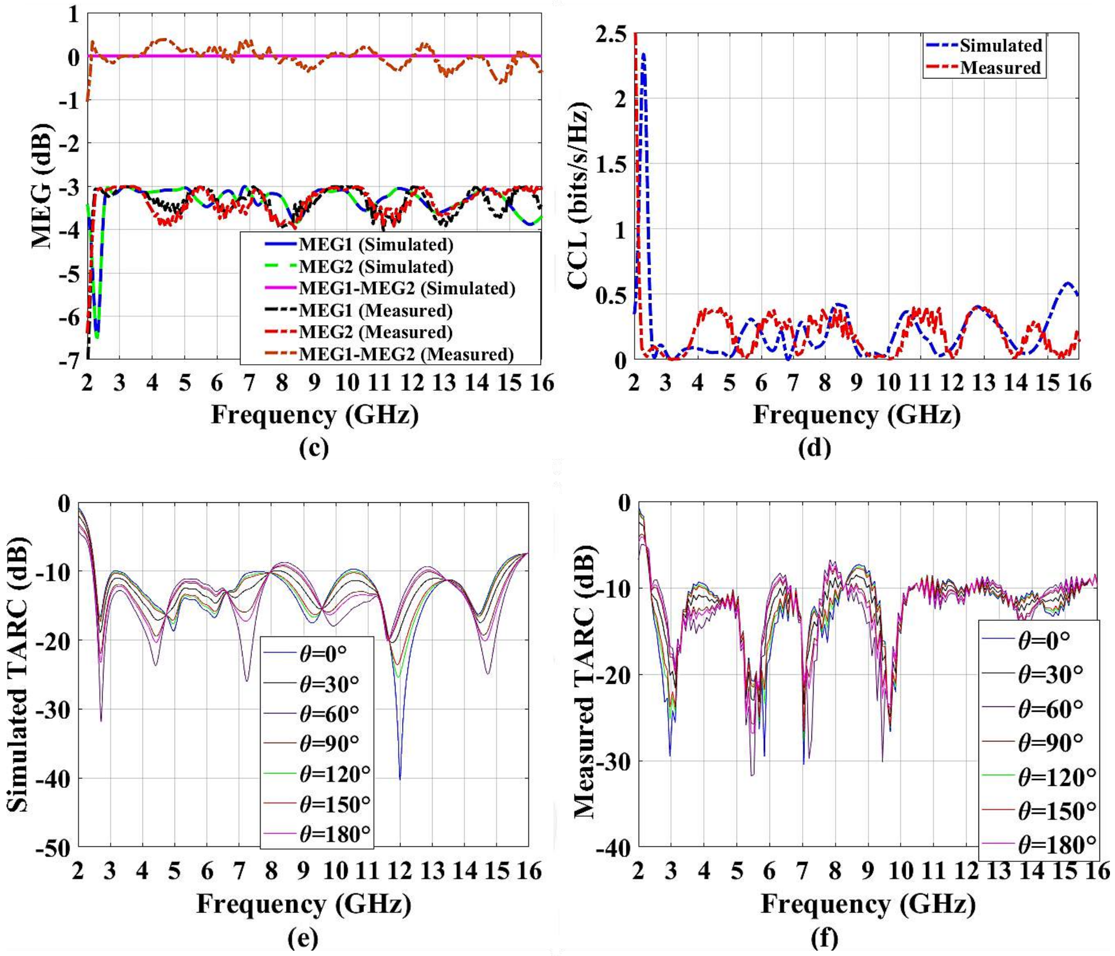

Figure 3.58 Diversity metrics (a) ECC (Simulated/Measured) (b) DG (Simulated/Measured) (c) MEG (Simulated/Measured) (d) CCL (Simulated/Measured) (e, f) TARC (Simulated/Tested)

3.7 Conclusion

This chapter covers the first objective of the proposed doctoral research work. Here, six different dual-port MIMO antennas incorporated with different fractal and DGS geometries are successfully modeled, simulated and experimentally verified to realize the desired UWB characteristics. The first design demonstrates an aperture-coupled Sierpinski gasket fractal (2nd order) MPA array integrated with spiral-shaped DGS to cover a simulated UWB properties from 4.3-11.6 GHz (91.8% FBW) with an acceptable inter-element isolation ($S_{12}/S_{12} \leq -15.8$ dB) and maximal gain of 4.7dBi (at the resonance of 9.2GHz). In the second design, an aperture coupled MPA array with a 2nd iterative circular fractal and rectangular spiral-shaped DGS geometries to achieve the desired operational band from 4.6-16.8 GHz (114% FBW) with a maximal gain of 4.57dBi (at the resonance of 6.6GHz) and a high port-to-port isolation ($S_{12}/S_{21} \leq -19$dB) between the array elements. The third design illustrates an offset-fed aperture coupled, modified Pythagorean tree fractal (2nd order) antenna array integrated with two complementary hexagonal spiral DGS to cover a wide UWB range of 3.71-10.64GHz (96.8% FBW) with a peak gain of 4.34dBi (at 9.4GHz) and good degree of isolation ($S_{12}/S_{21} \leq -16.1$dB) between the two ports of the array. The fourth design presents a semi-circular MIMO antenna combined with 2nd iterative Koch-curve fractal and DGS approach to function in 4.395-10.184GHz (79.4% FBW) with a maximal gain of 3.84dBi (at 8.9GHz) and acceptable port-to-port isolation ($S_{12}/S_{21} \leq -16.1$dB) response. In the fifth design, a circular MIMO antenna incorporated with a modified Koch-Snowflake fractal (4th iteration), offset-feeding and DGS technique is designed to yield an FBW of 138% (3.3-18GHz) with a considerable level of isolation ($S_{21}/S_{12} \leq -16$dB) and peak gain of 5.39dBi (at 13.5GHz). In the last design, a compact microstrip-fed Koch Anti-snowflake fractal MIMO antenna integrated with the DGS technique is designed to successfully cover a large frequency band from 2.48-15.42 GHz (144.6% FBW) with a peak gain of 5.16dBi (at 7.48 GHz) and significant degree of isolation ($S_{21}/S_{12} \leq -17$dB) between the antenna ports. Therefore, from the above-designed array's it is concluded that a fractal geometry excites multiple frequency bands and a DGS which is resonant at the same bands can be used to improve the impedance bandwidth for the antennas in the array configuration.

Also, the designed MPA arrays incorporated with different fractal geometries aids in realizing size miniaturization characteristics desired for application in portable wireless devices. The first fractal design offers a size reduction of 46% as compared to a conventional MPA. The notable feature of the third fractal design is the elimination of the base square (0th iteration level) as compared to the standard tree fractal geometry that lowers the total fractal height by 12.11mm. The fourth, fifth and sixth fractal patch configurations yields a reduction in patch area of 41.2%, 46.7% and 52.6% respectively as compared to the conventional circular patch. Various diversity performance parameters like low ECC, high DG, low $|MEG_1 - MEG_2|$ (< 3 dB), low CCL (≤ 0.4 bits/s/Hz), and acceptable TARC values across the working range affirm the application of all six designed fractal UWB array in diversity combining schemes (at reception end). A reasonable resemblance is obtained between the simulation and experimental results (for FBW, port-isolation, far-field characteristics and diversity metrics) which confirms the practical functionality of the designed UWB array. Hence, the feasibility of all the designed fractal MPA arrays to function in UWB-MIMO communication devices is supported by their reduced size, large impedance bandwidth, good isolation properties and acceptable diversity operation.

CHAPTER 4

Four-Port Fractal MIMO Antennas with Improved UWB and Isolation Characteristics

This chapter presents the design and development of two quad-port fractal MPA arrays, covering the third objective of the proposed doctoral study. Here, for better operation in receive diversity schemes, the previously designed two-port Sierpinski gasket and Koch snowflake fractal MIMO antennas (in chapter 3 for objective 1) are configured to four-port networks. By utilizing the concept of offset-feeding and introducing some modifications in the ground plane geometry, the designed four-port fractal MPA arrays offer an improved operational behavior in terms of impedance bandwidth, inter-element isolation, and diversity performance characteristics. The designed arrays are fabricated and measured for S-parameters and far-field characteristics through the Keysight VNA (model no. E5063A) and anechoic chamber respectively.

The following sections of this chapter present the detailed investigation of the designed four-port fractal MPA arrays for 4G/5G UWB communication systems and are arranged as follows: Section 4.1 demonstrates an offset-fed, aperture-coupled, four-port UWB Sierpinski gasket fractal antenna designed with archimedean spiral and X-shaped DGS. Likewise, Section 4.2 demonstrate an offset-fed, four-port UWB Koch Snowflake fractal antenna with a partial ground surface incorporated with semi-circular rings and an inverted ‘ II’ decoupling structure.

4.1 Design and Development of Quad-element Sierpinski Gasket Fractal UWB Antenna

In this section, a quad-port fractal MIMO antenna is configured, simulated, and experimented for operation in UWB communication systems. The antenna is assembled on dual 1.57mm thick FR4 dielectric substrates wherein the top substrate comprises four 2nd iterative Sierpinski gasket fractal patches and the bottom substrate incorporates a feeding arrangement. The aperture-coupled feeding approach is employed to activate the fractal radiators. The multi-frequency response produced by fractal antenna elements is transformed into a wide working range by modifying apertures (clipped from the ground surface) into spiral-shaped structures and offsetting the feedlines towards the right. The designed array effectively radiates in the 3.07-11GHz range while maintaining a good level of inter-element isolation (16.19dB) response. For implementation in MIMO systems, the several diversity performance parameters (ECC, DG, MEG, CCL) of the proposed array are analyzed. To validate the simulated responses, the proposed prototype is tested for S-parameters and radiation characteristics.

4.1.1 Array Configuration

The structure and configurational parameters of the UWB fractal array are illustrated in Figure 4.1(a-c). The proposed four-port antenna is configured on two versatile and widely available 80×99.4 mm^2 FR4 substrates, each with ε_r, thickness (‘h_1’), and tan δ of 4.4, 1.57 mm, and 0.024 respectively. The modeling and simulated responses of the antenna array are analyzed in CST microwave studio software by applying the perfect boundary approximation.

Figure 4.1(a) displays the top view of the upper FR4 (also termed as antenna substrate) which consists of four identical fractals (equilateral triangle) radiators, optimized to the 2nd iteration order with the reduction factor of 0.5. The fractal radiating elements are arranged in the mirror-image configuration with the common ground so that the designed antenna can emit uncorrelated signals in the open space. To attain an acceptable degree of isolation between the array elements, the center-to-center spacing between the fractal radiators labeled as 'A1' and 'A2' is optimized to 'd1' whereas the fractal radiators labeled as 'A1' and 'A4' are kept at the separation of 'd'. Here the fractal patches are arranged in a complementary configuration as the edge midpoints of the newly iterated copies are joined to the vertices of the previously iterated copies of the fractal geometry. The geometry of the designed fractal is recursively generated according to the IFS method, given by Equation 10 (in chapter 1). The IFS transformations of the proposed fractal (first iteration) are provided by the following set from W_1 to W_{15} and its generator curve is defined by Equation 31.

$$W_1 = \begin{bmatrix} 0.25 & -0.433 \\ 0.433 & 0.25 \end{bmatrix}\begin{bmatrix} x \\ y \end{bmatrix} + \begin{bmatrix} 0.5 \\ 0 \end{bmatrix}, W_2 = \begin{bmatrix} 0.25 & -0.433 \\ 0.433 & 0.25 \end{bmatrix}\begin{bmatrix} x \\ y \end{bmatrix} + \begin{bmatrix} 0.6429 \\ 0.2474 \end{bmatrix},$$

$$W_3 = \begin{bmatrix} 0.25 & -0.433 \\ 0.433 & 0.25 \end{bmatrix}\begin{bmatrix} x \\ y \end{bmatrix} + \begin{bmatrix} 0.5 \\ 0.2474 \end{bmatrix}, W_4 = \begin{bmatrix} 0.25 & 0.433 \\ -0.433 & 0.25 \end{bmatrix}\begin{bmatrix} x \\ y \end{bmatrix} + \begin{bmatrix} 0.7857 \\ 0.7423 \end{bmatrix},$$

$$W_5 = \begin{bmatrix} 0.25 & -0.433 \\ 0.433 & 0.25 \end{bmatrix}\begin{bmatrix} x \\ y \end{bmatrix} + \begin{bmatrix} 0.8571 \\ 0.6186 \end{bmatrix}, W_6 = \begin{bmatrix} -0.5 & 0 \\ 0 & -0.5 \end{bmatrix}\begin{bmatrix} x \\ y \end{bmatrix} + \begin{bmatrix} 1 \\ 0.866 \end{bmatrix},$$

$$W_7 = \begin{bmatrix} 0.25 & 0.433 \\ -0.433 & 0.25 \end{bmatrix}\begin{bmatrix} x \\ y \end{bmatrix} + \begin{bmatrix} 0.7143 \\ 0.866 \end{bmatrix}, W_8 = \begin{bmatrix} -0.5 & 0 \\ 0 & -0.5 \end{bmatrix}\begin{bmatrix} x \\ y \end{bmatrix} + \begin{bmatrix} 1 \\ 0.866 \end{bmatrix},$$

$$W_9 = \begin{bmatrix} 0.25 & -0.433 \\ 0.433 & 0.25 \end{bmatrix}\begin{bmatrix} x \\ y \end{bmatrix} + \begin{bmatrix} 0.2143 \\ 0.7423 \end{bmatrix}, W_{10} = \begin{bmatrix} -0.5 & 0 \\ 0 & -0.5 \end{bmatrix}\begin{bmatrix} x \\ y \end{bmatrix} + \begin{bmatrix} 0.2857 \\ 0.866 \end{bmatrix},$$

$$W_{11} = \begin{bmatrix} 0.25 & 0.433 \\ -0.433 & 0.25 \end{bmatrix}\begin{bmatrix} x \\ y \end{bmatrix} + \begin{bmatrix} 0 \\ 0.866 \end{bmatrix}, W_{12} = \begin{bmatrix} 0.25 & -0.433 \\ 0.433 & 0.25 \end{bmatrix}\begin{bmatrix} x \\ y \end{bmatrix} + \begin{bmatrix} 0.1429 \\ 0.6186 \end{bmatrix},$$

$$W_{13} = \begin{bmatrix} 0.25 & 0.433 \\ -0.433 & 0.25 \end{bmatrix}\begin{bmatrix} x \\ y \end{bmatrix} + \begin{bmatrix} 0.2143 \\ 0.7423 \end{bmatrix}, W_{14} = \begin{bmatrix} -0.5 & 0 \\ 0 & -0.5 \end{bmatrix}\begin{bmatrix} x \\ y \end{bmatrix} + \begin{bmatrix} 0.5 \\ 0.2474 \end{bmatrix},$$

$$W_{15} = \begin{bmatrix} 0.25 & 0.433 \\ -0.433 & 0.25 \end{bmatrix}\begin{bmatrix} x \\ y \end{bmatrix} + \begin{bmatrix} 0.3571 \\ 0.2474 \end{bmatrix}$$

$$W = W_1 \cup W_2 \cup W_3 \cup W_4 \cup W_5 \cup W_6 \cup W_7 \cup W_8 \cup W_9 \cup W_{10} \cup W_{11} \cup W_{12} \cup W_{13} \cup W_{14} \cup W_{15} \tag{31}$$

The proposed array is activated through an aperture-coupled feed approach to excite a relatively broad operational bandwidth. For this reason, the feed substrate (lower FR4) consists of a ground defected with four spiral-shaped slots on its top and a quartet of 2.8 mm ('f1') broad feedlines on its rear surface. As illustrated in Figure 4.1(b), four rectangular apertures (centrally located under the patches) are clipped off from a copper-coated ground to support the maximum transmission of microwave power from the microstrip lines to the active radiators. A DGS is next achieved by converting each aperture slot into a dual-arm archimedean spiral on the antenna's ground surface. The spiral designed for each fractal geometry reflects a complementary constitution since the arm width 'v' of each spiral slot (part of FR4 substrate) is similar to the separation distance 'w' between the two contiguous arm slots (copper part). To improve the matching characteristics in the excited functional range, the outermost segment of one arm of the spiral is terminated by a horizontal ɩ-shaped slot whereas the two mirror-imaged spirals are interconnected via a ‘Ӿ’-shaped slot. Furthermore, these ‘Ӿ’-shaped slots (positioned between the spirals A1, A2, and A3, A4) are linked via an ‘X’ shaped slot (placed in the center of the ground plane) to cover the lower UWB band with a good degree of inter-port isolation.

As demonstrated in Figure 4.1(c), the rear side of the bottom FR-4 is composed of four 50Ω, right offset-fed microstrip lines for driving each fractal radiating patch respectively. Offsetting the transmission line towards the right by a 1.85mm distance (from the center feed location) have a significant influence on matching characteristics and also aids in shifting the frequency band towards the lower side. Additionally, a vertical slot is removed from the lower portion of each microstrip line to achieve the desired matching performance and enhance the bandwidth of operation. The optimized value (mm) for each parameter of the proposed array is indicated in Table 4.1.

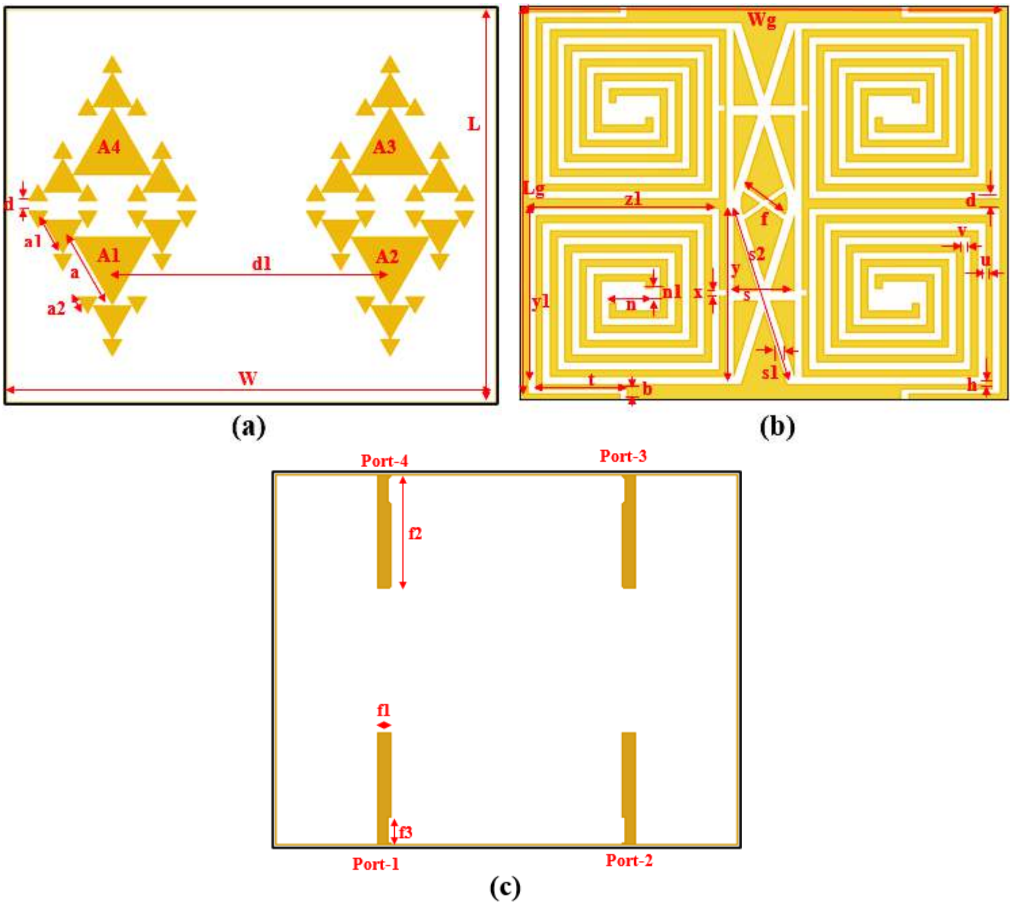

(a) (b) (c)

Figure 4.1 (a) Four fractal patches (upper view of top FR4) (b) Ground with spiral-shaped slots (upper surface of lower FR4) (c) Microstrip feed lines (rear side of lower FR4 substrate)

Table 4.1 Parametric dimensions of the quad-port fractal UWB-MIMO antenna

Parameter	L	W	a	a1	a2	d	d1	Lg	Wg	y
Value (mm)	80	99.4	16.16	8.08	4.04	2	54.4	80	99.4	36
Parameter	z1	n	n1	t	b	h	s	s1	s2	o
Value (mm)	39	9	3	18.75	2	1	12.4	1.5	38.08	4
Parameter	v	x	f1	f2	f3	y1	f	u		
Value (mm)	1.5	1	2.8	24.35	5.5	36	10.41	1.5		

4.1.2 Design Procedure of the Proposed Fractal UWB MIMO Antenna

(1) The design process of the proposed array initiates with a simple equilateral triangular SISO antenna (Stage I in Figure 4.2(a)), occupying a total volume of 41×43×3.245 mm^3. The side length (‘a’) of the equilateral triangular (0th iteration order) patch (top of antenna FR4 substrate) is computed for 6.8 GHz resonance using Equations (10-13), given in chapter 1. For the proposed antenna, the aperture-coupled feeding mechanism is utilized for the transmission of microwave power from the feedline (back view of the feed substrate) to the triangular radiator. To support this coupling technique, a slot (aperture) with dimensions of 3×9 mm^2 is etched from the upper layer of the feed substrate. The corresponding S_{11}(dB) for the SISO antenna (Stage I) is shown by a black curve in Figure 4.2(b).

(2) Next, to enhance the operational frequency band, the aperture slot in the antenna’s ground is transformed into a dual-arm Archimedean spiral configuration (Stage II in Figure 4.2(a)). Each arm of the spiral (with width ‘v’) is designed with 12 segments (3 windings) whose length is determined by using Equations (15,16) stated in chapter 3. As observed from the brown curve in Figure 4.2(b), the incorporation of the spiral slots in the ground surface of the designed SISO antenna excites a UWB spectrum from 5.83-10.62 GHz (58.24% FBW).

(3) Stage III in Figure 4.2(a) represents the 1st iteration of the designed fractal patch with a scale-down value of 0.5. This patch geometry is constructed by joining the three newly generated triangular copies (each with side ‘a1’= 8.08 mm) on the vertices of an initial equilateral triangular patch (0th iteration). The pink line in Figure 4.2(b) illustrates that the fractal antenna design in Stage III occupies a UWB bandwidth (>500 MHz) in two frequency bands of 4.575-5.178 GHz and 6.483-10.74 GHz respectively. To achieve a wider UWB response, Stage IV in Figure 4.2(a) illustrates the 2nd iteration order of the Sierpinski gasket fractal patch which is constructed by adding nine non-overlapping copies (each with side ‘a2’= 4.04 mm) on the vertices of the previously iterated Sierpinski gasket fractal (three on each) patch. The simulation results (green curve in Figure 4.2(b)) indicate that Stage IV (2nd iteration order) provides a UWB operation in two frequency ranges of 4.422-5.511 GHz and 5.664-11.01 GHz respectively. Thus, from the above observations, it is deduced that 2nd fractal iteration provides a better UWB response than those achieved by 1st and 2nd iterated geometries.

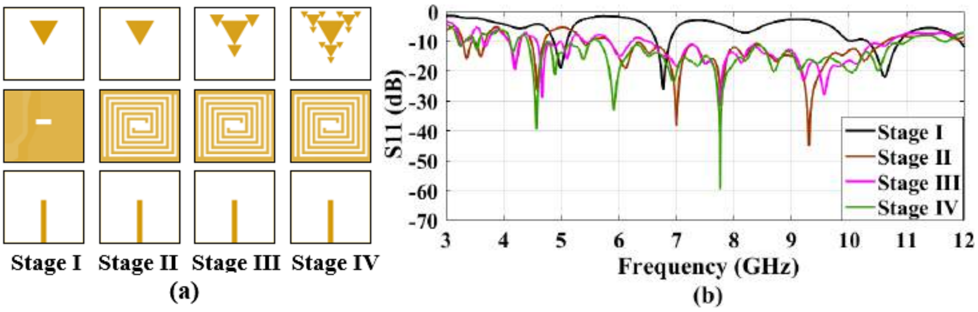

(a) (b)

Figure 4.2(a) Step-by-step design approach followed for achieving UWB response (b) Corresponding S_{11} (dB) versus frequency response of the proposed SISO antenna

(4) Next, to construct a dual-element MIMO antenna, the width of the two FR-4 substrates is increased twofold and the aforementioned fractal SISO antenna (Stage IV in Figure 4.3(a)) is symmetrically replicated on the printed circuit boards where the center-to-center separation between the two radiators is fixed to 54.4 mm (Stage V in Figure 4.3(a)). The frequency response of this newly developed MIMO antenna reveals a dual UWB operation (brown curve in Figure 4.3(b)) with a minimum isolation of 20dB (yellow curve in Figure 4.3(b)).

(5) For the designed antenna array to practically operate under the influence of reflections from the surroundings, resulting in high impedance mismatch losses, this step specifies the changes made in the proposed MIMO structure to achieve good impedance matching performance ($S_{11}/S_{22} \leq$ -15 dB). Firstly, two horizontal ˪-shaped slots (each connected to the spiral base) are etched from the ground as represented by Stage VI in Figure 4.3(a). The frequency response of S_{11}/S_{22} (dB) reveals an improved matching performance with a slight shift in the frequency band towards the lower side (green curve in Figure 4.3(b)) while retaining an admissible isolation level ($S_{21}/S_{12} \leq$ -20dB) between the array elements (orange-colored curve in Figure 4.3(b)). To further refine the matching characteristics and realize a wider UWB response, the two mirror-imaged spirals are linked via a ‘Ӿ’-shaped slot (center of the ground plane) as depicted by Stage VII in Figure 4.3(a). The pink and black curve in Figure 4.3(b) illustrates that the proposed array operates in a large frequency range from 4.3-10.94 GHz (86.8% FBW) with an acceptable level of isolation response ($S_{21}/S_{12} \leq$ -15.8dB) respectively. Although the MIMO antenna illustrated by Stage VII covers a wide operational range, the required matching criteria ($S_{11}/S_{22} \leq$ -15dB) to function in a realistic environment are not met. Therefore, a vertical slot is truncated from the lower region of each microstrip feed (Stage VIII in Figure 4.3(a)) to minimize the signal reflections in a large working band (4.4-11.5GHz) with an optimal isolation level (as illustrated by the blue and grey curve in Figure 4.3(c) respectively).

(6) To accomplish the manuscript’s fundamental objective of covering the entire FCCs allocated unlicensed UWB spectrum, Stage IX in Figure 4.3(a) depicts that the two transmission lines are right offset by a distance of 1.85mm from the center feed point to excite the lower UWB band (red curve in Figure 4.3(c)) while maintaining isolation ≥ 16.8dB in most of the operating range (orange curve in Figure 4.3(c)). After this, a four-element MIMO antenna design based on Stage IX in Figure 4.3(a) is designed and investigated. As illustrated by Stage X (Figure 4.4(a)), the two MIMO antennas (Stage IX) are arranged in cross-configuration with a separation distance (‘d’) of 2mm without altering the final optimized parametric values. The frequency response ($S_{11}/S_{22}/S_{33}/S_{44}$ (dB)) of Stage X reveals a dual-band operation with the FBW of 27.45% (3.08-4.06 GHz) and 89.6% (4.16-10.91 GHz) as depicted by a black colored curve in Figure 4.4(b)). The brown curve in Figure 4.4(c) depicts a good degree of isolation between port 1 and port 3 ($S_{31} \leq$ 20 dB) for the complete operating band which is mainly due to the space separation method. The orange (Figure 4.4(b)) and green (Figure 4.4(c)) curves show an acceptable isolation performance between port-1, port-2, and port-1, port-4 respectively, especially in the higher working range with slight isolation improvement required in the 3-5 GHz frequency band.

Next, in Stage XI, the two 'Ӿ'-shaped slots (joining the spirals of antenna elements A1, A2, and A3, A4 respectively) are interconnected via an X-shaped slot (positioned in the middle of the ground). Also, a horizontal slot of length 'm' is extended along the two corners of each 'Ӿ'-shaped slot to excite the lower UWB range with a low degree of coupling. Hence, the proposed quad-port fractal array successfully covers the entire UWB range from 3.07-11 GHz with 112.7% FBW (red curve in Figure 4.4(b)) while realizing an agreeable inter-port isolation response ($S_{21} \leq 17.1$ dB (blue line in Figure 4.4(b)), $S_{31} \leq 16.8$ dB (purple line in Figure 4.4(c)) and $S_{41} \leq 16.19$ dB (pink line in Figure 4.4(c))) for the complete operational bandwidth.

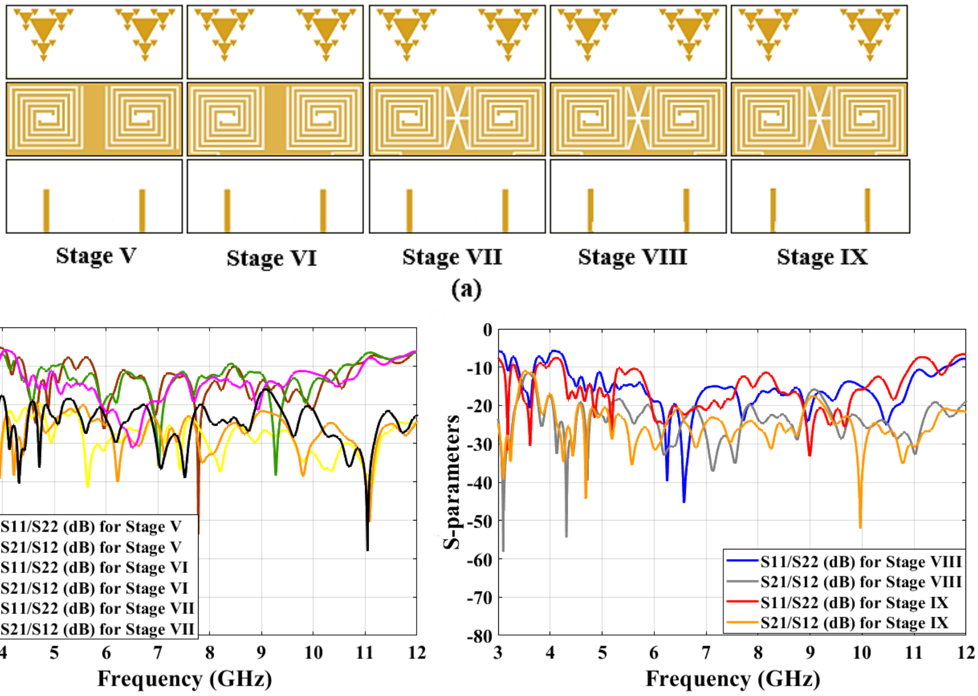

(a)

(b)

(c)

Figure 4.3 (a) Methodology adopted for achieving UWB range from the proposed two-port MIMO antenna (b) Corresponding S_{11}/S_{22} (dB) and S_{21}/S_{12} (dB) against frequency response (Stage V-VII) (c) S_{11}/S_{22} (dB) and S_{21}/S_{12} (dB) against frequency response (Stage VIII-IX)

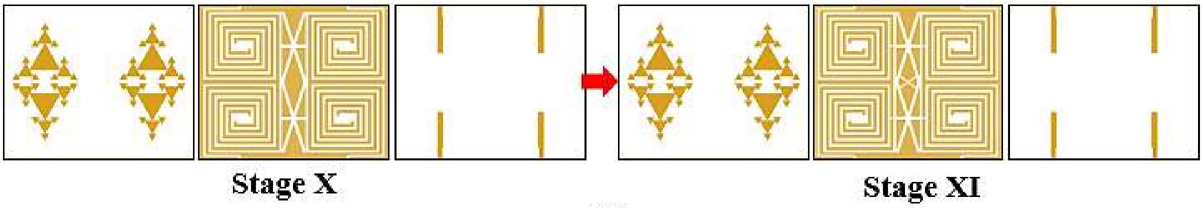

(a)

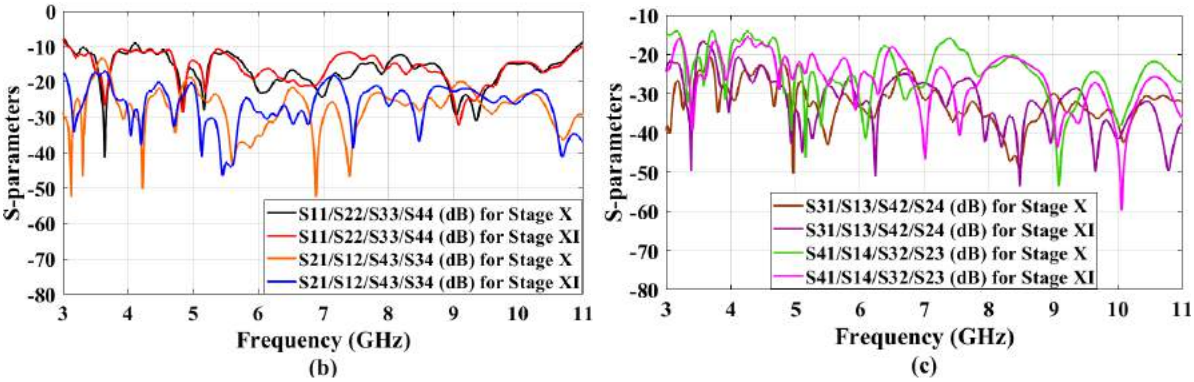

Figure 4.4 (a) Design procedure for realizing UWB characteristics from the proposed four-port MIMO antenna (b) Respective $S_{11}/S_{22}/S_{33}/S_{44}$ (dB) and $S_{21}/S_{12}/S_{43}/S_{34}$ (dB) versus frequency (Stage X-XI) (c) $S_{31}/S_{13}/S_{42}/S_{24}$ (dB) and $S_{41}/S_{14}/S_{23}/S_{32}$ (dB) versus frequency (Stage X-XI)

4.1.3 Surface Current Analysis for Verifying Inter-element Isolation Performance

According to the Figure 4.5(a, b), the port-1 of the designed MIMO antenna is energized with IW simulated input power in CST software to observe the flow of current on the fractal patch, spiral ground, and feed at the resonating frequencies of 4.85 GHz and 6.94 GHz respectively. At 4.85 GHz resonance, Figure 4.5(a) depicts that the current is distributed uniformly across the patch, ground, and feed of the antenna ‘A1’ but the maximum current of 98.78 A/m is distributed at the junction where the upper right 1st iterative fractal is integrated with the 2nd iterative fractal structure. Figure 4.5(b) demonstrates the highest intensity of current (80.26 A/m) is concentrated across the upper left fractal patch (1st iterative fractal joins the 2nd iterative fractal geometry), the outermost arm of the archimedean spiral and bottom of rectangular slot (etched from the feed) of the antenna ‘A1’. Therefore, the incorporation of fractal patch geometry helps in exciting lower and higher-order resonant frequencies whereas the DGS geometry in the ground aids in maintaining a sufficient degree of inter-port isolation response. Also, for the triggered port-1 of the array, the current from the fractal radiator (port-1) is perturbed by the ‘Ӿ’-shaped slot and a negligible degree of current is coupled to the non-radiating units (port-2, port-3, and port-4) at both the frequencies. In nutshell, the influence of mutual coupling is minimal and most of the energy is radiated by the antenna element connected with port-1.

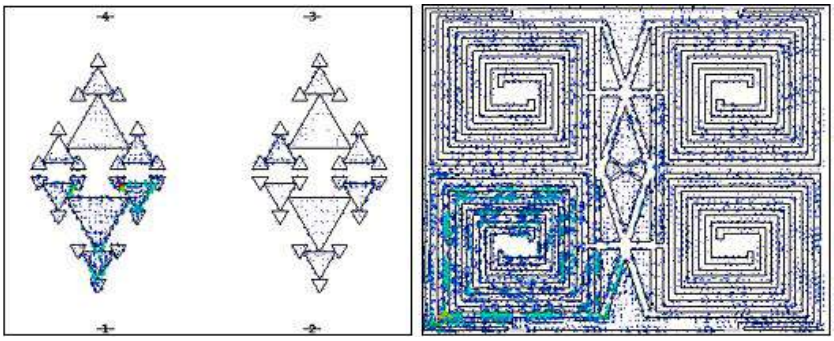

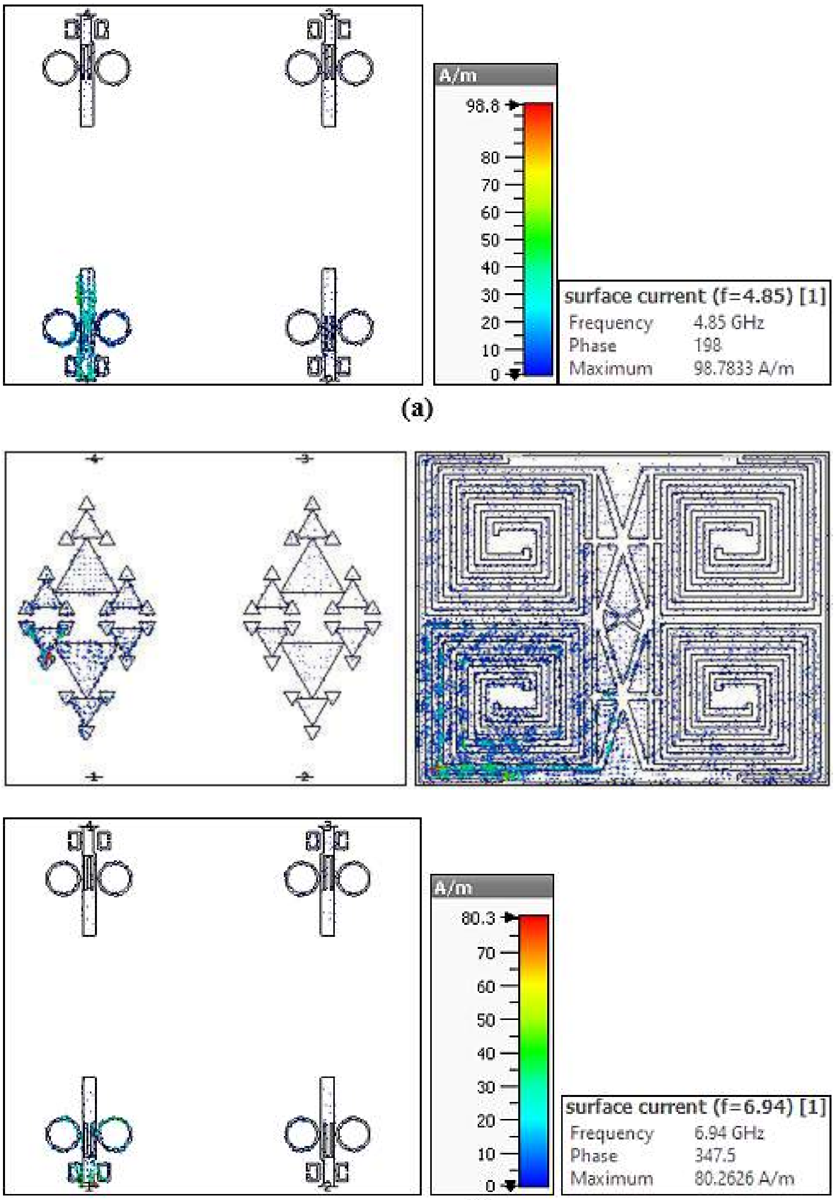

(a)

(b)

Figure 4.5 Current distribution on the patch, ground, and feed of the designed array at the excited resonances of (a) 4.85 GHz (b) 6.94 GHz for the activated port-1

4.1.4 Simulation and Measurement Results

To support the array's realistic functioning, it is developed according to the photolithography method on a set of two 1.57 mm thick, cost-efficient FR4 substrates. For authenticating the UWB functionality, Figure 4.6(a-c) demonstrates the fabricated images of the four-port fractal radiators (upper surface of first FR-4 substrate), ground defected with spiral slots (upper surface of the second FR4), and four microstrip feeds (back of the second FR4) respectively. To energize the fractal radiators, a 50Ω SMA connector is soldered at each feed point.

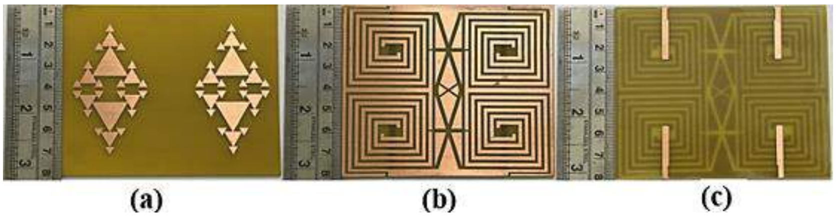

Figure 4.6 Fabricated photographs of (a) fractal patches (b) Defected ground surface (c) Transmission lines

4.1.4.1 Scattering Parameters and Gain Performance

The variation of software simulated and tested S-parameter (dB) results versus the operating band (GHz) for the four-port UWB antenna is illustrated in Figure 4.7(a-d). It excites a frequency bandwidth (simulated) of 7.93GHz in the range of 3.07-11 GHz (with 112.7% FBW) while accomplishing an admissible port isolation characteristic ($S_{21} \leq 17.1$dB, $S_{31} \leq 16.8$dB, $S_{41} \leq 16.19$dB) for the complete working range. The simulation response shows a close resemblance with the experimental results where the fabricated array prototype offers FBW of 117.46% (3.12-12 GHz) while maintaining a reduced level of mutual coupling ($S_{21} \leq 16.6$ dB, $S_{31} \leq 15.84$ dB, $S_{41} \leq 17.1$ dB) between the actively radiating array elements.

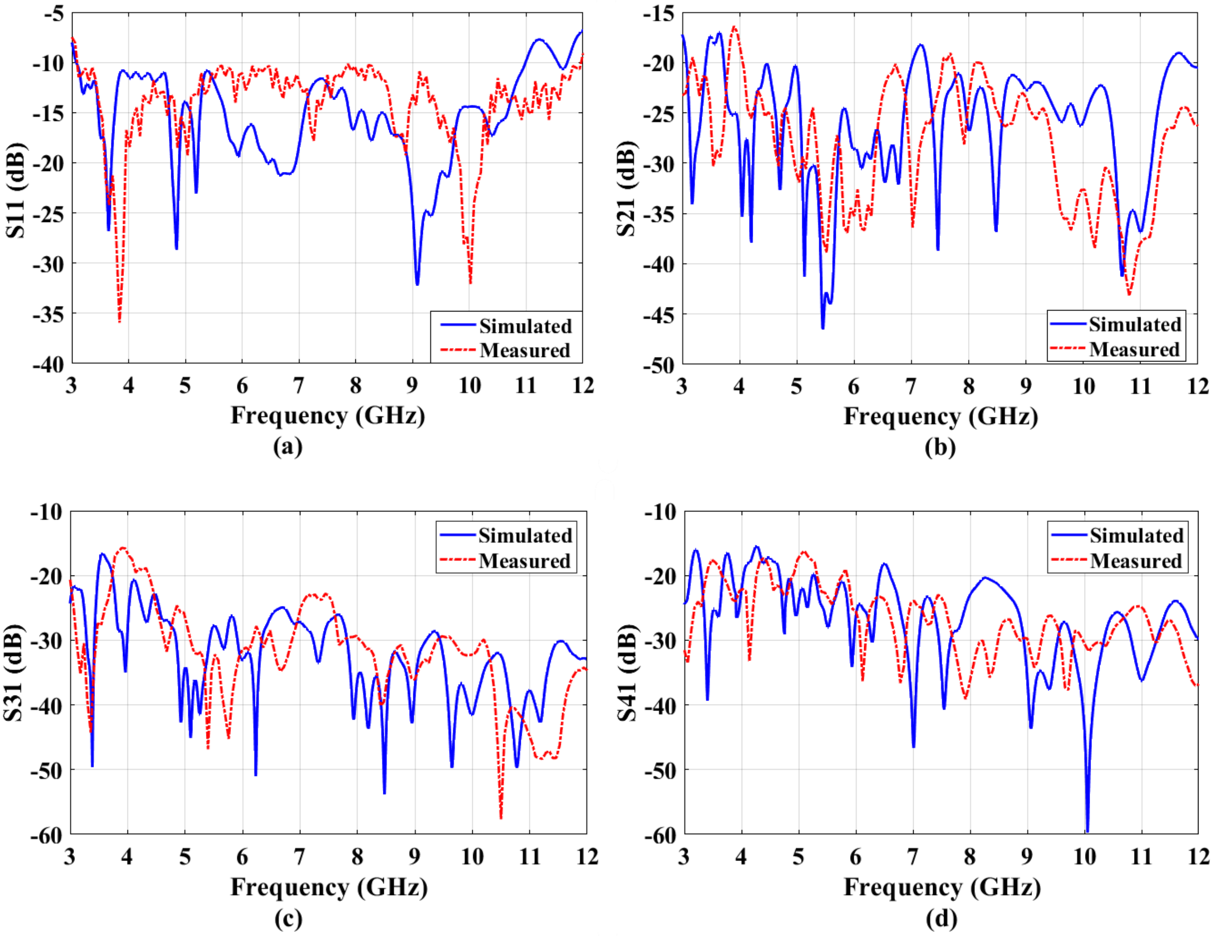

Figure 4.7 Simulated and measured (a) S_{11} (b) S_{21} (c) S_{31} (d) S_{41} versus frequency of the designed four-port fractal UWB antenna

On activating port-1 of the four-port UWB antenna, the simulated gain variations against the functional UWB range is presented in Figure 4.8. The basic four-port UWB-MIMO antenna provides an average gain of 2.95dBi (simulated) across the complete band of operation with 4.88dBi (at 9.3GHz) being the maximal gain. Thereby, the proposed array is a suitable candidate for the effective functioning of UWB communication devices in the real-time world.

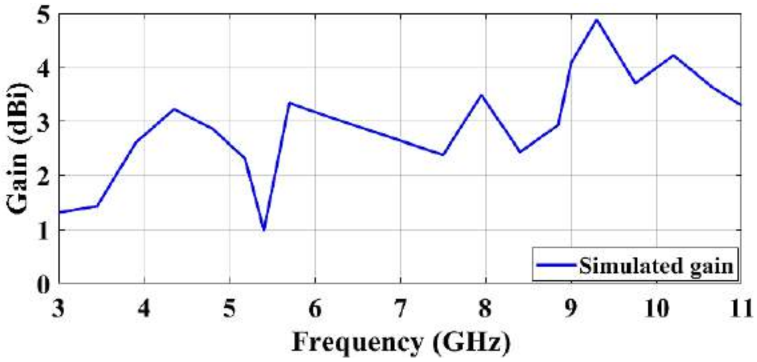

Figure 4.8 Gain versus frequency plot for the complete operational band

4.1.5 Diversity Metrics

In this subsection, to govern the optimal functionality of the designed MIMO antenna (without and with stopbands) in the multi-channel environment, several diversity metrics like ECC, DG, MEG, CCL, and TARC are computed through the MATLAB code and also validated with the experimental values. The comparative plots of simulated and measured values of diversity metrics are depicted in Figure 4.9(a-e).

In a MIMO antenna configuration, the amount of coupling between the different array radiators and the level of correlation between them in multipath propagation surroundings is assessed by ECC. For a quad-port MIMO antenna (N = 4), Equation 32 reports the ECC between port-i and port-j using the S-parameter technique [27].

$$\rho_e(i,j,4) = \frac{\left|S_{i1}^{*}S_{1j}+S_{i2}^{*}S_{2j}+S_{i3}^{*}S_{3j}+S_{i4}^{*}S_{4j}\right|^2}{(1-|S_{1i}|^2-|S_{2i}|^2-|S_{3i}|^2-|S_{4i}|^2)(1-\left|S_{2j}\right|^2-\left|S_{1j}\right|^2-\left|S_{3j}\right|^2-\left|S_{4j}\right|^2)} \qquad (32)$$

DG is a MIMO performance metric that quantifies a rise in the SNR of the mixed signal in an antenna diversity system owing to the adoption of some diversity combining approach at the receiver end. It is estimated from the ECC using Equation 3 (given in chapter 1).

For a multi-port MIMO antenna functioning in a mobile environment, MEG estimates the average received signal strength of every antenna element individually. For the quad-port MIMO antenna, MEG can be estimated by the S-parameter technique according to Equation 33. For good channel characteristics, the antenna which meets the criterion of $|MEG_i\text{-}MEG_j| < 3$ dB is usually demanded.

$$MEG_i = 0.5(1-|S_{i1}|^2-|S_{i2}|^2-|S_{i3}|^2-|S_{i4}|^2) \qquad (33)$$

CCL is another important MIMO metric that indicates the highest threshold limit for continuous message transmission across the radio communication link with a loss ≤ 0.4

bits/s/Hz for the complete working band [3]. For a quad-port antenna, CCL is calculated from the correlation matrix (α^R) using Equations (34, 35) [27].

$$\mathrm{CCL} = -\log_2 \det(\alpha^R) = -\log_2 \det \begin{bmatrix} \alpha_{11} & \alpha_{12} & \alpha_{13} & \alpha_{14} \\ \alpha_{21} & \alpha_{22} & \alpha_{23} & \alpha_{24} \\ \alpha_{31} & \alpha_{32} & \alpha_{33} & \alpha_{34} \\ \alpha_{41} & \alpha_{42} & \alpha_{43} & \alpha_{44} \end{bmatrix} \tag{34}$$

$$\alpha_{ii} = 1 - \sum_{n=1}^{4} |S_{in}|^2 \text{ and } \alpha_{ij} = -\left|\sum_{n=1}^{4} S_{in}^{*} S_{nj}\right| \text{ for i, j =1,2,3 or 4} \tag{35}$$

TARC is an imperative MIMO parameter, mathematically computed as the square root of total reflected power divided by total incident power. For good diversity performance, TARC lower than 0 dB is generally required and is estimated by Equation 36 [27].

$$\mathrm{TARC} = \sqrt{\frac{|S_{11}+S_{12}+S_{13}+S_{14}|^2+|S_{21}+S_{22}+S_{23}+S_{24}|^2+|S_{31}+S_{32}+S_{33}+S_{34}|^2+|S_{41}+S_{42}+S_{43}+S_{44}|^2}{4}} \tag{36}$$

Table 4.2 lists the simulated and experimental levels of the analyzed diversity metrics for the excited UWB spectrum. As observed, the admissible levels of various diversity metrics of the designed four-port UWB antenna verify the accomplishment of considerable diversity operation imperative for MIMO communication systems.

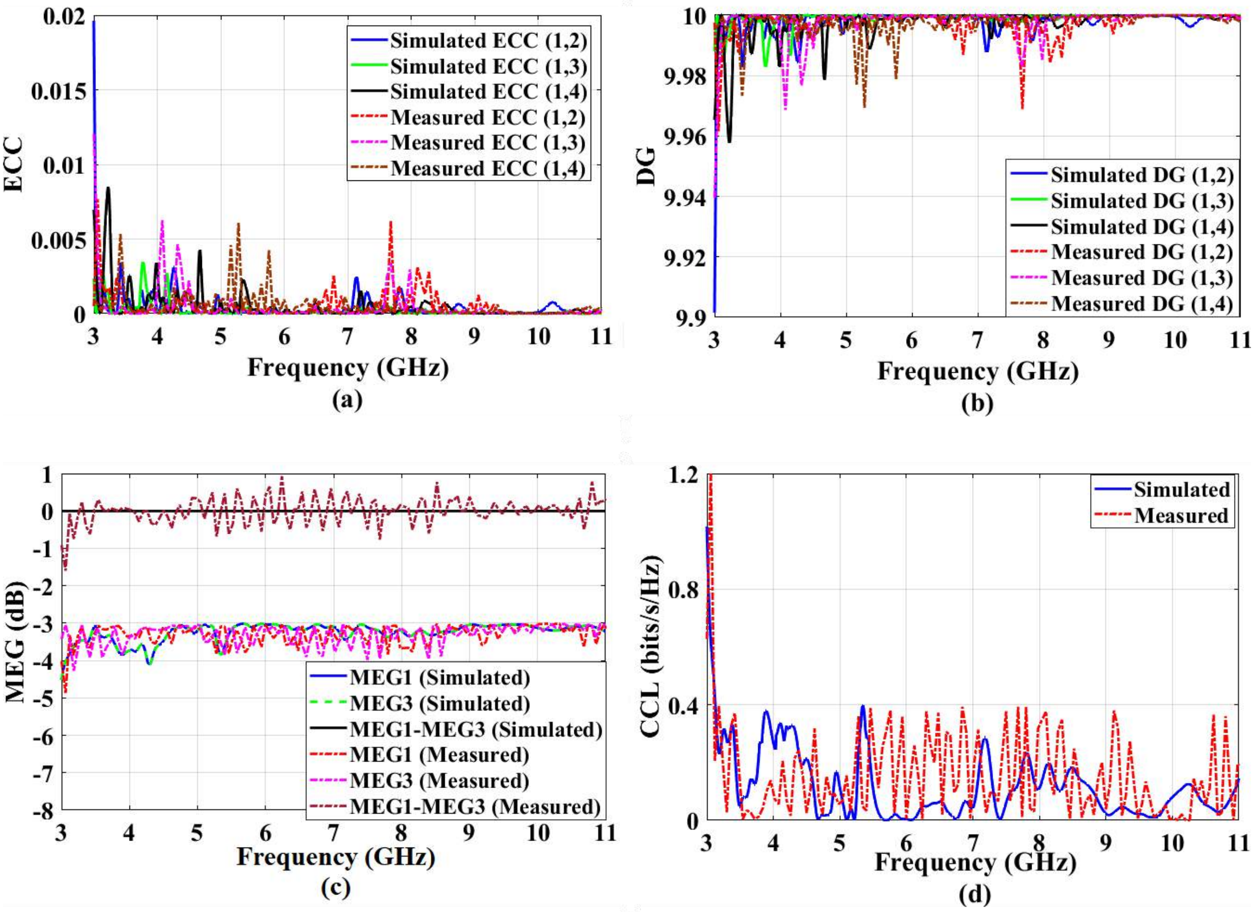

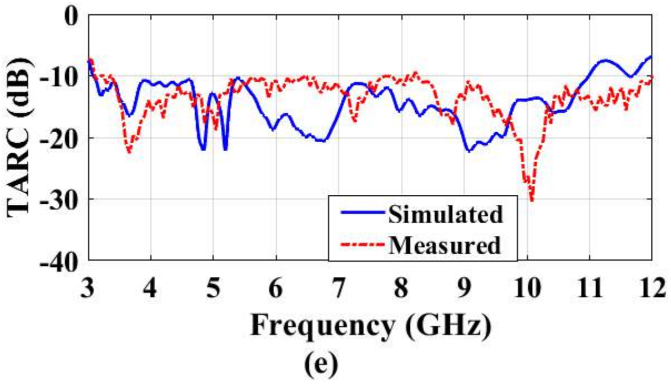

(e)

Figure 4.9 Variation of the simulated and tested diversity metrics (a) ECC (b) DG (c) MEG (d) CCL (e) TARC versus frequency

Table 4.2 Simulated and tested levels of diversity parameters

Metrics	ECC		DG		MEG (dB)		CCL(bits/s/Hz)	TARC (dB)	
Proposed UWB antenna	Sim.	Tested	Sim.	Tested	Sim.	Tested	Sim. / Tested	Sim.	Tested
	≤0.004	≤0.006	≥9.98	≥9.97	≤-4.1	≤-3.92	≤ 0.4	≤ -10	≤ -9.372

The subsequent section of this chapter demonstrates the next proposed quad-element fractal geometry with two circular radiators integrated with a modified Koch Snowflake fractal geometry and a partially defected ground surface for UWB applications.

4.2 Design and Simulation of Quad-element Koch Snowflake Fractal UWB Antenna

In this section, a four-port Koch Snowflake fractal MIMO antenna is prototyped and simulated, for its application in portable UWB devices. The array is configured on a 1.57mm thick FR4 epoxy substrate which consists of four tapered and offset-fed circular radiators (each slotted with 4th order modified Koch Snowflake fractal) and defected ground surface, targeted to realize 141% FBW (3.1-18GHz) with a significant degree of inter-port isolation response. To justify the array's operation in a rich scattering environment, several diversity performance metrics are examined. Also, the fabricated array prototype is tested for S-parameters and radiation characteristics.

4.2.1 Array Geometry

The design configuration and parameters of the final optimized UWB array with four fractal radiating elements and common ground with DGS are displayed in Figure 4.10. The fractal array with 80×71×1.64mm^3 volumetric dimensions is configured on a low-priced, easily obtainable FR4 (lossy) substrate with a thickness tan δ, and ε_r of 1.57mm, 0.024, and 4.4 respectively.

According to Figure 4.10(a), the upper FR4 surface is configured with four identical circular radiating patches (copper-coated), each embedded with an optimized 4th iterative transformed Koch snowflake fractal geometry (resulting in hen-shape) with a scale-down factor of 0.5. For emitting non-correlated signals in open space, the fractal radiating units are assembled in a mirror-image layout with the common ground. To suppress the effect of mutual coupling between the array elements, the distance between the midpoints of fractal patches marked as

‘C1’ and ‘C2’ is optimized to ‘t1’ while ‘C1’ and ‘C4’ radiators are kept at the spacing of ‘t2’. Each fractal patch is activated by a 3.4 mm wide microstrip transmission line which is further tapered and right-offset (by 3.2mm from the center) to considerably realize a 50Ω matching performance and shift the frequency range towards the left to accomplish the lower UWB of operation respectively. Figure 4.10(b) depicts the expanded transitional iterations for the construction of a modified Koch Snowflake fractal optimized to the 4th order. The proposed fractal geometry is constructed through the transformed Koch snowflake fractal, generated by firstly splitting every segment of the 0th-order equilateral triangle into two identical parts and then arranging the newly iterated equilateral triangle (1st order with 0.5 scaling factor) on the first half of each segment of the former equilateral triangle with the central purpose of attaining the desired miniaturization. For the generation of each iteration, the same procedure is repeated, and the variables ‘a0’, ‘a1’, ‘a2’, ‘a3’, and ‘a4’ symbolizes the side lengths for the 0th, 1st, 2nd, 3rd, and 4th iteration order of hen-shaped fractal respectively. The proposed fractal design is recursively developed based on the IFS approach, given by Equation 10 (in chapter 1). The below set from W1 to W9 indicates the IFS transformations for the 1st iteration of the hen-shaped fractal geometry and its generator curve is reported in Equation 37.

$$W_1 = \begin{bmatrix} \frac{1}{2} & 0 \\ 0 & \frac{1}{2} \end{bmatrix} \begin{bmatrix} x \\ y \end{bmatrix} + \begin{bmatrix} 0 \\ 0 \end{bmatrix}, W_2 = \begin{bmatrix} \frac{1}{4} & -\frac{\sqrt{3}}{4} \\ \frac{\sqrt{3}}{4} & \frac{1}{4} \end{bmatrix} \begin{bmatrix} x \\ y \end{bmatrix} + \begin{bmatrix} 9 \\ 0 \end{bmatrix}, W_3 = \begin{bmatrix} \frac{1}{2} & 0 \\ 0 & \frac{1}{2} \end{bmatrix} \begin{bmatrix} x \\ y \end{bmatrix} + \begin{bmatrix} 13.5 \\ 7.79 \end{bmatrix},$$

$$W_4 = \begin{bmatrix} -\frac{1}{4} & -\frac{\sqrt{3}}{4} \\ \frac{\sqrt{3}}{4} & -\frac{1}{4} \end{bmatrix} \begin{bmatrix} x \\ y \end{bmatrix} + \begin{bmatrix} 22.5 \\ 7.79 \end{bmatrix}, W_5 = \begin{bmatrix} -\frac{1}{2} & 0 \\ 0 & -\frac{1}{2} \end{bmatrix} \begin{bmatrix} x \\ y \end{bmatrix} + \begin{bmatrix} 18 \\ 15.59 \end{bmatrix}, W_6 = \begin{bmatrix} -\frac{1}{4} & -\frac{\sqrt{3}}{4} \\ \frac{\sqrt{3}}{4} & -\frac{1}{4} \end{bmatrix} \begin{bmatrix} x \\ y \end{bmatrix} +$$

$$\begin{bmatrix} 9 \\ 15.59 \end{bmatrix}, W_7 = \begin{bmatrix} -\frac{1}{4} & \frac{\sqrt{3}}{4} \\ -\frac{\sqrt{3}}{4} & -\frac{1}{4} \end{bmatrix} \begin{bmatrix} x \\ y \end{bmatrix} + \begin{bmatrix} 4.5 \\ 23.38 \end{bmatrix}, W_8 = \begin{bmatrix} \frac{1}{4} & \frac{\sqrt{3}}{4} \\ -\frac{\sqrt{3}}{4} & \frac{1}{4} \end{bmatrix} \begin{bmatrix} x \\ y \end{bmatrix} + \begin{bmatrix} 0 \\ 15.59 \end{bmatrix}, W_9 =$$

$$\begin{bmatrix} -\frac{1}{4} & \frac{\sqrt{3}}{4} \\ -\frac{\sqrt{3}}{4} & -\frac{1}{4} \end{bmatrix} \begin{bmatrix} x \\ y \end{bmatrix} + \begin{bmatrix} 4.5 \\ 7.79 \end{bmatrix}$$

$$W = W_1 \cup W_2 \cup W_3 \cup W_4 \cup W_5 \cup W_6 \cup W_7 \cup W_8 \cup W_9 \tag{37}$$

As illustrated in Figure 4.10(c), the reduced ground integrated with the DGS approach is assembled on the rear FR4 surface. To diminish the impact of severe mutual coupling between the antenna ports (especially S_{21}/S_{43}), an inverted ‘Π’ decoupling structure is protruded orthogonal to the reduced ground surface. Additionally, two rectangular (back side of the microstrip lines) and ‘+’ shaped (near the ‘Π’shaped decoupler) slots are clipped off from the copper-clad ground to realize a performance enhancement in frequency bandwidth, impedance match, and inter-port isolation. For the proposed array, the overall inter-element isolation (particularly $S_{41}/S_{32}/S_{42}/S_{31}$) is enhanced by fusing two semi-circular rings (mirror images of each other) at the middle of the vertical decoupler. Table 4.3 depicts the final structural dimensions (mm) of the designed four-port array.

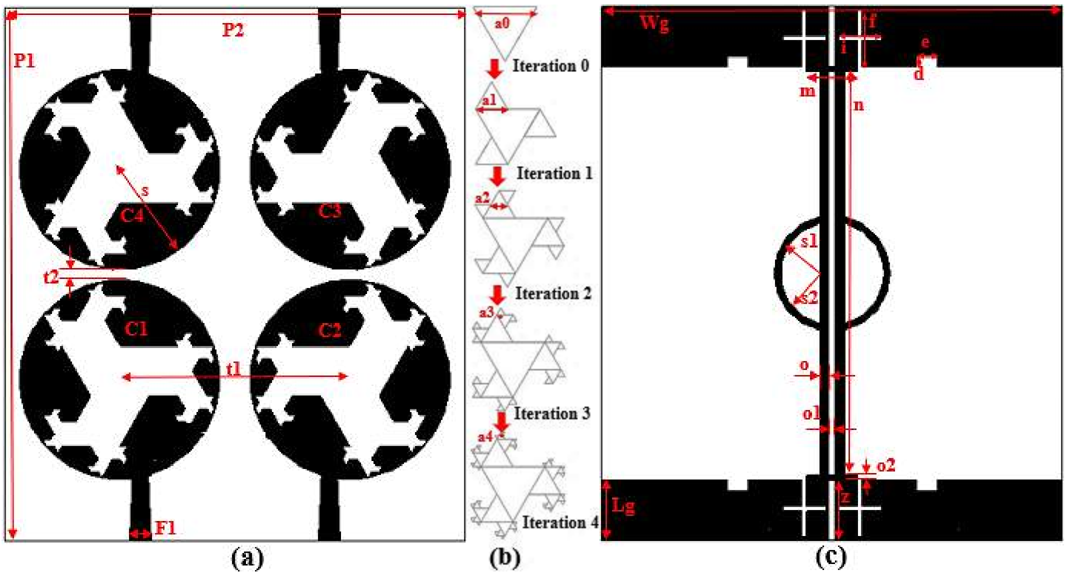

Figure 4.10 (a) Circular patches defected with modified Koch Snowflake fractal (b) Intermediary iteration levels of modified Koch Snowflake fractal (c) Reduced and defected ground surface

Table 4.3 Optimized dimensions (mm) of proposed four-port antenna geometry

Parameter	P1	P2	s	Lg	F1	e	d	f	t1	t2
Value (mm)	80	71	14.3	9.3	3.4	3.2	1.63	8.8	32.4	2.8
Parameter	o1	o2	z	o	Wg	i	s1	s2	m	n
Value (mm)	9	0.75	9.3	1.45	82	6.65	7.1	6.1	7.8	59.9
Parameter	a0	a1	t2	a2	a3	a4				
Value (mm)	18	9	2.8	4.5	2.25	1.125				

4.2.2 Design Evolution and Simulation Results of the Proposed Quad-port Fractal Antenna for Realizing UWB Response

(1) For the proposed array, the evolutionary process commences with a basic microstrip-fed circular SISO antenna with a reduced ground plane (Stage I in Figure 4.11(a)), extended over an area of 41×35mm^2. Limiting the ground dimension (‘Lg’ = 9.3mm) across the y-axis leads to more power radiation (due to fringing fields), thus, assisting to cover a wide operational range. The radius ‘s’ of a circular patch is approximated by utilizing Equation 17 (given in chapter 3). The corresponding S_{11}/S_{22}(dB) response for Stage I (pink curve in Figure 4.11(b)) illustrates a triple-band operation from 3-5.4GHz (57.14%), 6.96-11.86GHz (52.07%) and 14.64-16.54GHz (12.18%).

(2) Next, to excite a wider operational bandwidth with improved matching performance, the microstrip line of the proposed antenna is right offset by 3.2mm, and a rectangular slot is clipped off from reduced ground (immediately behind the feedline) as represented by Stage II and Stage III in Figure 4.11(a) respectively. As observed, the fusion of offset feeding and DGS technique moves the excited resonances towards the left and aids the proposed antenna to operate in two frequency spectrums from 3-5.54GHz and 6.64-18GHz with FBW of 59.48% and 92.2% respectively (brown curve in Figure 4.11(b)).

(3) Further, the hen-shaped self-similar design is introduced in the patch of the proposed antenna to accomplish the desired antenna compactness along with the wideband frequency response. Stage IV depicts the 0th iteration order of the hen-shaped fractal where an equilateral triangle of side length 'a0' is embedded in the middle of the circular patch. This fractal design minimizes the patch area by 21.83% (compared to Stage III) and supports the antenna's functioning in three frequency ranges (purple curve in Figure 4.11(b)) with FBW of 20.89% (3-3.7GHz), 22.96% (4.24-5.34GHz) and 97.95% (6.165-18GHz). Stage V displays the circular patch defected with 1st order hen-shaped fractal which is generated by partitioning each line of the 0th order equilateral triangle into two halves and inserting a 0.5 scaled-down equilateral triangle (facing outwards) on the first half of each line resulting in the 1st iteration order of hen-shaped fractal. Along each line of 0th order hen-shaped fractal, the 1st-order fractal inserts a new equilateral triangle of side 'a1' and provides a 38.21% reduction of the patch area. This methodology is repetitively followed for every iteration of the hen-shaped fractal. As observed from the black curve in Figure 4.11(c), the Stage V antenna shifts the resonant bands towards the left and operates in 4.56-5.75GHz, 5.97-7.635GHz, and 7.96-18GHz with 23.08%, 23.48%, and 77.35% FBW respectively. The circular radiator integrated with 2nd order hen-shaped fractal (Stage VI) implants six new equilateral triangles (side 'a2') along the line segments of 1st order fractal to diminish the metallic area by 46.4% and yields FBW of 26.64%, 21.19%, and 83.02% in 4.36-5.7GHz, 5.865-7.255GHz and 7.44-18GHz ranges respectively (green curve in Figure 4.11(c)). Stage VII antenna represents the 3rd iteration order of hen-shaped fractal (addition of 12 new equilateral triangles of side 'a3') truncated from the radiating unit to left-shift the excited frequency bands of 4.245-6.3GHz (38.98%), 7.035-15.06GHz (72.64%) and 15.71-18GHz (13.59%) (blue curve in Figure 4.11(c)) with a size miniaturization of 50.49%. To further enhance the bandwidth characteristics with the aimed miniaturization, Stage VIII demonstrates the circular patch integrated with the final hen-shaped self-similar design iterated to the 4th order. This radiator structure offers a better wideband operation in two frequency ranges from 4.065-6GHz (38.45%) and 6.57-18GHz (93.04%) (red curve in Figure 4.11(c)) with a 52.6% decrease in patch area. In a nutshell, as the iteration order of the hen-shaped self-similar structure increases, the frequency spectrum deviates toward the lower end. Also, the incorporation of fractal design enhances the average electrical length of the radiating element that results in the miniaturization of the proposed antenna.

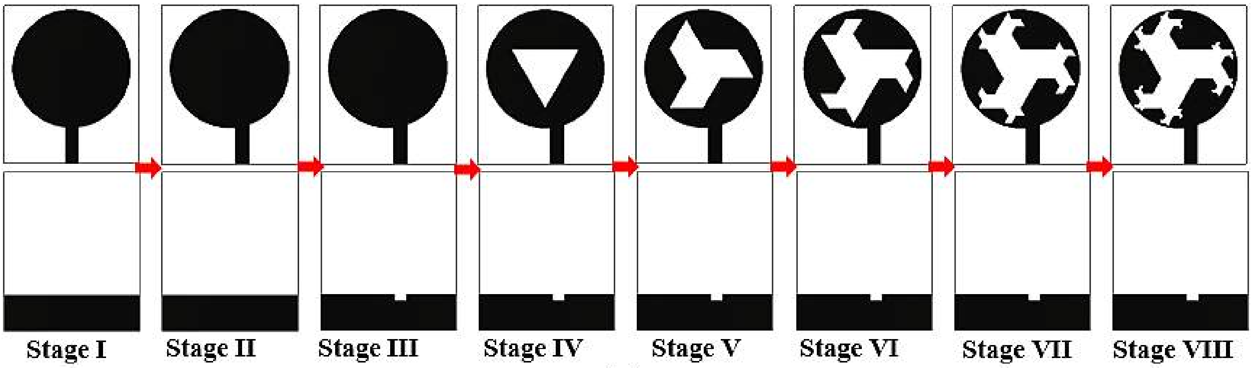

(a)

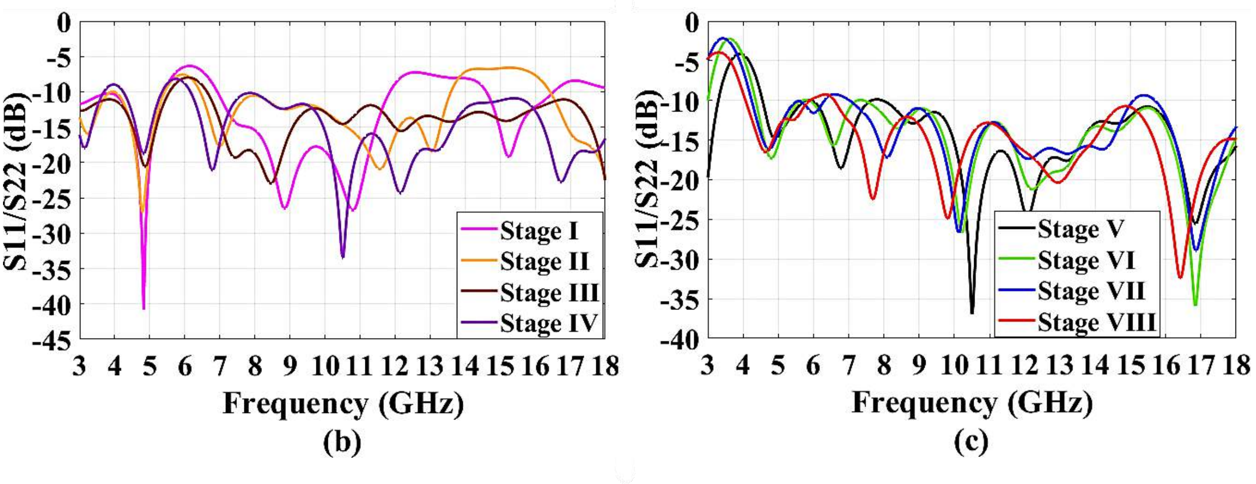

Figure 4.11 (a) Stage-by-stage transition of the proposed antenna (b) S_{11}/S_{22} versus frequency for the corresponding stages in the proposed SISO antenna

(4) Further, to combat the multipath fading effects and enhance the channel capacity, a two-port MIMO antenna configuration is developed by expanding the width of the FR4 substrate twice and symmetrically replicating the above-described SISO fractal antenna geometry (Stage VIII in Figure 4.11(a)) on the dielectric substrate where the spacing between the midpoints of two radiators is optimized to ‘t1’ (Stage IX in Figure 4.12(a)). The frequency characteristics of this recently generated MIMO antenna reports a triple-band functionality (4.2-6.09GHz, 7-8.46GHz, and 9.08-18GHz) with a poor response of inter-element isolation as demonstrated by the black curve in Figure 4.12(b, c) respectively.

(5) To implement the proposed MIMO antenna in a realistic scenario with potential environmental reflections (contributing to severe mismatch losses), this step details the modifications introduced in the array structure to realize good inter-port isolation with acceptable matching performance across a single UWB spectrum. Initially, an inverted ‘ŧŧ’shaped decoupler is elongated orthogonal from the middle of the common ground plane (as illustrated by Stage X in Figure 4.12(a)). The green S_{11}/S_{22}(dB) response (Figure 4.12(a)) for the Stage X depicts the transition of the frequency bandwidth towards the lower end while minimizing the coupling ($S_{21}/S_{12} \leq -14.4$dB) level between the antenna ports (green curve in Figure 4.12(c)). To realize a 50Ω impedance match across the UWB range with an optimal degree of port isolation, each fractal radiator is activated by a tapered microstrip line as displayed by Stage XI in Figure 4.12(a). This array geometry functions in a large operational band from 3.55-18 GHz (134% FBW) while retaining a minimal 14dB isolation throughout the working range (blue curves in Figure 4.12(b, c) respectively). Although the Stage XI MIMO antenna derives a wide frequency bandwidth, the desired inter-element isolation is not yet achieved. Therefore, two ‘+’ shaped slots (around the ‘ŧŧ’shaped decoupler) are clipped off from the upper edge of the copper-clad common ground (Stage XII in Figure 4.12(a)) to realize 138% FBW (3.3-18GHz) with an admissible degree of port-to-port isolation ($S_{21}/S_{12} \leq -16$dB), as represented by the red curve in Figure 4.12(b, c) respectively.

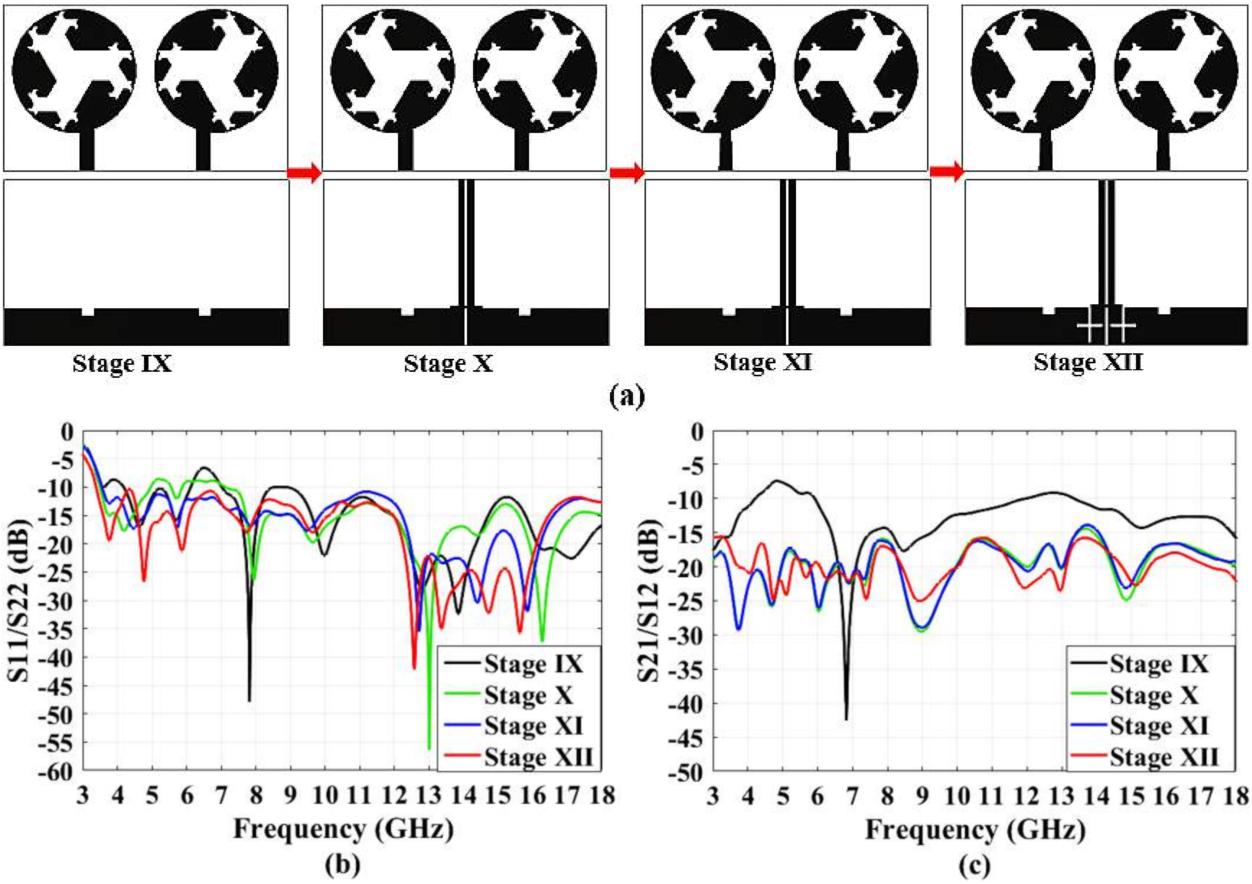

Figure 4.12 (a) Approach applied for attaining UWB behavior from the dual-element MIMO antenna (b) Respective S_{11}/S_{22}(dB) and S_{21}/S_{12}(dB) versus frequency for Stage IX-XII (c) S_{11}/S_{22} (dB) and S_{21}/S_{12}(dB) versus frequency for Stage IX-XII

(6) Finally, a quad-port MIMO antenna with four self-similar radiating elements and common ground (with 80×71mm^2 dimensions), according to a two-port array configuration (Stage XII in Figure 4.12(a)), is developed and examined in this step. Fixing the parametric dimensions of the array constant, Stage XIII (Figure 4.13(a)) is constructed by assembling the two dual-element arrays (Stage XII) in cross-configuration with a spacing (‘t2’) optimized to 2.8mm. As displayed by the green S_{11}/S_{22}/S_{33}/S_{44} (dB) curve in Figure 4.13(b), Stage XIII exhibits a dual-band functionality with FBWs of 59.6% (3.3-6.1GHz) and 91.5% (6.48-18GHz). The utilization of the space-separation approach is primarily accountable for realizing an acceptable isolation response between the antenna elements C1/C3 ($S_{31}\leq$-15.45dB) and C1/C4 ($S_{41}\leq$-17.5dB) as shown by the orange and brown curve in Figure 4.13(c) respectively. Next, to cover the lower UWB spectrum with an improved impedance match and overall port-isolation characteristics, two semi-circular rings (mirror-images of each other) are combined at the middle of the vertical decoupler (Stage XIV in Figure 4.13(a)). Thus, the designed quad-port fractal array effectively operates in 141% FBW from 3.1-18GHz (red curve in Figure 4.13(b)) while accomplishing an admissible degree of inter-port isolation ($S_{21}\leq$-17.7dB (blue line in Figure 4.13(b)), $S_{31}\leq$-16.7dB (pink line in Figure 4.13(c)) and $S_{41}\leq$-20dB (purple line in Figure 4.13(c))) for the entire operational band.

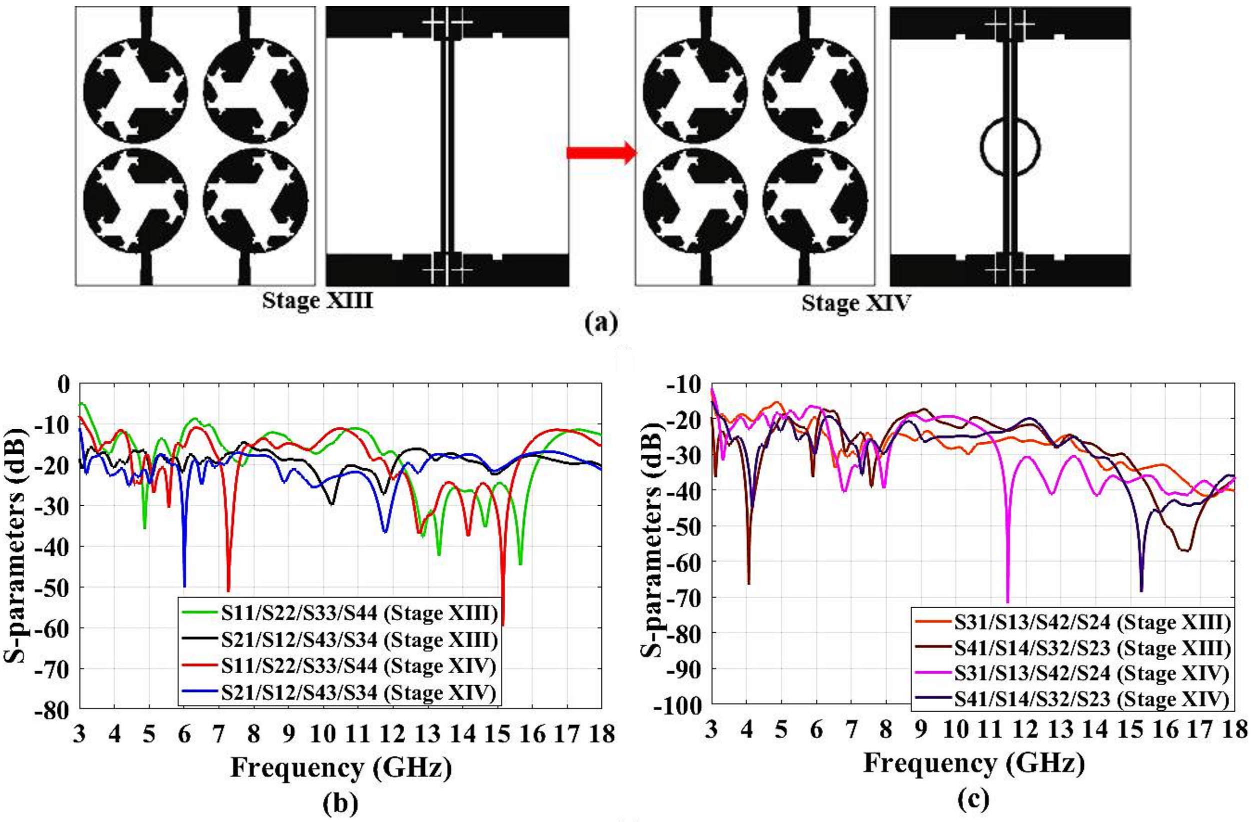

Figure 4.13 (a) Geometrical variations for achieving UWB response from the proposed quad-port antenna (b) Corresponding $S_{11}/S_{22}/S_{33}/S_{44}$(dB) and $S_{21}/S_{12}/S_{43}/S_{34}$(dB) versus frequency for Stage XIII-XIV (c) $S_{31}/S_{13}/S_{42}/S_{24}$(dB) and $S_{41}/S_{14}/S_{23}/S_{32}$(dB) versus frequency for Stage XIII-XIV

4.2.3 Simulation and Measurement Results

To practically verify the simulated array's application in a rich scattering medium, it is fabricated utilizing the photolithography method on a dielectric FR4 substrate ($\varepsilon_r = 4.4$) with 1.57 mm thickness. The fabricated four-port UWB antenna fused with four SMA connectors at the feed points is presented in Figure 4.14(a, b).

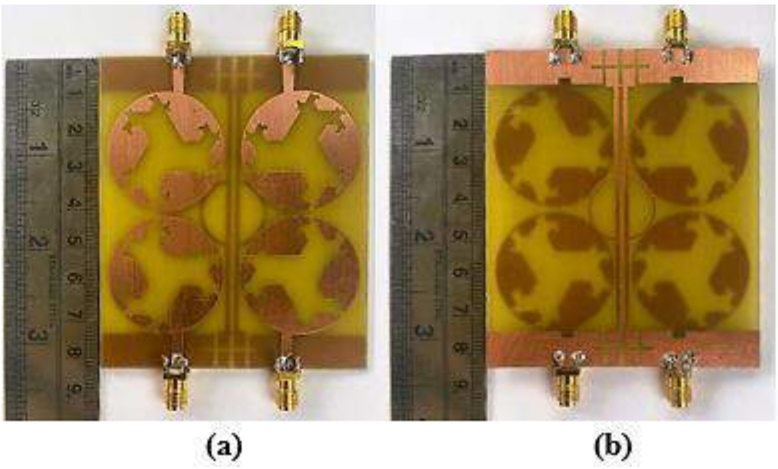
(a) (b)

Figure 4.14 (a) Top FR4 layer with four fractal radiators (b) Bottom FR4 layer showing reduced ground with DGS

4.2.3.1 Scattering Parameters and Gain Performance

The variation of software simulated and tested S-parameter (dB) results versus the operating band (GHz) for the four-port UWB antenna is illustrated in Figure 4.15(a-d). It excites FBW (simulated) of 141% in the range of 3.1-18GHz while accomplishing an acceptable port isolation characteristic ($S_{21} \leq 17.7$dB, $S_{31} \leq 16.7$dB, $S_{41} \leq 20$dB) for the entire functional band. The simulated results show a close resemblance with the experimental results where the fabricated array prototype offers FBW of 139.5% (3.21-18 GHz) while maintaining a reduced level of mutual coupling ($S_{21} \leq 16.6$ dB, $S_{31} \leq 19.17$dB, $S_{41} \leq 19.53$dB) between the actively radiating array elements.

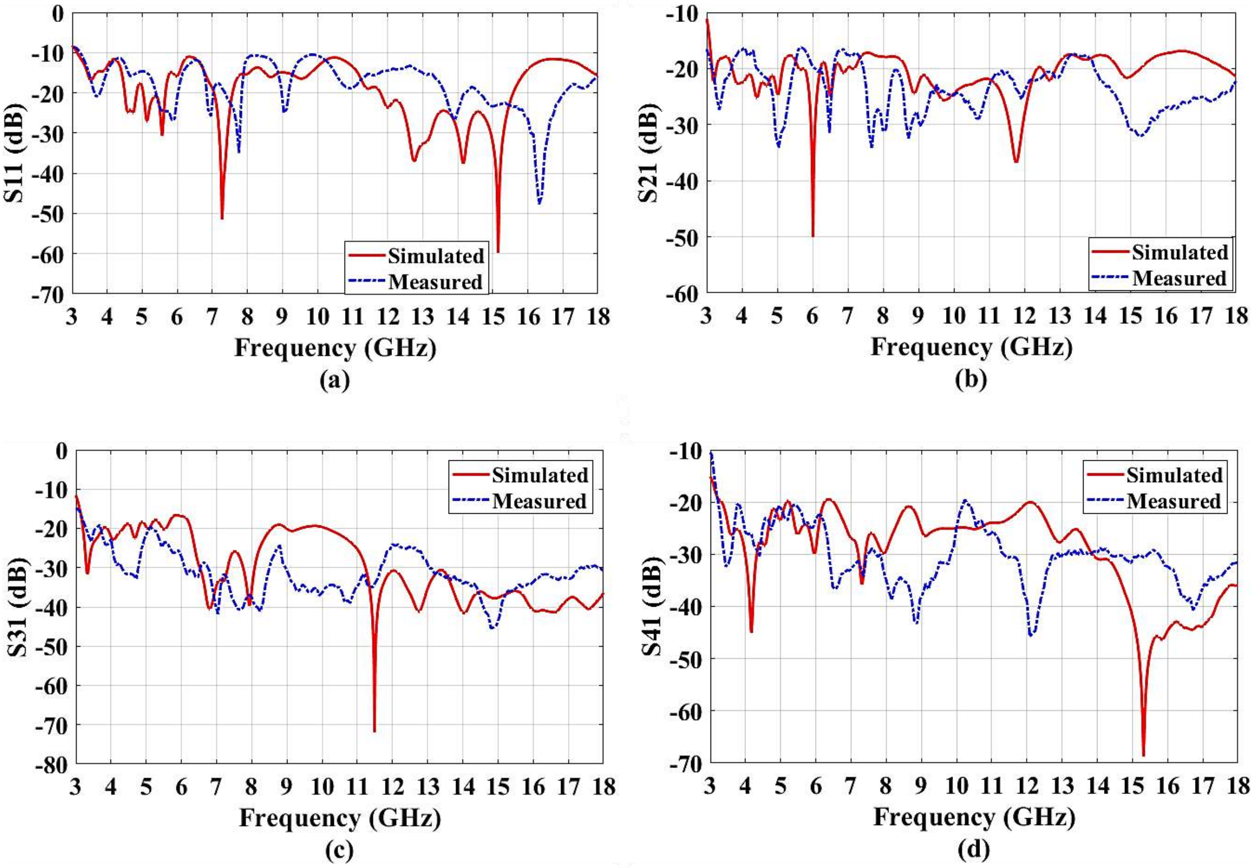

(a)

(b)

(c)

(d)

Figure 4.15 Simulated and measured (a) S_{11} (b) S_{21} (c) S_{31} (d) S_{41} against frequency of the proposed quad-port fractal UWB antenna

By activating antenna port-1, Figure 4.16 shows the gain response for the entire operational range of the designed UWB array. The primary quad-port UWB array offers a 4.14dBi average gain across the simulated functional range with 6.028dBi (at 14GHz) being the highest gain value.

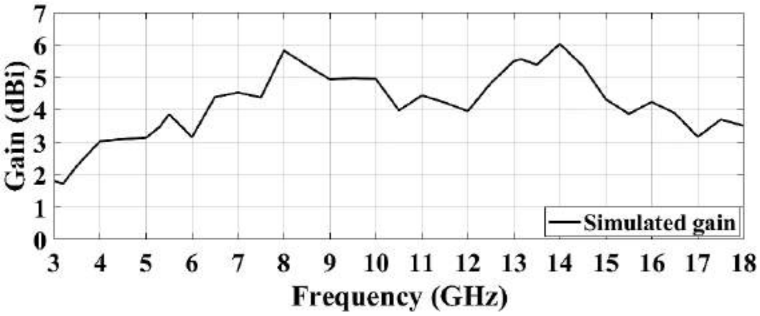

Figure 4.16 Broadband gain versus frequency plot for the complete operational range

4.2.4 Diversity Performance Metrics

In this subsection, to determine the optimal operation of the proposed array in the multipath scenario, several diversity parameters are evaluated through the simulation and measurement values of scattering parameters. The comparative plots of simulated and tested diversity parameters against frequency are depicted in Figure 4.17(a-d).

For the proposed quad-port MIMO antenna (N = 4), Equation 32 (section 4.1.5) reports the ECC between port-i and port-j using the S-parameter approach. DG is another important diversity metric estimated from the ECC using Equation 3 (given in chapter 1). For good channel characteristics, the antenna which meets the criterion of $|MEG_i - MEG_j| < 3dB$ is usually desired. For the quad-port UWB array, MEG can be estimated by the S-parameter technique according to Equation 33 (section 4.1.5). For a significant MIMO operation, CCL ≤ 0.4bits/s/Hz is needed for the complete working range. For the proposed quad-port antenna, CCL is calculated from the correlation matrix (α^R) using Equations (34, 35) (section 4.1.5).

Table 4.4 lists the simulated and experimental levels of ECC, DG, MEG, and CCL for the excited UWB spectrum. As observed, the permissible levels of various diversity metrics of the designed four-port UWB antenna verify the accomplishment of considerable diversity operation imperative for MIMO communication systems.

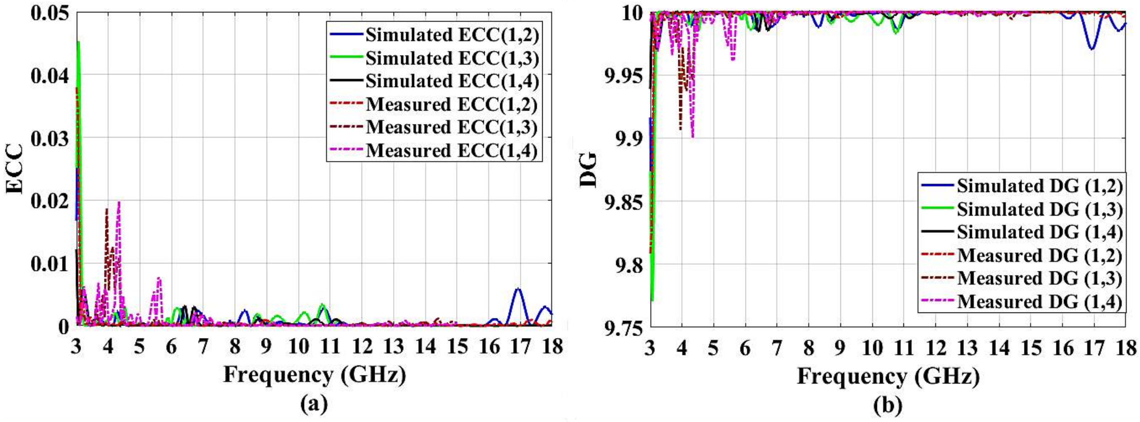

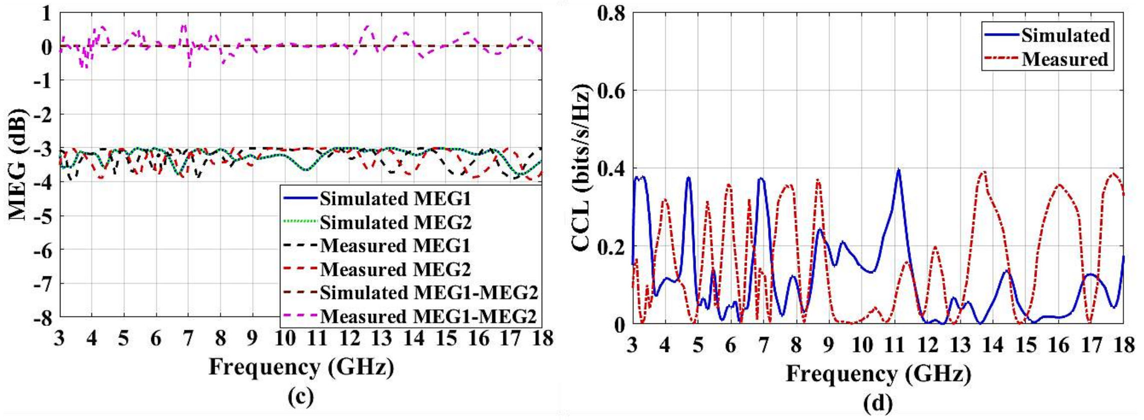

Figure 4.17 Simulated and tested (a) ECC (b) DG (c) MEG (d) CCL levels versus frequency

Table 4.4 Simulated and tested levels of diversity parameters for excited range of operation

Metrics	ECC		DG		MEG (dB)		CCL(bits/s/Hz)
Proposed UWB antenna	Sim.	Tested	Sim.	Tested	Sim.	Tested	Sim. /Tested
	≤0.006	≤0.02	≥9.969	≥9.89	≤-3.78	≤-3.975	≤ 0.4

4.3 Conclusion

This chapter successfully designs, simulates and experimentally examines the UWB characteristics from two quad-element fractal MPA arrays, thereby covering the third objective of the proposed doctoral research work. Here, two previously designed two-port fractal MIMO antennas are extended to four-port configurations to enhance the overall array performance. The first design reports a quad-port, aperture-coupled Sierpinski gasket fractal (iterated to 2nd order) antenna, incorporated with spiral-shaped DGS and offset-feeding approach to effectively resonate in 3.07-11GHz range with the FBW of 112.7%. An optimum isolation response between the antenna ports is realized by carefully selecting the center-to-center spacing between the antenna elements and truncating an X-shaped slot from the center of the ground. In the second design, a microstrip-fed, quad-port Koch Snowflake fractal (4th iteration order) MIMO antenna is effectively modeled and analyzed for UWB operation. By employing the principle of DGS and modifying the feedline geometries (tapering and offsetting), the multi-band frequency response generated by integrating fractal geometry in the proposed array design is efficiently converted into the desired UWB spectrum (3.1-18GHz). A considerable isolation behavior is accomplished by carefully optimizing the separation distance between the array elements and incorporating the decoupling network (vertical ground stubs and semi-circular rings) in the common ground plane.

For the application of the designed four-port MPA arrays in receive diversity techniques, various MIMO operation metrics are examined and are found to lie within their acceptable standards. A favorable approximation between the simulated and experimental outcomes (in terms of the operational band, isolation, and diversity metrics) affirms the realistic operability of the designed array, thus, making it a promising contender for UWB communication applications incorporating MIMO antenna technology.

CHAPTER 5

Two-Port and Four-Port Fractal UWB-MIMO Antennas with Band Notch Characteristics

After attaining the UWB behavior from the fractal antenna arrays, the next target is to effectively suppress the signal interference between the FCC's assigned UWB radio spectrum (3.1-10.6GHz) and existing undesired narrowband applications. Therefore, to overcome the negative impact of unwanted EMI, additional band-notch filtering circuits can be utilized in UWB devices, that in turn add to the system expenses, complexity, and overall dimensions [49]. In the past few years, researchers have investigated different filtering techniques such as CSRR [51], parasitic elements [56-60], slots [62-64], etc. to introduce multi-band notch capability in compact UWB arrays in the absence of extra filtering circuits.

The current chapter realizes the second objective of the proposed doctoral study. Here, the formerly designed dual-port (Pythagorean Tree and Koch Anti-Snowflake) and quad-port (Sierpinski Gasket and Koch Snowflake) fractal MPA arrays for UWB applications (in chapter 3 and chapter 4 respectively) are incorporated with the band-notch structures to reject the EMI introduced by various unwanted narrow bands (namely WiMAX, WLAN and uplink/downlink satellite bands in C-band and X-band) prevalent in the operational UWB spectrum. For validating their operability in the real-world scenario, the experimental investigation (S-parameters, radiation, and diversity performance parameters) of the fabricated antenna arrays is also conducted.

5.1 Triple Band-Stop Characteristics from a Dual-port UWB Pythagorean Tree Fractal Antenna

In the present section, the previously designed dual-port Pythagorean tree fractal array for UWB applications (Section 3.3 in chapter 3) is integrated with three different band-notch elements to reject the interference associated with space-to-earth satellite communications (C-band), WLAN, and earth-to-space satellite communications (X-band) in the excited UWB (3.7-10.64GHz) range while maintaining an acceptable inter-element isolation behaviour. A comprehensive study of diversity metrics and length optimization of band-stop structures is performed. The fabricated array is experimented with and compared with simulation responses to justify the array's functionality in a practical environment.

5.1.1 Array Geometry

The configuration and parametric values of the designed array integrated with three different notching structures are presented in Figure 5.1 (a-c). The antenna units are assembled on dual 37.5×81.5 mm^2 FR4 substrates, each with 'ε_r' and height of 4.4 and 1.57mm respectively. The 3rd iterative tree fractal patch, ground with DGS and feedline geometry along with their parametric values of the designed array for attaining UWB performance is already detailed in Section 3.3.1 (chapter 3). To combat the impact of EMI associated with narrowband applications such as downlink C-band, WLAN, and uplink X-band, each feedline of the designed UWB array is incorporated with dual L-shaped slits, a U-shaped slot, and SRRs respectively, as presented in Figure 5.1(c). Table 5.1 highlights the parametric values of the designed band-notch UWB array.

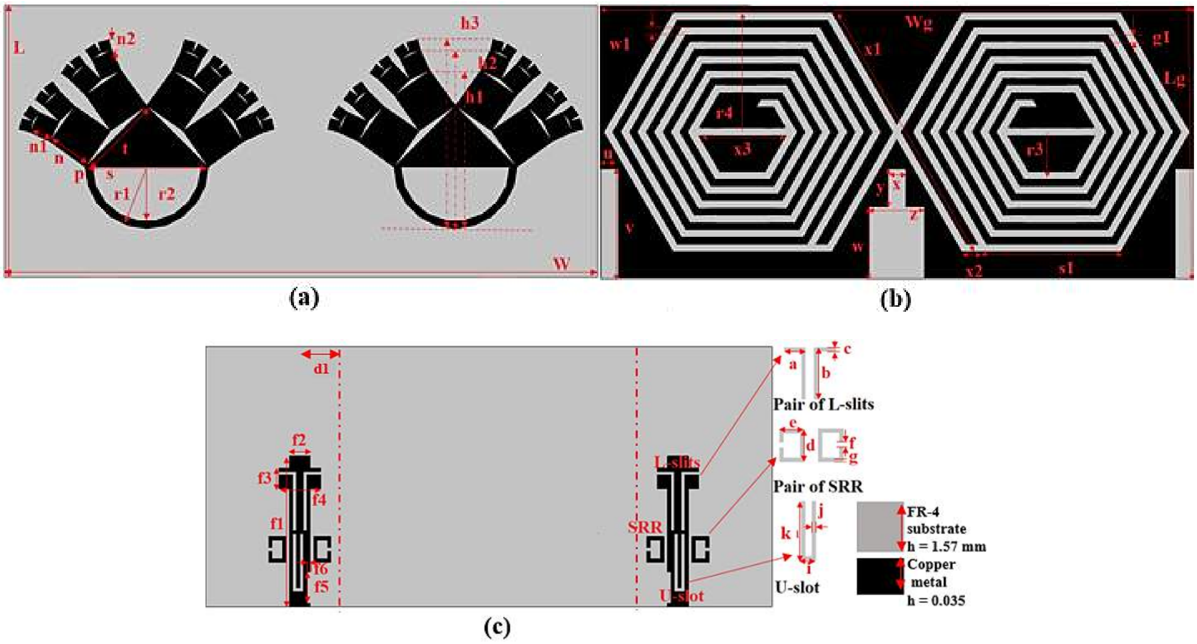
(a)

(b)

(c)

Figure 5.1 (a) Modified Pythagorean tree fractal patches (upper surface of antenna substrate) (b) Top view of the feed substrate showing a common ground defected with spiral DGS (c) Rear view of feed substrate with notched microstrip feedlines

Table 5.1 Parametric dimensions (mm) of the designed band-notch array

Parameter	L	W	s	t	r1	r2	n	n1	n2	x	y	z
Unit (mm)	37.5	81.5	16.97	12	8.485	7.485	6.0924	3.0931	1.5704	2.5	5.25	7.5
Parameter	v	w	h1	h2	h3	Lg	Wg	w1	r3	r4	g1	x1
Unit (mm)	15	9.75	21.833	24.594	26.088	37.5	81.5	1	6.5	16.5	1	36.95
Parameter	x3	s1	f1	f2	f3	f4	f5	f6	a	b	c	d
Unit (mm)	12.12	19.05	21.75	3	3	6	4.5	0.5	2.5	8.5	0.5	4.5
Parameter	f	g	j	k	i	p	u	x2	e			
Unit (mm)	0.5	0.5	0.5	8.3	1.5	45°	2.5	2.809	2.5			

5.1.2 Realization of triple band-stop operation from the designed UWB fractal array

After attaining the UWB behavior from the proposed fractal array (Section 3.3 in chapter 3), the next target is to effectively suppress the signal interference between the UWB and existing licensed wireless applications namely space-to-earth satellite communications (C-band), WLAN, and earth-to-space satellite communications (X-band). To address this problem, three different notch elements are individually embedded in each feedline of the proposed array (as depicted in Figure 5.2(a-c)) to implement the final optimized notched geometry with three notch elements altogether (Figure 5.2(d)) while keeping the patch and ground configuration fixed. For the sake of simplicity, the width of each notching element is kept fixed at 0.5 mm (‘c’ = ‘g’ = ‘j’). By selecting the position and length of three notching elements appropriately, the desired stop-band frequency can be realized proficiently. The simulated S_{11}/S_{22} (dB) results versus frequency for the respective notch geometries are shown in Figure 5.3.

As presented in Figure 5.2(a), two symmetrical L-shaped slits are removed from the upper edge of each feedline of the proposed fractal array to obtain the stop-band corresponding to downlink satellite communication in C-band at 3.95 GHz ($f_{notch-1}$). In this case, the overall length of each slit ($L_{L\text{-}slit}$) is one-quarter of the guided wavelength (λ_g) and is approximated using Equation 38.

$$L_{L-slit} = a + b = \frac{\lambda_g}{4} = \frac{\lambda_o}{4\sqrt{\varepsilon_{eff}}} = \frac{c_o}{4f_{notch-1}}\sqrt{\frac{2}{\varepsilon_r+1}} \tag{38}$$

where λ_o is the free-space wavelength. The pink-colored curve in Figure 5.3 (for Figure 5.2(a)) shows the rejection of undesired C-band (for downlink satellites) from 3.9-4.19GHz.

The band suppression characteristic corresponding to the licensed WLAN band is realized by eliminating a U-shaped slot from the lower edge of each feedline of the proposed fractal array (as shown in Figure 5.2(b)). Each U-shaped slot is half-wavelength long ($\lambda_g/2$) and its length ($L_{U\text{-}slot}$) is determined according to Equation 39 for the rejection frequency ($f_{notch-2}$) of 5.5 GHz.

$$L_{U-slot} = \frac{\lambda_g}{2} = \frac{\lambda_o}{2\sqrt{\varepsilon_{eff}}} = 2k + i = \frac{c_o}{2f_{notch-2}}\sqrt{\frac{2}{\varepsilon_r+1}} \tag{39}$$

As depicted in Figure 5.3 (green curve), the proposed band-notch configuration (Figure 5.2(b)) filters out the WLAN (5.3-5.95GHz) band from the operational UWB spectrum.

To mitigate the impact of EM interference resulting from the satellite communications in the X-band (uplink), a pair of rectangular SRRs are symmetrically positioned around each feedline of the proposed fractal array (as presented in Figure 5.2(c)). For achieving a band-notch at 8.15 GHz ($f_{notch-3}$), the length (L_{SRR}) of rectangular SRR ($\lambda_g/2$) is computed according to Equation 40.

$$L_{SRR} = \frac{\lambda_g}{2} = \frac{\lambda_o}{2\sqrt{\varepsilon_{eff}}} = 2e + (2d - f) = \frac{c_o}{2f_{notch-3}}\sqrt{\frac{2}{\varepsilon_r+1}} \tag{40}$$

As seen in Figure 5.3 (blue curve), the proposed fractal array integrated with two rectangular SRRs effectively rejects the interfering X-band (uplink) in the range of 7.83-8.24 GHz.

Figure 5.2(d) demonstrates the optimized design of the proposed fractal array with three band-stop resonators. For the proposed fractal array, the notching elements namely dual L-shaped slits, a U-shaped slot, and rectangular SRRs effectively resonate at 3.98 GHz ($f_{notch-1}$), 5.47 GHz ($f_{notch-2}$), and 8.03 GHz ($f_{notch-3}$) respectively (red curve in Figure 5.3). Table 5.2 lists the comparison between the mathematically computed and simulated dimensions for three notch structures.

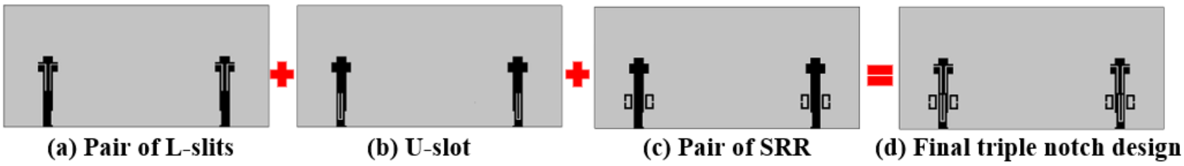
(a) Pair of L-slits (b) U-slot (c) Pair of SRR (d) Final triple notch design

Figure 5.2 Evolution process for designing a final optimized triple band-stop fractal array

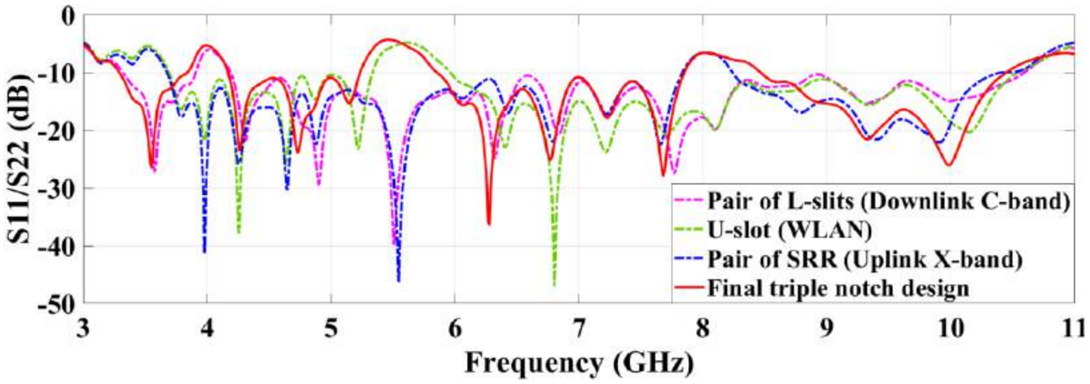

Figure 5.3 Variation of simulated return loss (S_{11}/S_{22} (dB)) performances versus frequency for three individual band-stop elements of the proposed fractal array

Table 5.2 Mathematically computed and simulated length of three individual band-stop elements

Length ↓/Band-stop→	C-band (downlink)	WLAN	X-band (uplink)
Computed (mm)	11.6	16.6	11.2
Simulated (mm)	11	18.1	13.5
Error	-0.05	0.08	0.17

5.1.3 Parametric Optimization of the rejection bands and Surface current distribution

All band-notch designs examined under Section 5.1.2 are integrated to model the optimized UWB-MIMO antenna with triple-band suppression capability. In this section, optimization of each band-notch design is performed individually, by modifying the value of a single parameter at a time with other parametric values remaining constant. Figure 5.4(a-c) demonstrates the simulated S_{11}/S_{22} (dB) response of the proposed fractal array for different values of 'b' (length of L-slits), 'k' (length of U-slot) and 'f' (a gap between the SRRs) respectively, while their respective widths ('c', 'g' and 'j') are fixed at 0.5 mm.

As the length of each L-slits ('b' from 8.5 mm to 8.8 mm) and U-slot ('k' from 7.7 mm to 8.3 mm) increases, the overall length of each L-slit ($L_{L\text{-slit}}$) and U-slot ($L_{U\text{-slot}}$) for the downlink C-band and WLAN interfering band respectively, also increases. Due to this, the operating bandwidth of the respective stopband shows a transition from high to low-frequency end (as illustrated in Figure 5.4(a, b)). For the uplink X-band rejection, an increase in the gap between the SRRs ('f' from 0.5 mm to 0.9 mm) decreases the overall length of each rectangular SRR (L_{SRR} from 13.5 mm to 12.6 mm). As a result, rectangular SRR of a shorter length shifts the central notch frequency for the uplink X-band towards the higher frequency side (as shown in Figure 5.4(c)). This inverse relation between the stop-band resonance and the overall notch length can also be verified by Equation (38-40). The optimum stopband performance of the proposed fractal array is observed for 'b', 'k', and 'f' equal to 8.5mm, 8.3mm, and 0.5mm respectively. Therefore, it is inferred that the desired operating band and resonant frequency for a rejection band can be controlled by correctly adjusting the parametric values and position of the respective band-notch structures. Observations also indicate that change in the total notch length of each rejection band have negligible influence on the other stop bands. Hence, all rejection bands are mutually independent of each other.

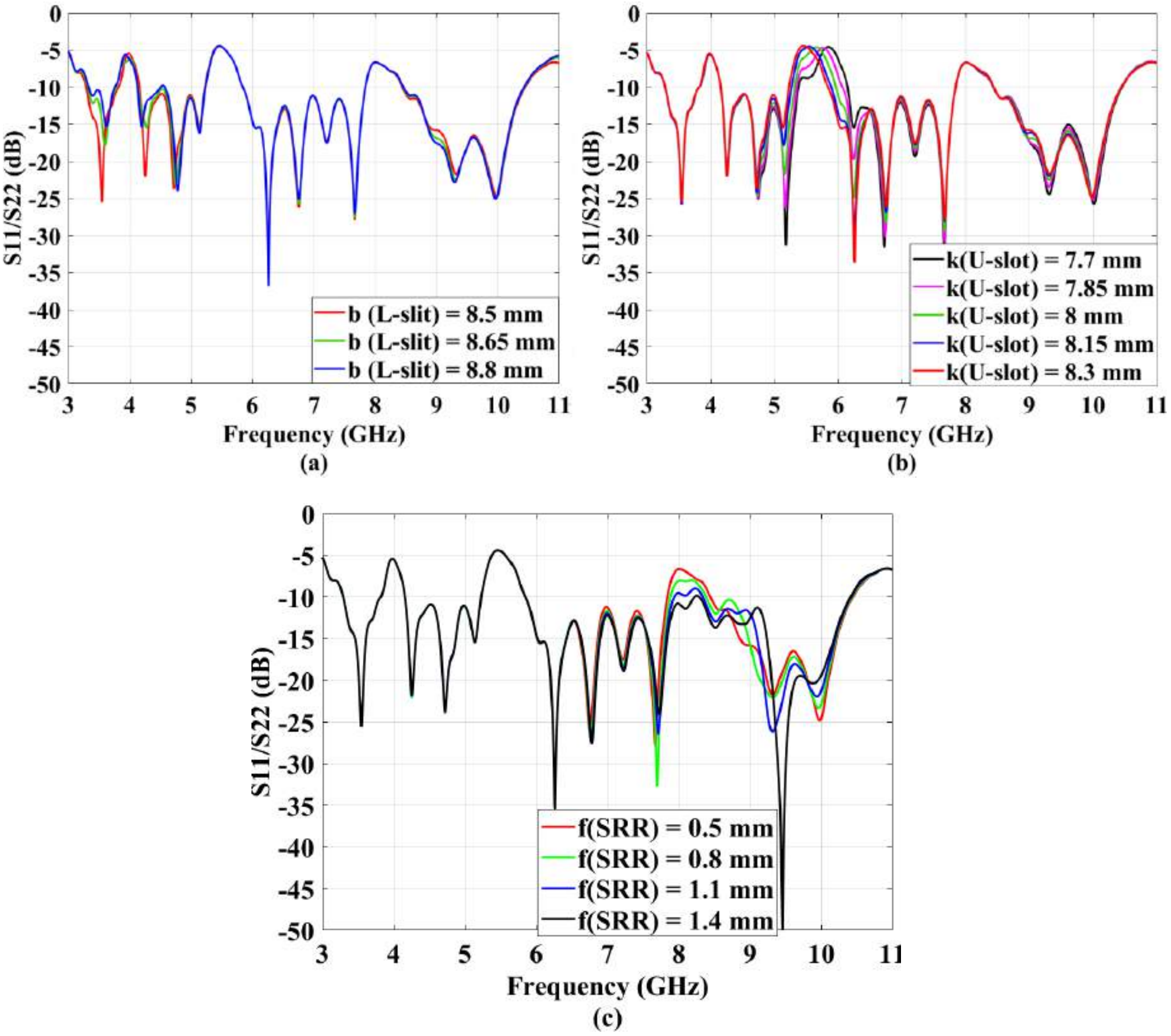

Figure 5.4 S_{11}/S_{22} (dB) characteristics against frequency for various values of (a) ‘b’ for L-slits (b) ‘k’ for U-slot (c) ‘f’ for SRR pair

To further examine the band rejection mechanism of the proposed fractal array, the current density distribution (A/m) is observed at the back surface of the lower FR4 substrate (feedlines) at the simulated stopband frequencies of 3.98 GHz (for downlink C-band), 5.47 GHz (for WLAN) and 8.03 GHz (for uplink X-band). On energizing port-1 with a simulated IW power, Figure 5.5(a-c) depicts a strong concentration of current around the edges of pair of L-slits (268.402 A/m), U-slot (456.07 A/m) and SRR pair (246.418 A/m) at 3.98GHz, 5.47GHz and 8.03GHz stopband frequencies respectively. Therefore, a large amount of energy is mainly stored in the notching elements which introduces a high impedance mismatching resulting in non-radiation of signals at the desired stopband frequencies.

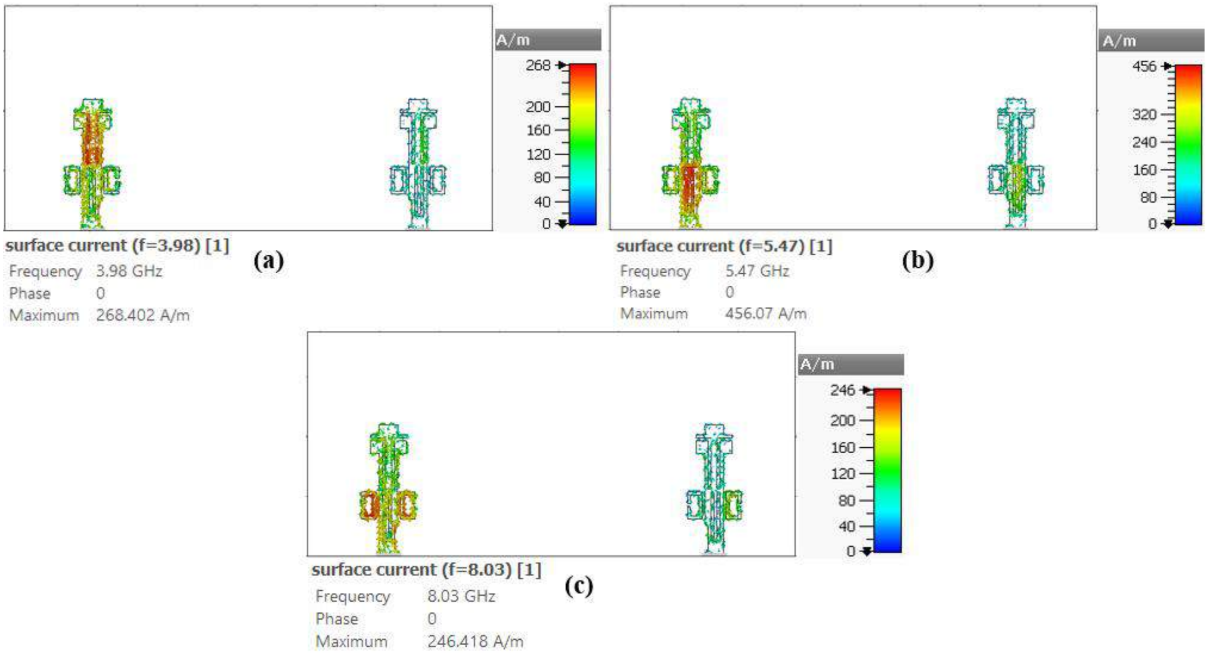

Figure 5.5 Distribution of current on the surface of feedlines at (a) 3.98GHz (b) 5.47GHz (c) 8.03GHz stopband frequencies for port-1 excitation

5.1.4 Simulated and Tested Responses

For ensuring the band-stop capability of the designed array, Figure 5.6(a-d) displays the fabricated snapshots of the modified Pythagorean tree fractal radiators (top view of the first substrate), ground with spiral DGS (top view of the second FR-4 substrate), a pair of 50 Ω notched feedlines (rear view of the second substrate) and 3D layout respectively. The proposed fractal array is fused with two 50 Ω SMA connectors at the feed points for energizing the fractal patches.

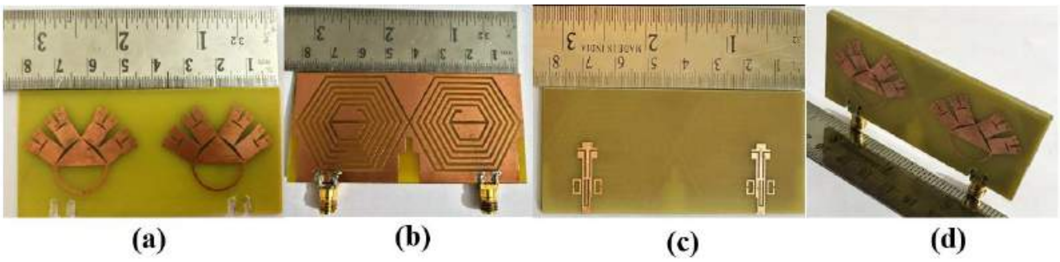

Figure 5.6 (a-d) Fabricated photographs of the proposed UWB array with band-notches

5.1.4.1 S-parameter Results

To practically verify the capability of the designed UWB array to eliminate the intrusion resulting from downlink satellite communication in C-band, WLAN, and uplink satellite communication in X-band, the fabricated notched UWB array is tested for S-parameters using VNA. The comparison between the simulated and tested S-parameter responses is plotted against frequency in Figure 5.7(a, b). It depicts that the proposed UWB fractal array is effective in suppressing the three interfering frequency bands (downlink satellite communication in C-band: 3.81-4.16GHz, WLAN: 5.22-5.84GHz and uplink satellite communication in X-band:

7.84-8.44GHz) coexisting in the excited bandwidth of operation (simulated: 3.7-10.64GHz, measured: 3.495-11.73GHz) while maintaining a good degree of isolation (simulated: $S_{21}/S_{12} \leq -16.1$dB, measured: $S_{21}/S_{12} \leq -15.4$dB) between the two ports of the proposed array. Table 5.3 highlights the comparison between the simulated and tested results of the designed UWB array at the three interfering bands in terms of rejected bandwidth and central stop-band frequency. A slight divergence between the results obtained from simulation and experimental measurement is observed. These variations are due to the antenna testing process in a normal laboratory setup (with numerous reflecting objects), inaccurate copper etching, misalignment of antenna layers, and faulty soldering of connectors.

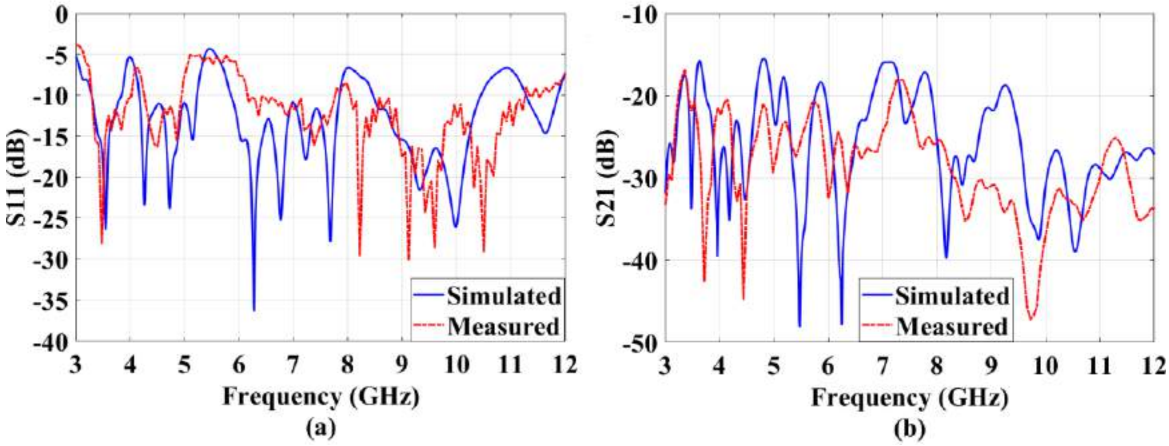

Figure 5.7 Variation of simulated and tested (a) S_{11} (b) S_{21} versus frequency for the designed UWB notched fractal array

Table 5.3 Simulation and experimental results of the designed fractal array at the rejected bands

Characteristics/Notched bands	Satellite communication in C-band (downlink)	WLAN	Satellite communication in X-band (uplink)
Assigned frequency band (GHz)	3.7-4.2	5.15-5.85	7.9-8.4
Simulated frequency band (GHz)	3.81-4.16	5.22-5.84	7.84-8.44
Measured frequency band (GHz)	4.02-4.26	4.95-6.13	7.74-8.04
Theoretical band-stop frequency (GHz)	3.95	5.5	8.15
Simulated band-stop frequency (GHz)	3.98	5.47	8.03
Measured band-stop frequency (GHz)	4.08	5.1	7.98

5.1.4.2 Radiation Performance

According to the Figure 5.8(a-c), the simulation and experimental two-dimensional (2D) radiation plots of the designed UWB notched fractal array is investigated along two principal planes: E-plane and H-plane at the passband resoanances of 4.72GHz, 6.26GHz, and 9.97GHz respectively. At all three resonances, the proposed array offers a directional and quasi-omnidirectional polar response in the y-z plane and x-z plane correspondingly. A considerable resemblance is realized between the simulated as well as experimental far-field patterns with few disparities arising as a result of the potential reflections from port-2, connector leakages, and feed cable implications. For the triggered port-1, the gain values for the excited bandwidth for the designed UWB array with and without the rejection bands are represented in Figure 5.9. The designed UWB array (without rejection bands) provides a peak simulated gain of 4.04 dBi at 9.5 GHz. For the notched UWB array, a sharp reduction in gain is observed at the three stop-band frequencies which verifies the negligible radiation and non-responsive behavior of the designed MIMO antenna in the respective rejection bands (downlink C-band, WLAN, and uplink X-band). The simulation and experimental gain values for the designed UWB array (with rejection bands) vary in the range from -5.29 to 4.04dBi and -4.79 to 4.3dBi respectively for the complete operational range. Simulated gain values show a good similitude with the experimental results.

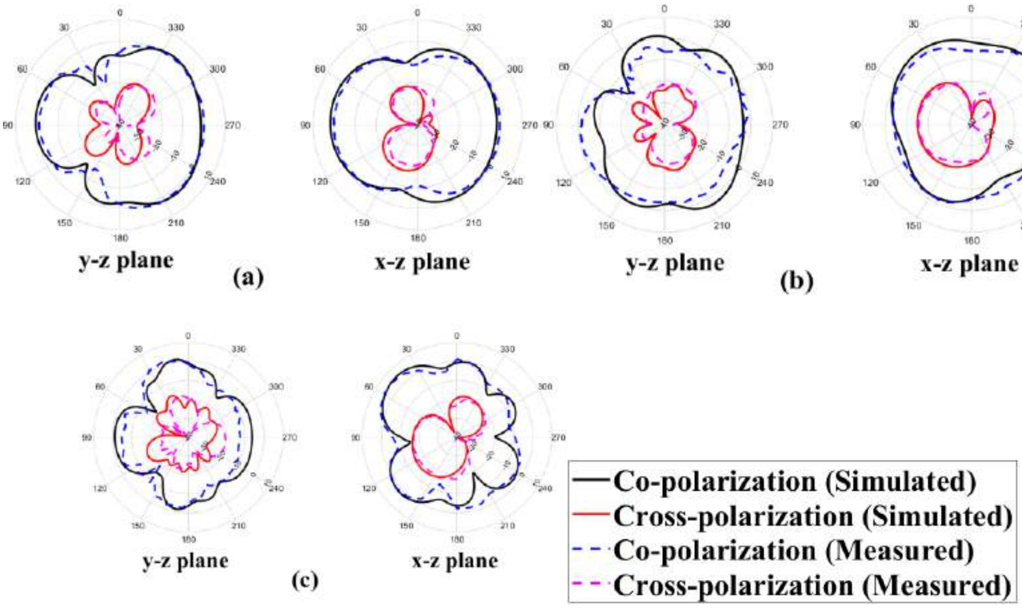

Figure 5.8 Simulated and tested 2D far-field patterns (with activated port-1) in y-z plane and x-z plane at (a) 4.72GHz (b) 6.26GHz (c) 9.97GHz

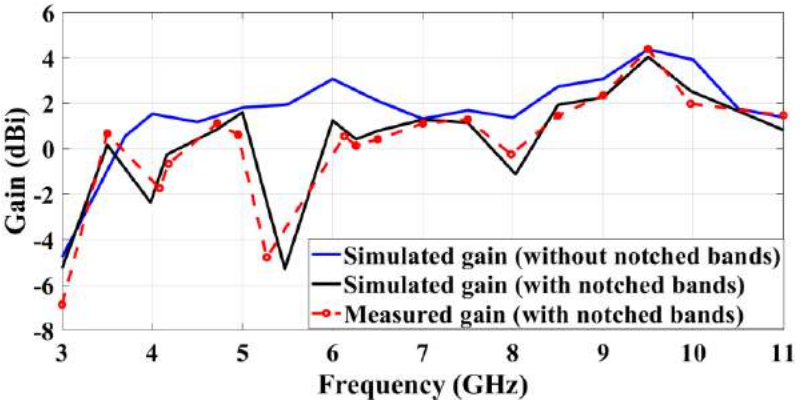

Figure 5.9 Simulated and experimental gain versus frequency for the excited port-1

5.1.5 Diversity performance metrics

In this subsection, the proposed UWB notched array is examined for some important diversity parameters for its operation in a rich scattering environment.

Figure 5.10(a) depicts the variation of ECC values versus frequency for the designed UWB array with three notches by using Equation 2 (chapter 1). An ECC level ≤ 0.0084 (simulated) and ≤ 0.0095 (measured) is obtained for the complete working band including the notch ranges.

In a MIMO system, DG specifies the increment in signal quality (at the receiving end) due to the implementation of some diversity combining scheme and is estimated through Equation 3 (chapter 1). Figure 5.10(b) presents the DG level ≥ 9.957 (simulation) and ≥ 9.952 (experimental) across the whole working range including the rejection ranges for the proposed UWB notched array.

According to Figure 5.10(c), both simulated and measured MEG (calculated using Equation (4, 5) in chapter 1) for the proposed UWB array with rejection bands are close to -3dB for the complete functional range except at the three interfering bands. The simulated $|\text{MEG}_1\text{-MEG}_2|$ = 0dB and tested -2.62dB < $|\text{MEG}_1\text{-MEG}_2|$ < 2.33dB is realized which justifies a good diversity operation of the designed array.

As depicted in Figure 5.10 (d), the simulation and measurement CCL values (calculated using Equation 7 in chapter 1) for the designed UWB array with notched bands is ≤ 0.4 bits/s/Hz (excluding the rejection ranges)

The TARC value (calculated using Equation 8 in chapter 1) of < -4.4 dB (simulated/tested) is realized for entire functional range for the designed UWB array with rejection bands as presented in Figure 5.10 (e) respectively, which is essential for efficient MIMO antenna.

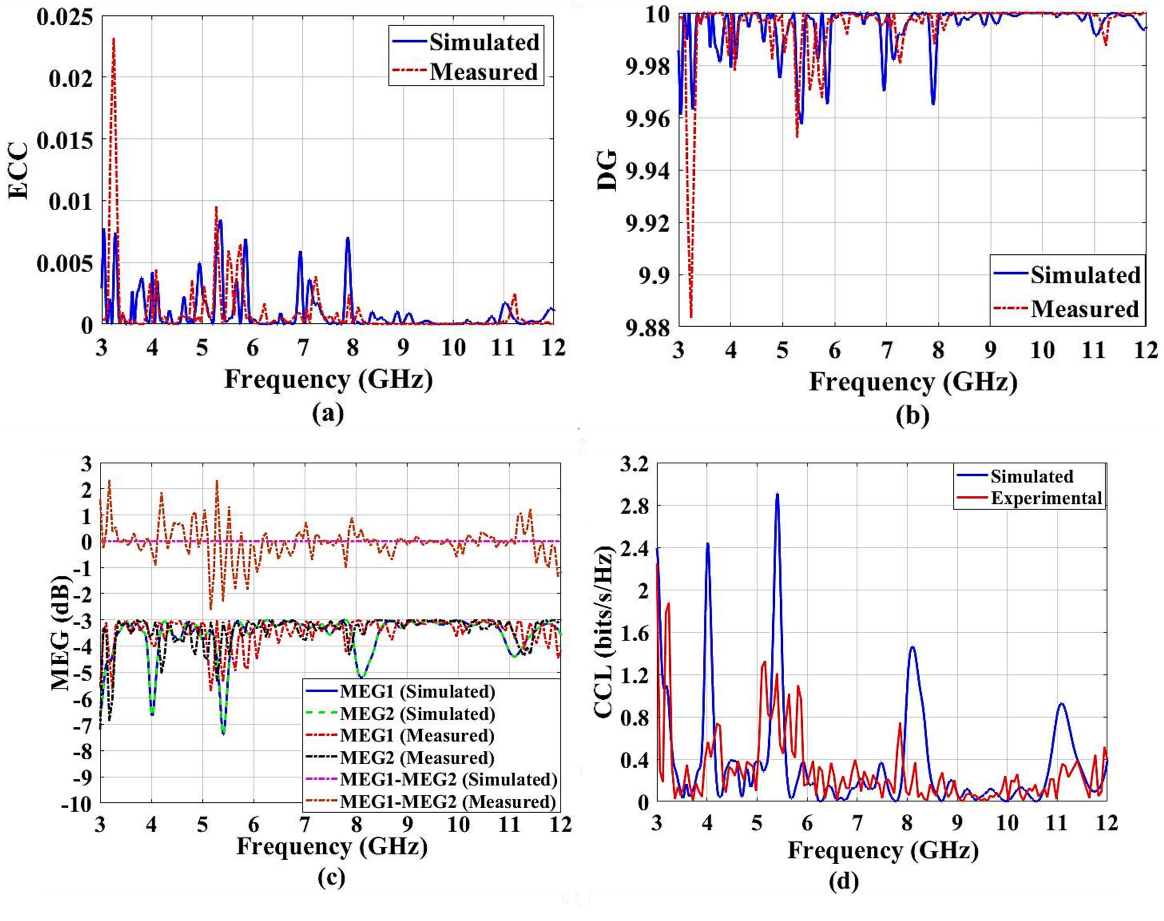

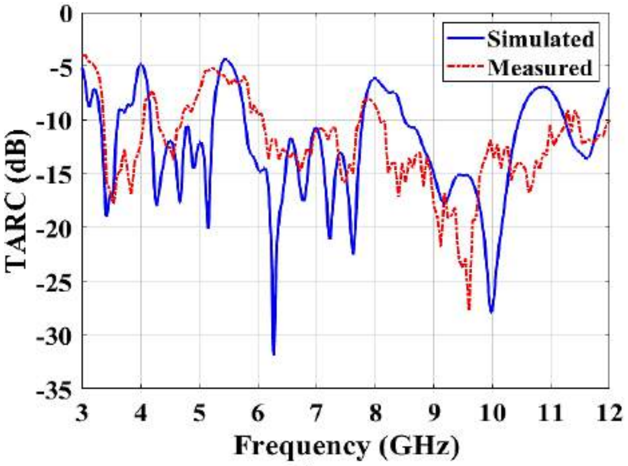

(e)

Figure 5.10 Simulation and experimental (a) ECC (b) DG (c) MEG (d) CCL (e) TARC (dB) values against frequency for the designed UWB array with rejection bands

The following section of this chapter accomplishes the rejection of six interfering bands from the formerly designed UWB Koch Anti-Snowflake fractal array.

5.2 Sextuple Band-Stop Characteristics from a Dual-port Koch Anti-Snowflake Fractal UWB Antenna

In this section, the formerly modeled UWB Koch Anti-Snowflake fractal (3rd iteration order) antenna (Section 3.6 in chapter 3) is employed to filter out six interfering narrow bands from an excited operational band (2.48-15.42GHz) with an optimum isolation performance. The proposed UWB array is incorporated with six different band-stop elements for realizing the stop-band functionality at WiMAX, INSAT (reception), WLAN, super-extended C-band, ITU-8, and amateur radio bands. A detailed parametric analysis is done to better understand the effect of dimensional variations of these band notch structures on the specific rejection bands. The array's design and simulation is accomplished using a time-domain solver of CST version 18 software. For validating the array's practical operation, the fabricated array is experimented with and compared with simulation results.

5.2.1 Array Layout

The structural arrangement of proposed array with modified Koch Anti-Snowflake fractal radiators and reduced ground with DGS (dimensions 29.5×43.5mm^2) is illustrated in Figure 5.11 (a-d). The structure of the microstrip-fed, 3rd iterative fractal patches and ground with DGS of the proposed fractal array for attaining UWB performance is already reported in Section 3.6.1 (chapter 1). Additionally, to suppress the EMI associated with WiMAX and INSAT applications, the upper portion of each semi-circular fractal radiator is defected with two $\lambda_g/4$ (λ_g is the guided wavelength) notching elements namely a Z-shaped and inverted L-shaped slits respectively (as shown in Figure 5.11(a)). To obtain notches for super-extended C-band and ITU-8 applications, two $\lambda_g/2$ rectangular SRR pairs are arranged (as parasitic elements) near the upper and lower junction of each feedline respectively. A $\lambda_g/2$ G-shaped slot is truncated from the center of each feedline to overcome the intrusion resulting from the amateur radio band. As demonstrated in Figure 5.11(c), two L-shaped slits (mirror images) are removed from the two corners of the reduced ground to suppress the interfering WLAN band across the functional UWB range. According to Figure 5.11(d), the designed array is arranged in the x-y plane with its thickness in the z-plane. Table 5.4 lists the final parametric values (mm) of each band-notch element of the designed array.

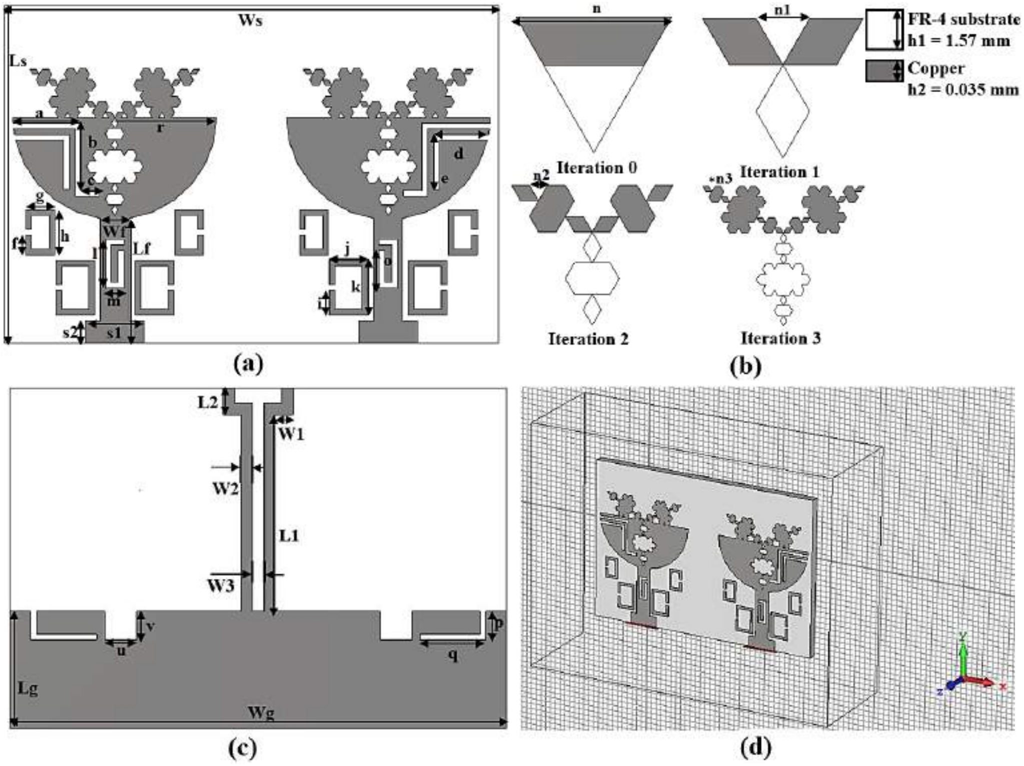

Figure 5.11 (a) Koch Anti-snowflake fractal radiators with five notching elements (b) expanded fractal view (c) partial ground with DGS (d) 3D geometry

Table 5.4 Parametric dimensions (mm) of the proposed band-notch fractal UWB array

Parameters	Ls	Ws	r	Lf	Wf	s1	s2	a	b	c
Values (mm)	29.5	43.5	9	11	2.6	5.2	2	5.98	5.96	1.6
Parameters	d	e	f	g	h	i	j	k	l	m
Values (mm)	4.87	4.86	1.73	2.55	3.97	2.15	3.4	4.8	4.3	1.6
Parameters	o	p	q	n	n1	n2	n3	Lg	Wg	u
Values (mm)	3.3	2.5	5.8	15	5	1.667	0.556	10.3	43.5	2.8
Parameters	v	L1	L2	W1	W2	W3				
Values (mm)	2.5	17.26	2.34	1.59	1	1				

5.2.2 Realization of Band-Notch Performance from the Proposed UWB Fractal Array

On achieving the UWB of operation from the proposed fractal array with DGS, the next objective is to combat the severe EMI caused by several narrow frequency bands that fall within the UWB range. Therefore, various notch structures are embedded individually in fractal patches (Z-shaped slit, upturned L-shaped slit), ground plane (L-shaped slit), and feedlines (parasitic SRR, G-shaped slot) of the proposed array design (as illustrated in Figure 5.12(a-f)) to realize the final sextuple stop-band configuration as demonstrated in Figure 5.12(g). For easy implementation, the width of each notch geometry is fixed at 0.5 mm. The adequate choice of length and position of each notch structure aids in effectively eliminating the desired interfering frequency band. Figure 5.13(a-f) presents the simulated S_{11}/S_{22} results for different notch geometries incorporated in the proposed array across the complete range of operation. According to Figure 5.12(a, b), the stop-band functionality corresponding to WiMAX and INSAT (reception) frequency bands is accomplished by removing an unsymmetrical Z-shaped and inverted L-shaped slit from the upper edge of each fractal radiator respectively. As illustrated in Figure 5.12(c), to filter out the interfering WLAN band from the operational range, two L-shaped slits (mirror images) are clipped off from the two corners of the reduced ground geometry respectively. The overall length of each $\lambda_g/4$ slit for the required rejection frequency is approximately evaluated using Equation 41.

$$L_i = \frac{\lambda_g}{4} = \frac{\lambda_o}{4\sqrt{\varepsilon_{eff}}} = \frac{c_o}{4f_{notch-i}}\sqrt{\frac{2}{\varepsilon_r+1}} \tag{41}$$

where λ_o is the wavelength of free space, ε_r is the dielectric constant, c_o is the speed of light, L_i is the length of the slit ($L_1 = a + b + c$ for Z-shaped slit, $L_2 = d + e$ for inverted L-shaped slit and $L_3 = p + q$ for L-shaped slit) for a particular notch frequency ($f_{notch-i}$) where i=1, 2, 3. Figure 5.13(a-c) depicts the elimination of undesired WiMAX (3.3-3.92 GHz), INSAT (4.22-5.06 GHz), and WLAN (4.89-5.81 GHz) bands respectively from the excited band of operation.

As presented in Figure 5.12(d, e), to counter the impact of EMI associated with super-extended C-band and ITU-8 applications, two rectangular SRR pairs are symmetrically arranged near the lower and upper junction of each feedline respectively. Further, a G-shaped slot is trimmed from the middle of each feedline (as shown in Figure 5.12(f)) to get rid of unwanted amateur-radio band co-existing in the functional UWB range. The total effective length of SRRs and G-shaped slot for obtaining the desired notch frequency is approximately computed using Equation 42.

$$L_i = \frac{\lambda_g}{2} = \frac{\lambda_o}{2\sqrt{\varepsilon_{eff}}} = \frac{c_o}{2f_{notch-i}}\sqrt{\frac{2}{\varepsilon_r+1}} \tag{42}$$

where L_i is the length of a resonator ($L_4 = 2j + k + 2i$ for SRR1, $L_5 = 2f + 2g + h$ for SRR2, and $L_6 = l + 2m + o$ for G-shaped slot) for a particular notch frequency ($f_{notch-j}$) where i = 4, 5, 6. Figure 5.13(d-f) shows the individual notches for super-extended C-band (6.34-6.98 GHz), ITU-8 (7.78-8.73 GHz), and amateur radio (9.95-11.18 GHz) band respectively.

Figure 5.12(g), therefore, presents the optimized UWB array integrated with all six notching elements. For the designed band-reject UWB array, the six notch geometries namely a Z-shaped slit, inverted L-shaped slit, pair of L-shaped slits, two rectangular SRR pairs, and G-shaped slot effectually resonates at 3.46 GHz ($f_{notch-1}$), 4.78 GHz ($f_{notch-2}$), 5.55 GHz ($f_{notch-3}$), 6.57 GHz ($f_{notch-4}$), 8.23 GHz ($f_{notch-5}$) and 10.22 GHz ($f_{notch-6}$) frequencies respectively (as presented in Figure 5.13(g)). Table 5.5 presents the computed and optimized lengths of each stop-band geometry.

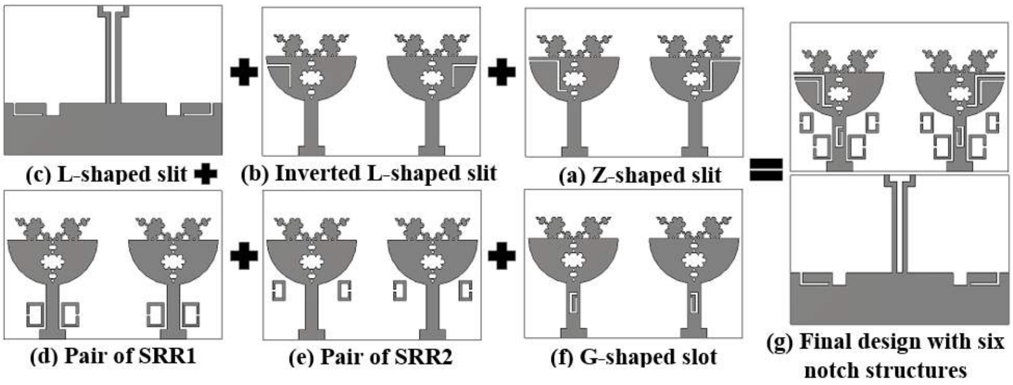

Figure 5.12 Methodology for realizing sextuple band-stop operation from the proposed UWB array

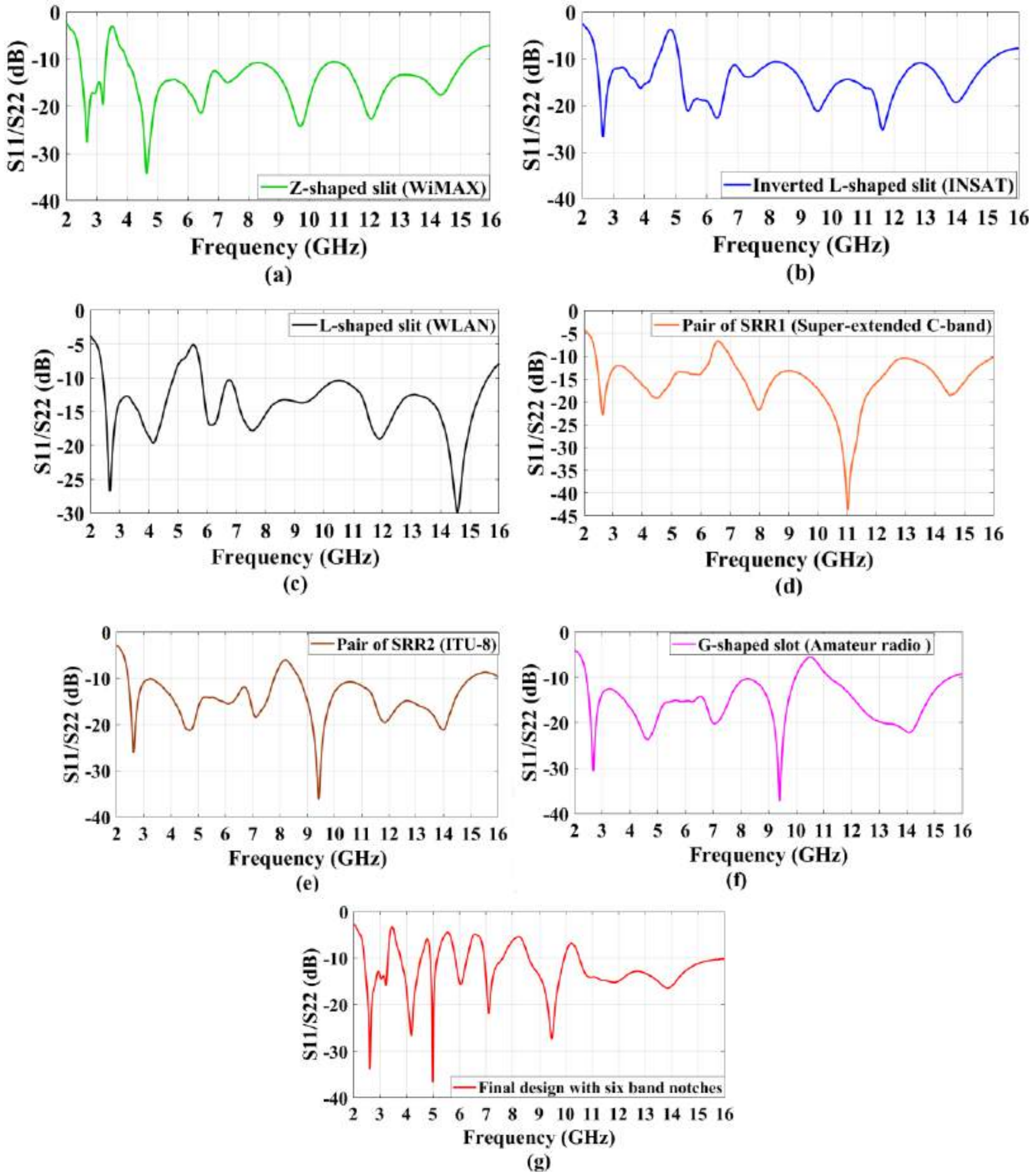

Figure 5.13 Simulated S_{11}/S_{22} (dB) performance versus frequency for the (a-f) individual six band-notch geometries and (g) final band-notch design of the proposed UWB array

Table 5.5 Computed and simulated values (mm) of lengths for each band notch geometry

Band-notch/ Length	WiMAX	INSAT	WLAN	C-band (super-extended)	ITU-8	Amateur radio band
Computation using the design equation	13.04	9.82	8.3	13.88	11.13	8.91
Simulation	13.54	9.73	8.25	15.9	12.5	10.8
Error	0.03	-0.009	-0.006	0.12	0.1	0.17

5.2.3 Length optimization of band-reject structures and surface current analysis

As already mentioned, for eliminating the interference caused by narrow frequency bands, UWB antennas are integrated with stop-band functionality. In addition to this feature, several advanced communication devices also demand independent operation of each rejection band. Equation (41, 42) illustrates that the required rejection resonance is varied by modifying the total length of the corresponding resonator. Therefore, Figure 5.14(a-f) presents the length optimization of each notch geometry (carried out individually) by altering the parameters namely ‘c’ (Z-shaped slit), ‘e’ (inverted L-shaped slit), ‘q’ (L-shaped slits), ‘j’ (rectangular SRR1), ‘g’ (rectangular SRR1) and ‘o’ (G-shaped slot) respectively, whereas the other design parameters are maintained constant. Observations prove that by increasing the values of parameters namely ‘c’ (from 1.3-1.9 mm), ‘e’ (from 4.66-5.06 mm), ‘q’ (from 5.6-6 mm), ‘j’ (from 3.3-3.5 mm), ‘g’ (from 2.45-2.65 mm) and ‘o’ (from 3.1-3.5 mm), the respective center rejection frequency shifts from the higher to the lower frequency side while the remaining stop-bands are approximately unaffected. The proposed fractal array exhibits an optimal notch behavior at ‘c’, ‘e’, ‘q’, ‘j’, ‘g’, and ‘o’ equal to 1.6mm, 4.86mm, 5.8mm, 3.4mm, 2.55mm, and 3.3mm respectively. Hence, as per the demand, the desired transition in the rejection band can be easily realized while retaining an optimum UWB behavior from the proposed fractal array.

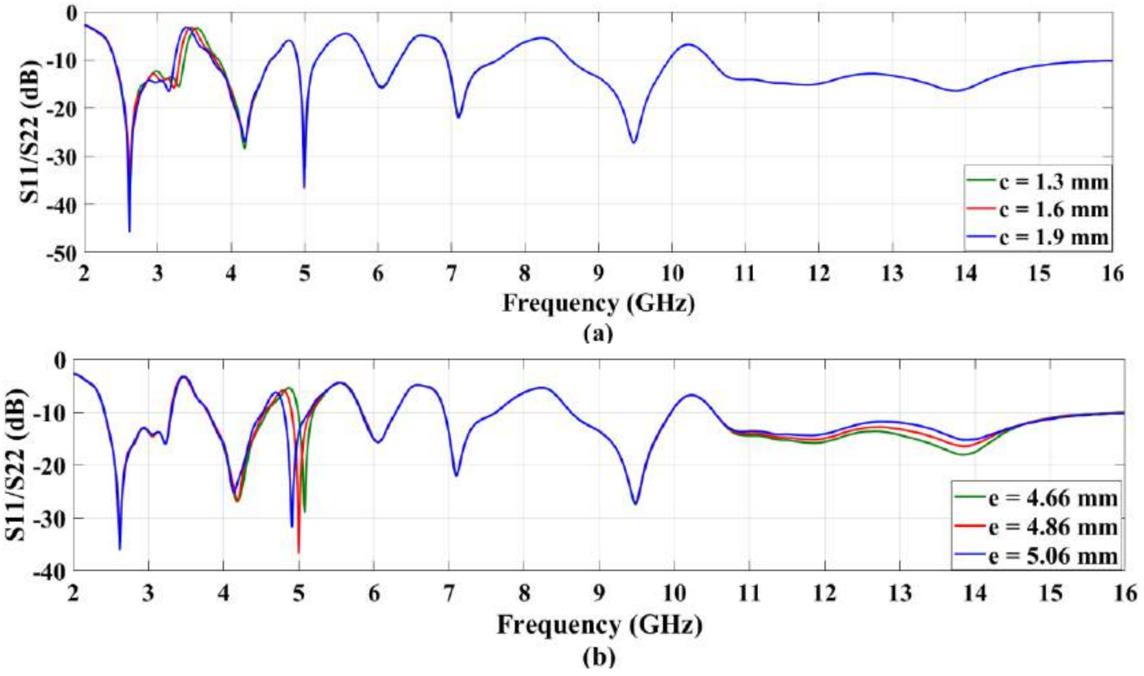

(a)

(b)

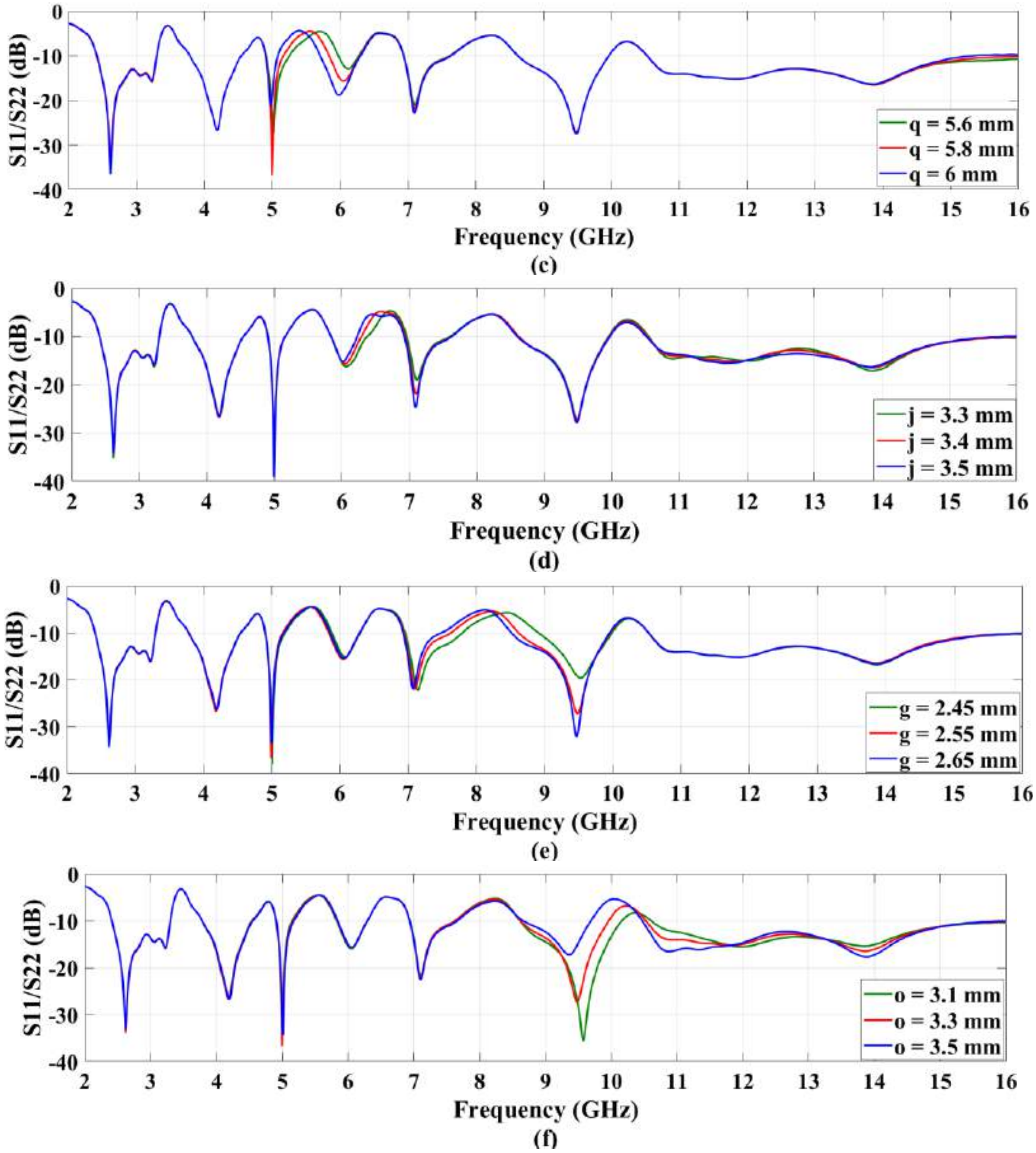

Figure 5.14 Simulated S_{11}/S_{22} (dB) results by varying length of (a) Z-shaped slit (b) inverted L-shaped slit (c) L-shaped slits (d) rectangular SRR1 (e) rectangular SRR2 (f) G-shaped slot

For a more comprehensive analysis of the stop-band operation of the proposed fractal array, the flow of current is viewed on the surface of the fractal radiating patches and reduced ground structure at the rejection frequencies of 3.46 GHz (WiMAX), 4.78 GHz (INSAT), 5.55 GHz (WLAN), 6.57 GHz (C-band), 8.23 GHz (ITU-8) and 10.22 GHz (amateur radio). On triggering the antenna port-1 (with simulated 1W power) and ceasing port-2 (with 50Ω load), Figure 5.15(a-f) demonstrates that the intensity of the current is strong near the edges of a Z-shaped slit (481.734 A/m), inverted L-shaped slit (459.499 A/m), pair of L-shaped slits (470.258 A/m), rectangular SRR1 (169 A/m), rectangular SRR2 (214.122 A/m) and G-shaped slot (317.003 A/m) at the notch frequencies of 3.46GHz, 4.78GHz, 5.55GHz, 6.57GHz, 8.23GHz and 10.22GHz respectively and no energy is radiated in open space. Each stop-band structure, therefore, behaves like a non-radiator resulting in poor return loss in the respective rejection bands.

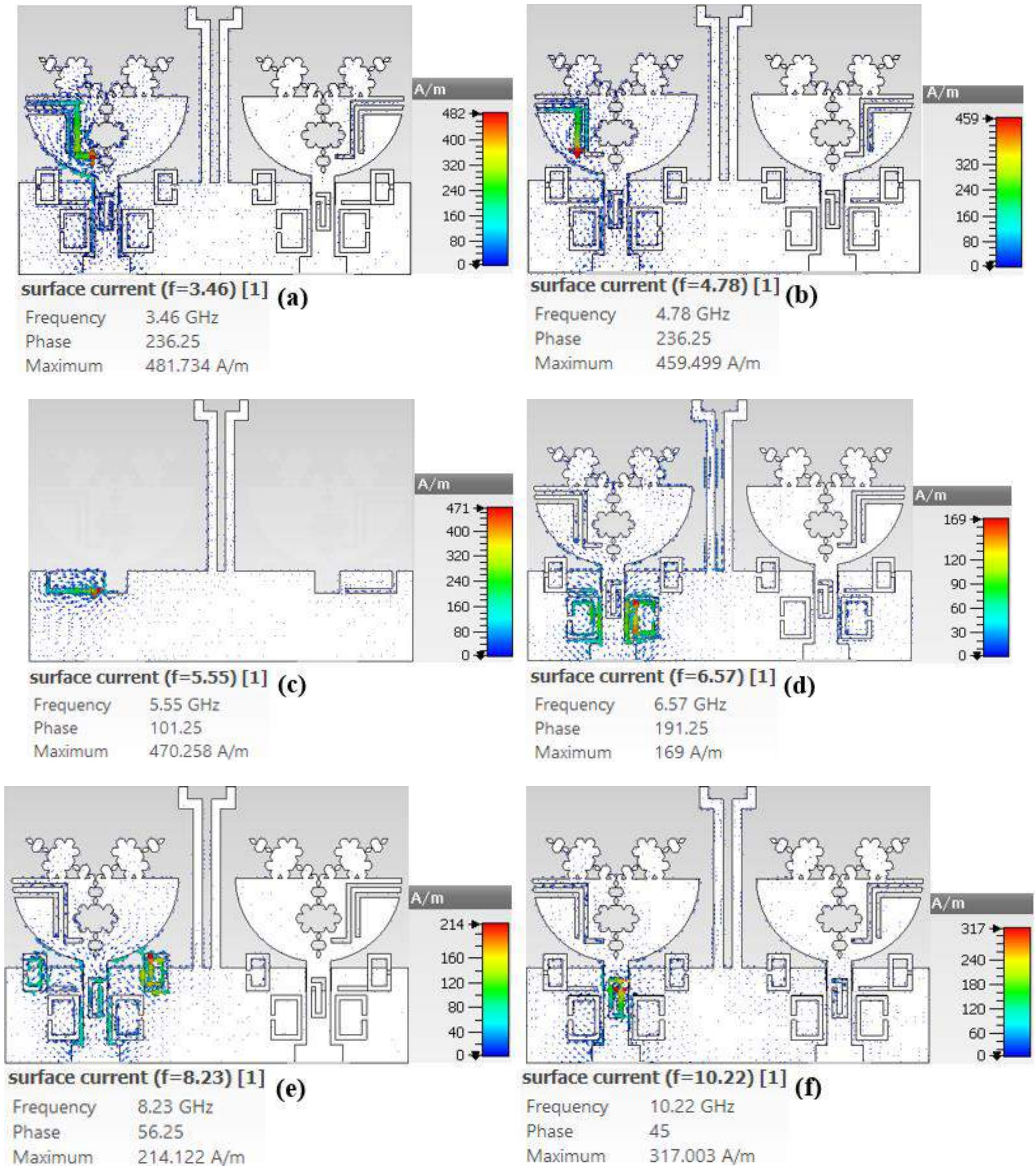

Figure 5.15 Current distribution for activated port-1 at the rejection frequencies of (a) 3.46GHz (b) 4.78GHz (c) 5.55GHz (d) 6.57GHz (e) 8.23GHz (f) 10.22GHz

5.2.4 Simulation and Experimental Analysis

To verify the EMI suppression operation of the designed UWB array, Figure 5.16(a, b) displays the fabricated model of the band-notched UWB array (according to the photolithography process) where the fractal patches are integrated with Z-shaped, inverted L-shaped, two rectangular SRR pairs and G-shaped notching elements and the reduced ground is defected with two L-shaped notching elements.

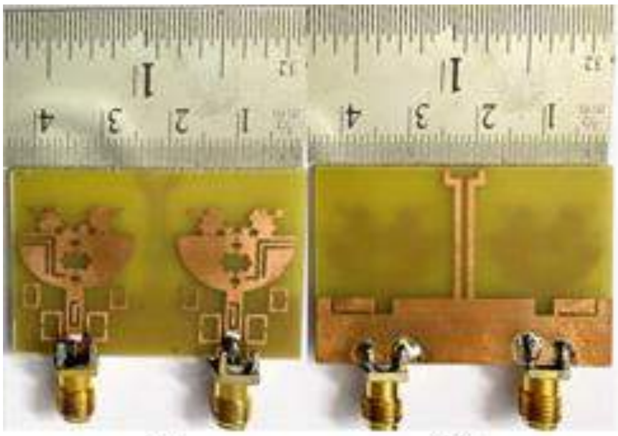

(a) (b)

Figure 5.16 Fabricated band-notch fractal array (a) patch (b) ground

5.2.4.1 Scattering Parameters

For justifying the band-suppression functionality of the designed UWB array, the fabricated UWB array integrated with six different stop-band structures is experimentally tested for S-parameters with the use of VNA. The obtained experimental S-parameter results are compared with the simulation ones as illustrated in Figure 5.17(a, b). It reveals that the designed UWB array effectively eliminates the EMI resulting from the WiMAX (3.3-3.78GHz), INSAT (reception: 4.52-4.9GHz), WLAN (5.16-5.84GHz), super-extended C-band (6.3-6.93GHz), ITU-8 (7.63-8.62GHz) and amateur radio bands (9.96-10.52GHz), concurrent in the excited operational range (simulated: 2.48-15.42 GHz and tested: 2.34-15.52 GHz) and maintains an optimal isolation level (simulated/ tested: $S_{12}/S_{21} \leq -18.1$dB) between the two fractal radiators. Table 5.6 illustrates the variation of simulation results from the tested ones of the designed fractal UWB array at the six suppressed narrow bands in form of the notched bandwidth and center notch frequency. The experimental results present a considerable resemblance with the simulated ones with a little deviation which may arise due to inaccurate etching of copper, improper soldering of SMA connectors, and reflections from the nearby objects in free space.

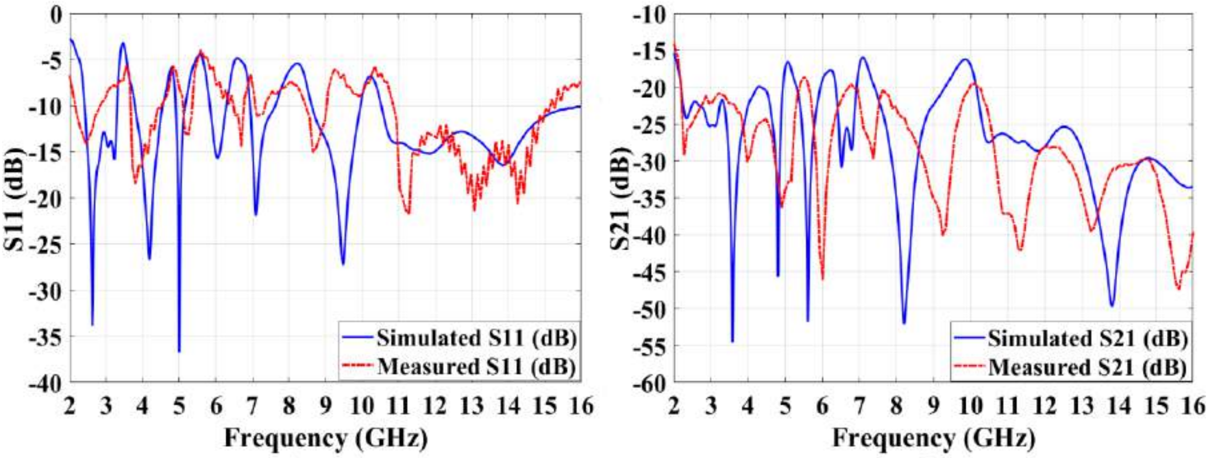

(a) (b)

Figure 5.17 Simulated and tested (a) S_{11} (b) S_{21} versus frequency

Table 5.6 Simulated and tested results of the designed fractal array at the rejection bands

Rejection range	WiMAX	INSAT	WLAN	Super extended C-band	ITU-8	Amateur radio
Assigned notch range (GHz)	3.3-3.7	4.5-4.8	5.15-5.85	6.425-6.725	7.9-8.5	10-10.5
Simulated notch range (GHz)	3.3-3.78	4.52-4.9	5.16-5.84	6.3-6.93	7.63-8.62	9.96-10.52
Tested notch range (GHz)	2.87-3.685	4.485-5.08	5.335-6.42	6.72-7.1	7.375-8.48	9.04-10.86
Theoretical stopband frequency (GHz)	3.5	4.65	5.5	6.575	8.2	10.25
Simulated stopband frequency (GHz)	3.46	4.78	5.55	6.57	8.23	10.22
Tested stopband frequency (GHz)	3.55	4.825	5.59	6.92	8.05	10.35

5.2.4.2 Far-field Performance

The software simulated and experimentally measured two-dimensional (2D) radiation patterns of the designed UWB notched array along the y-z plane (E-plane) and x-z plane (H-plane) at the operational resonances of 2.61 GHz, 4.9 GHz, 7.09 GHz, and 9.47 GHz are compared in Figure 5.18(a-d) respectively, for the activated port-1. As per the observations, the x-z co-polarization component of the proposed design exhibits a nearly omnidirectional far-field pattern whereas the y-z co-polarization component exhibits a directional pattern. A good similitude is realized between the simulation and measurement plots. Figure 5.19 demonstrates the variations of the gain curves for the basic UWB fractal array and the designed UWB fractal array with six rejection ranges for the activated port-1. For the basic UWB fractal array, an average simulated gain of 3.58 dBi is observed across the complete working range with a peak gain of 5.16 dBi at 7.48 GHz. At the six notched frequency points, a substantial drop in gain values is noted which affirms the interference rejection capability of the designed UWB notched array for WiMAX, INSAT (reception), WLAN, super-extended C-band, ITU-8, and amateur radio bands. The experimental gain values range from -3.18 to 4.31dBi with an average gain of 2.96 dBi (in the working range) while the simulation gain deviates from -2.93 to 4.75 dBi with an average gain of 3.04 dBi for the entire band of operation.

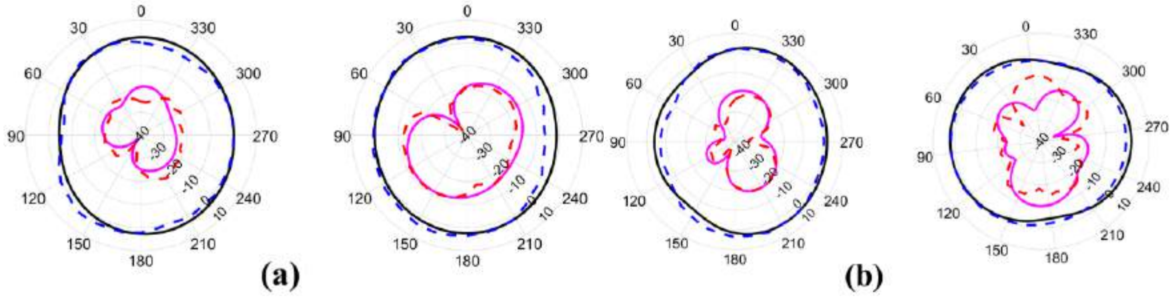

(a) (b)

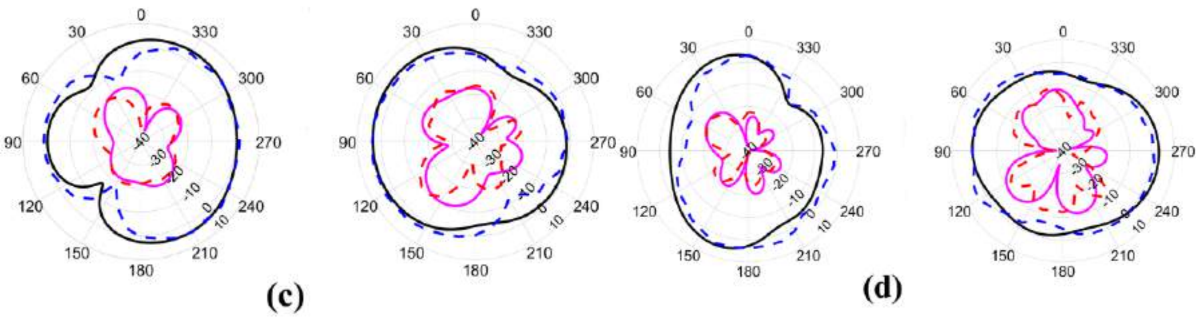

—	Co-polarization (Simulated)	– – –	Co-polarization (Measured)
—	Cross-polarization (Simulated)	-------	Cross-polarization (Measured)

Figure 5.18 Simulated and experimental radiation plots (with triggered port-1) in E-plane and H-plane at (a) 2.61GHz (b) 4.9GHz (d) 7.09GHz (d) 9.47GHz

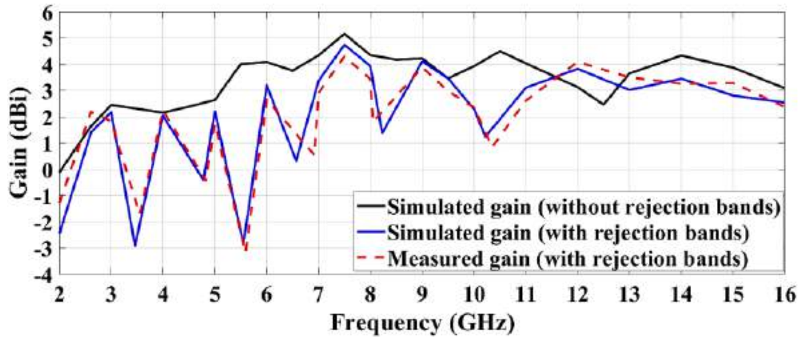

Figure 5.19 Gain (simulated and measured) versus frequency for the energized port-1

5.2.5 Diversity characteristics

The ECC and DG values for the signals received at the two ports of the proposed array can be evaluated from its S-parameters, given by Equations (2, 3) respectively in chapter 1. As illustrated in Figure 5.20(a), ECC <0.0449 (both experimental and simulated) is achieved for the whole band of interest together with the six eliminated narrow frequency bands. For validating the diversity characteristics for the band-notched array, the DG >9.9985 (simulation) and >9.989 (tested) are realized in the excited UWB range including the rejection bands (as presented in Figure 5.20(b)).

Figure 5.20(c) reveals that MEG (calculated using Equation (4, 5) in chapter 1) for each antenna port (both simulated and tested) is approximately equal to -3dB across the entire operational range and declines at the six eliminated narrow bands. The pink and brown curves in Figure 5.20(c) show that $|MEG_1 - MEG_2|$ deviates in the range of -1.77dB to 1.15dB (tested) and 0dB (simulated) which indicates that the designed array exhibits a good gain performance for the whole operational band.

With the integration of notch structures in the UWB-MIMO antenna design, both simulated and experimental CCL levels (calculated using Equation 7 in chapter 1) are also lower than 0.4 bits/s/Hz (excluding the rejected interfering bands) for whole working band (as given in Figure 5.20(d)). This ensures the potency of the proposed band-notch MIMO antenna to provide significant data transmission rates in a multipath fading domain. According to the Fig. 24(a, b), by introducing notch elements in the array design, TARC <-3.12 dB (simulation) and <-2.59 dB (measured) is realized for the entire bandwidth (calculated using Equation 8 in chapter 1). Hence, it is concluded that the frequency characteristics of the designed array with notches are slightly influenced by the different variations in the phase angles which is the prerequisite for an effective MIMO antenna functioning.

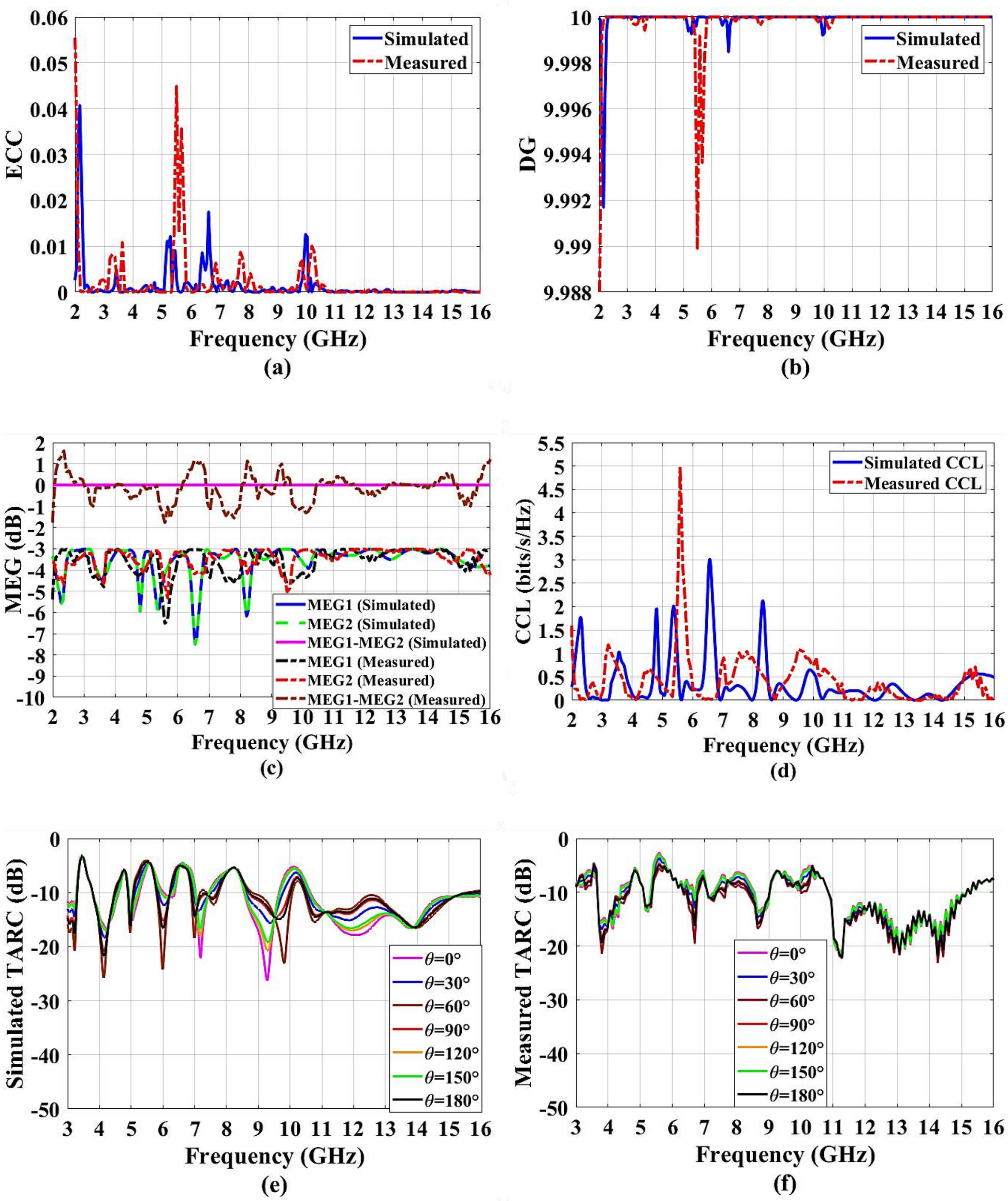

Figure 5.20 Simulation and experimental (a) ECC (b) DG (c) MEG (d) CCL (e, f) TARC (dB) values against frequency for the designed array with rejection bands

The next section of this chapter deals with the elimination of three interfering bands from the formerly designed four-port Sierpinski Gasket fractal array for UWB-MIMO systems.

5.3 Triple Band-Stop Functionality from a Quad-port Sierpinski Gasket Fractal UWB-MIMO Antenna

In this section, the previously configured quad-port Sierpinski gasket fractal MIMO antenna for ultra-wideband performance (Section 4.1 in chapter 4) is further integrated with three distinct notch structures to eliminate the three unwanted bands such as C-band (downlink satellite), WLAN, and radio-location. A comprehensive parametric study is carried out to gain a better insight into the geometrical deviations of each stopband element on the corresponding notched range. The array is designed and simulated through the CST version 2018 software. Several diversity metrics are also analyzed to justify the array operation in a real scattering environment. At last, the array is fabricated and tested for S-parameters and far-field behavior.

5.3.1 Array Geometry

The structure and configurational parameters of the UWB fractal array combined with three distinct stopband elements are illustrated in Figure 5.21(a-d). The proposed four-port antenna is configured on two versatile and widely available, 1.57mm thick 80×99.4 mm^2 FR4 dielectric substrates. The complementary Sierpinski gasket fractal patches (2nd iteration), ground with spiral-shaped DGS and feedline geometry along with their parametric values of the proposed quad-port fractal array for realizing UWB characteristics as previously described in Section 4.1.1 (chapter 4). To surmount the EMI issue associated with some narrowband applications (namely downlink C-band, WLAN, and radio-location) prevailing in the realized UWB of operation, three distinct band-stop structures namely a U-shaped slot, circular SRR pair, and rectangular SRR pair respectively are introduced in each transmission line. The optimized value (mm) for each parameter of the proposed band-notch UWB fractal array is indicated in Table 5.7.

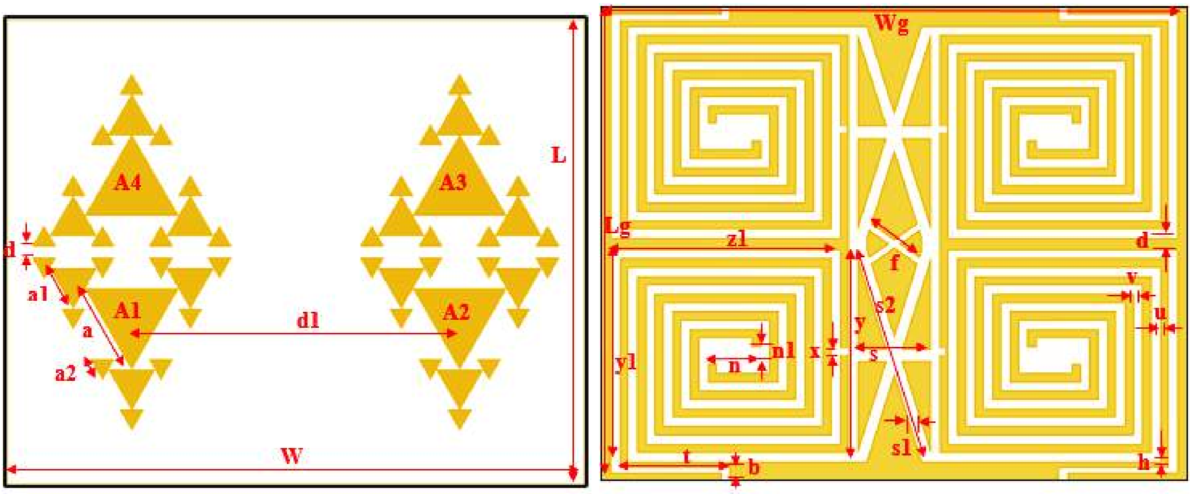

(a) (b)

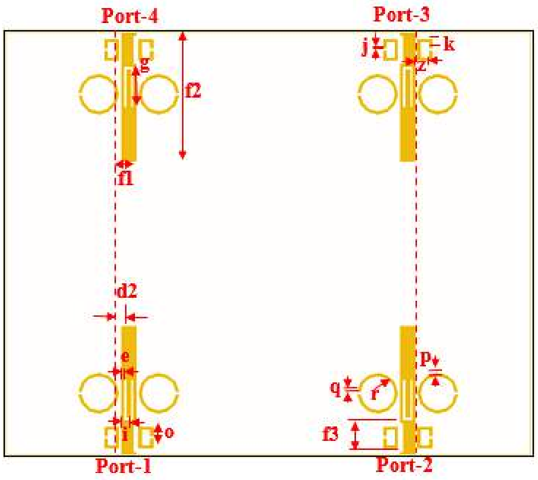

(c)

Figure 5.21 (a) Four fractal patches (upper view of top FR4) (b) Ground with spiral-shaped slots (upper surface of lower FR4) (c) Microstrip feed lines combined with three distinct notching elements (rear surface of lower FR4 substrate) White: FR-4 substrate, Tan: Copper

Table 5.7 Parametric dimensions of the quad-port band-notched fractal UWB-MIMO antenna

Parameter	L	W	a	a1	a2	d	d1	Lg	Wg	y
Value (mm)	80	99.4	16.16	8.08	4.04	2	54.4	80	99.4	36
Parameter	z1	n	n1	t	b	h	s	s1	s2	o
Value (mm)	39	9	3	18.75	2	1	12.4	1.5	38.08	4
Parameter	v	x	f1	f2	f3	j	k	g	d2	e
Value (mm)	1.5	1	2.8	24.35	5.5	0.5	1.75	7.7	1.85	0.5
Parameter	p	q	r	y1	z	f	u	i		
Value (mm)	0.5	0.5	3.8	36	2.7	10.41	1.5	1.8		

5.3.2 Approach for Realizing Triple Band-Notch Operation from the Proposed UWB fractal array

After having obtained the UWB characteristics with the fractal MIMO antenna, the following objective is to effectively curb the critical EM interference problem associated with some licensed narrow frequency applications like downlink satellite-based communication (C-band), WLAN, and radio-location prevailing in the excited frequency spectrum. Thus, three distinct stop-band structures are introduced one by one in each microstrip feed of the designed array (as demonstrated in Figure 5.22(a-c)) to effectuate the optimized array configuration embedded with all triple band-notch structures (Figure 5.22(d)) whereas the radiator and ground geometry is kept constant. For simplification purposes, the width of each band-stop structure is kept at 0.5 mm. The judicious selection of length and location of each notching element assists in suppressing the required interfering application. The software simulated $S_{11}/S_{22}/S_{33}/S_{44}$ (dB) responses (for the complete band of operation) realized on incorporating respective notch structures is shown in Figure 5.23.

To mitigate the interference associated with the C-band (downlink satellite), two circular SRRs are symmetrically placed near the middle of each microstrip feed of the designed UWB fractal antenna (Figure 5.22(a)) to realize a notch at 3.95 GHz (f_1). Here, the overall length of each circular SRR (L_{CSRR}) is guided wavelength (λ_g) dived by two and is approximately evaluated by Equation 43. According to the pink curve in Figure 5.23, a circular SRR pair effectively rejects the interfering C-band (downlink satellite) in the range of 3.63-4.34 GHz.

$$L_{CSRR} = \frac{\lambda_g}{2} = \frac{\lambda}{2\sqrt{\varepsilon_{eff}}} = 2\pi r - q = \frac{c_o}{2f_1}\sqrt{\frac{2}{\varepsilon_r+1}} \tag{43}$$

As depicted in Figure 5.22(b), the band-stop functionality related to the interfering WLAN is accomplished by truncating a U-slot from the bottom region of each microstrip feed (just above the feedline slot) of the designed array. For the stopband frequency (f_2) at 5.5 GHz, the overall length of each U-shaped slot (L_U) is computed with Equation 44. The green curve in Figure 5.23 illustrates that the UWB array amalgamated with the U-shaped slots (Figure 5.22(b)) successfully eradicates the frequency range of 5.29-5.82 GHz (WLAN) from the excited frequency bandwidth.

$$L_U = \frac{\lambda_g}{2} = \frac{\lambda}{2\sqrt{\varepsilon_{eff}}} = 2g + i = \frac{c_o}{2f_2}\sqrt{\frac{2}{\varepsilon_r+1}} \tag{44}$$

According to Figure 5.22(c), two rectangular SRRs are symmetrically arranged near the lower junction of each feedline of the proposed UWB array to curb the EM interference corresponding to the radio-location band at 8.75 GHz (f_3). Each rectangular SRR is $\lambda_g/2$ long and its length (L_{RSRR}) is mathematically approximated using Equation 45. The blue curve in Figure 5.23 illustrates the elimination of unwanted radio-location band (8.49-9.13GHz) from the working UWB range after the incorporation of two rectangular SRRs in the feedline arrangement of the proposed array.

$$L_{RSRR} = \frac{\lambda_g}{2} = \frac{\lambda}{2\sqrt{\varepsilon_{eff}}} = 2z + (2o - j) = \frac{c_o}{2f_3}\sqrt{\frac{2}{\varepsilon_r+1}} \tag{45}$$

Figure 5.22(d) presents the optimized MIMO antenna design integrated with three different notch resonators altogether. For the designed UWB array, the band-stop structures namely circular SRRs, U-slot, and rectangular SRRs successfully introduce notches at 4.01 GHz (f_1), 5.56 GHz (f_2), and 8.8 GHz (f_3) respectively, as shown by the red curve in Figure 5.23. Table 5.8 shows the variation between the estimated and software-optimized lengths for the designed band-reject structures.

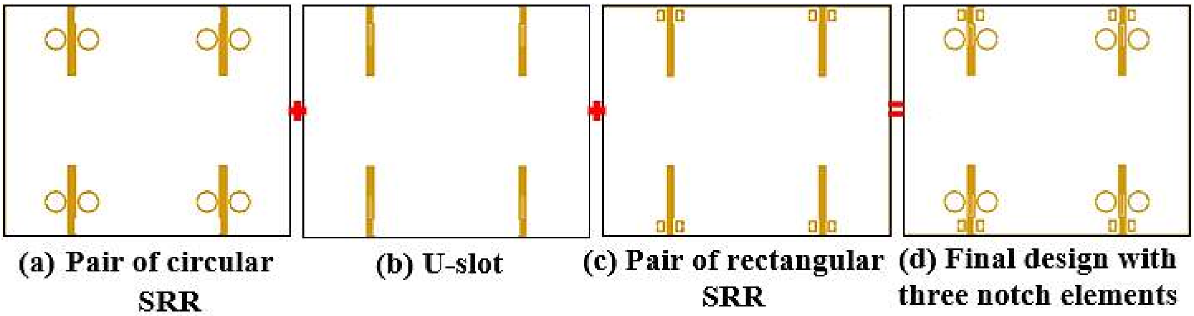

(a) Pair of circular SRR **(b) U-slot** **(c) Pair of rectangular SRR** **(d) Final design with three notch elements**

Figure 5.22 Methodology for attaining triple band rejection from the designed UWB array

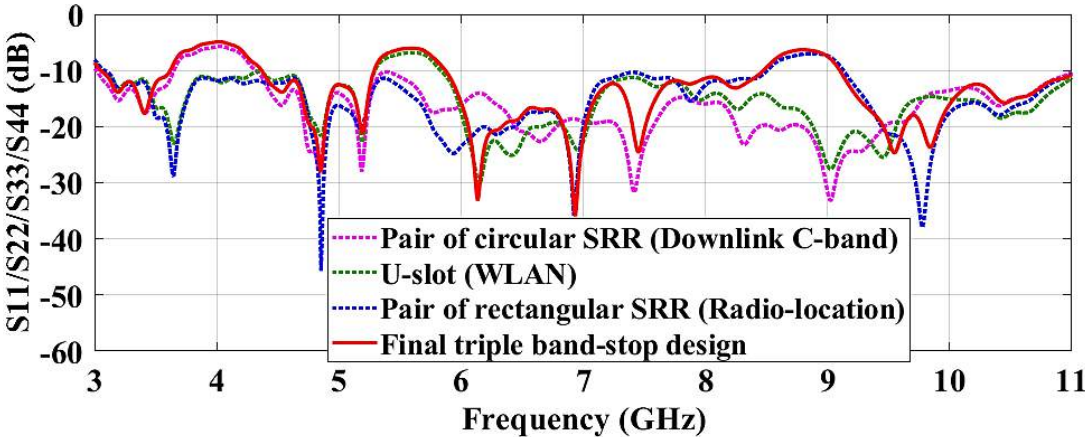

Figure 5.23 Variation of simulated $S_{11}/S_{22}/S_{33}/S_{44}$ (dB) responses across the excited operational range on the incorporation of three distinct notch elements in the proposed UWB array design

Table 5.8 Mathematical and software simulated lengths of three band-stop geometries

Length↓/Rejection →	C-band (downlink satellite communication)	WLAN band	Radio-location band
Evaluated (mm)	23.11	16.6	10.43
Software optimized (mm)	23.36	17.2	12.9
Error	0.011	0.035	0.19

5.3.3 Parametric optimization of the band-stop elements and surface current analysis

As stated before, to eradicate the severe EMI resulting from some licensed narrow bands, the UWB antennas are incorporated with the band-rejection mechanism. Along with this functionality, several high-tech communication equipment also requires an independent rejection phenomenon. Equations (43-45) verify that the required stopband resonance can be obtained by changing the overall length or radius of the respective notch structure. Therefore, in the present section, the length optimization of each stopband element is conducted separately by varying the dimension of a single variable namely ‘r’ (radius of circular SRR), ‘g’ (U-slot length), and ‘j’ (separation gap in rectangular SRR), however, other design parameters are kept fixed. Observations from Figure 5.24(a, b) evidence that a rise in the values of ‘r’ from 3.65mm to 4.1mm (downlink C-band) and ‘g’ from 7.55mm to 8mm (WLAN) increments the total length of circular SRRs (L_{CSRR}) and U-slot (L_U) respectively. Consequently, the center notch frequency of the corresponding stop-band presents a transit from the higher to lower frequency side, although the other notch bands remain nearly unaffected. For the radio-location notch band, as the separation distance between the rectangular SRRs enlarges (‘j’ from 0.5mm to 1.4mm), the total length of rectangular SRR (L_{RSRR}) reduces (12.9 mm to 12 mm) which in turn shifts the central band-stop frequency in the direction of higher frequency as depicted in Figure 5.24(c). The proposed UWB array demonstrates an optimum band-notch functionality for ‘r’, ‘g’, and ‘j’ equal to 3.8mm, 7.7mm, and 0.5mm correspondingly. Thus, it is deduced that all notch ranges are independent of each other and the desired rejection bandwidth and frequency can be effectively realized by adequately selecting the parametric dimensions and location of the corresponding stopband structure.

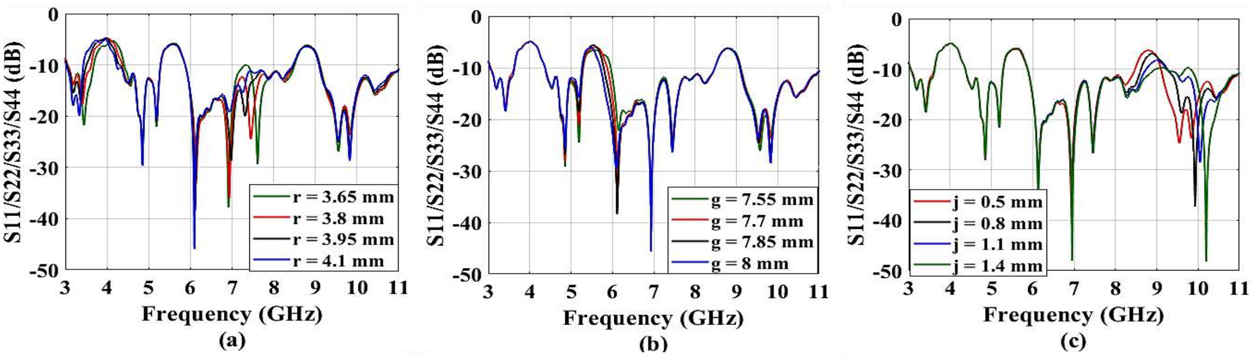

Figure 5.24 $S_{11}/S_{22}/S_{33}/S_{44}$ (dB) variation relative to the frequency for different values of (a) ‘r’ for the pair of circular SRR (b) ‘g’ for U-slot (c) ‘j’ for the two rectangular SRRs

To investigate further the band-stop capability of the designed MIMO antenna, the distribution of current (A/m) is viewed on the rear side of the feed substrate at the rejection resonances of 4.01GHz (C-band), 5.56GHz (WLAN), and 8.8GHz (radio-location) respectively. On supplying 1W simulated power to the antenna port-1, Figure 5.25(a-c) reveals that the maximum current is deposited along the sides of circular SRRs (169.029 A/m), U-shaped slot (348.282 A/m), and rectangular SRRs (156.04 A/m) at the stopband resonances of 4.01GHz, 5.56GHz, and 8.8GHz respectively. As each band-stop structure confines a significant amount of EM energy without any radiation in free space, therefore, it functions as a non-radiator which gives rise to high mismatch losses and inadequate return loss behavior in the corresponding notch ranges.

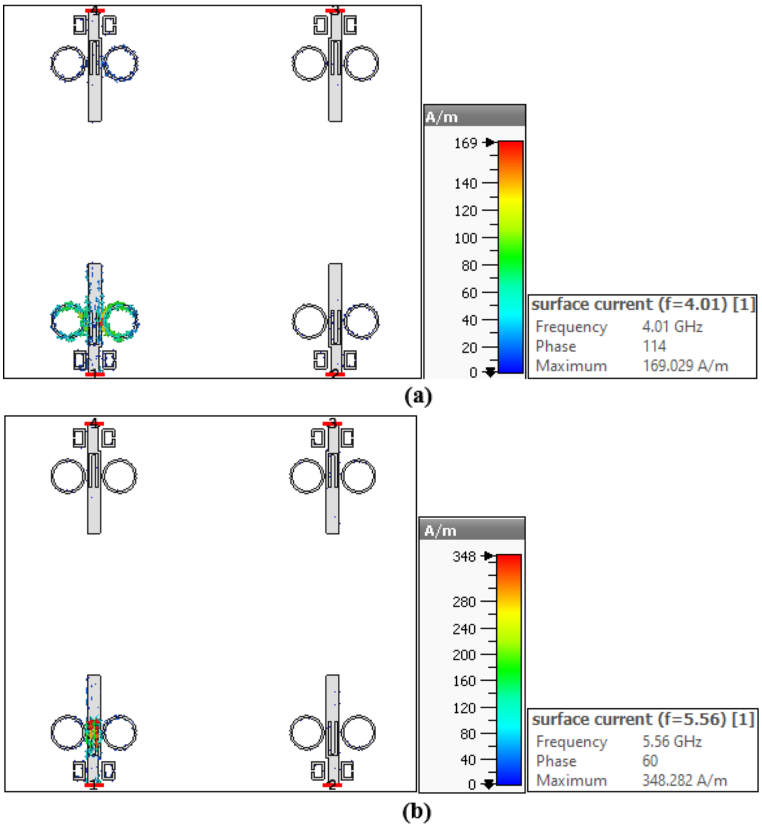

(a)

(b)

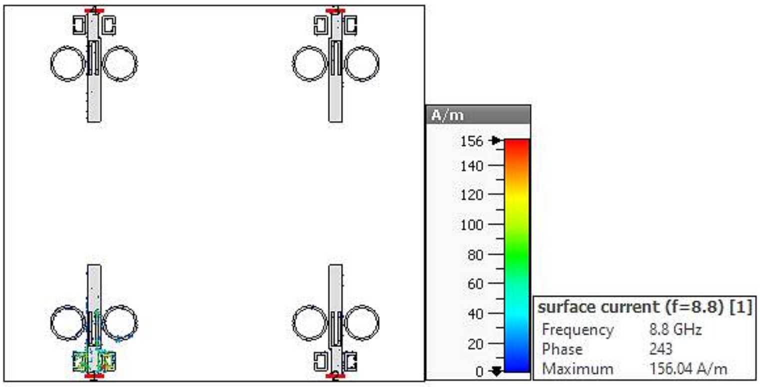

(c)

Figure 5.25 Current flow on the rear surface of the feed substrate at the stopband resonances of (a) 4.01GHz (b) 5.56GHz (c) 8.8GHz with port-1 excitation

5.3.4 Simulation and Measurement Results

The designed array is developed according to the photolithography method on a set of two 1.57 mm thick, FR4 substrates. To substantiate the stop-band ability of the designed UWB-MIMO antenna, the patch and the ground geometry remains the same (Section 4.1.4 in chapter 4) while three distinct notch structures namely a U-shaped slot, pair of circular SRRs, and two rectangular SRRs are introduced in each microstrip feed of the fabricated model as shown in Figure 5.26.

(a) (b) (c)

Figure 5.26 Photographs of the fabricated array (a) fractal patches (b) ground (c) notched feeds

5.3.4.1 Scattering Parameters

The fabricated four-port notched UWB antenna is placed under test on VNA to realistically justify the ability of the four-port UWB antenna to suppress three interfering narrow bands prevailing in the operational UWB spectrum. The plots showing the comparison between the simulated and tested S-parameters are illustrated in Figure 5.27(a-d). As observed, the designed UWB-MIMO antenna effectively eliminates the intrusion introduced by C-band (downlink satellite: 3.62-4.31GHz), WLAN (5.23-5.87GHz), and radio-location (8.47-9.09 GHz) band prevailing from the simulated (3.07-11 GHz) and tested (3.12-12GHz) functional range while realizing an acceptable isolation response between the four antenna elements of the array. The tested results depict a favorable agreement with the simulation ones with a slight discrepancy that could occur as a result of fallacious soldering of SMA connectors at the feed point, feed cable leakages, imprecise copper etching during the fabrication process, misaligned layers of the antenna array, and reflections from the numerous laboratory equipment as the antenna testing is performed in an open space environment. Table 5.9 reflects the variation of software-simulated outcomes of the proposed UWB array from the measured ones at the triple rejection ranges in form of eliminated frequency band and center stopband frequency.

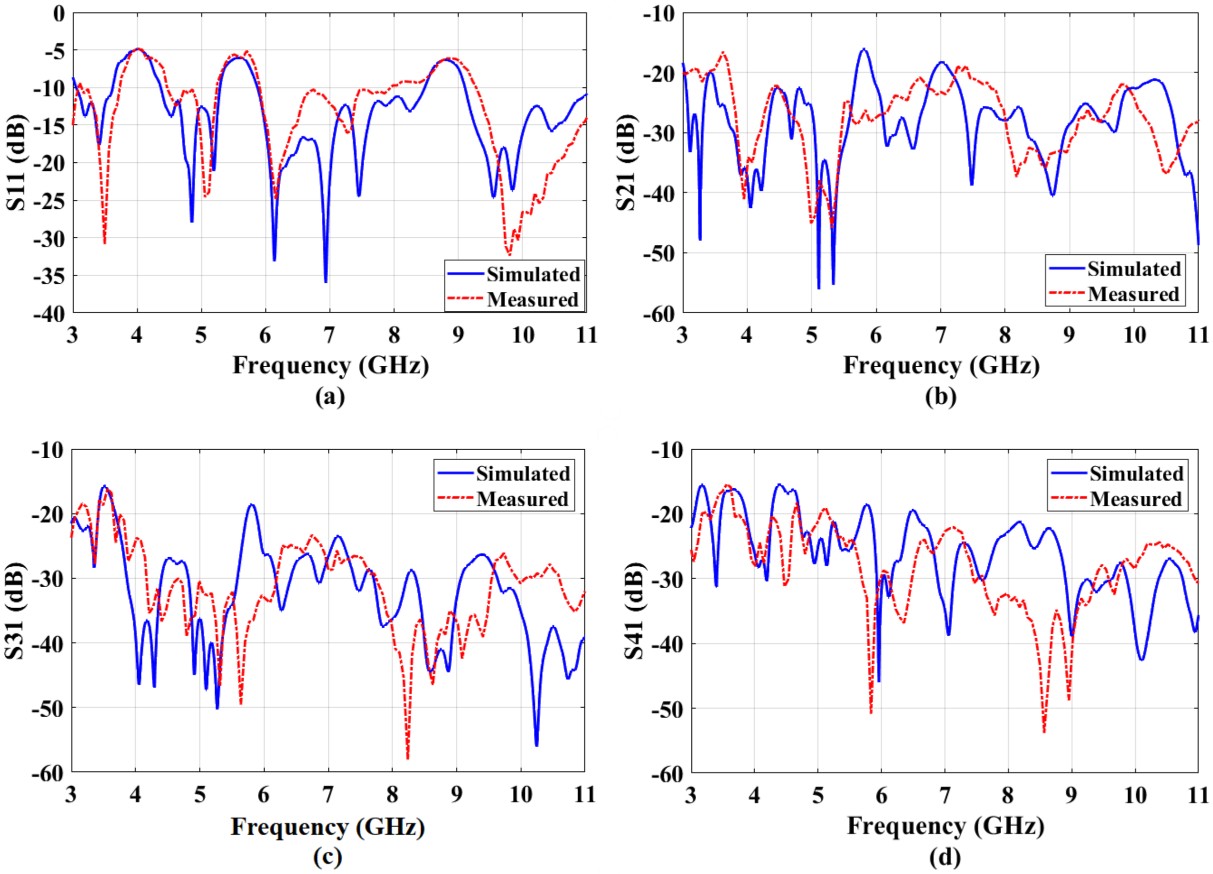

Figure 5.27 Variation of simulated and measured (a) S_{11}(b) S_{21} (c) S_{31} (d) S_{41} versus frequency

Table 5.9 Simulated and measurement outcomes of the designed UWB-MIMO antenna at the three suppressed ranges

Attributes/Suppressed bands	C-band (Downlink satellite)	WLAN	Radio-location band
Allocated bandwidth (GHz)	3.7-4.2	5.15-5.85	8.5-9
Software simulated bandwidth (GHz)	3.62-4.31	5.23-5.87	8.47-9.09
Experimental bandwidth (GHz)	3.71-4.47	5.25-5.9	7.98-9.28
Designed band-notch frequency (GHz)	3.95	5.5	8.75
Simulated notch frequency (GHz)	4.01	5.56	8.8
Tested notch frequency (GHz)	4.015	5.51	8.89

5.3.4.2 Radiation Performance

As demonstrated in Figure 5.28, the simulation and laboratory-tested 2D far-field pattern of the designed band-notch array is analyzed along the two principal planes namely YZ plane and XZ plane, at 4.85GHz and 6.93GHz passband resonances for the excited port-1. As observed, the YZ plane demonstrates a directional radiation pattern while the XZ plane illustrates a quasi-directional pattern plot at the two resonances. The simulated far-field pattern exhibits an acceptable resemblance with the measured ones where slight disparities may occur due to possible reflections from the other non-energized antenna ports, feed cable limitations, improper connector soldering, and unavoidable challenges posed during the fabrication process. On activating port-1 of the four-port UWB antenna (with and without stopbands), the gain variations against the functional UWB range are presented in Figure 5.29. The basic four-port UWB-MIMO antenna provides an average gain of 2.95 dBi (simulated) across the complete band of operation with 4.88dBi (at 9.3GHz) being the maximal gain. As observed, the band-stop UWB-MIMO antenna shows a substantial decrease in gain values at the three rejection resonances which justifies that the array is not responding in the corresponding rejection ranges (downlink satellite C-band, WLAN, and radio location). The simulated and tested values of gain of the designed array (with notches) deviate from -2.47 to 4.25dBi and -2.449 to 4.02dBi respectively in the operational range. Thereby, the proposed array exhibits a reasonable similitude between simulated and tested results which is desired for the effective functioning of UWB communication devices in a real-time world.

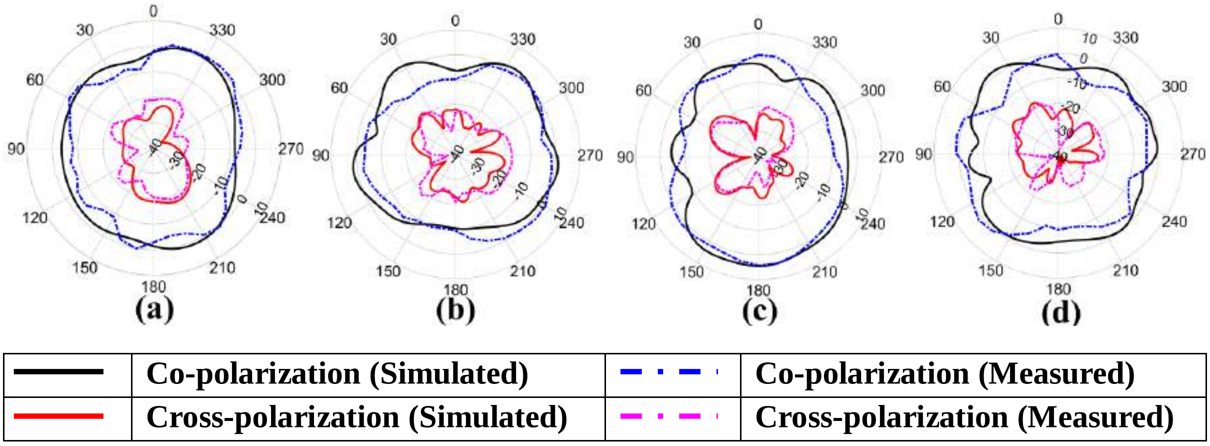

Figure 5.28 Simulated and tested far-field pattern plots (with activated port-1) at (a) 4.85GHz (YZ plane) (b) 4.85GHz(XZ plane) (c) 6.93 GHz(YZ plane) (d) 6.93GHz (XZ plane)

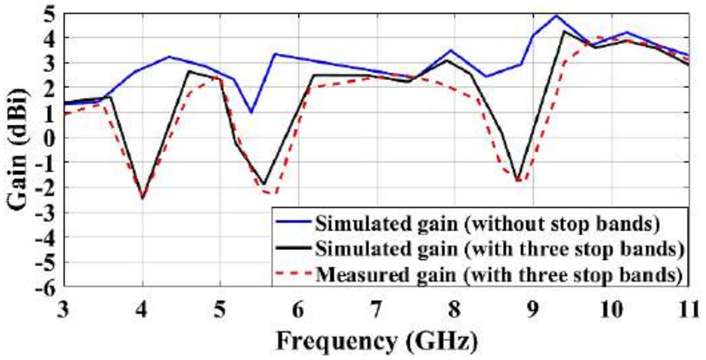

Figure 5.29 Simulated and tested values of gain versus frequency plot for energized port-1

5.3.5 Diversity Performance Metrics

In this subsection, to govern the optimal functionality of the designed band-notch UWB-MIMO antenna in the multi-channel environment, various diversity parameters are computed and also validated with the experimental values. The comparative plots of simulated and measured values of diversity metrics are depicted in Figure 5.30(a-e). Table 5.10 lists the simulated and experimental levels of various diversity parameters for the excited UWB spectrum. The values of these diversity metrics like ECC, DG, MEG, CCL, and TARC are estimated by the S-parameter approach using Equation 32 (chapter 4), Equation 3 (chapter 1), Equation 33 (chapter 4), Equation (34, 35) (chapter 4) and Equation 36 (chapter 4) respectively. As observed, the admissible levels of various diversity metrics of the designed four-port UWB antenna with stopband operation verify the realization of considerable diversity operation imperative for MIMO communication systems.

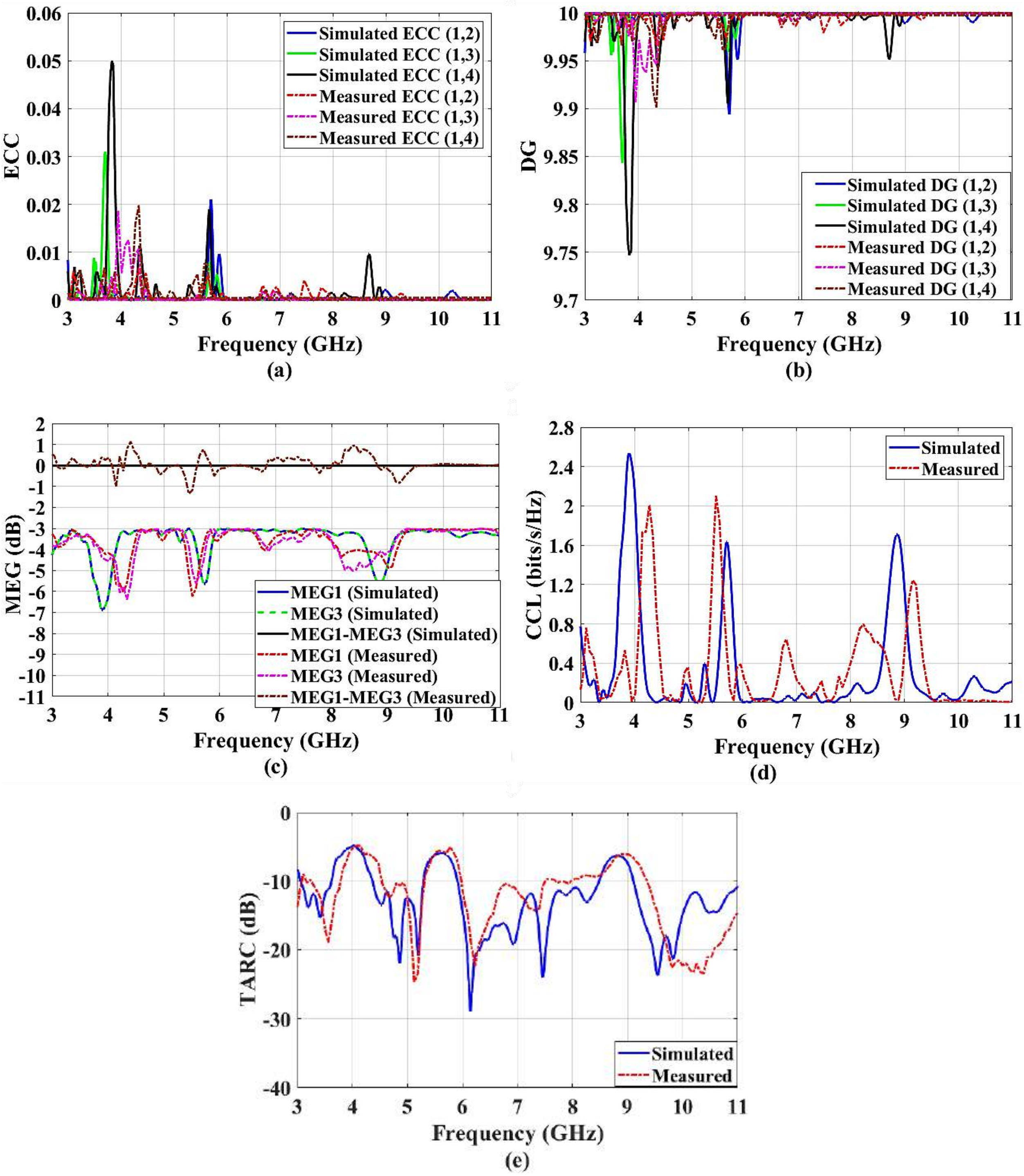

Figure 5.30 Simulated and experimental (a) ECC (b) DG (c) MEG (d) CCL (e) TARC levels against frequency for the designed band-notch UWB array

Table 5.10 Simulated and tested levels of diversity metrics for the excited operational range

Metrics	ECC			DG			MEG (dB)		CCL(bits/s/Hz)	TARC (dB)	
	S-parameter		Far-field	S-parameter		Far-field	S-parameter		S-parameter	S-parameter	
	Sim.	Meas.	Sim.	Sim.	Meas.	Sim.	Sim.	Meas.	Sim.	Sim.	Meas.
With notches	≤0.049	≤0.02	≤0.107	≥9.75	≥9.89	≥9.45	≤-6.86	≤-6.38	≤ 0.4 (working band)	≤-5.077	≤ -4.926

The next section of this chapter integrates the formerly designed quad-port Koch Snowflake fractal UWB-MIMO antenna with the eradication of four interfering narrowband applications.

5.4 Quad Band-Notch Capability of a Quad-port Koch Snowflake Fractal UWB-MIMO Antenna

In this section, the formerly reported four-port Koch Snowflake fractal MIMO antenna for ultra-wideband characteristics (Section 4.2 in chapter 4) is further combined with four distinct band-stop elements to eradicate four undesired applications like C-band (downlink satellite), WLAN, INSAT and ITU-8 band. A comprehensive parametric study is conducted to analyze the influence of length variations of these notching elements on their respective rejection ranges. Various diversity parameters are also examined to justify the array's implementation in a real scattering environment. At last, the array is fabricated and experimentally investigated for S-parameters and far-field characteristics.

5.4.1 Array Configuration

The design configuration and parameters of the final optimized band-stop UWB array with four fractal radiating elements and common ground with DGS are displayed in Figure 5.31(a-c). The proposed fractal array with 80×71×1.64mm^3 volumetric dimensions is assembled on a low-priced, easily obtainable FR4 substrate with height and 'ε_r' of 1.57mm and 4.4 respectively. The geometry for circular patches (each integrated with 4th iterative modified Koch Snowflake fractal) and the partial ground plane with DGS for realizing UWB of operation is already examined under Section 4.2.1 (chapter 4). In this section, the main aim is to combat the unwanted narrow bands from the excited UWB range by incorporating various band-notch structures in the array design. So, as shown in Figure 5.31(a), each radiator is defected with a modified Z-shaped slot (corner) and rectangular SRR (just above the feedline) to eliminate the EM intrusion arising from satellite communication in C-band (downlink) and INSAT (transmission) band respectively. To reject the unwanted ITU-8 range, an inverted U-shaped slot is removed from the center of each microstrip line. Moreover, a rectangular SRR pair is embedded around each rectangular slot in the ground surface (shown in Figure 5.31(c)) to notch WLAN from the working UWB range. Table 5.11 depicts the final structural dimensions (mm) of the designed four-port band-notch UWB array.

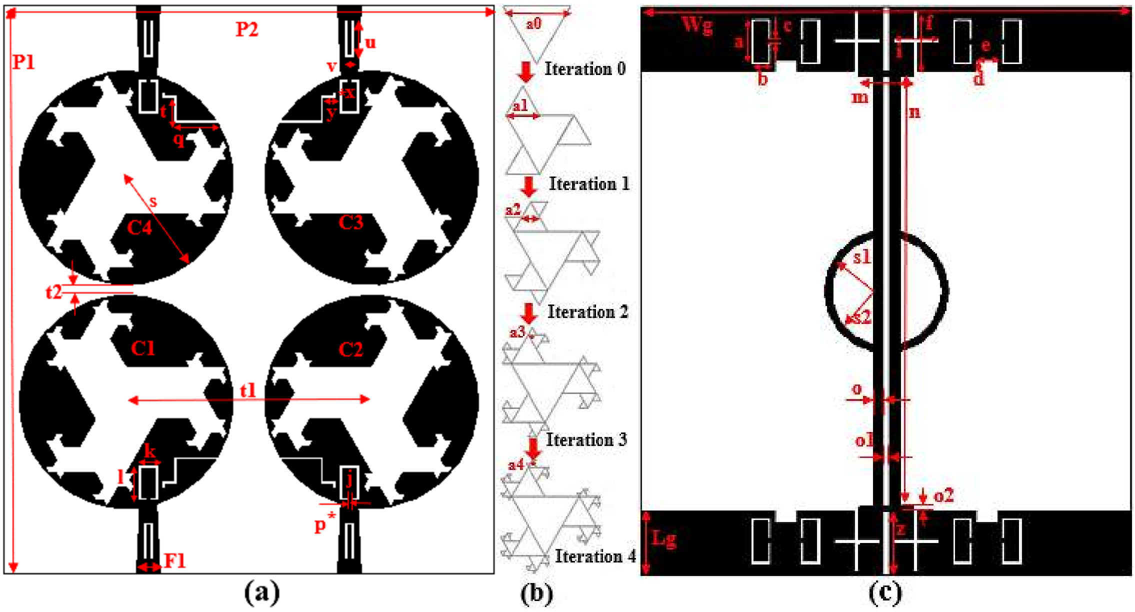

Figure 5.31 (a) Circular patches defected with hen-shaped fractal design (top layer of FR4) (b) Intermediary iteration levels of hen-shaped fractal (c) Reduced and defected ground surface (rear view of FR4) (*black region: copper, white region: FR4 substrate)

Table 5.11 Optimized dimensions (mm) of proposed four-port UWB array with notched ranges

Parameter	P1	P2	s	y	F1	a	b	c	p	j
Value (mm)	80	71	14.3	1.7	3.4	6.4	2.8	0.5	0.5	0.5
Parameter	l	t	q	Lg	u	e	d	f	v	x
Value (mm)	5.1	3.5	6.3	9.3	5.4	3.2	1.63	8.8	1.5	1
Parameter	o1	o2	z	o	Wg	i	s1	s2	m	n
Value (mm)	9	0.75	9.3	1.45	82	6.65	7.1	6.1	7.8	59.9
Parameter	a0	k	a1	t2	a2	a3	a4	t1	t2	
Value (mm)	18	2.9	9	2.8	4.5	2.25	1.125	32.4	2.8	

5.4.2 Methodology to Achieve Band-Notch Functionality from the Proposed UWB Fractal Array

Having realized the UWB operability from the designed quad-port fractal antenna, the following goal is to adequately filter out the EM interference emerging from the downlink C-band, WLAN, INSAT, and ITU-8 narrow bands that fall within the excited frequency bandwidth. Thereby, four distinct notch elements are merged individually in each circular radiator (modified Z-slot and rectangular SRR), microstrip line (inverted U-slot), and reduced ground (pair of rectangular SRR) of the designed array (as presented in Figure 5.32(a-d)) to effectuate the final optimized quad band-notch geometry as displayed in Figure 5.32(e). For ease of application, the width of every band-stop element is set to 0.5mm. By suitably selecting the total length and placement of the notching element, the required interfering application can be successfully eradicated. Figure 5.33(a, b) illustrates the simulated band-notch response for the various notch elements embedded in the array design over the entire working band.

As depicted in Figure 5.32, a modified Z-shaped slot is trimmed from the lower corner of each circular radiator to counter the interfering C-band (downlink satellite) at 3.95GHz. Each modified Z-shaped notch structure is $\lambda_g/4$ (where λ_g is guided wavelength) long and its overall length ($L_{n,1}$) is numerically estimated according to Equation 46.

$$L_{n,1} = q + t + y + x = \frac{\lambda_g}{4} = \frac{\lambda_o}{4\sqrt{\varepsilon_{eff}}} = \frac{v_o}{4f_{n,1}}\sqrt{\frac{2}{\varepsilon_r+1}} \tag{46}$$

here variables v_o, λ_o, ε_{eff}, and $f_{n,1}$ symbolize the light speed, free-space wavelength, the effective dielectric constant of FR4 substrate, and center notch frequency respectively. According to the pink curve in Figure 5.33, the modified Z-shaped slots adequately reject the intrusive C-band (satellite downlink communication) in the 3.92-4.51GHz range from the excited working band of the designed quad-port antenna.

To combat the EM interference evolving from the WLAN narrowband (at 5.5GHz), four rectangular SRR pairs are sliced from the reduced ground (surrounding the feedlines) of the designed array as shown in Figure 5.32(b). The stop-band ability corresponding to the INSAT (uplink) application (at 6.875GHz) is attained by cutting off a rectangular SRR from each circular patch (immediately above the feedlines) of the proposed array. Also, an inverted U-shaped slot is removed from the center of each microstrip line to notch 7.9-8.5GHz (ITU-8) band. The total length of each $\lambda_g/2$ notch structure is arithmetically estimated with the help of Equation 47.

$$L_{n,i} = \frac{\lambda_g}{2} = \frac{\lambda_o}{2\sqrt{\varepsilon_{eff}}} = \frac{c_o}{2f_{n,i}}\sqrt{\frac{2}{\varepsilon_r+1}} \tag{47}$$

here $L_{n,i}$ is the overall length of the band-stop element ($L_{n,2} = 2a + 2b - c$ for SRR pair, $L_{n,3} = 2l + 2k - j$ for SRR, and $L_{n,4} = 2u + v$ for inverted U-slot) for a respective band-notch resonance ($f_{n,i}$) for i=2,3,4. The orange, blue, and green curve in Figure 5.33 demonstrates the suppression of undesired WLAN (5.27-5.89GHz), INSAT (6.48-7.22GHz), and ITU-8 (7.85-8.92GHz) narrowband respectively, from the working frequency bandwidth.

Figure 5.32(e) illustrates the final configuration of the optimized quad-port antenna amalgamated with all four stop-band structures. For the designed array, the red curve in Figure 5.33 depicts that the notching elements namely a modified Z-slot (patch), SRR pair (ground), SRR (patch), and inverted U-slot (feedline) successfully notch the interfering frequencies of 4.01GHz ($f_{n,1}$), 5.41GHz ($f_{n,2}$), 6.882GHz ($f_{n,3}$), and 8.18GHz ($f_{n,4}$) respectively. Table 5.12 lists the the computed and simulated (optimized) lengths for band-stop element.

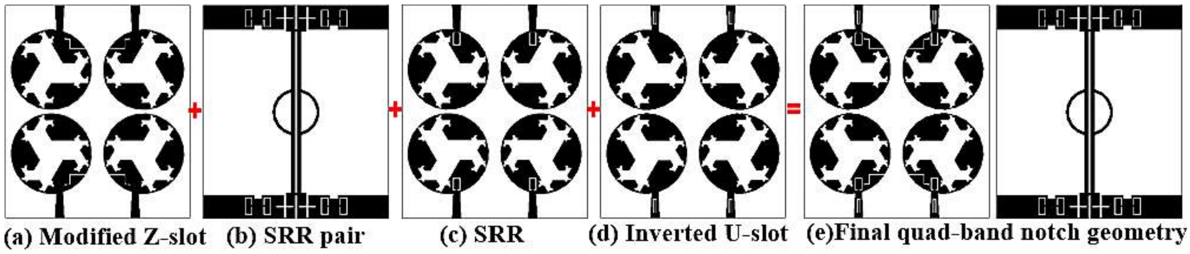

(a) Modified Z-slot (b) SRR pair (c) SRR (d) Inverted U-slot (e)Final quad-band notch geometry

Figure 5.32 Stepwise approach followed for accomplishing quad band-notch operation from the designed fractal array

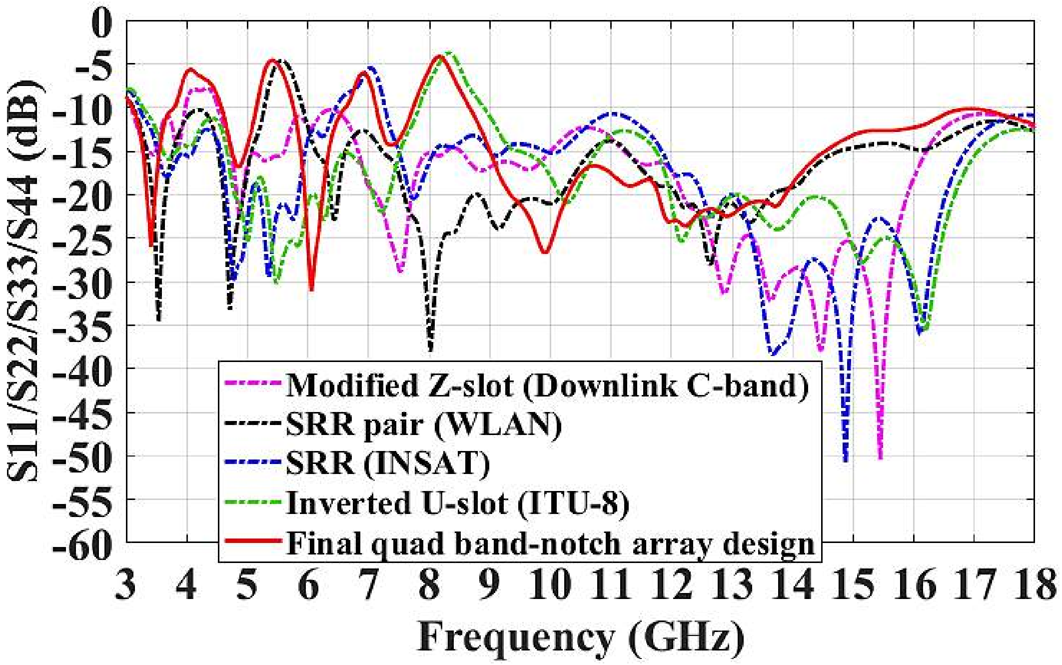

Figure 5.33 Simulated $S_{11}/S_{22}/S_{33}/S_{44}$ (dB) curves across the entire range of operation on the integration of four different notch structures in the designed quad-port UWB antenna design

Table 5.12 Numerically evaluated and simulated (CST MSW) length of four stopband structures

Length ↓/Band notch→	C-band (downlink)	WLAN	INSAT (uplink)	ITU-8
Theoretical (mm)	11.6	16.6	13.28	11.13
Simulated (mm)	12.5	17.9	15.5	12.3
Error	0.077	0.078	0.16	0.1

5.4.3 Parametric optimization of each stopband structure and study of the surface current

As described earlier, to get rid of the critical interference owing to some narrowband applications, the UWB arrays are built-in with band-suppression capability. Besides this characteristic, a variety of modern-day communication devices also urge independent stopband operability. For further study, in this section, the optimization of the overall length of every notch structure is executed on an individual basis by altering only one parameter value that is ‘y’ (an arm of a modified Z-slot), ‘a’ (an arm of rectangular SRR pair), ‘l’ (an arm of rectangular SRR) and ‘u’ (inverted U-slot arm), while considering other design variables steady. The observations from Figure 5.34(a-d) depict that by rising the parametric values of ‘y’ (1.3mm to 1.7mm), ‘a’ (6.2mm to 6.6mm), ‘l’ (4.9mm to 5.5mm), and ‘u’ (5mm to 5.6mm), the central band-stop resonance of the respective notched band moves from the higher to lower frequency side, however other rejected bands are the same. In nutshell, all stop-bands are mutually independent and the required notch resonance can be achieved easily by a suitable selection of values and placement of each notch element.

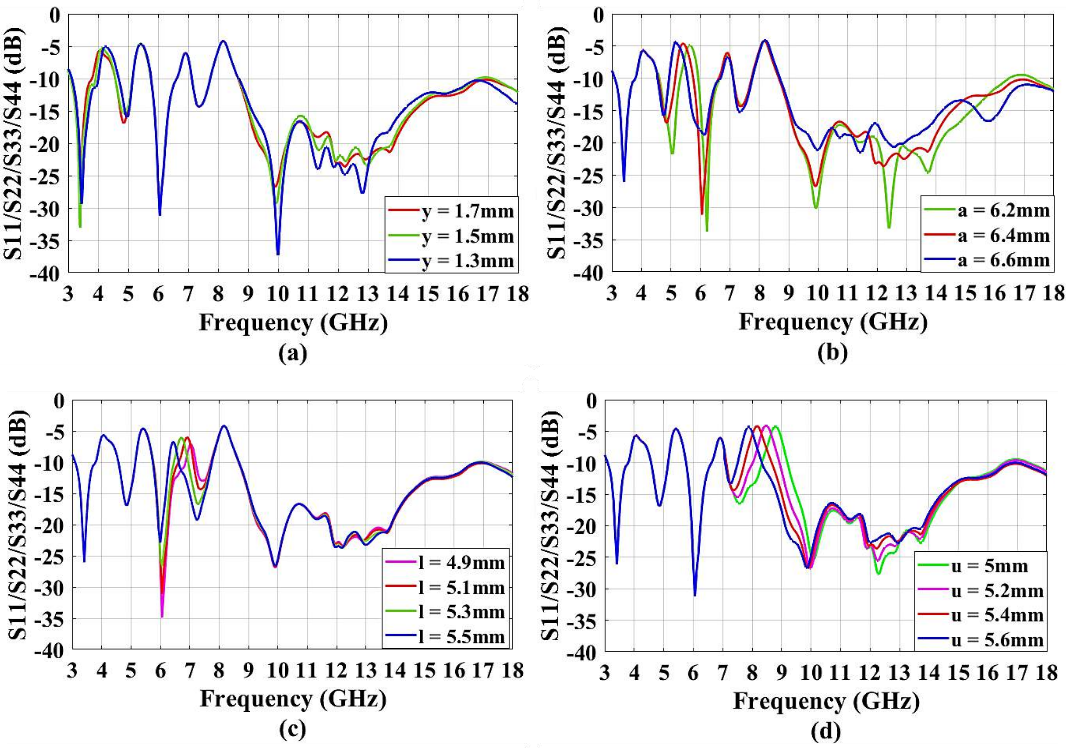

Figure 5.34 Various $S_{11}/S_{22}/S_{33}/S_{44}$ (dB) versus frequency curves for distinct values of (a) 'y' for modified Z-slot (b) 'b' for SRR pair (c) 'l' for SRR (d) 'u' for inverted U-slot

The band-suppression mechanism of the designed UWB array is further explored by perceiving the current flow (A/m) on the surface of circular radiators, microstrip feedlines, and reduced ground structure at the notch resonances of 4.01GHz (downlink C-band), 5.41GHz (WLAN), 6.882GHz (INSAT) and 8.18GHz (ITU-8). By stimulating the array port-1 with IW power, Figure 5.35(a-d) reports a greater concentration of current around the edges of the modified Z-shaped slot (133.978A/m), rectangular SRR pair (340.135A/m), rectangular SRR (352.78A/m) and inverted U-shaped slot (383.5A/m) at 4.01GHz, 5.41GHz, 6.882GHz and 8.18GHz notches respectively. It can be inferred that each notch element reserves a maximal EM energy and works as a non-radiator which eventually results in mismatch losses and inferior return loss performance in the respective notched range.

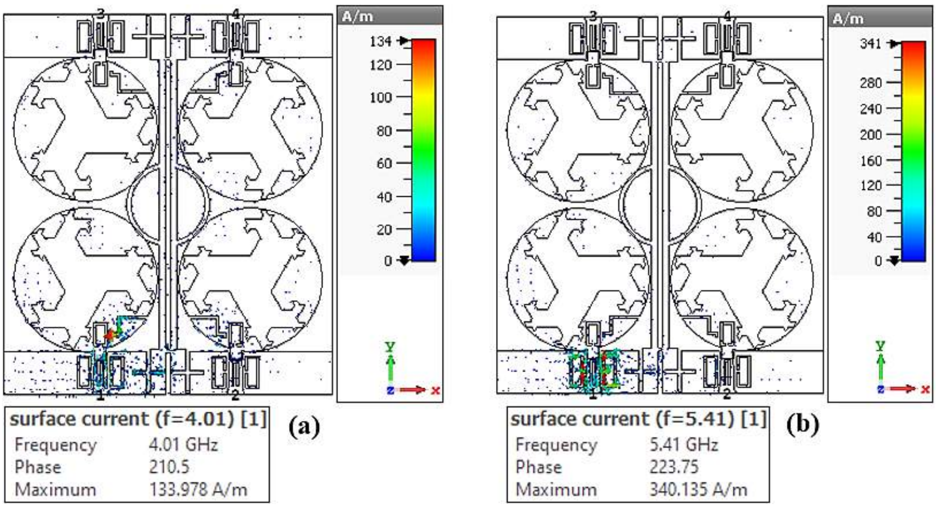

surface current (f=4.01) [1]
Frequency 4.01 GHz
Phase 210.5
Maximum 133.978 A/m

surface current (f=5.41) [1]
Frequency 5.41 GHz
Phase 223.75
Maximum 340.135 A/m

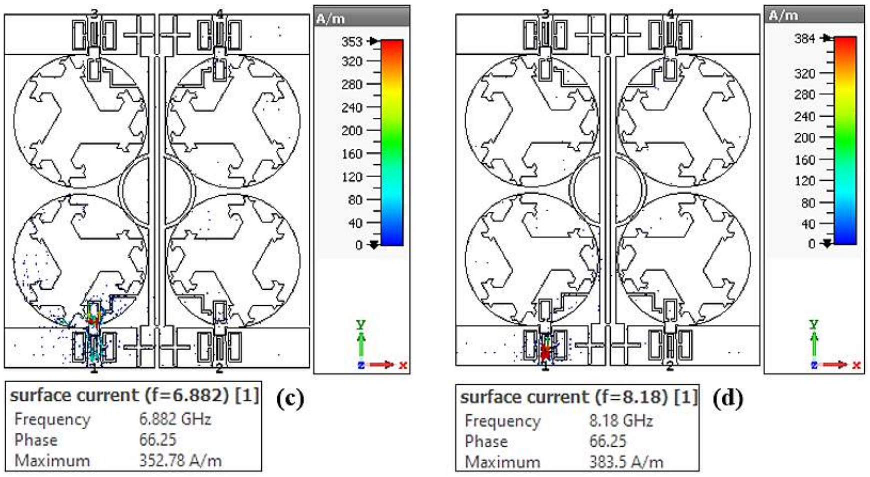

Figure 5.35 Current distribution on the array surface at (a) 4.01GHz (radiator) (b) 5.41GHz (ground) (c) 6.882GHz (radiator) (d) 8.18GHz (feedline) notches with triggered port-1

5.4.4 Results accomplished from simulation and measurement

To practically vindicate the simulated array's application in a rich scattering medium, it is fabricated utilizing the photolithography method on a dielectric FR4 substrate ($\varepsilon_r = 4.4$) with 1.57 mm thickness. The fabricated four-port UWB notched antenna fused with four SMA connectors at the feed points is represented in Figure 5.36(a, b).

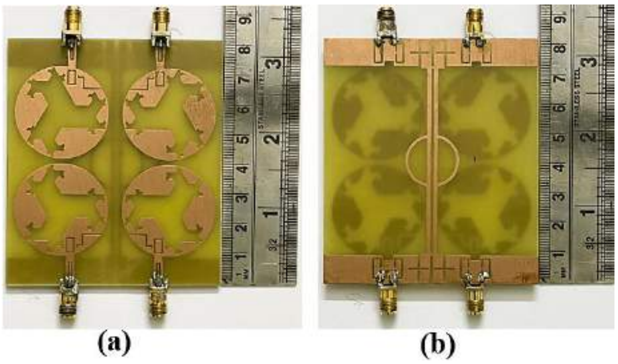

Figure 5.36 Fabricated quad-port fractal antenna design displaying (a) top view (b) rear view

5.4.4.1 Scattering parameters

The plots indicating the variation between the software-simulated and experimental S-parameters are displayed in Figure 5.37 (a-d). Observations report that the designed array effectively filters out the interfering C-band (downlink), WLAN, INSAT (uplink), and ITU-8 narrow bands from the operational simulated and measured frequency bandwidth while sustaining an adequate degree of isolation (simulation: $S_{21} \leq -18.01$dB, $S_{31} \leq 17.9$dB, $S_{41} \leq -20.23$dB, tested: $S_{21} \leq -18.12$dB, $S_{31} \leq -17.32$dB, $S_{41} \leq -20.39$dB) between the four radiating elements of the array. The experimental results display a reasonable match with the software ones with a little disparity that could be a result of erroneous connector soldering at feed points, fabrication imprecision, leakages from the power supply cable, and reflections from the miscellaneous equipment as S-parameter measurements are conducted in standard laboratory settings. Table 5.13 reveals the deviation of simulation outcomes of the designed UWB notched array from the tested ones at the four suppressed bands in form of rejection range and central notch resonance.

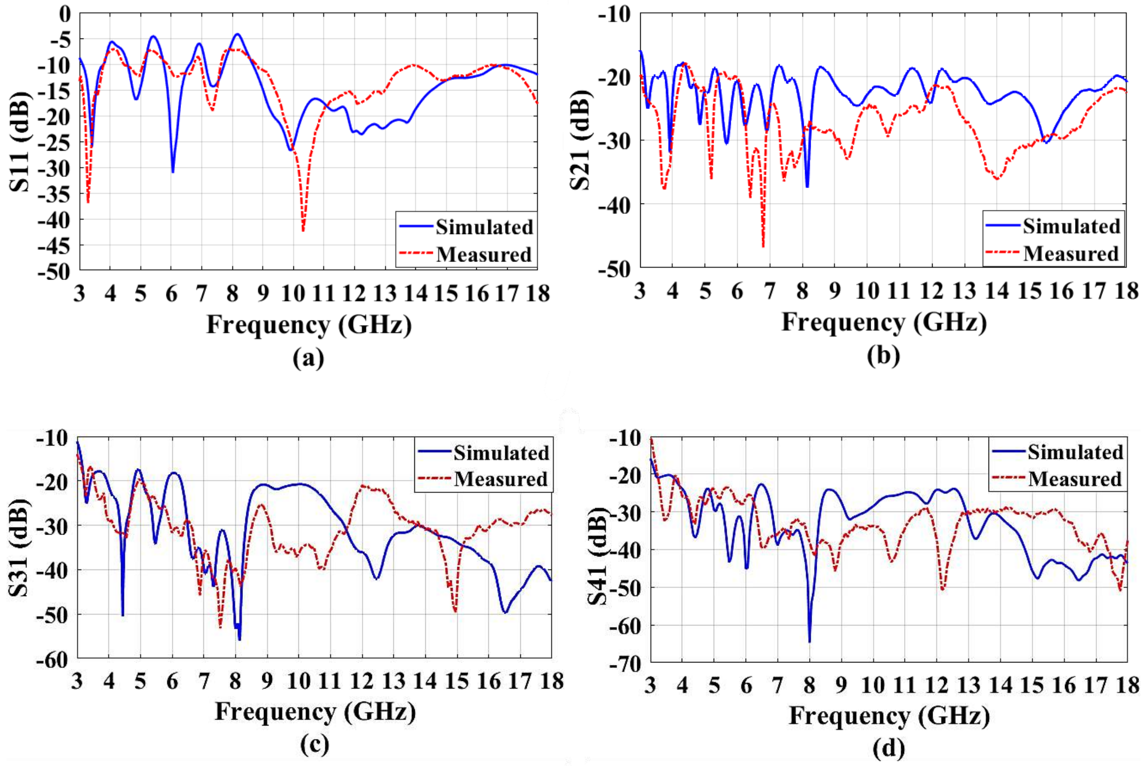

Figure 5.37 (a) S_{11} (b) S_{21} (c) S_{31} (d) S_{41} responses (simulated and tested) across the functional bandwidth of the designed UWB array with the quad band-stop capability

Table 5.13 Simulation and test results of the designed UWB array at the four-notch bands

Features/ Notched narrow bands	C-band (Downlink)	WLAN	INSAT (Uplink)	ITU-8
Allotted bandwidth (GHz)	3.7-4.2	5.15-5.85	6.725-7.025	7.9-8.5
Simulated notch band (GHz)	3.76-4.58	5.15-5.77	6.647-7.118	7.765-8.647
Measured notch band (GHz)	3.76-4.48	5.12-5.84	6.74-7.04	7.65-8.72
Allotted notch resonance (GHz)	3.95	5.5	6.875	8.2
Simulated stopband resonance (GHz)	4.01	5.41	6.882	8.18
Measured stopband resonance (GHz)	4.08	5.36	6.88	8.24

5.4.4.2 Far-field Properties

As presented in Figure 5.38(a-d), the normalized 2D radiation pattern (both simulated and experimented) of the designed UWB notched array (activated port-1) is visualized along the y-z plane and x-z plane at the passband frequencies of 3.47GHz, 6.05GHz, and 9.88GHz respectively. Based on the observations at the three frequencies, a directional and quasi-directional polar pattern is indicated in the y-z and x-z planes respectively. The measured far-field pattern shows a close agreement with the software patterns. A slight deviation between tested/simulated patterns arises as a result of faulty soldering of SMA connectors, fatal fabrication challenges, and potential reflections from non-energized antenna ports. By activating antenna port-1, Figure 5.39 shows the gain response for the entire operational range of the designed UWB array (with and without notches). The primary quad-port UWB array offers a 4.14dBi average gain across the simulated functional range with 6.028dBi (at 14GHz) being the highest gain value. By incorporating the band-stop feature in the designed UWB array, the gain values decline significantly at the four notches which evidences the unresponsive operation in the respective stop-bands (downlink C-band, WLAN, uplink INSAT, and ITU-8). For the proposed UWB notched array, the simulated and experimental values of gain fluctuate from -1.781 to 5.258dBi and -1.402 to 5.36dBi respectively throughout the frequency bandwidth, therefore, presenting a favorable match that is required for the adequate real-time operation of UWB communication systems.

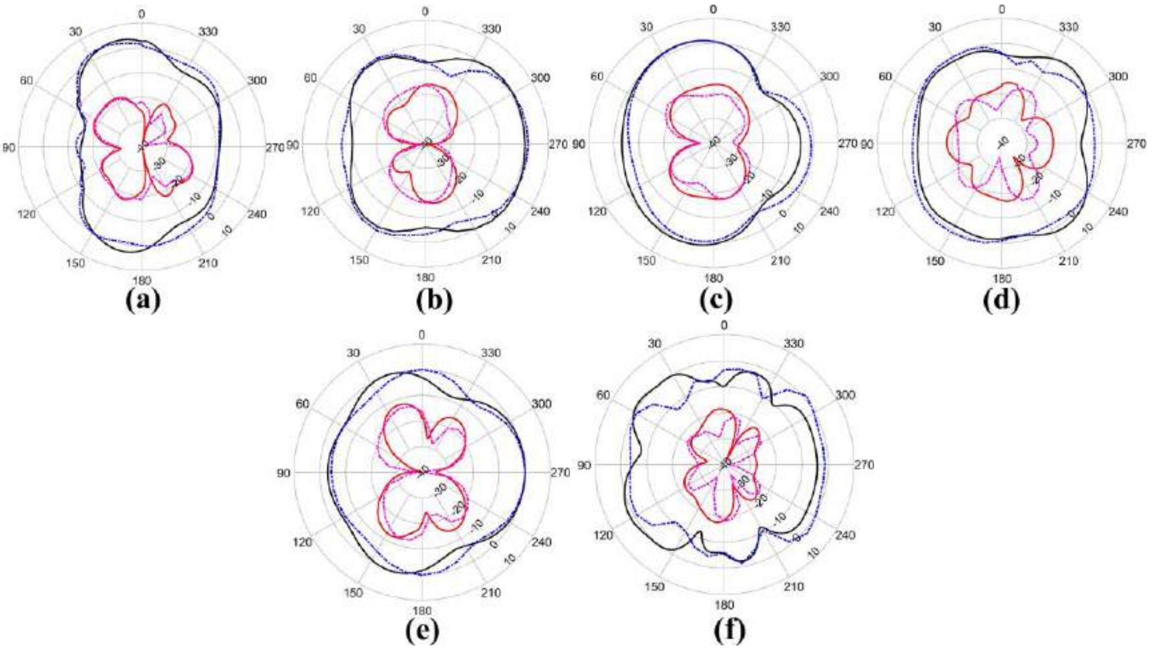

━━	**Co-polarization (Simulated)**	‒ · ‒	**Co-polarization (Measured)**
━━	**Cross-polarization (Simulated)**	‒ · ‒	**Cross-polarization (Measured)**

Figure 5.38 Polar pattern plots (simulated/measured) for triggered port-1 at (a) 3.47GHz (y-z plane) (b) 3.47GHz (x-z plane) (c) 6.05GHz (y-z plane) (d) 6.05GHz (x-z plane) (e) 9.88GHz (y-z plane) (f) 9.88GHz (x-z plane)

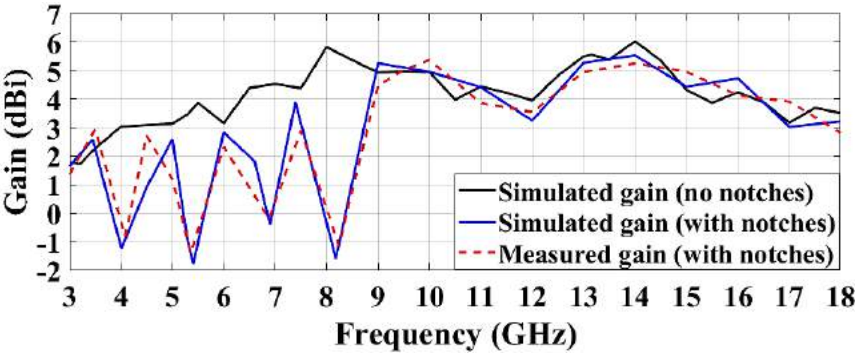

Figure 5.39 Gain plots (Simulated/tested) against frequency by energizing port-1

5.4.5 Analysis of Diversity Parameters

To adequately govern the array’s functionality in a real propagation scenario, several MIMO metrics are estimated and evidenced by the measured values. The variation of simulated and tested performances of the diversity metrics for the complete frequency bandwidth are illustrated in Figure 5.40 (a-e).

The simulated and experimental values of the aforementioned ECC, DG, MEG, CCL, and TARC for the complete frequency range are highlighted in Table 5.14. The values of diversity parameters namely ECC, DG, MEG, CCL, and TARC are estimated by the S-parameter approach using Equation 32 (chapter 4), Equation 3 (chapter 1), Equation 33 (chapter 4), Equation (34, 35) (chapter 4) and Equation 36 (chapter 4) respectively. Various diversity operation metrics inhere within their permissible standard limits make the designed four-port array appropriate for implementation in rich propagation environments (exposed to fading effects), therefore, preferable for UWB-MIMO communication systems.

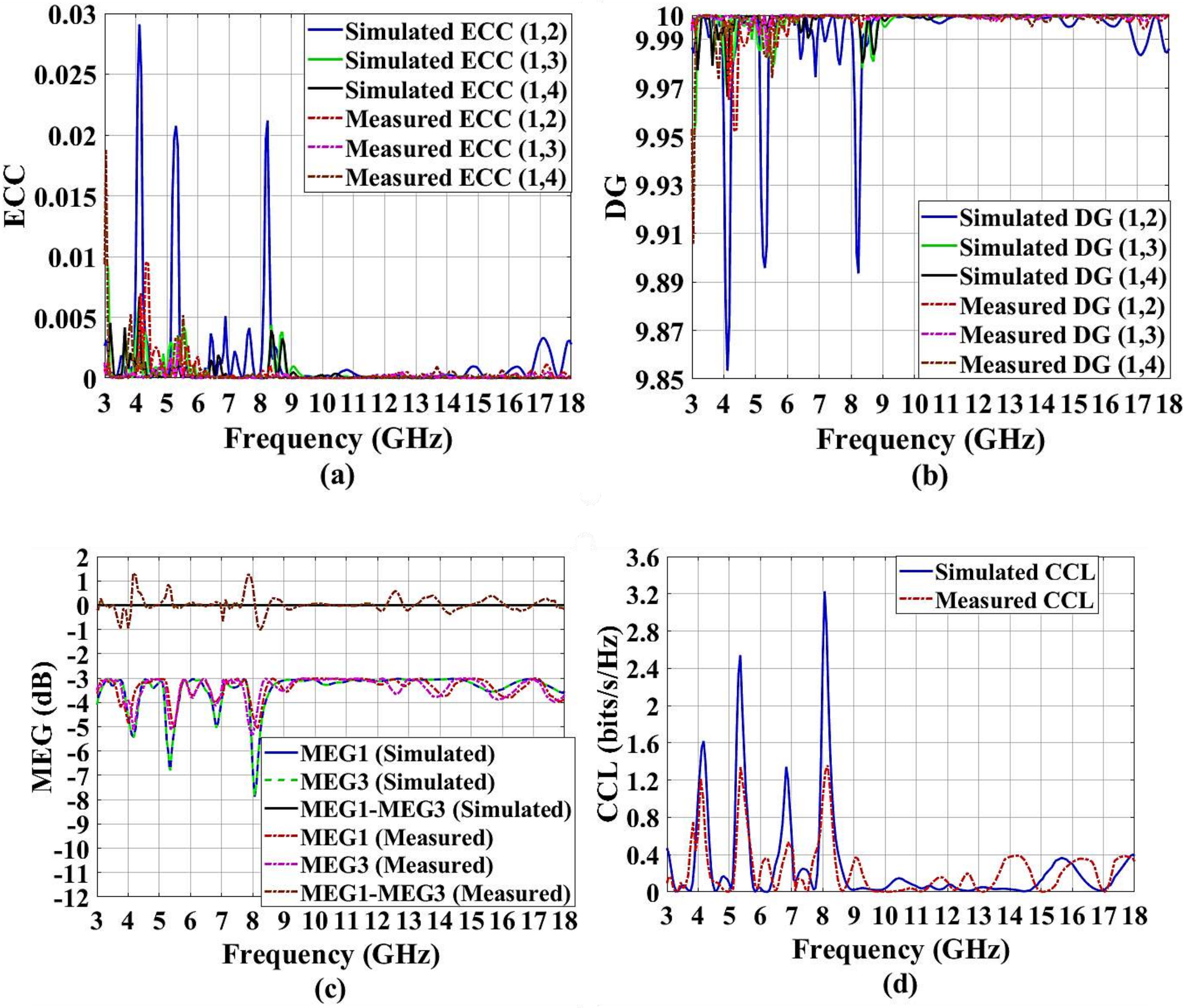

(a)

(b)

(c)

(d)

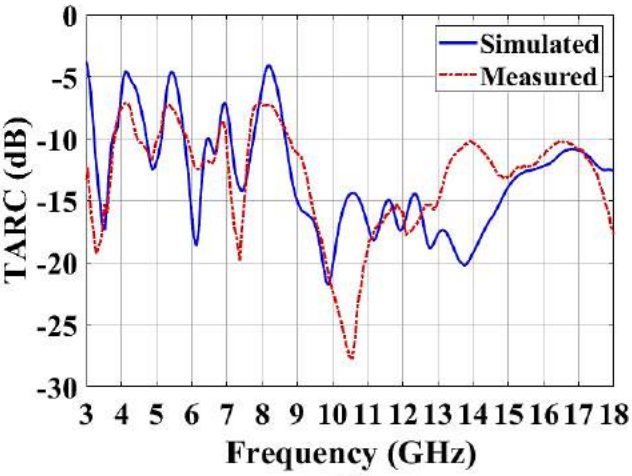

(e)

Figure 5.40 Simulated and experimental curves of (a) ECC (b) DG (c) MEG (d) CCL (e) TARC for the entire range of operation

Table 5.14 Simulation and measurement values of MIMO parameters for the whole excited band

Metrics	ECC		DG		MEG (dB)		CCL(bits/s/Hz)		TARC (dB)	
	S-parameter		S-parameter		S-parameter		S-parameter		S-parameter	
	Sim.	Test.	Sim.	Test.	Sim.	Meas.	Sim.	Test.	Sim.	Test.
Proposed array with band notches	≤0.029	≤0.009	≥9.85	≥9.95	≤-7.87	≤-5.34	≤ 0.4 (operation range)	≤ 0.4 (operation range)	≤-4.066	≤ -7.07

5.5 Conclusion

The present chapter covers the second objective of the proposed doctoral study. Here, two dual-element and two quad-port fractal MIMO antennas, already designed for UWB characteristics in chapter 3 and chapter 4 respectively, are incorporated with different band-notch structures to suppress the EMI associated with various narrow bands applications prevalent in the excited UWB of operation. All the proposed UWB fractal arrays are successfully modeled, simulated, and experimentally verified to realize multi-band reject functionality. In the first design, the dual-port Pythagorean tree fractal (2nd iteration) UWB antenna successfully rejects the three interfering ranges (downlink C-band: 3.81-4.16GHz, WLAN: 5.22-5.84GHz, X-band: 7.84-8.44GHz) coherent in the functional UWB spectrum (3.71-10.64GHz) by incorporating dual L-shaped slits, a U-shaped slot, and an SRR pair respectively in each feedline of the proposed array. In the second design, a dual-port transformed Koch Anti-Snowflake fractal (3rd iteration) UWB antenna is designed for filtering six interfering narrow bands from an excited operational band (2.48-15.42 GHz) with an optimum isolation performance. For realizing the stop-band functionality at WiMAX (3.3-3.78 GHz), INSAT (reception: 4.52-4.9GHz), WLAN (5.16-5.84GHz), super-extended C-band (6.3-6.93GHz), ITU-8 (7.63-8.62GHz) and amateur radio

(9.96-10.52GHz) bands, the proposed UWB array is incorporated with six different band-stop elements namely a Z-shaped slit (patch), inverted L-shaped slit (patch), pair of L-shaped slits (reduced ground plane), two rectangular SRR pairs (feedline) and G-shaped slot (feedline) respectively. In the third design, a quad-port aperture-coupled Sierpinski gasket fractal (iterated to 2nd order) antenna is successfully employed to realize triple stopband ability from the excited UWB range (3.07-11GHz). To curb the EM interference caused by C-band (at 4.01GHz), WLAN (at 5.56GHz), and radio-location (at 8.8GHz) band in the working UWB range, three distinct notch structures namely circular SRRs, U-shaped slot, and rectangular SRRs are integrated into each feedline of the array geometry. In the fourth design, a four-element, microstrip-fed, hen-shaped fractal (4th iteration order) MIMO antenna is effectively modeled and analyzed in this article for UWB operation with quad-band suppression ability. To eliminate the interfering C-band (downlink satellite: 4.01GHz), WLAN (at 5.56GHz), (uplink satellite: 6.882GHz), and ITU-8 (at 8.18GHz) from the functional UWB range, four distinct band-stop elements namely modified Z-shaped slot (patch), rectangular SRR pair (reduced ground), rectangular SRR (patch) and U-shaped slot (feedline) are loaded in the array design.

All the above-proposed array designs exhibit admissible values of MIMO metrics like ECC, DG, MEG, CCL, and TARC that justify the application of the designed arrays for SNR enhancement using the diversity combining approaches. Satisfactory proximity between the simulation and experimental outcomes (in terms of working UWB range, inter-element isolation, radiation properties, and MIMO performance parameters) evidences the implementation of proposed arrays in futuristic real-world UWB-MIMO applications.

CHAPTER 6

Conclusion and Future Scope

The key target of the doctoral study formulated in this thesis is to effectively model and develop some compact-sized fractal MPA arrays in MIMO configuration to operate in a UWB spectrum along with band-notch operation. In this context, five dual-port and two quad-port fractal MIMO antennas with UWB characteristics have been designed and developed to be utilized in portable 4G/5G UWB communication devices. Further, to surmount the EMI introduced by some narrow bands pre-existing in the operational UWB range, four of the previously designed UWB fractal arrays are integrated with the band-notch capability. The next sections of this chapter summarize the conclusions set out and the future scope of the research performed in this thesis.

6.1 Conclusion

The tremendous development in the sector of mobile wireless technology (from the current 4G to the upcoming ultra-fast 5G standard) has increased the demand for incorporating high-speed, economical, wideband, and low-powered UWB antennas in modern wireless devices. Nowadays, the UWB-MIMO communication systems are captivating the interests of many researchers to enhance data transmission rate, channel capacity, and system reliability. Therefore, the three key challenges namely compactness, optimum isolation, and rejection of the interfering bands (in excited UWB range) involved while modeling multi-port UWB antennas for modern wireless gadgets drive the research conducted in this thesis.

In this context, some fractal MPA arrays in MIMO configurations are reported in this thesis work to realize the desired antenna performance in terms of large bandwidth of operation, optimal inter-element isolation response, compact dimensions, and multi-band-notch ability acceptable for UWB communication systems. The summary of the proposed doctoral research is demonstrated in the form of a flowchart in Figure 6.1.

Chapter 1 presents the basic introduction to fractal UWB-MIMO antennas and the necessity to conduct the research study in this thesis. Chapter 2 details extensive research reported in the field of development and usage of different fractal geometries in the design of multi-port MPAs for UWB communication systems that further aids in identifying the research gaps and formulating the objectives for the proposed doctoral work. The research performed in the context of the modeling and development of fractal antenna arrays for UWB characteristics is described in the succeeding chapters as per each objective of the proposed doctoral research work.

Chapter 3 covers the first objective of the proposed research work. It includes the design, simulation, and experimental investigation of six different two-port MIMO antenna configurations integrated with different fractal (Sierpinski Gasket, Pythagorean tree, Circular, Koch curve, Koch Snowflake, and Koch Anti-Snowflake) and DGS geometries for UWB communication systems.

The first design presents a two-layered, dual-element Sierpinski gasket fractal antenna with two Sierpinski gasket equilateral triangular fractal patches (up to 2nd order of iteration) printed on the top FR-4 substrate layer to achieve a multiband performance. The feed network of the proposed array has a DGS and feedlines printed on the lower FR-4 substrate layer (top and bottom respectively). The fractal patches excited through an aperture-coupled feed scheme, where apertures etched in the ground are modified to archimedean spirals interconnected with an ‘X’ slot to enhance the operational bandwidth and allow the array to show simulated UWB properties from 4.3-11.6 GHz. The spacing between two fractal patches is optimized to achieve an optimal inter-element isolation ($S_{12}/S_{21} \leq -15.8$ dB) response. Further, the fabricated array is tested for S-parameters and radiation characteristics which are found to be in good agreement with the simulated ones. Several diversity performance parameters like ECC, DG, MEG, and CCL are also investigated and are found to lie within their standard levels. A size reduction of 46% as compared to a conventional MPA is also obtained for the proposed fractal MPA array.

The second design presents a dual-port aperture coupled MPA array integrated with circular fractal geometry. The array is designed on dual FR4 substrates where the upper substrate is composed of two circular fractal patches, optimized up to 2nd iteration for exciting multiple resonances. The lower FR4 substrate consists of a metallic ground plane with DGS (top) and two microstrip feedlines (bottom). The apertures etched from the metallic ground are converted to rectangular spirals and a tree-shaped slots to realize the desired frequency bandwidth from 4.6-16.8 GHz with a high isolation performance between the array elements. The proposed array provides a good diversity performance in terms of low ECC, high DG, low CCL, high MEG, and acceptable TARC. A reasonable agreement is achieved between the simulated and tested results of the proposed fractal MPA array. Therefore, it is concluded that the proposed array satisfies the UWB-MIMO criterion of low-profile, high FBW, good port-to-port isolation, and acceptable diversity performance which makes it a good candidate for 4G/5G, satellite/radar imaging, and ISS communication systems.

The third design reports a dual-port Pythagorean tree fractal UWB antenna, arranged on a pair of 1.57 mm thick FR-4 substrates. Two modified Pythagorean tree fractal patches (optimized up to 2nd iteration order) designed on the upper substrate surface are mainly responsible for realizing a multi-resonant performance. To facilitate the coupling mechanism from the transmission lines to the radiating fractal elements, two apertures (arranged centrally under the radiators) are truncated from the common ground surface. These apertures are further modified to two complementary hexagonal spiral DGS (interlinked by an X-shaped slot), designed to cover a wide UWB range of 3.71-10.64 GHz with a good degree of port-to-port isolation. A considerable agreement is realized between the simulation and measurement performances (in form of fractional bandwidth, inter-element isolation, radiation properties, and diversity parameters) which justifies the practical workability of the proposed UWB array.

The fourth design reports a dual-port, microstrip-fed semi-circular MPA array combined with Koch curve fractal geometry, engraved on a 1.57 mm thick FR-4 substrate. The parametric analysis of the proposed array indicates that the two optimized Koch curve fractal (2nd iteration order) radiators (upper substrate layer) provide optimum matching performance in a wide operational band (4.395-10.184 GHz) and minimize the patch area by 41.2% as compared to the conventional circular patch. To realize good port-to-port isolation, the reduced ground is slotted and incorporated with a funnel-shaped decoupling structure at the center. The prototype of the proposed array is fabricated and experimentally tested to justify the simulated S-parameter results. The simulation and experimental diversity characteristics like ECC, DG, MEG, CCL, and TARC lie within the standard levels and show a good resemblance.

The fifth design presents a compact, two-element fractal MPA array with a partial ground structure, configured on a 1.57mm thick FR4 substrate. Each circular radiator is defected with a modified Koch-Snowflake fractal (4th iteration) to achieve a size miniaturization of 46.7%. The array yields a 3.3-18GHz band by defecting the partial ground and offsetting the tapered feedlines. By embedding an H-shaped decoupler and plus-shaped slots in the ground, significant isolation is accomplished. Various diversity metrics are investigated and are found to follow their permissible standards. To justify the simulated results, the fabricated array is tested where a favorable match between the results makes it a suitable candidate for high data-rate wireless applications.

The sixth design presents a compact, dual-port fractal UWB antenna, modeled on a readily available FR4 substrate. It consists of two microstrip-fed modified Koch anti-snowflake fractal (iterated up to 3rd order) patches and a defected ground configuration, aimed to achieve 144.6% fractional bandwidth (2.48-15.42GHz) with optimum isolation characteristics ($S_{21}/S_{12} \leq -17$dB). The proposed fractal geometry minimizes the patch area by 42.4% as compared to the circular configuration. Various diversity parameters for the designed array are examined and are found within their permissible levels. The experimental results of the fabricated array present an acceptable resemblance with the simulated ones, therefore assuring the practical implementation of the designed array in UWB communication systems.

In a nutshell, it is observed that each above-mentioned fractal geometry excites multiple frequency bands and a DGS which is resonant at the same bands can be used to improve the impedance bandwidth for the antennas in the array configuration. Table 6.1 highlights the simulated and measured responses of the aforementioned fractal MPA arrays for UWB applications.

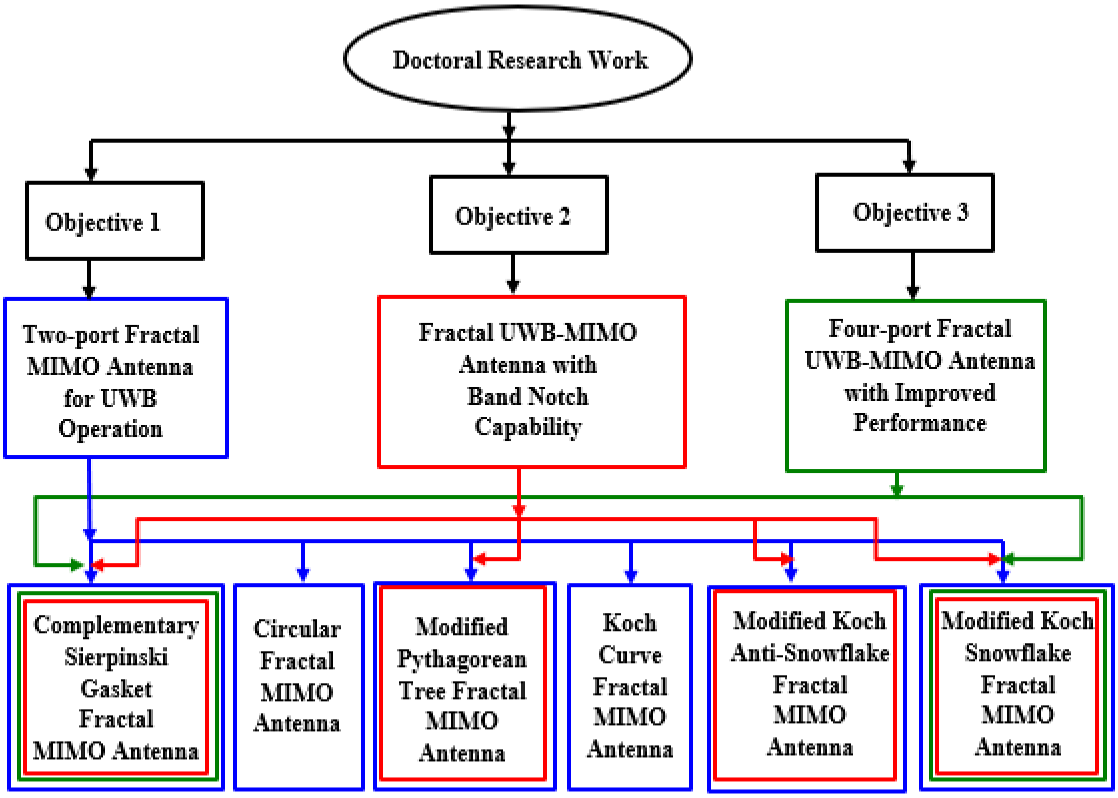

Figure 6.1 Flow chart of the proposed research objectives

Table 6.1 Simulated and measured performances of the proposed fractal MPA arrays for UWB applications

No. of ports	Design	Total area (mm^2)	Feeding Technique	Operational band (GHz)	Minimal Isolation (dB)	Peak ECC	Maximum gain (dBi)
2	Complementary Sierpinski gasket fractal MIMO antenna	41×99.4	Aperture coupled	Simulated: 4.3-11.6 Measured: 4.1-4.25, 4.7-5.3, 5.7-12	Simulated :15.8 Measured :17.9	Simulated :0.002 Measured :0.006	Simulated :4.7 Measured :4.32
2	Circular fractal MIMO antenna	34×68.7	Aperture coupled	Simulated: 4.6-16.8 Measured: 4.7-5.3 7.44-7.92 8.48-17	Simulated :19 Measured :23.24	Simulated :0.001 Measured :0.007	Simulated :4.57 Measured :4.12
2	Modified Pythagorean Tree fractal MIMO antenna	37.5×81.5	Aperture coupled	Simulated: 3.7-10.64 Measured: 3.495-11.73	Simulated :16.1 Measured :15.4	Simulated :0.006 Measured :0.003	Simulated :4.34
2	Koch curve fractal MIMO antenna	30.5 × 47	Microstrip line	Simulated: 4.395-10.184 Measured: 4.6-10.45	Simulated :16.8 Measured :19.3	Simulated :0.0021 Measured :0.0023	Simulated :3.84 Measured :3.81

2	Modified Koch-Snowflake fractal MIMO antenna	41×71	Microstrip line	Simulated: 3.3-18 Measured: 3.28-18	Simulated: 16 Measured :17.4	Simulated :0.02 Measured :0.03	Simulated :5.39 Measured :5.19
2	Modified Koch Anti-Snowflake fractal MIMO antenna	29.5×43.5	Microstrip line	Simulated: 2.48-15.42 Measured: 2.34-15.52	Simulated :17 Measured :18.1	Simulated :0.009 Measured :0.0089	Simulated :5.16

Chapter 4 states the modeling, simulation, and measurement analysis of two quad-element fractal UWB MPA arrays, covering the third objective of the proposed research work. Here, the formerly reported dual-port complementary Sierpinski gasket and modified Koch snowflake fractal MPA arrays (in chapter 3 for objective 1) are extended to four-port MPA array configurations to realize an enhanced operational performance in terms of fractional bandwidth, port-to-port isolation, and diversity performance metrics.

The first design presents a quad-port, aperture-coupled complementary Sierpinski gasket fractal (iterated to 2nd order) UWB MPA array, successfully developed and experimentally examined on a pair of 1.57mm thick FR4 substrates. By introducing some modifications in the metallic ground with spiral-shaped DGS and offsetting the transmission lines (as compared to the dual-port Sierpinski gasket fractal UWB array designed in chapter 3), the designed array effectively provides an improved UWB of operation from 3.07-11GHz. An optimum isolation response between the antenna ports is realized by carefully selecting the distance between the antenna units and truncating an X-shaped slot from the center of the ground. For application in receive diversity techniques, various MIMO operation metrics are examined and are found to lie within their acceptable standards. A favorable approximation between the simulated and experimental outcomes (in terms of the operational band, isolation, far-field characteristics, and diversity metrics) affirms the realistic operability of the designed UWB-MIMO antenna.

In the second design, a four-element, microstrip-fed, modified Koch Snowflake fractal (4th iteration order) antenna is effectively modeled on a 1.57mm thick FR4 substrate and analyzed for UWB characteristics. By employing the principle of DGS and modifying the feedline geometries (tapering and offsetting) as compared to dual-port 4th iterative Koch Snowflake fractal MIMO antenna design presented in chapter 3, the multi-band frequency response generated by fractal geometry is efficiently converted into an improved UWB performance (3.1-18GHz). A considerable isolation behavior is accomplished by carefully optimizing the separation distance between the array elements and incorporating the decoupling network (vertical ground stubs and semi-circular rings) in the common ground plane. The admissible values of MIMO parameters like ECC, DG, MEG, CCL, and TARC justify the application of the proposed array for SNR enhancement using the diversity combining approaches. Satisfactory proximity between the simulation and experimental outcomes (in terms of working UWB range, inter-element isolation, radiation properties, and MIMO performance parameters) evidences the array's implementation in futuristic real-world UWB-MIMO applications.

Observations from the above-mentioned quad-port array designs state that by employing the concept of offset-feeding and introducing some modifications in the ground plane geometry, the above-designed four-port fractal MPA arrays offer an improved impedance bandwidth, inter-element isolation, and diversity performance response as compared to the dual-port array designs reported in chapter 3. Table 6.2 highlights the simulated and tested results of the aforementioned quad-port fractal MPA arrays for UWB applications.

Table 6.2 Performance comparison of the proposed quad-port fractal UWB MPA arrays

No. of ports	Design	Total area (mm^2)	Feeding Technique	Bandwidth (GHz)	Minimum Isolation(dB)	Maximal ECC	Peak gain (dBi)
4	Complementary Sierpinski gasket fractal MIMO antenna	80×99.4	Aperture coupled	Simulated: 3.07-11 Measured: 3.12-12	Simulated: 16.19 Measured: 16	Simulated: 0.004 Measured: 0.006	Simulated :4.88
4	Modified Koch-Snowflake fractal MIMO antenna	80×71	Microstrip line	Simulated: 3.1-18 Measured: 3.21-18	Simulated: 18 Measured: 16.6	Simulated :0.006 Measured :0.02	Simulated :6.028

Chapter 5 covers the second objective of the proposed doctoral work. Here, the previously modeled two-port (Pythagorean Tree and Koch Anti-Snowflake) and four-port (Sierpinski Gasket and Koch Snowflake) fractal UWB MPA arrays (in chapter 3 and chapter 4 respectively) are integrated with different notching elements structures to suppress the interference resulting from various undesired narrowband applications, pre-existing in the working UWB range. For justifying their realistic operation, the experimental analysis (S-parameters, radiation, and diversity performance parameters) of the fabricated array prototypes is also performed.

The first design proposes to accomplish triple band-suppression characteristics from the formerly reported dual-port modified Pythagorean Tree fractal UWB array in Section 3.3 (chapter 3). Therefore, three different stop-band structures namely two L-shaped slits, a U-shaped slot, and an SRR pair are incorporated in each feedline of the proposed array to eliminate the problem of unwanted interference resulting from satellite communication in the C-band (space to earth 3.81-4.16 GHz), WLAN (5.22-5.84 GHz) and satellite communication in X-band (earth to space 7.84-8.44 GHz) respectively, coherent in the functional UWB spectrum (3.7-10.64 GHz) while retaining good port-to-port isolation characteristics. It can be inferred from the parametric optimization of each notch element that the desired operating bandwidth and resonant frequency for a rejection band can be controlled by correctly adjusting the parametric values and position of the respective band-notch structures. Observations also indicate that variation in the total notch length of one rejection band negligibly influences other rejection bands. Hence, all three rejection bands are mutually independent of each other. For the notched UWB array, a sharp reduction in gain is observed at the three stop-band frequencies which verifies the negligible radiation and non-responsive behavior of the designed MIMO antenna in the respective rejection bands (downlink C-band, WLAN, and uplink X-band). Simulated results show a good similitude with the experimental ones.

In the second design, a dual-port modified Koch Anti-snowflake fractal UWB antenna (previously modeled in Section 3.6 in chapter 3) is simulated and experimentally verified for

UWB performance with hexa-band suppression functionality. To realize the band-notch characteristics, various notch geometries are incorporated in each of the patches (Z-shaped slit and inverted L-shaped slit), feedline (two rectangular SRR pairs and G-shaped slot), and the reduced ground (pair of L-shaped slits) to introduce notches at 3.46GHz (WiMAX), 4.78GHz (INSAT), 6.57GHz (super extended C-band), 8.23GHz (ITU-8), 10.22GHz (amateur radio) and 5.55GHz (WLAN) frequencies respectively, prevalent in the operational UWB range (2.48-15.42 GHz). A detailed parametric analysis is done to better understand the effect of dimensional variations of these band notch structures on the specific rejection bands. It is observed that the desired transition in the rejection band can be easily realized as per the demand while retaining an optimum UWB behavior as all notched bands are almost interdependent of each other. At last, the array prototype is fabricated and a good match is achieved between the simulated and tested results.

The third design targets to achieve triple band-stop operation from the formerly reported quad-port Sierpinski Gasket fractal array designed in Section 4.1 (chapter 4). So, to curb the EMI caused by the C-band (at 4.01GHz), WLAN (at 5.56GHz), and radio-location (at 8.8GHz) band in the working UWB range (3.07-11 GHz), three distinct notch structures namely circular SRRs, U-shaped slot, and rectangular SRRs are integrated into each feedline of the array design. A close resemblance is realized between the simulated and theoretically assigned notch ranges. Also, the proposed band-stop UWB-MIMO antenna shows a substantial decrease in gain values at the three rejection resonances which justifies that the array is not responding in the corresponding rejection ranges (downlink satellite C-band, WLAN, and radio location). The proposed array exhibits a reasonable similitude between simulated and tested results. The admissible levels of various diversity metrics (ECC, DG, MEG, CCL, and TARC) of the designed four-port UWB antenna with stopbands verify the accomplishment of considerable diversity operation imperative for MIMO communication systems.

The fourth design aims to realize quad band-reject functionality from the previously designed quad-port Koch Snowflake fractal MIMO antenna (Section 4.2 in chapter 4). So, to eliminate the interfering C-band (downlink satellite: at 4.01GHz), WLAN (at 5.56GHz), INSAT (uplink satellite: at 6.882GHz), and ITU-8 (at 8.18GHz) from the functional UWB range (3.1-18GHz), four distinct band-stop elements namely modified Z-shaped slot (patch), rectangular SRR pair (reduced ground), rectangular SRR (patch) and U-shaped slot (feedline) are loaded in the array design. Also, the parametric optimization of each notch element is carried out and it is observed all stop-bands are mutually independent and the required notch resonance can be achieved easily by a suitable selection of dimensions and placement of the respective notch element. Table 6.3 lists the simulated and tested results of the aforementioned band-stop UWB fractal MPA arrays.

Table 6.3 Performance comparison of the proposed band-notched fractal UWB MPA arrays

No. of ports	Design	Total area (mm^2)	Operational band (GHz)	Minimal Isolation (dB)	No. of Notch	Type of Notch Element	Notched range (GHz) corresponding to the interfering

							narrowband application
2	Modified Pythagorean Tree fractal MIMO antenna	37.5×81.5	Simulated: 3.7-10.64 Measured: 3.495-11.73	Simulated :16.1 Measured :15.4	3	Two L-shaped slits U-shaped slot Rectangular SRR	Simulated: 3.81-4.16 (C-band) 5.22-5.84 (WLAN) 7.84-8.44 (X-band) Measured: 4.02-4.26 (C-band) 4.95-6.13 (WLAN) 7.74-8.04 (X-band)
2	Modified Koch Anti-Snowflake fractal MIMO antenna	29.5×43.5	Simulated: 2.48-15.42 Measured: 2.34-15.52	Simulated :17 Measured: 18.1	6	Z-shaped slit Inverted L-shaped slit Pair of L-shaped slits Two rectangular SRR pairs G-shaped slot	Simulated: 3.3-3.78 (WiMAX) 4.52-4.9 (INSAT) 5.16-5.84 (WLAN) 6.3-6.93 (Super extended C-band) 7.63-8.62 (ITU-8) 9.96-10.52 (amateur radio) Measured: 2.87-3.685 (WiMAX) 4.485-5.08 (INSAT) 5.335-6.42 (WLAN) 6.72-7.1 (Super extended C-band) 7.375-8.48 (ITU-8) 9.04-10.86 (amateur radio)
4	Complementary Sierpinski gasket fractal MIMO antenna	80×99.4	Simulated: 3.07-11 Measured: 3.12-12	Simulated :16.19 Measured :16	3	Circular SRRs U-shaped slot Rectangular SRRs	Simulated: 3.62-4.31 (C-band) 5.23-5.87 (WLAN) 8.47-9.09 (radio-location band) Measured:

							3.71-4.47 (C-band) 5.25-5.9 (WLAN) 7.98-9.28 (radio-location)
4	Modified Koch-Snowflake fractal MIMO antenna	80×71	Simulated: 3.1-18 Measured:	Simulated :18 Measured: 16.6	4	Modified Z-shaped slot Rectangular SRR pair Rectangular SRR U-shaped slot	Simulated: 3.76-4.58 (Downlink C-band) 5.15-5.77 (WLAN) 6.647-7.118 (uplink INSAT) 7.765-8.647(ITU-8) Measured: 3.76-4.48 (Downlink C-band) 5.12-5.84 (WLAN) 6.74-7.04 (INSAT) 7.65-8.72 (ITU-8)

This thesis work is devoted to address the three objectives of the proposed doctoral study i.e., to model, simulate and fabricate some compact-sized, band-notched fractal MPA arrays in dual-port and quad-port MIMO configurations for UWB applications. Valuable conclusions and some novel fractal designs have been reported in this thesis work. However, the research presented in this thesis can be extended in the future to realize miniaturized MPA arrays for more efficient operational performance desired for portable 45/5G wireless devices.

6.2 Future Scope

Even though comprehensive research is conducted in this thesis to design and develop some compact-sized, two- and four-port fractal MPA arrays to accomplish UWB characteristics along with band-notch ability, there is still room for future work in this field. Some of the topics that are not considered in this thesis and can be explored in the future are listed below.

1. In this research, dual-port and quad-port MPA arrays are designed for UWB communication systems. In the future, massive MIMO antenna configurations can be developed for enhancing the performance characteristics of futuristic 5G communication devices.

2. Novel fractal geometries can be explored to design more compact-sized MPA arrays to be employed in portable electronic gadgets

3. The design of wearable MPA arrays combined with fractal geometries for biomedical applications is also an open area of research.

4. Different substrate materials such as Rogers and Taconic that are less prone to losses can be employed for designing UWB MPA arrays.
5. The improvement of MIMO antenna performance in form of operational bandwidth and gain, through the use of meta-surfaces, is also an open area of research.

References

[1] D. Porcino and W. Hirt, “Ultra-wideband radio technology: potential and challenges ahead,” *IEEE Communications Magazine*, vol. 41, no. 7, pp. 66-74, 2003, doi: 10.1109/MCOM.2003.1215641. T.

[2] Nahar and S. Rawat “Survey of various bandwidth enhancement techniques used for 5G antennas,” *International Journal of Microwave and Wireless Technologies*, vol. 14, no. 2, pp. 204-224, 2022, doi: 10.1017/S1759078720001804.

[3] R. Yadav and L. Malviya, “UWB antenna and MIMO antennas with bandwidth, band-notched, and isolation properties for high-speed data rate wireless communication: A review,” *International Journal of RF and Microwave Computer-Aided Engineering*, vol. 30, e22033, 2020, doi: 10.1002/mmce.22033.

[4] R. A. Fayadh, H. A. Fadhil, F. S. Abdullah, F. Malek and S. A. Dawood, "Selective update euclidean direction search algorithm for adaptive filtering in indoor wireless rake-receiver," *2014 International Conference on Computer, Communications, and Control Technology (I4CT),* Langkawi, Malaysia, 2014, pp. 329-332, doi: 10.1109/I4CT.2014.6914199.

[5] C.X. Mao and Q.X. Chu, “Compact Coradiator UWB-MIMO Antenna With Dual Polarization,” *IEEE Transactions on Antennas and Propagation*, vol. 62, no. 9, pp. 4474-4480, 2014, doi: 10.1109/TAP.2014.2333066.

[6] S. Chouhan, D.K. Panda, M. Gupta and S. Singhal, “Multiport MIMO antennas with mutual coupling reduction techniques for modern wireless transreceive operations: A review,” *International Journal of RF and Microwave Computer-Aided Engineering*, vol. 28, e21189, 2018, doi: 10.1002/mmce.21189.

[7] A. K. Sarangi and A. Datta, "Capacity Comparison of SISO, SIMO, MISO & MIMO Systems," *2018 Second International Conference on Computing Methodologies and Communication (ICCMC),* Erode, India, 2018, pp. 798-801, doi: 10.1109/ICCMC.2018.8488147.

[8] S. Sharma, C.C. Tripathi and R. Rishi, "Two Port Integrated Reconfigurable Microstrip Patch Antenna," *Progress In Electromagnetics Research C*, vol. 89, pp. 39-50, 2019, doi:10.2528/PIERC18100901.

[9] A.W..M Saadh, K. Ashwath, P. Ramaswamy, T. Ali and J. Anguera, “A uniquely shaped MIMO antenna on FR4 material to enhance isolation and bandwidth for wireless applications,” *AEU-International Journal of Electronics and Communications*, vol. 123, 153316, 2020, doi: 10.1016/j.aeue.2020.153316.

[10] J. Thaysen and K.B. Jakobsen, “Envelope correlation in (*N*, *N*) MIMO antenna array from scattering parameters,” *Microwave and Optical Technology Letters*, vol. 48, pp. 832-834, 2006, doi: 10.1002/mop.21490.

[11] S. Blanch, J. Romeu and I. Corbella, “Exact representation of antenna system diversity performance from input parameter description,” *Electronics Letters*, 2003, vol. 39, no. 9, pp. 705-707, doi: 10.1049/el:20030495.

[12] A.A.R Saad and H.A. Mohamed, “Printed millimeter-wave MIMO-based slot antenna arrays for 5G networks,” *AEU-International Journal of Electronics and Communications*, vol. 99, pp. 59-69, 2019, doi: 10.1016/j.aeue.2018.11.029.

[13] T. Addepalli and V. Anitha V, "A very compact and closely spaced circular shaped uwb mimo antenna with improved isolation," *AEU-International Journal of Electronics and Communications*, vol. 114, 153016, 2020, doi: 10.1016/j.aeue.2019.153016.

[14] J. Kulkarni, A. Desai and C.Y.D. Sim, "Wideband Four-Port MIMO antenna array with high isolation for future wireless systems," *AEU-International Journal of Electronics and Communications*, vol. 128, 153507, 2021, doi: 10.1016/j.aeue.2020.153507.

[15] A. Kumar, A.Q. Ansari, B.K. Kanaujia, J. Kishor and S. Kumar, "An ultra-compact two-port UWB-MIMO antenna with dual band-notched characteristics," *AEU-International Journal of Electronics and Communications*, vol. 114, 152997, 2020, doi: 10.1016/j.aeue.2019.152997.

[16] R.N. Tiwari, P. Singh and B.K. Kanaujia, "A compact UWB MIMO antenna with neutralization line for WLAN/ISM/mobile applications," *International Journal of RF and Microwave Computer-Aided Engineering*, vol. 29, e21907, 2019, doi: 10.1002/mmce.21907.

[17] S. Ahmad, S. Khan, B. Manzoor, M. Soruri, M. Alibakhshikenari, M. Dalarsson and F. Falcone, "A Compact CPW-Fed Ultra-Wideband Multi-Input-Multi-Output (MIMO) Antenna for Wireless Communication Networks," *IEEE Access*, vol. 10, pp. 25278-25289, 2022, doi: 10.1109/ACCESS.2022.3155762.

[18] S.P. Biswal and S. Das, "A low-profile dual port UWB-MIMO/diversity antenna with band rejection ability," *International Journal of RF and Microwave Computer-Aided Engineering*, vol. 28, e21159, 2018, doi: 10.1002/mmce.21159.

[19] L. Malviya, R. Panigrahi, and M. Kartikeyan, "MIMO antennas with diversity and mutual coupling reduction techniques: A review," *International Journal of Microwave and Wireless Technologies*, vol. 9, no. 8, pp. 1763-1780, 2017, doi:10.1017/S1759078717000538

[20] A. Arya, K. Machavaram and A. Patnaik, "Defected Ground Structure in the perspective of Microstrip Antennas: A Review," *Frequenz*, vol. 64, no. 5-6, pp. 79-84, 2010, doi: 10.1515/FREQ.2010.64.5-6.79.

[21] F.Y. Zulkifli, E.T. Rahardjo and D. Hartanto, "Mutual Coupling Reduction Using Dumbbell Defected Ground Structure for Multiband Microstrip Antenna Array," *Progress In Electromagnetics Research Letters*, vol. 13, pp. 29-40, 2010, doi: 10.2528/PIERL09102902.

[22] J. Zhu, B. Feng, B. Peng, L. Deng and S. Li, "A dual notched band MIMO slot antenna system with Y-shaped defected ground structure for UWB applications," *Microwave and Optical Technology Letters*, vol. 58: pp. 626-630, 2016, doi: 10.1002/mop.29632

[23] S.K. Dhar and M.S. Sharawi, "A UWB semi-ring MIMO antenna with isolation enhancement," *Microwave and Optical Technology Letters*, vol. 57, pp. 1941-1946, 2015, doi: 10.1002/mop.29245

[24] J. Acharjee, K. Mandal and S. Mandal, "Reduction of mutual coupling and cross-polarization of a MIMO/diversity antenna using a string of H-shaped DGS," *AEU-International Journal of Electronics and Communications*, vol. 97, pp. 110-119, 2018, doi: 10.1016/j.aeue.2018.09.037.

[25] C.M. Luo, J.S. Hong and L.L. Zhong, "Isolation Enhancement of a Very Compact UWB-MIMO Slot Antenna with Two Defected Ground Structures," *IEEE Antennas and*

Wireless Propagation Letters, vol. 14, pp. 1766-1769, 2015, doi: 10.1109/LAWP.2015.2423318.

[26] S. Zhang and G.F. Pedersen, “Mutual Coupling Reduction for UWB MIMO Antennas With a Wideband Neutralization Line,” *IEEE Antennas and Wireless Propagation Letters*, vol. 15, pp. 166-169, 2016, doi: 10.1109/LAWP.2015.2435992.

[27] R. N. Tiwari, P. Singh, B. K. Kanaujia and K. Srivastava, “Neutralization technique based two and four port high isolation MIMO antennas for UWB communication,” *AEU-International Journal of Electronics and Communications*, vol. 110, 152828, 2019, doi: 10.1016/j.aeue.2019.152828.

[28] M.S. Khan, A.D. Capobianco, M.F. Shafique, B. Ijaz, A. Naqvi and B.D. Braaten BD, “Isolation enhancement of a wideband MIMO antenna using floating parasitic elements,” *Microwave and Optical Technology Letters,* vol. 57, pp. 1677-1682, 2015, doi: 10.1002/mop.29162.

[29] S. Rekha and G.S. Let, “Design and SAR Analysis of Wearable UWB MIMO Antenna with Enhanced Isolation Using a Parasitic Structure,” *Iranian Journal of Science and Technology, Transactions of Electrical Engineering*, vol. 46, pp. 291-301, 2022, doi: 10.1007/s40998-022-00482-9.

[30] A. Radhi, R. Nilavalan, Y. Wang, H. Al-Raweshidy, A. Eltokhy and N.A. Aziz, “Mutual coupling reduction with a wideband planar decoupling structure for UWB–MIMO antennas,” *International Journal of Microwave and Wireless Technologies*, vol. 10, no. 10, pp. 1143-1154, 2018, doi:10.1017/S1759078718001010.

[31] A. Iqbal, O. A. Saraereh, A. W. Ahmad and S. Bashir, “Mutual Coupling Reduction Using F-Shaped Stubs in UWB-MIMO Antenna,” *IEEE Access*, vol. 6, pp. 2755-2759, 2018, doi: 10.1109/ACCESS.2017.2785232.

[32] M.S. Khan, A.D. Capobianco, S.M. Asif, D.E. Anagnostou, R.M. Shubair and B.D. Braaten, “A Compact CSRR-Enabled UWB Diversity Antenna,” *IEEE Antennas and Wireless Propagation Letters*, vol. 16, pp. 808-812, 2017, doi: 10.1109/LAWP.2016.2604843.

[33] F. Wang, Z. Duan, S. Li, Z.L. Wang and Y.B. Gong, “Compact UWB MIMO Antenna with Metamaterial-Inspired Isolator,” *Progress In Electromagnetics Research C*, vol. 84, pp. 61-74, 2018, doi:10.2528/PIERC18030201.

[34] H. Sakli, C. Abdelhamid, C. Essid and N. Sakli, “Metamaterial-Based Antenna Performance Enhancement for MIMO System Applications,” *IEEE Access*, vol. 9, pp. 38546-38556, 2021, doi: 10.1109/ACCESS.2021.3063630.

[35] M.U. Khan, M.S. Sharawi and R. Mittra, “Microstrip patch antenna miniaturisation techniques: a review,” *IET Microwaves, Antennas & Propagation*, vol. 9, pp. 913-922, 2015, doi: 10.1049/iet-map.2014.0602

[36] D. H. Werner and S. Ganguly, “An overview of fractal antenna engineering research,” *IEEE Antennas and Propagation Magazine*, vol. 45, no. 1, pp. 38-57, 2003, doi: 10.1109/MAP.2003.1189650.

[37] A. Ezhumalai, N. Ganesan and S. Balasubramaniyan, “An extensive survey on fractal structures using iterated function system in patch antennas,” *International Journal of Communication Systems*, vol. 35, no. 15, 2021, https://doi.org/10.1002/dac.4932.

[38] P. Ramanujam, C. Arumugam, R. Venkatesan and M. Ponnusamy, “Design of compact patch antenna with enhanced gain and bandwidth for 5G mm-wave applications,” IET Microwaves Antennas & Propagation, vol. 14, pp. 1455-1461, 2020, https://doi.org/10.1049/iet-map.2019.0891.

[39] A. Kaur and S. Gupta, “A complementary Sierpinski gasket fractal antenna array for wireless MIMO portable devices,” *Microwave and Optical Technology Letters,* vol. 61, pp. 436-442, 2019, https://doi.org/10.1002/mop.31584.

[40] R. Gurjar, D.K. Upadhyay, B.K. Kanaujia and A. Kumar, “A compact modified sierpinski carpet fractal UWB MIMO antenna with square-shaped funnel-like ground stub,” *AEU-International Journal of Electronics and Communications*, vol. 117, 153126, 2020, https://doi.org/10.1016/j.aeue.2020.153126.

[41] C. A. Balanis, Antenna Theory: Analysis and Design, 3rd ed. Hoboken, NJ, USA: Wiley, 2005.

[42] P. Kumari, P. Sarkar and R. Ghatak, “A Pythagorean tree fractal shape stub-loaded resonator as a UWB bandpass filter with wide stopband,” *International Journal of Microwave and Wireless Technologies,* vol. 13, no.5, pp. 442-446, 2021, doi:10.1017/S1759078720001750.

[43] J. Pourahmadazar, C. Ghobadi and J. Nourinia, “Novel Modified Pythagorean Tree Fractal Monopole Antennas for UWB Applications,” *IEEE Antennas and Wireless Propagation Letters*, vol. 10, pp. 484-487, 2011, doi: 10.1109/LAWP.2011.2154354.

[44] G. Khanna and N. Sharma, “Fractal Antenna Geometries: A Review,” *International Journal of Computer Applications,* vol. 153, pp. 29-32, 2016, doi: 10.5120/ijca2016912106.

[45] A. Kaur, “Semi Spiral G-shaped dual wideband Microstrip Antenna with Aperture feeding for WLAN/WiMAX/U-NII band applications,” *International Journal of Microwave and Wireless Technologies*, vol. 8, no. 6, pp. 931-941, 2016, doi: 10.1017/S1759078715000276.

[46] M.N. Hasan, S. Chu and S. Bashir, “A DGS monopole antenna loaded with U-shape stub for UWB MIMO applications,” *Microwave and Optical Technology Letters*, vol. 61, pp. 2141-2149, 2019. doi: 10.1002/mop.31877.

[47] J.Y. Deng, L.X. Guo and X.L. Liu, “An Ultrawideband MIMO Antenna With a High Isolation,” *IEEE Antennas and Wireless Propagation Letters*, vol. 15, pp. 182-185, 2016, doi: 10.1109/LAWP.2015.2437713.

[48] H. Kim-Thi, H.H. Tran, T.T. Le, “Circularly polarized MIMO antenna utilizing parasitic elements for simultaneous improvements in isolation, bandwidth and gain,” *AEU - International Journal of Electronics and Communications,* vol. 135, 153727, 2021, doi: 10.1016/j.aeue.2021.153727.

[49] P.P. Shome, T. Khan and R.H. Laskar, “A state-of-art review on band-notch characteristics in UWB antennas,” *International Journal of RF and Microwave Computer-Aided Engineering*, vol. 29, e21518, 2019, doi: 10.1002/mmce.21518.

[50] L. Kang, H. Li, X. Wang and X. Shi, “Compact Offset Microstrip-Fed MIMO Antenna for Band-Notched UWB Applications,” *IEEE Antennas and Wireless Propagation Letters,* vol. 14, pp. 1754-1757, 2015, doi: 10.1109/LAWP.2015.2422571.

[51] W. T. Li, Y. Q. Hei, H. Subbaraman, X. W. Shi and R. T. Chen, “Novel Printed Filtenna with Dual Notches and Good Out-of-Band Characteristics for UWB-MIMO Applications,” *IEEE Microwave and Wireless Components Letters,* vol. 26, no. 10, pp. 765-767, 2016, doi: 10.1109/LMWC.2016.2601298.

[52] N. Jaglan, S.D. Gupta, E. Thakur, D. Kumar, B.K. Kanaujia and S. Srivastva, “Triple band notched mushroom and uniplanar EBG structures based UWB MIMO/Diversity antenna with enhanced wide band isolation,” *AEU - International Journal of Electronics and Communications*, vol. 90, pp. 36-44, 2018, doi: 10.1016/j.aeue.2018.04.009.

[53] L. Wu and Y. Xia, “Compact UWB-MIMO antenna with quad-band-notched characteristic,” *International Journal of Microwave and Wireless Technologies,* vol. 9, no. 5, pp. 1147-1153, 2017, doi: 10.1017/S1759078716001239.

[54] G. Irene and A. Rajesh, “A Penta-Band Reject Inside Cut Koch Fractal Hexagonal Monopole UWB MIMO Antenna for Portable Devices,” *Progress In Electromagnetics Research C,* vol. 82, 225-235, 2018, doi:10.2528/PIERC18020604.

[55] Luo S, Chen Y, Wang D, Liao Y, Li Y. A monopole UWB antenna with sextuple band-notched based on SRRs and U-shaped parasitic strips,” *AEU - International Journal of Electronics and Communications,* vol. 120, 153206, 2020, doi: 10.1016/j.aeue.2020.153206.

[56] D. Yadav, M.P. Abegaonkar, S.K. Koul, V. Tiwari and D. Bhatnagar, “A compact dual band-notched UWB circular monopole antenna with parasitic resonators,” *AEU - International Journal of Electronics and Communications*, vol. 84, pp. 313-320, 2018, doi:10.1016/j.aeue.2017.12.020.

[57] M. Rostamzadeh, S. Mohamadi, J. Nourinia, C. Ghobadi and M. Ojaroudi, “Square Monopole Antenna for UWB Applications with Novel Rod-Shaped Parasitic Structures and Novel V-Shaped Slots in the Ground Plane,” *IEEE Antennas and Wireless Propagation Letters*, vol. 11, pp. 446-449, 2012, doi: 10.1109/LAWP.2012.2193866.

[58] N. Malekpour, M.A. Honarvar, A. Dadgarpur, B.S. Virdee and T.A. Denidni, “Compact UWB MIMO antenna with band-notched characteristic,” *Microwave and Optical Technology Letters,* vol. 59, pp. 1037-1041, 2017, doi: 10.1002/mop.30462.

[59] L. Liu, S.W. Cheung and T.I. Yuk, “Compact MIMO Antenna for Portable UWB Applications with Band-Notched Characteristic,” *IEEE Transactions on Antennas and Propagation*, vol. 63, no. 5, pp. 1917-1924, 2015, doi: 10.1109/TAP.2015.2406892.

[60] M. Abedian, S. K. A. Rahim, S. Danesh, S. Hakimi, L. Y. Cheong and M. H. Jamaluddin, “Novel Design of Compact UWB Dielectric Resonator Antenna with Dual-Band-Rejection Characteristics for WiMAX/WLAN Bands,” *IEEE Antennas and Wireless Propagation Letters,* vol. 14, pp. 245-248, 2015, doi: 10.1109/LAWP.2014.2360828.

[61] R. Chandel, A. K. Gautam and K. Rambabu, “Tapered Fed Compact UWB MIMO-Diversity Antenna with Dual Band-Notched Characteristics,” *IEEE Transactions on Antennas and Propagation,* vol. 66, no. 4, pp. 1677-1684, 2018, doi: 10.1109/TAP.2018.2803134.

[62] M.M. Hassan, M. Rasool, M.U. Asghar, Z. Zahid, A.A. Khan, I. Rashid, A. Rauf and F.A. Bhatti, “A novel UWB MIMO antenna array with band notch characteristics using parasitic decoupler,” *Journal of Electromagnetic Waves and Applications,* vol. 34, 1225-1238, 2020, https://doi.org/10.1080/ 09205071.2019.1682063.

[63] P. Pannu and D.K. Sharma, “A low-profile quad-port UWB MIMO antenna using defected ground structure with dual notch-band behavior,” *International Journal of RF and Microwave Computer-Aided Engineering*, vol. 30, e22288, 2020, https://doi.org/10.1002/mmce.22288.

[64] S. Tripathi, A. Mohan and S. Yadav, “A compact octagonal fractal UWB MIMO antenna with WLAN band-rejection,” *Microwave and Optical Technology Letters*, vol. 57, 1919-1925, 2015, https:// doi.org/10.1002/mop.29220.

[65] J.K. Park, H.S. An and J.N. Lee, “Design of the tree-shaped UWB antenna using fractal concept,” *Microwave and Optical Technology Letters*, vol. 50, pp. 144-150, 2008, https://doi.org/10.1002/mop.23010.

[66] G. Srivatsun and S. Subha Rani, “A compact wideband fractal cantor antenna for wireless applications,” *AEU-International Journal of Electronics and Communications*, vol. 65, pp. 719-723, 2011, https://doi.org/10.1016/j.aeue.2010.10.003.

[67] B.S. Dhaliwal, S.S. Pattnaik and J. Boparai, “A cross-stitch geometry-based multiband fractal antenna,” *Microwave and Optical Technology Letters*, vol. 56, pp. 667-671, 2014, https://doi.org/10.1002/mop.28177.

[68] A. Reha, A. El Amri, O. Benhmammouch, A.O. Said, A. El Ouadih and M. Bouchouirbat, “CPW-fed H-tree fractal antenna for WLAN, WIMAX, RFID, C-band, HiperLAN, and UWB applications,” *International Journal of Microwave and Wireless Technologies*, vol. 8, pp. 327-334, 2016, https://doi.org/10.1017/S175907871500001X.

[69] B. Roy, A. Bhattacharya, S.K. Chowdhury and A.K. Bhattacharjee, “Wideband Snowflake slot antenna using Koch iteration technique for wireless and C-band applications,” *AEU-International Journal of Electronics and Communications*, vol. 70, pp. 1467-1472, 2016, https://doi.org/10.1016/j.aeue.2016.08.010.

[70] S.J. Singh, G. Singh and G. Bharti, “Circular Microstrip Antenna with Fractal Slots for Multiband Applications,” *Journal of The Institution of Engineers (India): Series B*, vol. 98: pp. 441-447, 2017, https://doi.org/10.1007/s40031-017-0278-4.

[71] N. Rao and D.V Kumar, “Miniaturization of Microstrip Patch Antenna for Satellite Communication: A Novel Fractal Geometry Approach,” *Wireless Personal Communications*, vol. 97, pp. 3673-3683, 2017, https://doi.org/10.1007/s11277-017-4691-4.

[72] Y. Kumar and S. Singh, “Performance Analysis of Coaxial Probe Fed Modified Sierpinski-Meander Hybrid Fractal Heptaband Antenna for Future Wireless Communication Networks,” *Wireless Personal Communications*, vol. 94, pp. 3251-3263, 2017, https://doi.org/10.1007/s11277-016-3775-x.

[73] G. Singh and A.P. Singh, “On the design of planar antenna using Fibonacci word fractal geometry in support of public safety,” *International Journal of RF and Microwave Computer-Aided Engineering*, vol. 29, e21554, 2019, https://doi.org/10.1002/mmce.21554.

[74] R. Mark, N. Mishra, K. Mandal, P.P. Sarkar and S. Das, “Hexagonal ring fractal antenna with dumbbell shaped defected ground structure for multiband wireless applications,” *AEU-International Journal of Electronics and Communications*, vol. 94, pp. 42-50, 2018, https://doi.org/10.1016/j.aeue.2018.06.039.

[75] S.S. Bhatia, J.S. Sivia and N. Sharma, "An Optimal Design of Fractal Antenna with Modified Ground Structure for Wideband Applications," *Wireless Personal Communications*, vol. 103, pp. 1977-1991, 2018, https://doi.org/10.1007/s11277-018-5891-2.

[76] I.S. Bangi and J.S. Sivia, "Moore, Minkowski and Koch Curves Based Hybrid Fractal Antenna for Multiband Applications," *Wireless Personal Communications*, vol. 108, pp. 2435-2448, https://doi.org/10.1007/s11277-019-06531-7.

[77] N. Kaur and A. Kaur, "A Compact Plus Shaped Carpet Fractal Antenna with an I-shaped DGS for C-band/X-band/UWB/WIBAN applications," *Wireless Personal Communications*, vol. 109, pp. 1673-1687, 2019, https://doi.org/10.1007/s11277-019-06645-y.

[78] D. Tiwari, J.A. Ansari, A.K. Saroj and M. Kumar, "Analysis of a Miniaturized Hexagonal Sierpinski Gasket fractal microstrip antenna for modern wireless communications," *AEU - International Journal of Electronics and Communications*, vol. 123, 153288, 2020, https://doi.org/10.1016/j.aeue.2020.153288.

[79] P. Iyampalam and I. Ganesan, "Design of Sierpinski Knopp Inspired Fractal Antenna for Public Safety Applications," *Wireless Personal Communications*, vol. 114, pp. 227-239, 2020, https://doi.org/10.1007/s11277-020-07360-9.

[80] S. Nallapaneni and P. Muthusamy, "Design of multiband fractal antenna loaded with parasitic elements for gain enhancement," *International Journal of RF and Microwave Computer-Aided Engineering*, vol. 31, e22622, 2021, https://doi.org/10.1002/mmce.22622.

[81] H. Kaur and P. Chawla, "Design and Evaluation of a Fractal Wearable Textile Antenna for Medical Applications," *Wireless Personal Communications*, vol. 128, pp. 683-699, 2023, https://doi.org/10.1007/s11277-022-09973-8.

[82] J.S. Sivia and S.S. Bhatia, "Meander and Koch Hybrid Fractal Curve Based Dual Hexagonal Radiating Patch Antenna for Quad Band Wireless Applications," *Wireless Personal Communications*, vol. 126, pp. 665-677, 2022, https://doi.org/10.1007/s11277-022-09764-1.

[83] G. Bharti and J.S. Sivia, "A Design of Compact Wideband Antenna Based on Hybridization of Minkowski Fractal Curves on Hexagonal Patch and Partial Ground Plane with Truncated Corners," *Wireless Personal Communications*, vol. 124, pp. 1609-1621, 2022, https://doi.org/10.1007/s11277-021-09422-y.

[84] S. Palanisamy and B. Thangaraju, "Design and analysis of clover leaf-shaped fractal antenna integrated with stepped impedance resonator for wireless applications," *International Journal of Communication Systems*, vol. 35, e5184, 2022, https://doi.org/10.1002/dac.5184.

[85] M. Naghshvarian-Jahromi, "Novel Wideband Planar Fractal Monopole Antenna," *IEEE Transactions on Antennas and Propagation*, vol. 56, no. 12, pp. 3844-3849, 2008, doi: 10.1109/TAP.2008.2007393.

[86] R. Kumar and S. Hake, "Design of modified ground square-shaped fractal antenna for UWB applications," *Microwave and Optical Technology Letters*, vol. 53, pp. 2589-2592, 2011, https://doi.org/10.1002/mop.26365.

[87] R. Kumar and P.N. Chaubey, “On the design of inscribed pentagonal-cut fractal antenna for ultra wideband applications,” *Microwave and Optical Technology Letters*, vol. 53, pp. 2828-2830, 2011, https://doi.org/10.1002/mop.26415.

[88] H. Oraizi and S. Hedayati, “Miniaturized UWB Monopole Microstrip Antenna Design by the Combination of Giusepe Peano and Sierpinski Carpet Fractals,” *IEEE Antennas and Wireless Propagation Letters*, vol. 10, pp. 67-70, 2011, doi: 10.1109/LAWP.2011.2109030.

[89] R. Kumar and P.B. Nikam, “A modified ground apollonian ultra wideband fractal antenna and its backscattering,” *AEU-International Journal of Electronics and Communications*, vol. 66, pp. 647-654, 2012, https://doi.org/10.1016/j.aeue.2016.08.010.

[90] M. Susila, T. Rama Rao and A. Gupta, “A Novel Smiley Fractal Antenna (SFA) Design and Development for UWB Wireless Applications,” *Progress In Electromagnetics Research C*, vol. 54, pp. 171-178, 2014, http://doi.org/10.2528/PIERC14091803.

[91] S. Singhal, T. Goel and A.K. Singh, “Inner tapered tree-shaped fractal antenna for UWB applications,” *Microwave and Optical Technology Letters*, vol. 57, pp. 559-567, 2015, https://doi.org/10.1002/mop.28900.

[92] S. Singhal and A.K. Singh, “Asymmetrically CPW-fed ladder-shaped fractal antenna for UWB applications,” *Analog Integrated Circuits and Signal Processing*, vol. 92, pp. 91-101, 2017, https://doi.org/10.1007/s10470-017-0976-5.

[93] A.S. Brar and J.S. Sivia, “Modified Minkowski Fractal Antenna for Wireless Applications,” *Journal of The Institution of Engineers (India): Series B*, vol. 99, pp. 391-396, 2018, https://doi.org/10.1007/s40031-018-0342-8.

[94] S. Mohandoss, R.R. Thipparaju, B.N.B. Reddy, S.K. Palaniswamy and P. Marudappa, “Fractal based ultra-wideband antenna development for wireless personal area communication applications,” *AEU-International Journal of Electronics and Communications*, vol. 93, pp. 95-102, 2018, https://doi.org/10.1016/j.aeue.2018.06.009.

[95] N. Kaur, J. Singh and M. Kumar, “Hexagonal Ring-Shaped Dual Band Antenna Using Staircase Fractal Geometry for Wireless Applications,” *Wireless Personal Communications*, vol. 113, pp. 2067-2078, 2020, https://doi.org/10.1007/s11277-020-07307-0.

[96] R. Kumar, R. Sinha, A. Choubey and S.K. Mahto, “An ultrawide band monopole antenna using hexagonal-square shaped fractal geometry,” *Journal of Electromagnetic Waves and Applications*, vol. 35, pp. 233-244, 2021, http://doi.org/10.1080/09205071.2020.1829094.

[97] A. Mohanty and S. Sahu, “Compact wideband hybrid fractal antenna loaded on AMC reflector with enhanced gain for hybrid wireless cellular networks,” *AEU-International Journal of Electronics and Communications*, vol. 138, 153837, 2021, https://doi.org/10.1016/j.aeue.2021.153837.

[98] N. Sharma and S.S. Bhatia, “Ultra-wideband fractal antenna using rhombus shaped patch with stub loaded defected ground plane: Design and measurement,” *AEU-International Journal of Electronics and Communications*, vol. 131, 153604, 2021, https://doi.org/10.1016/j.aeue.2021.153604.

[99] M.H. Reddy, D. Sheela, A.S. Nisha and S.T. Niba, “Circular Fractal Antenna Design with Inscribed Square for Ultra-Wide Band Applications,” *Journal of Communications Technology and Electronics*, vol. 67, pp. 46-55, 2022, https://doi.org/10.1134/S1064226922010089.

[100] W.J. Lui, C.H. Cheng, Y. Cheng, H. Zhu, “Frequency notched ultra-wideband microstrip slot antenna with fractal tuning stub,” *Electronics Letters*, vol. 41, no. 6, pp. 294-296, 2005, doi: 10.1049/el:20058420.

[101] W. J. Lui, C. H. Cheng and H. B. Zhu, “Compact frequency notched ultra-wideband fractal printed slot antenna,” *IEEE Microwave and Wireless Components Letters*, vol. 16, no. 4, pp. 224-226, 2006, doi: 10.1109/LMWC.2006.872102.

[102] D.O. Kim, C.Y. Kim, J.K. Park and N.I. Jo, “Compact band notched ultra-wideband antenna using the Hilbert-curve slot,” *Microwave and Optical Technology Letters*, vol. 53, pp. 2642-2648, 2011, https://doi.org/10.1002/mop.26348.

[103] R. Ghatak, A. Karmakar, D.R. Poddar, “A Circular Shaped Sierpinski Carpet Fractal UWB Monopole Antenna with Band Rejection Capability,” *Progress In Electromagnetics Research C*, vol. 24, pp. 221-234, 2011, http://doi.org/10.2528/PIERC11082801.

[104] A. Karmakar, S. Verma, M. Pal and R. Ghatak, “An Ultra Wideband Monopole Antenna with Multiple Fractal Slots with Dual Band Rejection Characteristics,” *Progress In Electromagnetics Research C*, vol. 31, pp. 185-197, 2012, http://doi.org/10.2528/PIERC12052310.

[105] Y. Li, X. Yang, C. Liu and T. Jiang, “Miniaturization cantor set fractal ultrawideband antenna with a notch band characteristic,” *Microwave and Optical Technology Letters*, vol. 54, pp. 1227-1230, 2012, https://doi.org/10.1002/mop.26762

[106] Q. Zou and S.A. Jiang, “Compact flexible fractal ultra-wideband antenna with band notch characteristic,” *Microwave and Optical Technology Letters*, vol. 63, pp. 895-901, 2021, https://doi.org/10.1002/mop.32678.

[107] A. Karmakar, R. Ghatak, U. Banerjee, D.R. Poddar, “An UWB antenna using modified Hilbert curve slot for dual band notch characteristics,” *Journal of Electromagnetic Waves and Applications*, vol. 27, no. 13, pp. 1620-1631, 2013, http://doi.org/10.1080/09205071.2013.821676.

[108] M. Naser-Moghadasi, R. A. Sadeghzadeh, T. Sedghi, T. Aribi and B. S. Virdee, “UWB CPW-Fed Fractal Patch Antenna With Band-Notched Function Employing Folded T-Shaped Element,” *IEEE Antennas and Wireless Propagation Letters*, vol. 12, pp. 504-507, 2013, doi: 10.1109/LAWP.2013.2256455.

[109] R. Ghatak, B. Biswas, A. Karmakar and D.R. Poddar, “A circular fractal UWB antenna based on Descartes Circle Theorem with Band Rejection Capability,” *Progress In Electromagnetics Research C*, vol. 37, pp. 235-248, 2013, http://doi.org/10.2528/PIERC13011607.

[110] F.B. Zarrabi, A.M. Shire, M. Rahimi, N.P. Gandji, “Ultra-wideband tapered patch antenna with fractal slots for dual notch application,” *Microwave and Optical Technology Letters*, vol. 56, pp. 1344-1348, 2014, https://doi.org/10.1002/mop.28332.

[111] K. Shambavi and Z.C. Alex, “Fractal monopole antenna with electromagnetic bandgap structure for UWB applications,” *Microwave and Optical Technology Letters,* vol. 56, pp. 1872-1874, 2014, https://doi.org/10.1002/mop.28463.

[112] V. Rajeshkumar and S. Raghavan, “Bandwidth enhanced compact fractal antenna for UWB applications with 5-6 GHz band rejection,” *Microwave and Optical Technology Letters*, vol. 57, pp. 607-613, 2015, https://doi.org/10.1002/mop.28913.

[113] A. Gorai, A. Karmakar, M. Pal and R. Ghatak, “Multiple fractal-shaped slots-based UWB antenna with triple-band notch functionality,” *Journal of Electromagnetic Waves and Applications*, vol. 27, pp. 2407-2415, 2013, http://doi.org/10.1080/09205071.2013.852486.

[114] B. Biswas, R. Ghatak and D.R. Poddar, “UWB monopole antenna with multiple fractal slots for band-notch characteristic and integrated Bluetooth functionality,” *Journal of Electromagnetic Waves and Applications*, vol. 29, no. 12, pp. 1593-1609, 2015, http://doi.org/10.1080/09205071.2015.1054521.

[115] F.B. Zarrabi, Z. Mansouri, N.P. Gandji and H.Kuhestani, “Triple-notch UWB monopole antenna with fractal Koch and T-shaped stub,” *AEU-International Journal of Electronics and Communications*, vol. 70, pp. 64-69, 2016, https://doi.org/10.1016/j.aeue.2015.10.001.

[116] S. Tripathi, A. Mohan and S. Yadav, “A compact fractal UWB antenna with reconfigurable band notch functions,” *Microwave and Optical Technology Letters*, vol. 58, pp. 509-514, 2016, https://doi.org/10.1002/mop.29609.

[117] Z. Hu, Y. Hu, Y. Luo and W. Xin, “A Novel Rectangle Tree Fractal UWB Antenna with Dual Band Notch Characteristics,” *Progress In Electromagnetics Research C,* vol. 68, pp. 21-30, 2016, http://doi.org/10.2528/PIERC16072702.

[118] A. Gorai, M. Pal and R. Ghatak, “A Compact Fractal-Shaped Antenna for Ultrawideband and Bluetooth Wireless Systems With WLAN Rejection Functionality,” *IEEE Antennas and Wireless Propagation Letters,* vol. 16, pp. 2163-2166, 2017, doi: 10.1109/LAWP.2017.2702208.

[119] R. Ghatak, A. Karmakar and D.R. Poddar, “Hexagonal boundary Sierpinski carpet fractal shaped compact ultrawideband antenna with band rejection functionality,” *AEU-International Journal of Electronics and Communications*, vol. 67, pp. 250-255, 2013, https://doi.org/10.1016/j.aeue.2012.08.007.

[120] O. A. Safia and G. V. Eleftheriades, “A New Gosper Island Fractal UWB Monopole Antenna with Enhanced Bandwidth Characteristics,” *2018 IEEE International Symposium on Antennas and Propagation & USNC/URSI National Radio Science Meeting*, Boston, MA, USA, 2018, pp. 1043-1044, doi: 10.1109/APUSNCURSINRSM.2018.8608404.

[121] N. Nemati and M. Bemani, “A novel reconfigurable microstrip fractal UWB antenna with six variable rejection frequency bands,” *International Journal of Microwave and Wireless Technologies*, vol. 12, pp. 148-154, 2020, http://doi.org/10.1017/S1759078719001028.

[122] A.H. Nazeri, A. Falahati and R.M. Edwards, “A novel compact fractal UWB antenna with triple reconfigurable notch reject bands applications,” *AEU - International Journal*

of Electronics and Communications, vol. 101, pp. 1-8, 2019, https://doi.org/10.1016/j.aeue.2019.01.018.

[123] A.S. Abd El-Hameed, M.G. Wahab and A. Elboushi, "Miniaturized triple band-notched quasi-self-complementary fractal antenna with improved characteristics for UWB applications," *AEU - International Journal of Electronics and Communications*, vol. 108, pp. 163-171, 2019, https://doi.org/10.1016/j.aeue.2019.06.016.

[124] S.C. Puri, S. Das, M. Gopal Tiary, "An UWB trapezoidal rings fractal monopole antenna with dual-notch characteristics," *International Journal of RF and Microwave Computer-Aided Engineering*, vol. 29, e21777, 2019, https://doi.org/10.1002/mmce.21777.

[125] Q. Zou and S.A. Jiang, "Compact flexible fractal ultra-wideband antenna with band notch characteristic," *Microwave and Optical Technology Letters*, vol. 63, pp. 895-901, 2021, https://doi.org/10.1002/mop.32678.

[126] S. Kakkar, S. Rani and A.P. Singh, "Triple Band Notch Microstrip Patch Antenna with Fractal Defected Ground Structure," *IETE Journal of Research*, pp. 1-13, 2021, http://doi.org/10.1080/03772063.2021.1875894.

[127] C.M. Ramya and R.B. Rani, "A Circular Triangle Fractal Antenna for High Gain UWB Communications with Band Rejection Capability," *Progress In Electromagnetics Research M*, vol. 110, pp. 83-96, 2022, http://doi.org/10.2528/PIERM21110605.

[128] L. Zhang and Q. Feng, "Design of a Novel Fractal Quad-Band-Notched UWB Antenna with Bionic Structure," *Progress In Electromagnetics Research M*, vol. 111, pp. 41-52, 2022,
https://doi.org/10.2528/PIERM22030301.

[129] Y. K. Choukiker, S. K. Sharma and S. K. Behera, "Hybrid Fractal Shape Planar Monopole Antenna Covering Multiband Wireless Communications With MIMO Implementation for Handheld Mobile Devices," *IEEE Transactions on Antennas and Propagation*, vol. 62, no. 3, pp. 1483-1488, March 2014, doi: 10.1109/TAP.2013.2295213.

[130] A. Peristerianos, A. Theopoulos, A. G. Koutinos, T. Kaifas and K. Siakavara, "Dual-Band Fractal Semi-Printed Element Antenna Arrays for MIMO Applications," *IEEE Antennas and Wireless Propagation Letters*, vol. 15, pp. 730-733, 2016, doi: 10.1109/LAWP.2015.2470681.

[131] Guterman, Moreira and Peixeiro, "Microstrip fractal antennas for multistandard terminals," *IEEE Antennas and Wireless Propagation Letters*, vol. 3, pp. 351-354, 2004, doi: 10.1109/LAWP.2004.840253.

[132] S. Rajkumar, N. Vivek Sivaraman, S. Murali, K.T. Selvan, "Heptaband swastik arm antenna for MIMO applications," *IET Microwaves, Antennas & Propagation*, vol. 11, pp. 1255-1261, 2017, https://doi.org/10.1049/iet-map.2016.1098.

[133] S. Rajkumar, N. Srinivasan, A. Natesan and K.T. Selvan, "A penta-band hybrid fractal MIMO antenna for ISM applications," *International Journal of RF and Microwave Computer-Aided Engineering*, vol. 28, e21185, 2018, https://doi.org/10.1002/mmce.21185.

[134] S. Chouhan, D.K. Panda, V.S. Kushwah and S. Singhal, "Spider-shaped fractal MIMO antenna for WLAN/WiMAX/Wi-Fi/Bluetooth/C-band applications," *AEU-International*

Journal of Electronics and Communications, vol. 110, 152871, 2019, https://doi.org/10.1016/j.aeue.2019.152871.

[135] N. Sharma, H.S. Singh and R. Khanna, "Design and Analysis of Multiband Fractal Antenna for MIMO/Diversity Applications," *Wireless Personal Communications*, vol 122, pp. 3671-3686, 2022, https://doi.org/10.1007/s11277-021-09106-7.

[136] P.B. Saha, R.K. Dash and D. Ghoshal, "Triple-band Four-port MIMO Antenna with Reduced Mutual Coupling Using Minkowiski-modified Novel Fractal Loop," *Wireless Personal Communications*, vol. 117, pp. 2253-2271, 2021, https://doi.org/10.1007/s11277-020-07970-3.

[137] M. Alibakhshikenari, M. Khalily, B. S. Virdee, C. H. See, R. A. Abd-Alhameed and E. Limiti, "Mutual Coupling Suppression Between Two Closely Placed Microstrip Patches Using EM-Bandgap Metamaterial Fractal Loading," *IEEE Access*, vol. 7, pp. 23606-23614, 2019, doi: 10.1109/ACCESS.2019.2899326.

[138] K. Trivedi and D. Pujara, "Mutual coupling reduction in wideband tree shaped fractal dielectric resonator antenna array using defected ground structure for MIMO applications," *Microwave and Optical Technology Letters*, vol. 59, pp. 2735-2742, 2017, https://doi.org/10.1002/mop.30810.

[139] R. Gurjar, D.K. Upadhyay, B.K. Kanaujia and K. Sharma, "A novel compact self-similar fractal UWB MIMO antenna," *International Journal of RF and Microwave Computer-Aided Engineering*, vol. 29, e21632, 2019, doi: 10.1002/mmce.21632

[140] A. Abed, "Novel sunflower MIMO fractal antenna with low mutual coupling and dual wide operating bands," *International Journal of Microwave and Wireless Technologies*, vol. 12, pp. 323-331, 2020, https://doi.org/10.1017/S1759078719001375.

[141] S. Singhal, "Four element ultra-wideband fractal multiple-input multiple-output antenna," *Microwave and Optical Technology Letters*, vol. 61, pp. 2811-2818, 2019, https://doi.org/10.1002/mop.31980

[142] R. Gurjar, D.K. Upadhyay, B.K. Kanaujia and K. Sharma, "An 8-Shaped Self-affine Fractal MIMO Antenna for UWB Applications," *Applications of Artificial Intelligence Techniques in Engineering*, vol. 698, pp. 155-165, 2019, https://doi.org/10.1007/978-981-13-1819-1_16.

[143] S. Bukkawar and V. Ahmed, "Compact slot-loaded ultra-wideband multiple-input multiple-output antenna with fractal-inspired isolator," *International Journal of RF and Microwave Computer-Aided Engineering*, vol. 30, e22036, 2020, https://doi.org/10.1002/mmce.22036.

[144] E.A. Andrade-González, J.A. Tirado-Méndez, H. Jardón-Aguilar, M. Reyes-Ayala, A. Rangel-Merino and M. Pascoe-Chalke, "UWB four ports MIMO antenna based on inscribed Fibonacci circles," *Journal of Electromagnetic Waves and Applications*, vol. 35, pp. 1202-1220, 2021, https://doi.org/10.1080/09205071.2021.1873196.

[145] A. Mohanty and B.R. Behera, "Characteristics Mode Analysis: A Review of Its Concepts, Recent Trends, State-of-the-Art Developments and Its Interpretation with a Fractal UWB MIMO Antenna," *Progress In Electromagnetics Research B*, vol. 92, pp. 19-45, 2021, https://doi.org/10.2528/PIERB21020506

[146] A. Mohanty and B.R. Behera, “Insights on radiation modes and pattern diversity of two element UWB fractal MIMO antenna using theory of characteristics modes analysis,” *AEU-International Journal of Electronics and Communications*, vol. 135, 153726, 2021, https://doi.org/10.1016/j.aeue.2021.153726.

[147] R. Gurjar, D.K. Upadhyay, B.K. Kanaujia and A. Kumar, “A Compact U-Shaped UWB-MIMO Antenna with Novel Complementary Modified Minkowski Fractal for Isolation Enhancement,” *Progress In Electromagnetics Research C*, vol. 107, pp. 81-96, 2021, http://doi.org/10.2528/PIERC20091809.

[148] H.T. Sediq, J. Nourinia, C. Ghobadi and B. Mohammadi, “An epsilon-shaped fractal antenna for UWB MIMO applications,” *Applied Physics A*, vol. 128, pp. 1-15, 2022, https://doi.org/10.1007/s00339-022-05940-z.

[149] J. Banerjee, A. Karmakar, R. Ghatak, D.R. Poddar, “Compact CPW-fed UWB MIMO antenna with a novel modified Minkowski fractal defected ground structure (DGS) for high isolation and triple band-notch characteristic,” *Journal of Electromagnetic Waves and Applications*, vol. 31, pp. 1550-1565, 2017, http://doi.org/10.1080/09205071.2017.1354727.

[150] P. Debnath, A. Karmakar, A. Saha and S. Huda, “UWB MIMO Slot Antenna with Minkowski Fractal Shaped Isolators for Isolation Enhancement,” *Progress In Electromagnetics Research M*, vol. 75, pp. 69-78, 2018, http://doi.org/10.2528/PIERM18090506.

[151] A. Gorai, A. Dasgupta and R. Ghatak, “A compact quasi-self-complementary dual band notched UWB MIMO antenna with enhanced isolation using Hilbert fractal slot,” *AEU-International Journal of Electronics and Communications*, vol. 94, pp. 36-41, 2018, https://doi.org/10.1016/j.aeue.2018.06.035.

[152] G. Irene and A. Rajesh, “A penta-band reject inside cut koch fractal hexagonal monopole UWB MIMO antenna for portable devices,” *Progress In Electromagnetics Research C*, vol. 82, pp. 225-235, 2018, http://dx.doi.org/10.2528/PIERC18020604.

[153] S. Rajkumar, A. Anto Amala and K.T. Selvan, “Isolation improvement of UWB MIMO antenna utilising molecule fractal structure,” *Electronics Letters*, vol. 55, pp. 576-579, 2019, https://doi.org/10.1049/el.2019.0592.

[154] A. Bhattacharya, B. Roy, S.K. Chowdhury and A.K. Bhattacharjee, “An Isolation Enhanced, Printed, Low-Profile UWB-MIMO Antenna with Unique Dual Band-Notching Features for WLAN and WiMAX,” *IETE Journal of Research*, vol. 68, pp. 496-503, 2022, https://doi.org/10.1080/03772063.2019.1612284.

[155] R. Sampath and K.T. Selvan, “Compact hybrid Sierpinski Koch fractal UWB MIMO antenna with pattern diversity,” *International Journal of RF and Microwave Computer-Aided Engineering*, vol. 30, e22017, 2020, https://doi.org/10.1002/mmce.22017.

[156] A. Bhattacharya, B. Roy, S.K. Chowdhury and A.K. Bhattacharjee, “Computational and experimental analysis of a low-profile, isolation-enhanced, band-notch UWB-MIMO antenna,” Journal of Computational Electronics, vol. 18, pp. 680-688, 2019, https://doi.org/10.1007/s10825-019-01309-3.

[157] A. Bhattacharjee, A. Karmakar, A. Saha and D. Bhattacharya, “Design of a compact UWB MIMO-diversity antenna incorporating fractal inspired isolation structure with

band notch characteristics," *Microwave and Optical Technology Letters*, vol. 63, pp. 2597-2605, 2021, https://doi.org/10.1002/mop.32927

[158] Y. Cai, G. Cheng, X. Ren, J. Wu, H. Ren, K. Song, Z.X. Huang and X.L. Wu, "Highly Isolated Two-Elements Ultra-Wideband MIMO Fractal Antenna with Multi Band-Notched Characteristics," *Progress In Electromagnetics Research C*, vol. 116, pp. 13-24, 2021, http://doi.org/10.2528/PIERC21080401.

[159] H. Sudarsan, R. Gayathri and K. Mahendran, "A novel square fractal dual port MIMO antenna with tri band rejection capabilities," *Journal of Ambient Intelligence and Humanized Computing*, 2021, https://doi.org/10.1007/s12652-021-03035-w.

[160] B. Punna and P. Muthusamy, "Compact fractal based UWB mimo antenna with dual band dispensation," *Analog Integrated Circuits and Signal Processing*, vol. 112, pp. 485-494, 2022, https://doi.org/10.1007/s10470-022-02060-9.

[161] A. Mohanty and S. Sahu, "4-port UWB MIMO antenna with bluetooth-LTE-WiMax band-rejection and vias-MCP loaded reflector with improved performance," *AEU - International Journal of Electronics and Communications*, vol. 144, 154065, 2022, https://doi.org/10.1016/j.aeue.2021.154065.

[162] P.K. Keshri, S.K. Sahu and R. Chandel, "Compact UWB MIMO antenna with dual band-notch characteristics," *International Journal of Electronics*, 2022, doi: 10.1080/00207217.2022.2129813.

[163] J. Banerjee, A. Gorai and R. Ghatak, "A novel isolation improvement technique using fractal neutralization line with dual band rejection attributes in a compact UWB MIMO antenna," *International Journal of Microwave and Wireless Technologies*, pp. 1-12, 2022, doi:10.1017/S1759078722001349.

[164] M. Zou, J. Pan and Z. Nie, "A Wideband Circularly Polarized Rectangular Dielectric Resonator Antenna Excited by an Archimedean Spiral Slot," *IEEE Antennas and Wireless Propagation Letters*, vol. 14, pp. 446-449, 2015, doi: 10.1109/LAWP.2014.2364296.

[165] N. Singh, A.K. Singh and V.K. Singh, "Design and performance of wearable ultrawide band textile antenna for medical applications," *Microwave and Optical Technology Letters*, vol. 57, pp. 1553-1557, 2015, https://doi.org/10.1002/mop.29131.

[166] A.A. Omar, O. Abu Safia and M. Nedil, "UWB coplanar waveguide-fed coplanar strips rectangular spiral antenna," *International Journal of RF and Microwave Computer-Aided Engineering*, vol. 27, e21115, 2017, https://doi.org/10.1002/mmce.21115.

[167] M. Gupta and V. Mathur, "Planar array of right-angled isosceles triangular microstrip antenna using Koch and meander lines for the Internet of things," *Turkish Journal of Electrical Engineering and Computer Sciences*, vol. 25, no. 3, 2017, https://doi.org/10.3906/elk-1603-297.